Internal Report
DESY F31-88-01
February 1988

THE ELECTRON SPECTRUM FROM B MESON DECAYS

by

K. Wachs

The Electron Spectrum from B Meson Decays

Dissertation
zur Erlangung des Doktorgrades
des Fachbereiches Physik
der Universität Hamburg

vorgelegt von
Karl Wachs
aus Frankfurt / Oder

Hamburg
1988

Für Kristin

Abstract

The Crystal Ball detector at the e^+e^- storage ring DORIS II has been used to measure the energy spectrum of electrons from semileptonic B meson decays. Branching ratios and semileptonic widths have been deduced using several models for the hadronic matrix elements. The branching ratio for semileptonic B meson decays into charmed states X_c has been found to be $BR(B \rightarrow e\nu X_c) = (11.7 \pm 0.4 \pm 0.7)\%$ as an average of all models used. The result for the Kobayashi - Maskawa matrix element is $|V_{cb}| = 0.052 \pm 0.005 \pm 0.005$. Upper limits on $|V_{ub}/V_{cb}|$ have been obtained. The weakest upper limit, $|V_{ub}/V_{cb}| < 0.26$ is obtained using the model by Grinstein *et al.* with data of electron energy $E_e > 2.4\ GeV$. Using models by Altarelli *et al.*, Wirbel *et al.*, and Körner *et al.* one gets an upper limit of $|V_{ub}/V_{cb}| < 0.15$.

Zusammenfassung

Diese Arbeit behandelt die Messung des Energiespektrums der Elektronen aus semileptonischen B-Meson-Zerfällen, wie sie mit dem Crystal-Ball-Detektor am DORIS II-Speicherring durchgeführt wurde. Dabei wurden Verzweigungsverhältnisse und semileptonische Breiten unter Benutzung mehrerer Modelle für die hadronischen Matrixelemente bestimmt. Der Mittelwert aller Modelle ergibt ein Verzweigungsverhältnis der B - Mesonen in Mesonen mit einem Charmquark von $BR(B \rightarrow e\nu X_c) = (11.7 \pm 0.4 \pm 0.7)\%$. Das Ergebnis für das Kobayashi - Maskawa Matrixelement ist $|V_{cb}| = 0.052 \pm 0.005 \pm 0.005$. Für das Verhältnis der Matrixelemente $|V_{ub}|/|V_{cb}|$ wurden folgende obere Grenzen gefunden: Unter Benutzung des Modells von Grinstein *et al.* und von Elektronen mit mehr als 2.4 GeV Energie ergibt sich eine obere Schranke von $|V_{ub}/V_{cb}| < 0.26$. Einen Grenzwert von $|V_{ub}/V_{cb}| < 0.15$ erhält man bei Anwendung der Modelle von Altarelli *et al.*, Wirbel *et al.* und Körner *et al.*.

Contents

List of Figures

List of Tables

Chapter 1

Introduction

High-energy physics probes nature at very small distances and therefore can lead to a fundamental understanding of matter. The current picture of particles and interactions in the energy range up to about 100 GeV is called the Standard Model [1]. This model has some free parameters. The knowledge of the parameters allows the prediction of cross-sections and decay rates for a wide range of reactions. These free parameters have to be measured by experiment, they cannot yet be predicted by any theory. In this thesis we measure two of them, the $|V_{ub}|$ and $|V_{cb}|$ elements of the Kobayashi - Maskawa matrix [2].

The text is divided into the following parts.

First we discuss some theoretical foundations of particle interactions and the physical processes accessible to e^+e^- interactions. These interactions open a large window to interesting physics, especially to the production and decay of heavy quarks. In the next chapter (2.3) we discuss some aspects of the Standard Model pertinent to our measurement, **the semileptonic weak decay of b flavoured mesons**. Several models describing this decay are discussed and their predictions are used to interpret the measurement of the inclusive electron spectrum from B mesons.

Chapter 3 describes the experimental setup, the e^+e^- storage ring DORIS II, and the Crystal Ball detector, a non-magnetic calorimeter able to detect and measure electromagnetically showering particles.

Chapter 4 contains the description of the data analysis. In the first subchapter (4.1) we explain the nomenclature of the Crystal Ball experiment, the definition of tracks, directions, and energies of particles. Chapter 4.2 treats the event selection and the available data sample. The electron selection in the multi-hadron events is explained in the 3^{rd} subchapter. Chapter 4.4 discusses the efficiency of the selections and the background rejection. Also the method used to relate the theoretical predictions (from chapter 2) to the measured electron spectrum is described there.

The results of the interpretation are presented in chapter 5 where also a comparison with results from other experiments is given.

Chapter 6 draws the conclusions.

All subjects which do not sequentially fit into this scheme are treated in the appendices. There we find the energy calibration procedure as well as the energy resolution of the Ball. The presentation of this part as an appendix appears appropriate since it needs input from various chapters and is referred to in others. The measurement of the luminosity is also discussed there, together with the tube chamber calibration and performance. Throughout the whole appendix special emphasis was placed on the check of the long term stability and the quality of the data.

Chapter 2

Theoretical Foundations

2.1 Particles and Their Interactions

fermions					
particles			properties		
generations			electric		
1	2	3	charge	colour	
u	c	t?	+2/3	r b g	quarks
d	s	b	-1/3	r b g	quarks
ν_e	ν_μ	ν_τ	0	0	leptons
e	μ	τ	-1	0	leptons

bosons				interactions	
type	electric charge	colour	mass $[GeV/c^2]$	type	coupling strength at $\sqrt{q^2} = 1 - 10\ GeV$
Z	0	0	92.6	weak neutral	$\frac{\pi\alpha/sin^2\theta_W}{M_Z^2 cos^2\theta_W} = G_F/\sqrt{2}$ $G_F\ M_P^2 \approx 1.023\ 10^{-5}$
W	± 1	0	81.8	weak charged	$\frac{\pi\alpha/sin^2\theta_W}{M_W^2} = G_F/\sqrt{2}$ $G_F\ M_P^2 \approx 1.023\ 10^{-5}$
γ	0	0	0	electromagnetic (QED)	$\alpha = \frac{e^2}{4\pi\hbar c\epsilon_0} \approx 1/137$
g	0	8 different e.g. r$\bar{\text{b}}$	0	strong (QCD)	$\alpha_s \approx 0.15$

Table 2.1: *The three quark and lepton generations and the gauge bosons. In addition each fermion has its antiparticle with opposite sign of charge and colour. The generations are ordered according to the mass of the fermions. The top quark has not yet been found. The electric charge is in units of e. Colour is the charge of the strong interaction, here called red, blue, and green. G_F is the Fermi coupling constant, θ_W is the Weinberg angle, M_W, M_Z, M_P are the masses of the W, Z bosons and the proton, respectively [3].*

All known particles are composed of two types of fermions, the quarks and the leptons. There also exist bosons which mediate the forces between the fermions. The

fermions are arranged in generations - see table 2.1. No internal substructure of these particles has been found so far. The lepton families carry the lepton family number, - e.g. e, ν_e carry the electron family quantum number. These numbers are conserved in all known interactions. If e.g. an electron is produced, also a positron or a $\overline{\nu_e}$ must be produced in order to conserve the lepton quantum number of the electron family.

On the side of interactions the Glashow - Salam - Weinberg model [4] was able to unify the quantum electrodynamics (QED) and the weak forces to the electroweak theory. The gauge bosons are the photon γ, the massive neutral boson Z^0 of mass M_Z, and the massive charged boson $W^{\pm}$ of mass M_W.

The properties of the hadrons – the strongly interacting particles – are described by the quantum chromodynamics [5](QCD). The bosons mediating the forces in strong interactions are the coloured massless gluons. Although the quarks are different in mass and carry different electric charges, QCD does not distinguish between quark flavours ($u, d, s, c, b, \ldots$). The strong interaction acts only between the colour charge of quarks and gluons. Each quark appears in three different colours (red, blue, green) and the anti-quarks in anticolours (antired, antiblue, antigreen). The bi-coloured gluons act on the colour charge of the quarks. The gluon comes in 8 different colour-anticolour combinations e.g. (red, antiblue). In contrast to quarks and gluons hadrons are directly observable. They appear as mesons and as baryons. Mesons are composed of a $q\bar{q}$ pair, baryons consist of a quark triplet – qqq. Hadrons are colour neutral – also called white. The fact that no free quark or gluon has been observed so far has led theory to set up the confinement postulate for quarks and gluons.

The sum of the charges within a quark - lepton generation is zero. Here one has to count the quarks three times due to the three different colours. If the sum would not be zero, the standard model would have some divergences. Therefore also the 6^{th} quark, the top quark, has been postulated. Limits on its mass are $m_t > 50\ GeV$ [6].

The weak interaction of quarks and leptons is described in chapter (2.3). For three generations of quarks and leptons we have 21 parameters which are needed to describe the standard model:

- 12 massses of quarks and leptons;
- 4 numbers for the Kobayashi - Maskawa matrix, see chapter (2.3);
- the coupling strengths of the strong, weak, and electromagnetic interactions, α_s, G_F, α;
- θ_w, the Weinberg angle which fixes the relative strength of the neutral weak current and the electromagnetic current, and the Higgs mass. W and Z masses can be expressed as functions of G_F and θ_W[1].

2.2 Physical Processes Accessible to e^+e^- Interactions

In e^+e^- storage rings the electrons and positrons orbit in bunches in opposite directions in an evacuated beam pipe. They collide head-on in specific interaction regions where

[1]The ρ parameter was assumed to be 1.0, where $\sqrt{\rho} = M_W/(M_Z cos\theta_W^2)$. If more than one Higgs boson is present ρ can vary and therefore also the M_W/M_Z ratio. Hence the parameter ρ might be added to the list of free parameters.

the detectors are installed. Besides the energy of the beams, the luminosity $\mathcal{L}$ is the other important number needed to describe the properties of an e^+e^- storage ring. $\mathcal{L}$ is the proportionality constant between the cross-section σ and the production rate of a specific interaction:

$$\frac{dN}{dt} = \sigma\mathcal{L} \tag{2.1}$$

Storage rings are designed with the aim to maximize the luminosity. It can be calculated by the relation:

$$\mathcal{L} = \frac{n^+ \, n^- \, \nu \, N_{bunches}}{\sigma_x^* \sigma_y^*} \tag{2.2}$$

where n^+, n^- are the number of electrons and positrons per bunch,
ν is the revolution frequency, $N_{bunches}$ is the number of bunches per beam, and $\sigma_x^*\sigma_y^*$ is the crossing area of the electron and positron beams. The quantities σ_x^*, σ_y^* are difficult to measure. Therefore one uses well-known e^+e^- interactions to measure the luminosity.

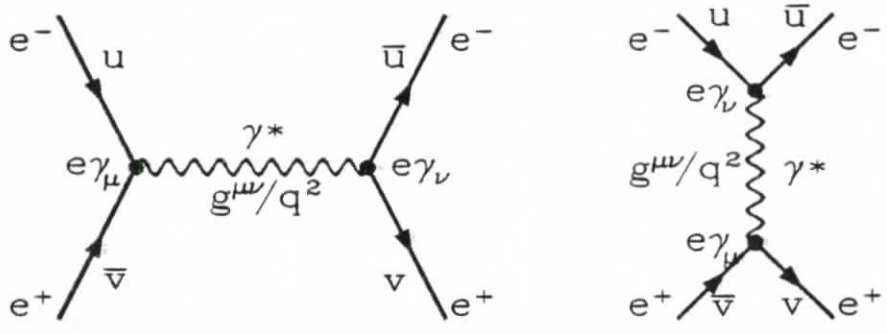

Figure 2.1: e^+e^- *Bhabha scattering: annihilation and exchange graphs.*

Feynman graphs are used to illustrate and calculate the interactions of particles. For the $e^+e^- \rightarrow e^+e^-$ interaction – called Bhabha scattering – we shall discuss the principle of how to obtain cross-sections. Radiative corrections are taken into account when we calculate the luminosity – see appendix B. Detailed discussions can be found in any text book about high-energy physics [7]. Figure 2.1 shows the lowest order diagram for Bhabha scattering. The interaction proceeds via the exchange of a virtual photon. 'Virtual' means that the mass of the photon is off shell, i.e. the square of the photon four momentum vector q is different from 0, the photon mass. The left-hand diagram in figure 2.1 shows a timelike photon with $q^2 = m^2 > 0$, wheras the photon momentum vector in the right-hand diagram is space-like with $q^2 = m^2 < 0$.

The differential cross-section is defined as :

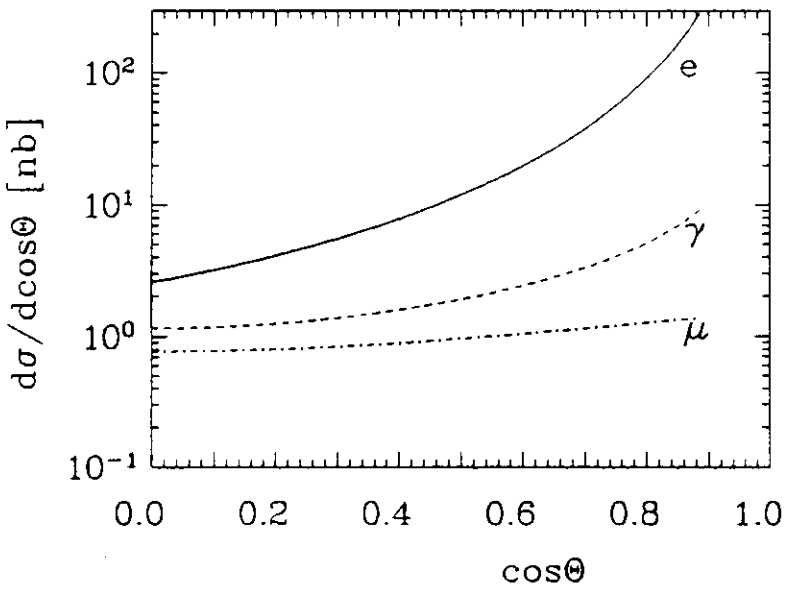

Figure 2.2: e^+e^- *QED cross-sections for the different processes* $e^+e^- \rightarrow e^+e^-, \gamma\gamma, \mu\overline{\mu}$ *at* $\sqrt{s} = 10.6$ *GeV. The cross-section to detect a single particle at a certain angle is plotted.*

$$d\sigma = |M|^2/FLUX \times dLips \tag{2.3}$$

where *dLips* is the Lorentz invariant phase space factor, $FLUX$ is the particle flux, and $|M|^2$ is the transition probability between the initial and the final state. M is the transition amplitude and consists of 2 contribution M_1, M_2 from the two graphs in figure 2.1; M_1 is defined as

$$\begin{aligned} M_1 &= j_\nu \quad \frac{g^{\nu\mu}}{q^2} \quad j_\mu \\ &= < e^-e^+|J_\nu|0 > \quad \frac{g^{\nu\mu}}{q^2} \quad < 0|J_\mu|e^+e^- > \\ &= \overline{u}_{e^-}(e\gamma_\nu)v_{e^+} \quad \frac{g^{\nu\mu}}{q^2} \quad \overline{v}_{e^+}(e\gamma_\mu)u_{e^-} \end{aligned} \tag{2.4}$$

and the amplitude M_2 for the second of the Feynman graphs is

$$\begin{aligned} M_2 &= j_\mu \quad \frac{g^{\mu\nu}}{q^2} \quad j_\nu \\ &= < e^+|J_\mu|e^+ > \quad \frac{g^{\mu\nu}}{q^2} \quad < e^-|J_\nu|e^- > \\ &= \overline{v}_{e^+}(e\gamma_\mu)v_{e^+} \quad \frac{g^{\mu\nu}}{q^2} \quad \overline{u}_{e^-}(e\gamma_\nu)u_{e^-} \end{aligned} \tag{2.5}$$

where the j is the leptonic current and J is the current operator between the final, $< |$, and initial, $| >$, states. $g^{\mu\nu}/q^2$ is the photon propagator. $u_{e^-}, \overline{v}_{e^+}$ are the spinors of

the electrons and positrons in the initial state. $\bar{u}_{e^-}, v_{e^+}$ are the spinors of the electrons and positrons in the final state.

In the center-of-mass frame of the reaction $e^+e^- \rightarrow e^+e^-$ (= laboratory frame of the strorage ring) the cross-section is

$$\frac{d\sigma}{d\cos\theta} = \pi\frac{\alpha^2\hbar^2c^2}{s}\left[\frac{cos^4\frac{\theta}{2}+1}{sin^4\frac{\theta}{2}} - \frac{2\ cos^4\frac{\theta}{2}}{sin^2\frac{\theta}{2}} + \frac{1}{2}\ (1+cos^2\theta)\right] \quad (2.6)$$

with

$$\pi\frac{\alpha^2\hbar^2c^2}{s} = 0.578nb$$
$$\text{at } \sqrt{s} = 10.6\ GeV \text{ center} - \text{of} - \text{mass energy.}$$

θ is the polar angle with respect to the beam axis. This cross-section has three contributions. The first term corresponds to the exchange scattering and the third term to the annihilation graph in figure 2.1. The second term is the interference term of the two graphs in $|M|^2 = |M_1|^2 + 2\ \Re(M_1\ M_2^*) + |M_2|^2$. Figure 2.2 shows the cross-section as a function of the polar angle. The cross-section is asymmetric in $cos\theta$ because of the exchange graph. When the charge of the final state electron is not taken into account, the dependence becomes symmetric again.

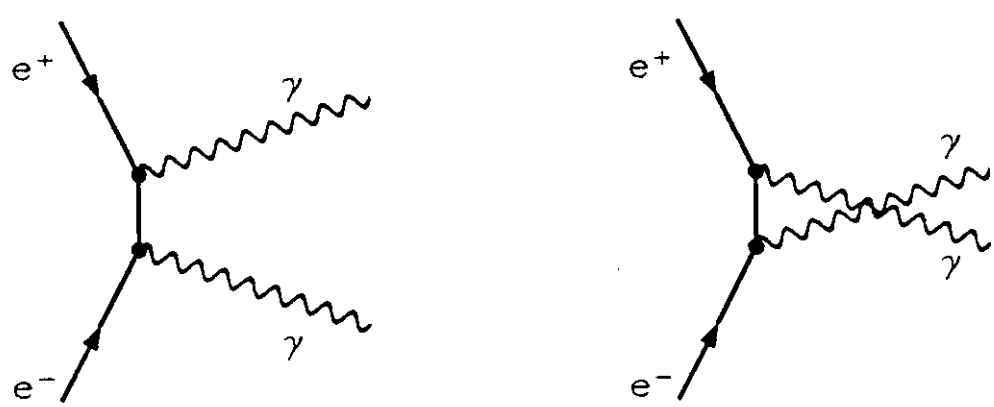

Figure 2.3: e^+e^- *annihilation graphs into two photons.*

Another process is shown in figure 2.3. There the e^+e^- pair annihilates and radiates two photons. For $P_e \approx \sqrt{s}/2$ the cross-section for this process $e^+e^- \rightarrow \gamma\gamma$ is:

$$\frac{d\sigma}{d\cos\theta} = 2\ \pi\frac{\alpha^2\hbar^2c^2}{s}\left[\frac{1+cos^2\theta}{1-cos^2\theta+\frac{(2m_e)^2}{s}cos^2\theta}\right] \quad (2.7)$$

with

$$2\,\pi\frac{\alpha^2\hbar^2c^2}{s} \;=\; 1.16nb \quad \text{at} \quad \sqrt{s} = 10.6\ GeV$$

Figure 2.2 shows the cross-section as a function of the polar angle. The cross-section is symmetric in $cos\theta$ as the photons in the final state are indistinguishable. These two processes are pure QED interactions. They are used to measure the luminosity. The integral over the differential cross-section of $e^+e^- \to e^+e^-$ diverges at $\theta = 0$. Therefore the total cross-section is not a meaningful quantity for this reaction.

In practice one measures the interactions in a certain solid angle interval and thus avoids problems with divergences. Using the Crystal Ball – see appendix A – the visible cross-section inside the solid angle $|cos\theta| < 0.75$ is about 12.8 nb and 1.6 nb for the processes $e^+e^- \to e^+e^-, \gamma\gamma$, respectively.

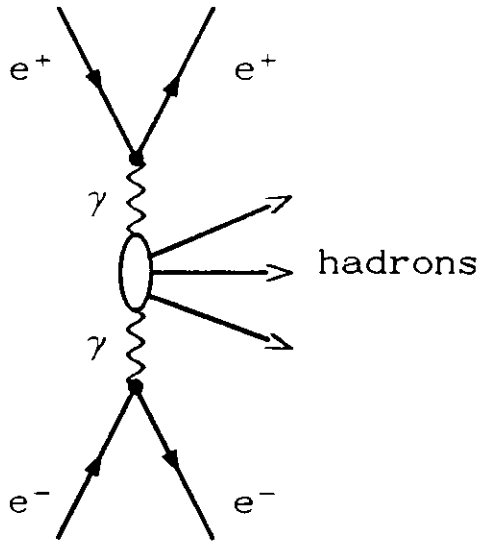

Figure 2.4: *Two-photon process in e^+e^- interactions.*

As the virtual photon in an e^+e^- annihilation has the quantum numbers $J^{P,C} = 1^{-,-}$ only final state systems with these quantum numbers can be produced directly. Another way to produce particles is via two-photon interactions as shown in figure 2.4. Both particles (e^+ and e^-) radiate a photon. Those two photons can then form an intermediate state with different quantum numbers e.g., $J^{P,C} = 0^{\pm+}, 2^{\pm+}, 3^{++}, 4^{\pm+}, 5^{+-}$....

Beside the QED reactions $e^+e^- \to e^-e^-, \gamma\gamma$ also the process $e^+e^- \to f\overline{f}$ can occur, where f is a charged fermion and $\overline{f}$ is its antifermion. Figure 2.5 shows a Feynman graph for this interaction. The virtual photon does not only produce an e^+e^- pair, but can also produce any other fermion-antifermion pair, if allowed by kinematics. For the QED processes $e^+e^- \to \mu\overline{\mu}$ or $e^+e^- \to \tau\overline{\tau}$ this graph can be calculated, too. The cross-section is

$$\frac{d\sigma}{d\cos\theta} \;=\; \frac{1}{4}\frac{\alpha^2\hbar^2c^2}{s}\beta\left[1 + cos^2\theta + (1-\beta^2)sin^2\theta\right] \qquad (2.8)$$

with

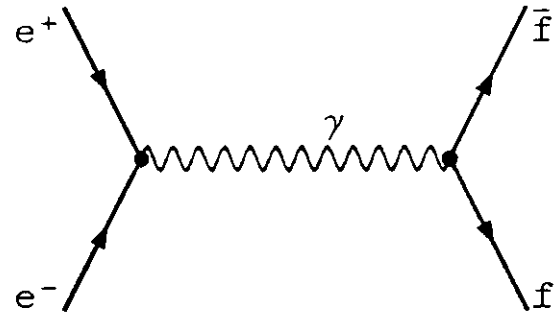

Figure 2.5: *Diagram of an e^+e^- annhilation resulting in a fermion antifermion pair.*

$$\frac{1}{4}\pi\frac{\alpha^2\hbar^2c^2}{s} = 0.29nb \text{ at } \sqrt{s} = 10.6\ GeV$$

$\beta = v/c$ represents the velocity of the final state fermions. The integration over $cos\theta$ results in

$$\sigma = \frac{4}{3\pi}\frac{\alpha^2\hbar^2c^2}{s}\frac{3\beta-\beta^3}{2} \tag{2.9}$$

$$= 0.77\ nb \text{ at } \sqrt{s} = 10.6\ GeV$$

In figure 2.2 also the cross-section for this process is shown. The two interactions used to measure the luminosity have clearly the highest cross-sections.

Instead of a $\mu\overline{\mu}$ or $\tau\overline{\tau}$ also a quark - antiquark pair ($q\overline{q}$) can be produced in e^+e^- annihilation. In the lowest order calculations this reaction has the same form as the reaction $e^+e^- \rightarrow \mu\overline{\mu}$. Only the different quark charges have to be taken into account. Hence the ratio R of $q\overline{q}$ pair to $\mu\overline{\mu}$ pair production is

$$R = \frac{\sigma(e^+e^- \rightarrow q\overline{q})}{\sigma(e^+e^- \rightarrow \mu\overline{\mu})} = 3\sum_{i=1}^{n}\left(\frac{e_{qi}}{e}\right)^2(1+\frac{\alpha_s}{\pi}), \tag{2.10}$$

where e is the charge of the muon and e_{qi} are the electric charges of the quarks. As the quarks can be produced in three different colour-anticolour pairs, the factor of 3 is present. The sum runs over the number of quarks which can be produced at the center-of-mass energy of the e^+e^- collision. The term $(1+\alpha_s/\pi)$ reflects the lowest order QCD corrections which are not discussed here. The produced quarks are not free particles like in the case of $\mu\overline{\mu}$. Due to the confinement they have to form either a meson (e.g. ρ^0) or undergo a fragmentation process in which many hadrons can be produced.

The quantity R can be used to search for resonances at different energies. The R value in the continuum has been found to be $(3.52\pm0.03\pm0.14)$ [10] at $\sqrt{s} = 9.46\ GeV$. A different value of R would indicate a resonance. Figure 2.6 shows the value of R as

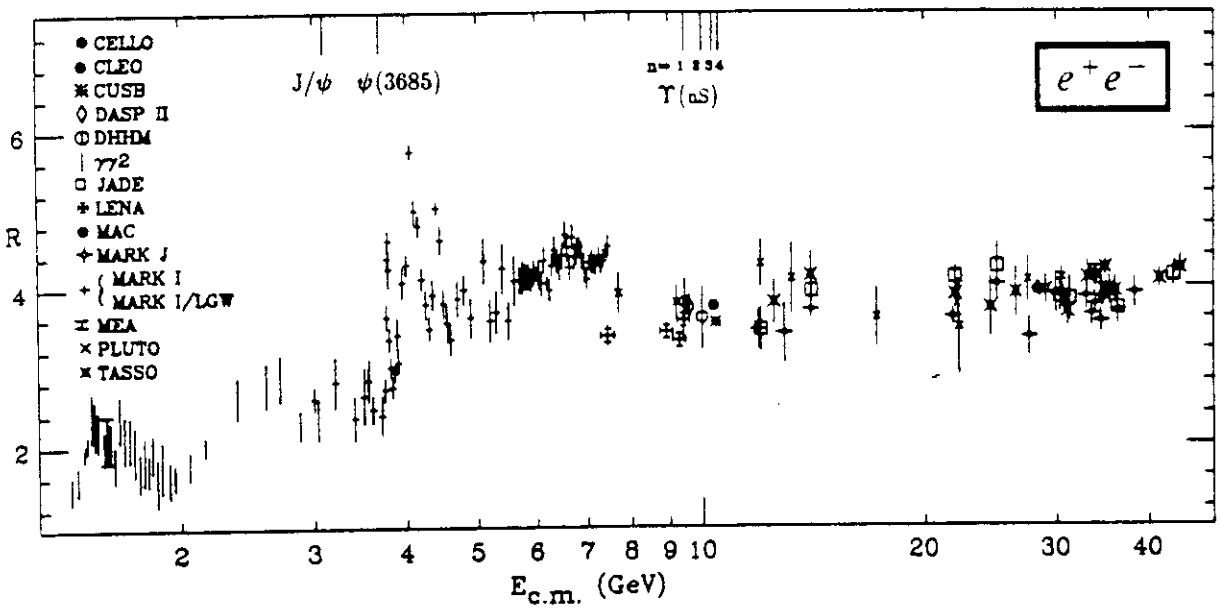

Figure 2.6: *Compilation of R from different experiments and center-of-mass energies, according to [8].*

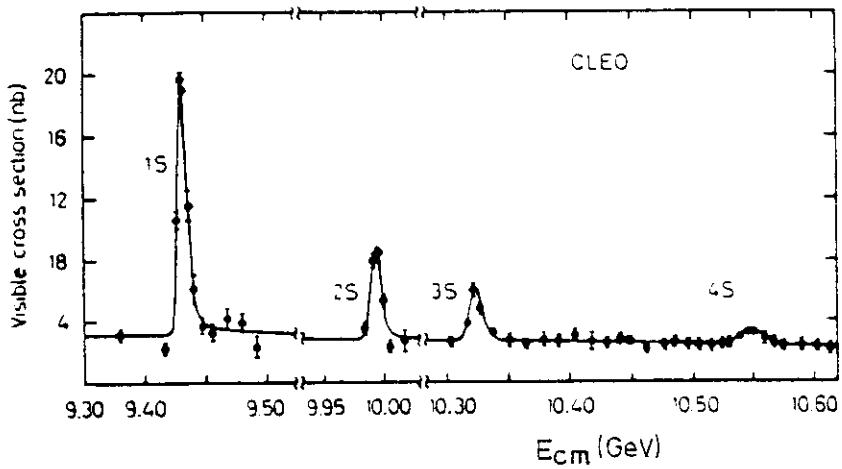

Figure 2.7: *Visible cross-section at the Υ resonances, as measured by the CLEO experiment at CESR [9].*

obtained from different experiments at various energies. Several steps and bumps at energies from 0.5 to 10 GeV are visible. There are the thresholds of the open flavour productions of the c, b flavoured mesons and the excitations of other meson resonances. The quantity R was used at PETRA experiments to search for the top quark since one would expect a rise of R by 4/3 when passing the top quark threshold.

Instead of plotting the ratio R, also $\sigma_{visible}(e^+e^- \rightarrow hadrons)$ can be used directly to perform a search for resonances. Figure 2.7 shows the visible cross-section in the energy range between 9.45 and 11.2 GeV as performed by the CLEO experiment at the CESR storage ring. Four clear peaks can be distinguished. They have been identified with the $\Upsilon(1S)$, $\Upsilon(2S)$, $\Upsilon(3S)$, and $\Upsilon(4S)$ resonances which are interpreted as bound states of $b\bar{b}$ quark pairs. The first three resonances lie below twice the mass of the lightest B meson of 5.279 GeV/c^2. Therefore they cannot decay into these mesons. QCD predicts that they will mostly decay via a three gluon intermediate state.

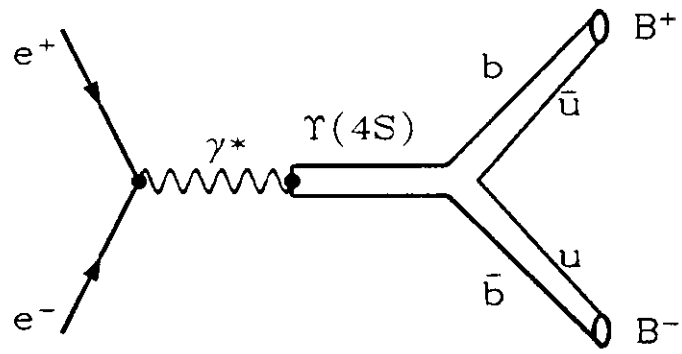

Figure 2.8: $\Upsilon(4S)$ *production in* e^+e^- *annihilation, with the subsequent decay into a* $B\overline{B}$ *pair.*

The $\Upsilon(4S)$ resonance at 10.580 GeV/c^2 lies above the $B\overline{B}$ threshold. Therefore it can decay into $B\overline{B}$ mesons as indicated in figure 2.8. The B mesons themselves $-B^{\pm}, \overline{B^0}, B^0$ - decay weakly. Hence the $\Upsilon(4S)$ resonance yields convenient access to an exciting field of physics, that of weak interactions of the b quark.

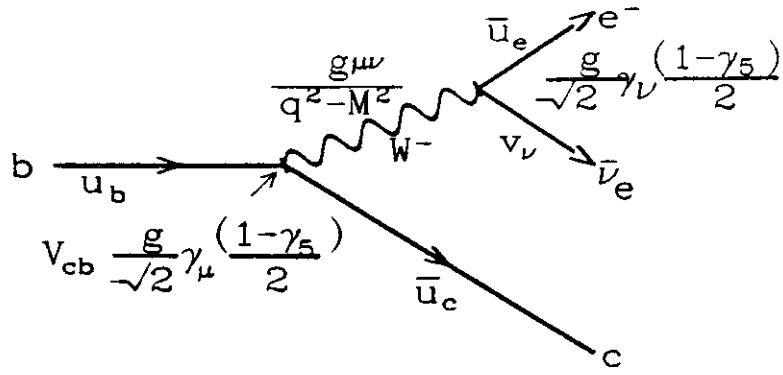

Figure 2.9: *Weak decay of a free b quark.*

2.3 Weak Interactions

The cross-sections or decay widths of processes under weak interaction are calculated in a similar way as shown for Bhabha $e^+e^- \rightarrow e^+e^-$ scattering. The weak interactions of leptons with quarks (hadrons) are described in the current-current picture ansatz – see equation (2.4). As the forces are carried by the heavy boson W, the photon propagator $g^{\mu\nu}/q^2$ has to be replaced by

$$\frac{g^{\mu\nu}}{q^2 - M_W^2}$$

The region of q^2 we are interested in ($q^2 < 2.5\ GeV^2$), q^2 is much smaller than the mass of the W boson. Hence the propagator times the coupling constant $g/\sqrt{2}$ and factors $1/2$ can be replaced by $G_F/\sqrt{2} = g^2/8M_W^2$, the Fermi coupling constant. This constant we shall use in the following instead of the coupling constant $g/\sqrt{2}$ and factors $1/2$ in $(1-\gamma_5)/2$.

The weak leptonic current in figure 2.9 is

$$\begin{aligned} j_\nu(lepton) &= < e\nu|J_\nu|0 > \\ &= \overline{u}_e \gamma_\nu (1-\gamma_5) v_\nu \end{aligned} \tag{2.11}$$

It has the vector - axial vector structure $V-A$.

The weak hadronic current has also the $V-A$ structure. In the free quark picture the current can be given explicitely. For the calculation of weak decays of hadrons (mesons) effects from QCD binding forces of the quarks inside the hadrons have to be taken into account. Therefore the current cannot be given explicitly like in the leptonic case. Approaches to solve this problem are give in the next chapter. First we shall discuss the free quark decays.

In addition, the eigenstates from QCD interactions do not need to be the eigenstates of the electroweak interactions. In order to explain the suppression of weak decays of strange particles - particles with an s or $\overline{s}$ quark - Cabbibo [12] introduced a mixing of the d and s quarks under weak interactions. Decays with $\Delta S = 1$ were suppressed by a factor of $sin\theta_c$, while $\Delta S = 0$ decays were multiplied by $cos\theta_c$, where $\theta_c \approx 14^0$. In order to explain the absence of neutral flavour changing neutral currents Glashow, Iliopoulos, and Maiani [11] extended this formalism to a concept mostly referred to as GIM mechanism. They introduced a new quark c - for charm - forming a doublet with the s quark. The weak hadronic current then is defined as:

$$j_\mu(quark) = (\overline{u}, \overline{c})\, \gamma_\mu (1-\gamma_5)\; V \begin{pmatrix} d \\ s \end{pmatrix} \tag{2.12}$$

with

$$V = \begin{pmatrix} cos\theta_c & sin\theta_c \\ -sin\theta_c & cos\theta_c \end{pmatrix} \tag{2.13}$$

Only one angle, the Cabbibo angle, is needed. This formalism was extended to three generations of quarks by Kobayashi and Maskawa [2]. The V matrix then is a 3×3 unitary matrix and the weak hadronic current becomes

$$j_\mu(quark) = (\overline{u}, \overline{c}, \overline{t})\, \gamma_\mu (1-\gamma_5)\; V \begin{pmatrix} d \\ s \\ b \end{pmatrix} \tag{2.14}$$

with

$$V = \begin{pmatrix} V_{ud} & V_{us} & V_{ub} \\ V_{cd} & V_{cs} & V_{cb} \\ V_{td} & V_{ts} & V_{tb} \end{pmatrix} \tag{2.15}$$

$$= \begin{pmatrix} c_1 & s_1c_3 & s_1s_3 \\ -s_1c_2 & c_1c_2c_3 - s_2s_3e^{i\delta} & c_1c_2s_3 + s_2c_3e^{i\delta} \\ -s_1s_2 & c_1s_2c_3 + c_2s_3e^{i\delta} & c_1s_2s_3 - c_2c_3e^{i\delta} \end{pmatrix}$$

$$= \begin{pmatrix} 0.9743 - 0.9757 & 0.219 - 0.225 & 0.0 - 0.008 \\ 0.219 - 0.225 & 0.9733 - 0.9748 & 0.039 - 0.055 \\ 0.002 - 0.017 & 0.037 - 0.048 & 0.9987 - 0.9993 \end{pmatrix}$$

in the parametrization according to Kobayashi - Maskawa [2]. As the matrix is unitary it has four independent numbers which influence physically observables. They are three angles $\theta_{1,2,3}$ and one complex phase factor δ. The quantities s_i, c_i are abbreviations for $sin\theta_i$ and $cos\theta_i$, respectively. θ_1 is the Cabbibo angle θ_c in the 2×2 matrix. Various other parametrization have been proposed [13]. They are not discussed here.

In equation (2.15) also the presently known values of the matrix elements are noted as intervals. They are only partly deduced from various measurements [14]. The elements in the last row are purely deduced by the unitarity requirement. The transitions within one generation – the diagonal elements – are enhanced compared to the transitions between the different generations – the off-diagonal elements. The corresponding decays are also called Cabbibo allowed and Cabbibo suppressed, respectively. Due to the complex phase factor in this matrix it is also possible to describe CP violating effects in weak decays, e.g. the K^0 decays. This is only true if none of these Kobayashi - Maskawa matrix elements is zero.

As the b quark cannot decay via neutral currents to an s or d quark, only two decay modes are left: $b \rightarrow u$ and $b \rightarrow c$. Hence the two matrix elements $|V_{ub}|$ and $|V_{cb}|$ can be measured in b quark decays. As the b quark cannot be produced as a free particle, one has to use e.g. B mesons to study its decays. In the next chapter we disuss this approach.

2.3.1 Semileptonic B Meson Decays

B mesons which can be produced at the $\Upsilon(4S)$ resonance are the $B^{\pm}, B^0$, and $\overline{B^0}$. They have the properties listed in table 2.2. The b quark inside the B mesons may

Meson	quark contents	mass $[MeV/c^2]$
B^+	$\bar{b}u$	$5279.3 \pm 0.8 \pm 2.0$
B^-	$b\bar{u}$	$5279.3 \pm 0.8 \pm 2.0$
B^0	$\bar{b}d$	$5281.3 \pm 0.8 \pm 2.0$
$\overline{B^0}$	$b\bar{d}$	$5281.3 \pm 0.8 \pm 2.0$

Table 2.2: *Masses, charges, and quark contents of B mesons [15].*

decay into a c or u quark emitting a W boson. Several theories predict the differential width $d\hat{\Gamma}$ for these decays:

$$d\Gamma = |V_{xb}|^2 \, d\hat{\Gamma} = |V_{xb}|^2 \left|\frac{M}{V_{xb}}\right|^2 dLips. \qquad (2.16)$$

First of all we shall discuss the model for a free b quark decay and apply some modifications to this model. Then we explain the predictions by various other models which calculate $d\hat{\Gamma}$ for the weak decay of a B meson to a final state meson containing a c or u quark.

Free Quark Spectator Model

We start with the description of the weak decay of a free b quark. In this part we follow the description of [16].

Figure 2.9 shows the Feynman graph of a weak semileptonic decay of a b quark. The explicit form of the weak current for the transition $b \to c$ is

$$\begin{aligned} j_\mu &= < c|J_\mu|b > \\ &= \overline{u}_c \gamma_\mu (1-\gamma_5) u_b V_{cb} \\ &= \hat{j}_\mu \, V_{cb} \end{aligned} \tag{2.17}$$

The coupling constant $g/\sqrt{2}$ and a factor $1/2$ have been absorbed into $G_F/\sqrt{2}$ appearing in M.

Hence the weak maxtrix element M is

$$\begin{aligned} M &= j_\mu(lepton) \times \frac{G_F}{\sqrt{2}} \times \hat{j}^\mu(quark) \; V_{cb} \\ &= < e,\nu|J_\mu(lepton)|0 > \frac{G_F}{\sqrt{2}} < c|\hat{J}^\mu(quark)|b > V_{cb} \\ &= \overline{u}_e \gamma_\mu (1-\gamma_5) v_\nu \; \frac{G_F}{\sqrt{2}} \; \overline{u}_c \gamma^\mu (1-\gamma_5) u_b V_{cb} \end{aligned} \tag{2.18}$$

The differential electron spectrum from free b quark decays leading to a c quark is found to be:

$$\frac{d\Gamma_{cb}^{f.q.}}{dx} \equiv |V_{cb}|^2 \times \frac{d\hat{\Gamma}(b \to e\nu c)}{dx} = |V_{cb}|^2 \times \frac{G_F^2 m_b^5}{96\pi^3} \times g(z,x) \tag{2.19}$$

with

$$g(z,x) = \frac{x^2[1-z^2-x]\;[(1-x)(3-2x)+(3-x)z^2]}{(1-x)^3}$$

and $z \equiv m_c/m_b$, $x = E_e/m_b$, where m_c (m_b) denote the c (b) quark masses, respectively. They are free parameters in this model.

Integrating equation (2.19) over the electron energy – x – yields the decay rate

$$\Gamma_{cb} \equiv |V_{cb}|^2 \, \Gamma^{\hat{f}.q.}(b \to e\nu c) = |V_{cb}|^2 \times \frac{G_F^2 m_b^5}{192\pi^3} \times f(z) \tag{2.20}$$

with $f(z) = 1 - 8z^2 + 8z^6 - z^8 - 24z^4 \ln z$.
Replacing c by u in equations (2.18) to (2.20) gives the results for the $b \rightarrow u$ transition.

Modified Free Quark Spectator Model

Altarelli, Cabibbo, Corbo, Maiani, and Martinelli (ACM) [16] have modified the free quark spectator model to include binding effects of the b quark inside the B meson. The b quark is assumed to be moving with momentum $\vec{p}$ inside the meson, where $\vec{p}$ is distributed according to a Gaussian in all three components:

$$\frac{dN(|\vec{p}|)}{d|\vec{p}|} = \frac{4\ |\vec{p}|^2}{\sqrt{\pi}\ p_F^3} \exp\left(-\frac{|\vec{p}|^2}{p_F^2}\right), \tag{2.21}$$

with an adjustable Fermi motion parameter p_F. Together with the spectator quark the b quark forms the B meson of mass M_B. Energy and momentum conservation yields for the effective b quark mass

$$m_b^2 = M_B^2 + m_{sp}^2 - 2M_B\sqrt{|\vec{p}|^2 + m_{sp}^2} \tag{2.22}$$

where m_{sp} is the mass of the spectator quark. $|\vec{p}|$ is constrained to a region where $m_b^2 > m_c^2$. As the term $M_B^2 = (5.280\,GeV/c^2)^2$ [15] is much bigger than the mass of the spectator $m_{sp}^2 \simeq (0.15\,GeV/c^2)^2$, a variation of this m_{sp} contribution can be neglected. A variation of the spectator mass in the argument of the square root can be absorbed by an effective change of the average momentum p_F. Hence the model has the three free parameters m_c, m_u, p_F. The B meson mass has been determined by measurements.

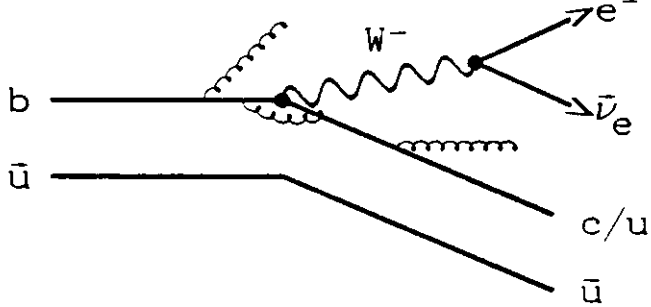

Figure 2.10: *Weak decay of a free b quark, with soft gluon radiation*

In addition the model takes into account the effect of soft gluon radiation, illustrated in figure 2.10. The correction factor can be written as: $Q(z,x) = 1 - 2\alpha_s G(z,x)/3\pi$. It has to be applied to the right-hand side of equations (2.19) and (2.20). For non-zero quark masses ($z > 0$) G depends only weakly on x and can be treated as a constant: $G'(z) = \overline{G(z,x)}$. G' is tabulated in literature [17]. With the quark masses $m_c = 1.60\ GeV/c^2$, $m_b = 4.85\ GeV/c^2$, $m_u = 0.15\ GeV/c^2$ and the strong coupling constant $\alpha_s = 0.24$ one obtains for the gluonic correction: $Q(z = 1.60/4.85) = 0.88$ in the $b \rightarrow c$ channel and $Q(z = 0.15/4.85) = 0.82$ in the $b \rightarrow u$ channel.

In figure 2.11 the predicted spectra for the $b \rightarrow u$ and $b \rightarrow c$ channels are compared for some different parameter settings of this model. The effect of a variation of the p_F

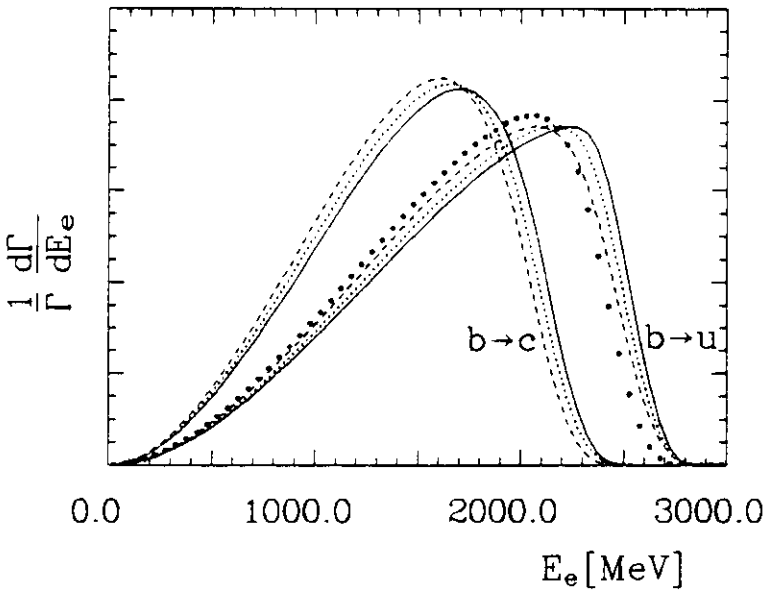

Figure 2.11: *The electron spectrum as predicted by the model of ACM. The b→c and b→u contributions are indicated. Different p_F and c, u quark masses have been used, all in units of MeV/c or MeV/c^2:*
$b \to c$ channel: Solid $p_F = 100, m_c = 1600$; dotted $p_F = 200, m_c = 1600$; dashed $p_F = 200, m_c = 1700$;
$b \to u$ channel: Solid $p_F = 100, m_u = 150$; dotted $p_F = 200, m_u = 150$; dashed $p_F = 300, m_u = 150$; boldface dotted $p_F = 200, m_u = 650$;

parameter is similar to the variation of the final state quark mass m_c or m_u. Larger p_F values soften the spectrum, as well as higher m_c or m_u values.

A change of p_F by $\Delta p_F = -100\ MeV/c^2$ gives about the same change in the middle of the electron spectrum as an increase of m_c, m_u by $100\ MeV/c^2$. The endpoint of the electron spectrum is determined by the final state quark mass, whereas p_F smears the spectrum, the quark mass sets strict kinematical limits.

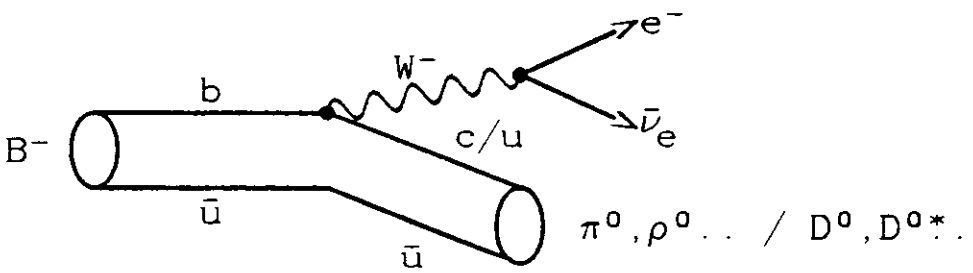

Figure 2.12: *Feynman graph of the weak decay of a B meson*

Meson Decay Models

In this chapter we follow the nomenclature of [18]. The Feynman graph of the decay of a B meson is shown in figure 2.12. In order to calculate the width in the meson decay models one has to develop the weak hadronic current $j(hadron) = V_{xb}\hat{j}(hadron) = V_{xb} < X|\hat{J}|B >$ between the B meson and the final state meson X.

The amplitude M is defined as

$$\begin{aligned} M &= j_\mu(lepton) \times \frac{G_F}{\sqrt{2}} \times \hat{j}^\mu(hadron)\ V_{xb} \\ &= < e,\nu|J_\mu(lepton)|0 > \frac{G_F}{\sqrt{2}} < X|\hat{J}^\mu(hadron)|B > V_{xb} \\ &= \overline{u}_e \gamma_\mu(1-\gamma_5) v_\nu \frac{G_F}{\sqrt{2}} < X|\hat{J}^\mu(hadron)|B > V_{xb} \end{aligned} \tag{2.23}$$

$|M|^2$ can be splitted into a lepton and a hadron part

$$|M|^2 = h_{\mu\nu} l^{\mu\nu}\ G_F^2/2\ |V_{xb}|^2 \tag{2.24}$$

with

$$\begin{aligned} h_{\mu\nu} &= \hat{j}^\dagger_\mu(hadron)\hat{j}_\nu(hadron) \\ \text{and} & \\ l^{\mu\nu} &= j^{\mu\dagger}(lepton) j^\nu(lepton) \end{aligned} \tag{2.25}$$

The leptonic part $l^{\mu\nu}$ can be calculated directly since the wave functions of the electron and neutrino are known.

The hadonic current operator can be splitted like

$$\hat{J}(hadron) = V(hadron) - A(hadron).$$

Hence the hadronic tensor $h_{\mu\nu}$ becomes

$$h_{\mu\nu} = < X|V_\mu - A_\mu|B >< B|V_\nu - A_\nu|X > \tag{2.26}$$

In general $h_{\mu\nu}$ can be developed as a function of the Lorentz invariant four momentum vectors P_X, P_B. Neglecting terms vanishing for a zero lepton mass $h_{\mu\nu}$ can be written as:

$$\begin{aligned} h_{\mu\nu} \approx & -\alpha g_{\mu\nu} \\ & +\beta(P_B + P_X)_\mu (P_B + P_X)_\nu \\ & +i\gamma \epsilon_{\mu\nu\rho\sigma}(P_B + P_X)^\rho (P_B - P_X)^\sigma \end{aligned} \tag{2.27}$$

The electron spectrum of the weak decay then is (in units where $\hbar = 1$ and $c = 1$):

$$\begin{aligned}\frac{d^2\hat{\Gamma}}{dx\ dy} = \frac{G_F^2 M_B^5}{32\pi^3} \times (\quad & \alpha \quad \frac{y}{M_B^2} \\ & +2\beta \quad \left[2x(1 - \frac{M_X^2}{M_B^2} + y) - 4x^2 - y\right] \\ & -\gamma \quad y\left[1 - \frac{M_X^2}{M_B^2} - 4x + y\right])\end{aligned} \tag{2.28}$$

with $x = E_e/M_B$, $y = (P_B - P_X)^2/M_B^2 = q^2/M_B^2$ and $P_B, M_B; P_X, M_X$ denoting the four-momenta and the masses of the initial and final state mesons, respectively. The form factors α, β, and γ are functions of q^2 and have to be calculated for the individual decays. They are calculated by comparing the hadronic tensor $h_{\mu\nu}$ with the predictions obtained by the models for this quantity. We shall give the explicit forms of the form factors for the channel $0^- \to 0^-$, e.g. $B \to D$ (neglecting terms vanishing for zero lepton masses):

$$\begin{aligned} < X|A_\mu|B > &= 0 \\ < X|V_\mu|B > &= f_+(P_B + P_X)_\mu \end{aligned} \tag{2.29}$$

and hence

$$\begin{aligned} \alpha &= 0 \\ \gamma &= 0 \\ \beta &= f_+^2 \end{aligned} \tag{2.30}$$

For the transition $O^- \to 1^-$, e.g. $B \to D^*$, one obtains

$$\begin{aligned} < X|A_\mu|B > &= f\epsilon_\mu^* + a_+(\epsilon^* \cdot P_B)(P_B + P_X)_\mu \\ < X|V_\mu|B > &= ig\epsilon_{\mu\nu\rho\sigma}\epsilon^{*\nu}(P_B + P_X)^\rho(P_B - P_X)^\sigma \end{aligned} \tag{2.31}$$

where ϵ^* is the polarization of the final state meson X, which results in

$$\begin{aligned} \alpha &= f^2 + 4m_B^2 P_X^2 g^2 \\ \gamma &= 2gf \\ \beta &= \frac{1}{4}\frac{f^2}{m_X^2} - m_B^2 y g^2 + \frac{1}{2}\left[\frac{m_B^2}{m_X^2}(1 - y) - 1\right] f a_+ + \frac{m_B^2 P_X^2}{m_X^2} a_+^2 \end{aligned} \tag{2.32}$$

For the higher excited states which have been used so far only by [18] we refer to the above reference. The meson decay models discussed now use different approaches to calculate the matrix elements $< X|J|B >$ and therefore get different form factors f_+, f, a_+,and g.

Non-relativistic Constituent Quark Model

Grinstein, Isgur and Wise (GIW) [18] use a non-relativistic constituent quark model. Their $q\bar{q}$ potential has the form

$$V(r) = -\frac{4\alpha_s\hbar c}{3r} + c + \frac{br}{\hbar c} \tag{2.33}$$

with $\alpha_s = 0.5, c = -0.84\ GeV$, and $b = 0.18\ GeV^2$. Harmonic oscillator wave functions are used to calculate the meson wave functions. The form factors for the decay to 0^- and 1^- are:

$$\begin{aligned} f_+ &= A \times F(q^2) \\ f &= B \times F(q^2) \\ g &= C \times F(q^2) \\ a_+ &= 0 \\ &with \\ F(q^2) &= D\ exp\left[-\frac{m_{sp}}{4\tilde{m}_X\tilde{m}_B}\left(\frac{q^2_{max}-q^2}{E}\right)\right] \end{aligned} \tag{2.34}$$

where A, B, C, D, E are functions of the quark and meson masses, $\tilde{m}_i = m_{q1} + m_{q2}$ are the so - called mock meson masses. q^2 is the momentum tarnsfer between the B meson and final state meson X as defined in equation(2.28). Furthermore also form factors for the transition to final state mesons with $2S$ quantum states are calculated by GIW.

The calculated transition rates ($B \rightarrow D, D^*, D^{**}$) saturate the electron spectrum above about 1.5 GeV. As the D^{**} contributes only about 10% to the inclusive rate, it is assumed that the higher excited states will contribute even less and therefore can be neglected.

For the $b \rightarrow u$ transitions mass states up to 1.5 GeV/c^2 are taken into account. As higher mass states will contribute only to electron energies below $\simeq 2.2\ GeV$ the predicted inclusive electron energy spectrum is valid only above $\simeq 2.2\ GeV$. Hence for the calculation of branching ratios and $|V_{ub}|$ we use the $b \rightarrow u$ prediction only above $E_e = 2.2\ GeV$. Thus only

$$\frac{BR(B \rightarrow e\nu X(1S, 1P, 2S)_u)}{BR(B \rightarrow e\nu X(1S, 1P, 2S)_c)} \text{ instead of } \frac{BR(B \rightarrow e\nu X_u)}{BR(B \rightarrow e\nu X_c)}$$

can be measured with the inclusive electron spectrum.

Corrections to the Non-Relativistic Constituent Quark Model

Altomari and Wolfenstein (AW) [19] have modified GIW's model in the $b \rightarrow c$ channel. They treat the constituent quark masses in a slightly different way, but obtain quite similar numbers for the $B \rightarrow e\nu D$ channel (table 2.3). In the $B \rightarrow e\nu D^*$ channel they

have tested the dependence of the semileptonic width as a function of '$a+$', a factor appearing in the calculation of the form factor β - see equations (2.34) and (2.28). It was set to 0 by GIW. With AW's preferred value for '$a+$' the semileptonic width $\Gamma(B \to e\nu D^*)$ becomes smaller by a factor of 1.78 compared to the prediction by GIW.

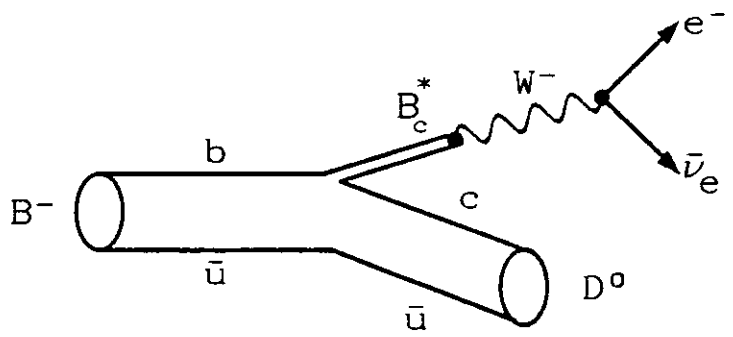

Figure 2.13: *Weak decay of a B meson in the nearest pole dominance picture.*

Relativistic Bound State Model I

The third model, by Wirbel, Stech and Bauer (WSB) [20], uses relativistic bound state wave functions to calculate the rates. Form factors are calculated in the infinite momentum frame at $q^2 = 0$, i.e. at the electron endpoint. The form factors are extrapolated to $q^2 \neq 0$ under the assumption of nearest pole dominance. Figure 2.13 illustrates this method. The form factors for the decay to 0^- and 1^- are:

$$\begin{aligned} f_+ &= I \times POLE(q^2, 1^-) \\ f &= I(M_X + M_B) \times POLE(q^2, 0^+) \\ a_+ &= I\frac{2}{M_X + M_B} \times POLE(q^2, 1^+) \\ g &= I\frac{1}{M_X + M_B} \times POLE(q^2, 1^-) \end{aligned} \qquad (2.35)$$

with

$$POLE(q^2, S) = \frac{1}{1 - q^2/M(S)^2}$$

where I is the integral of the overlap of the initial and final state meson wave functions and $M(S)$ is the mass of the B^*, see figure 2.13. Only transitions to the $1S$ final states D, D^* and π, ρ, respectively, have been calculated. Following the arguments discussed above, this implies a lower fit limit of $E_e \simeq 1.7\ GeV$ for the $b \to c$ transitions and $E_e \simeq 2.3\ GeV$ for $b \to u$. Only

$$\frac{BR(B \to e\nu\pi, \rho)}{BR(B \to e\nu D, D^*)} \text{ instead of } \frac{BR(B \to e\nu X_u)}{BR(B \to e\nu X_c)}$$

can be mesured with the inclusive spectrum.

Relativistic Bound State Model II

The fourth model to be discussed now (Körner and Schuler (KS) [21]) in principle uses the same ansatz as WSB, but takes dipole form factors instead of the monopole form factors used by WSB - see equation(2.35) - for the calculation of the decay into the 1^- mesons D^* and ρ:

$$POLE(q^2) = \left(\frac{1}{1 - q^2/M^2}\right)^2 \tag{2.36}$$

Similar numbers as in WSB's model for the overlap integral of the initial and final state meson and the pole masses are used. The validity limits for the prediction of the inclusive electron spectrum are the same as quoted for WSB.

Non-Relativistic 'Scalar + Vector' $q\bar{q}$ Potential

The last model for the decays to D and D^* mesons is proposed by Pietschmann and Schöberl (PS) [22]. The parameters of their quark potential model, where the potential consists of a scalar and a vector part, were tuned to fit the quarkonia states.

$$\begin{aligned} f_+ &= \sqrt{\frac{M_X^2 + M_B^2 - q^2}{2M_X^2}} \\ f &= \sqrt{2}\sqrt{M_X^2 + M_B^2 - q^2} \\ a_+ &= 0 \\ g &= 0 \end{aligned} \tag{2.37}$$

Since we already find serious discrepancies between the data and the prediction for the $b \to c$ channel, we cannot evaluate meaningful $(b \to u)/(b \to c)$ ratios with this model. Therefore we neither describe nor use their $b \to u$ prediction.

Comparison of Predictions

In table 2.3 the used parameters and predicted semileptonic widths are summarized. First we discuss the $b \to c$ channel. Applying AW's correction to GIW's model, the widths for ACM, GIW, WSB, and KS agree quite well. Only the model of PS gives a significantly higher width. Figure 2.14 shows the $b \to c$ spectra. They are normalized to 1 for ACM and GIW, whereas the model predictions by WSB, KS, and PS have been normalized to 0.9 assuming that the missing higher spin - and mass - states will contribute $\simeq 10\%$ to the rate. The shape of the contribution to the electron spectrum from these channels is determined by the large masses of the mesons involved. Except for the model by PS, all predicted shapes essentially agree. The spectrum of the model by PS is much softer.

The $b \to u$ spectra show a difference in shape and amplitude - see figure 2.14 and table 2.3. One reason for the different widths in the meson decay models is the different impact of the constituent quark masses in the models although the quark masses $m_{u,d}$

		Model					
		ACM	GIW	AW	WSB	KS	PS
m_b	$[GeV/c^2]$	4.85	5.120		4.900	4.900	5.240
m_c	$[GeV/c^2]$	1.607	1.820	1.800	1.700	1.700	1.850
$m_{u,d}$	$[GeV/c^2]$	0.150	0.330		0.350	0.350	0.340
form factor dependence		-	e^{-q^2}	pole	pole	pole	$\sqrt{a+q^2}$
normalization point, at $q^2 =$		-	max	max	0	0	
$\tilde{\Gamma}_{cb} \equiv \Gamma(B \to .)/(\hbar\|V_{cb}\|^2)\ 10^{12}/sec$							
$B \to e\nu\ D$			11.0	12.3	8.1	8.3	7.2
$B \to e\nu\ D^*$			41.2	23.1	21.9	25.8	68.8
$B \to e\nu\ (D + D^*)$			52.2	35.4	30.0	34.1	76.0
$B \to e\nu\ (D + D^*) + 10\%$			57.4	38.9	33.0	37.5	83.6
$B \to e\nu\ X_c$		36.5	58.0				
$\tilde{\Gamma}_{ub} \equiv \Gamma(B \to .)/(\hbar\|V_{ub}\|^2)\ 10^{12}/sec$							
$B \to e\nu\ \pi$			2.0		7.4	7.25	
$B \to e\nu\ \rho$			16.0		26.1	33.0	
$B \to e\nu\ (\pi + \rho)$			18.0		33.5	40.25	
$B \to e\nu\ X(1S, 1P, 2S)_u$			57.0				
$B \to e\nu\ X_u$		75.9					
form factors at $q^2 = 0$							
f^+	D	-	1.03	0.56	0.69	0.69	1.40
f^+	π	-	1.11		0.33	0.33	
f	D^*	-	6.24	6.52	4.72	4.72	7.90
f	ρ	-	2.33		1.70	1.82	
g	D^*	-	0.30	0.17	0.10	0.10	
g	ρ	-	0.43		0.05	0.05	
a^+	D^*	-	0.00	-0.15	-0.19	-0.19	
a^+	ρ	-	0.00		-0.10	-0.10	

Table 2.3: *Comparison of parameters and semileptonic widths predicted of the different models. The form factors are defined in equations (2.29-2.32).*

used are nearly identical. While GIW use the so - called 'mock masses' $\tilde{m}$ - the sum of the constituent quark masses - for the meson masses, KS and WSB use the meson masses themselves for the calculation of the form factors. Especially in the $B \to \pi$ channnel this choice has a major impact on the form factor β (α and γ are zero for this decay). β is proportional to $\exp(-1/\tilde{m}_\pi...)$ in GIW's model - see equation (2.34). Hence a choice of $\tilde{m}_\pi = 700$ or $140\ MeV$ easily explains the factor of about 3 between the predictions for the semileptonic width of the $B \to \pi$ transition by GIW and WSB, KS. For the decay to a D meson, the difference between the mock mass and the meson mass is much smaller and hence also smaller is the difference between the semileptonic widths of the models.

In this work we do not measure $b \to u$ branching ratios, but ratios of branching ratios $(b \to u)/(b \to c)$. This has the advantage that the b quark (B meson) mass does not need to be known very precisely, as the term m_b^5 (M_B^5) in the semileptonic widths in (2.20) and (2.28) cancels for this ratio.

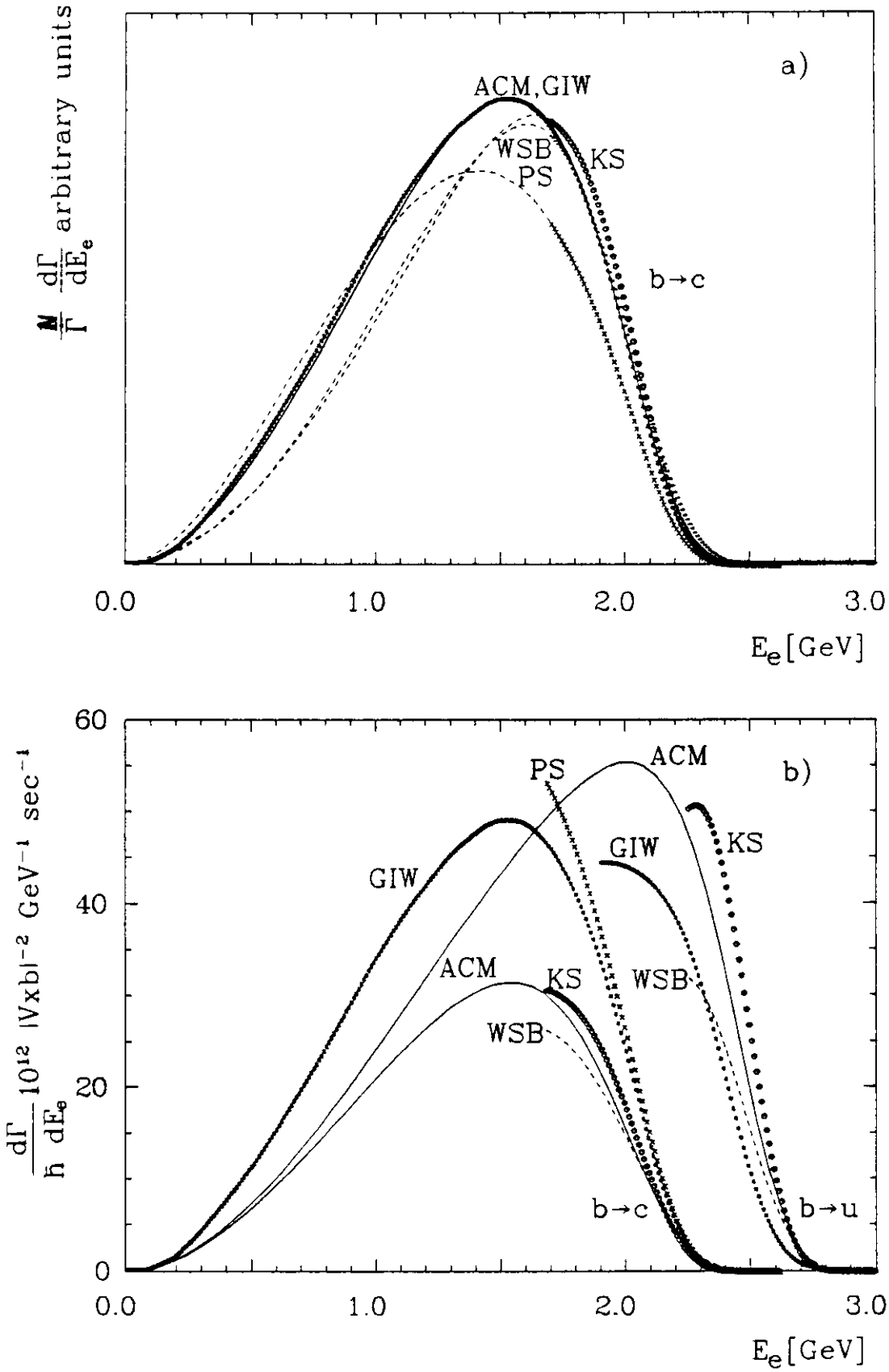

Figure 2.14: *The electron spectrum as predicted by ACM, GIW, KS, PS, and WSB, boosted with the B meson momentum and smeared with the detector resolution. The different predictions are labelled with the authors symbols. Those parts where the predictions are complete are shown in boldface symbols*
a) The normalized spectrum, $\frac{N}{\Gamma}\frac{d\Gamma}{dE_e}$. $N = 1.0, 1.0, 0.9, 0.9, 0.9$ *for the models ACM, GIW, WSB, KS, PS, respectively. b)* $|V_{cb}|^{-2} d\Gamma_{cb}/dE_e$ *and* $|V_{ub}|^{-2} d\Gamma_{ub}/dE_e$

Chapter 3

The Experimental Setup

This experiment was performed at the DORIS II [25] e^+e^- storage ring using the Crystal Ball detector. The detector was first used from winter 1978 to winter 1981 at the SPEAR storage ring at SLAC (Stanford Linear Accelerator Center, California) to study e^+e^- collisions at center-of-mass energies from 3.1 to 7.4 GeV. The data were used to study decays of the charmonium states. In April 1982 the Crystal Ball was moved to DORIS II at DESY (Deutsches Elektronen-SYnchrotron) in Hamburg, Germany, to study the decay of Υ states in the e^+e^- center-of-mass energy range from 9.4 to 10.6 GeV. The first data were taken in August 1982, and data-taking was finished in September 21, 1986. In fall 1987 the Crystal Ball was moved back to SLAC.

3.1 DORIS II

DORIS (DOppel-RIng-Speicher) was constructed in summer 1974 to study e^+e^- physics in the center-of-mass energy range from 2 to 6 GeV. The initial setup consisted of two separated rings on top of each other. The rings crossed each other in the two interaction regions. After the discovery of the $\Upsilon(1S)$ resonance in 1977 [23] DORIS was upgraded in several steps to reach the center-of-mass energies of the Υ systems. The double-ring structure was removed and replaced by a single ring. Additional cavities raised the available center-of-mass energy range to 9.4 - 10.6 GeV.

Mini - β quadrupoles close to the interaction regions increased the luminosity by more than an order of magnitude to 0.5 - 1 pb^{-1}/day. Figure 3.1 shows the integrated luminosity per month accepted by the Crystal Ball experiment during the whole data-taking period at DORIS II. Figure 3.2 shows the setup of the DORIS II ring together

	Resonance			
	$\Upsilon(1S)$	$\Upsilon(2S)$	$\Upsilon(4S)$	all
ON resonance	45.9	55.7	89.5	191.1
continuum	8.5	3.9	29.7	42.1
scan	15.6	3.9	11.4	30.9
				Σ 264.1

Table 3.1: *Luminosity collected at different beam energies during the data-taking at DORIS, in units of* pb^{-1}

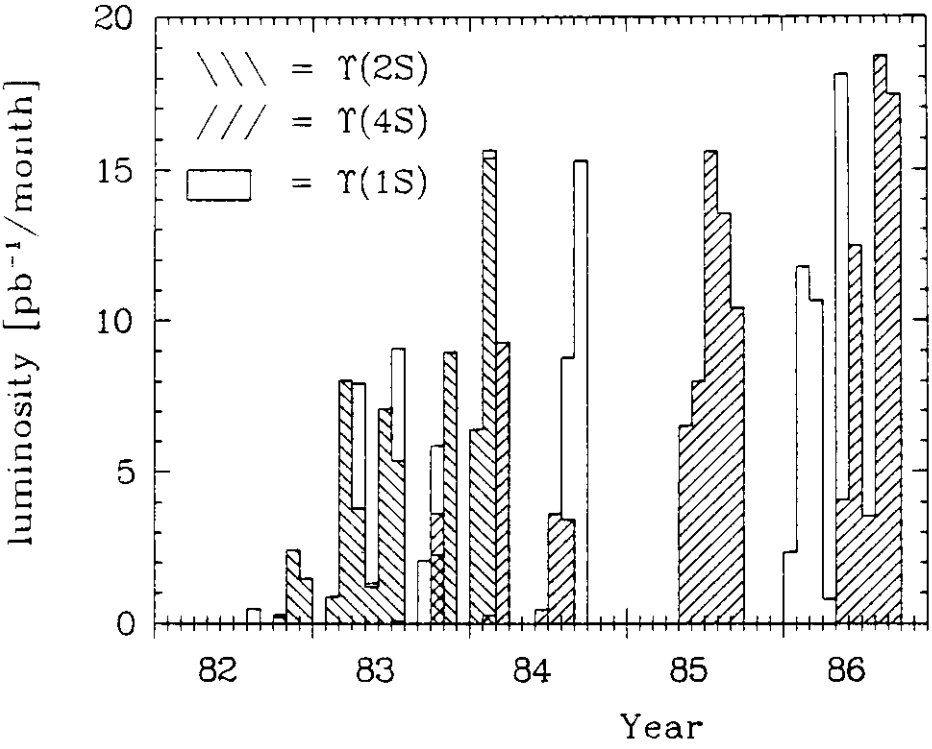

Figure 3.1: *Integrated luminosity per month. The data-taken at or close to the different resonances are indicated in the figure.*

with the injection system. Electrons are accelerated by the Linac I to about 63 MeV and then injected into DESY. They are accelerated in DESY to about 5 GeV, the beam energy of DORIS II. Through the injection system the electrons are guided to DORIS II. The procedure of filling in positrons is similar. First electrons of about 300 MeV accelerated by Linac II hit a tungsten target. The positrons produced in this process are accumulated in PIA (Positron Intensity Accumulator) and sent to DESY, too, and then to DORIS II in the same way as the electrons. In DORIS the electrons and positrons are packed into one bunch each. The maximum current of each package is about 50 mA. This process is called 'filling'. One filling takes about 2 - 10 minutes during normal running. The lifetime of the two bunches is about 1 - 2 hours. After about 30 minutes to 1 hour DORIS is filled again. Such a period of data-taking is called a run. In the two interaction regions of DORIS II the two experiments ARGUS [24] and Crystal Ball are located. In addition the synchrotron radiation light emitted in the arcs of DORIS II is used for e.g. solid state physics in the HASYLAB laboratory. The most important parameters of the storage ring are summarized in table 3.2

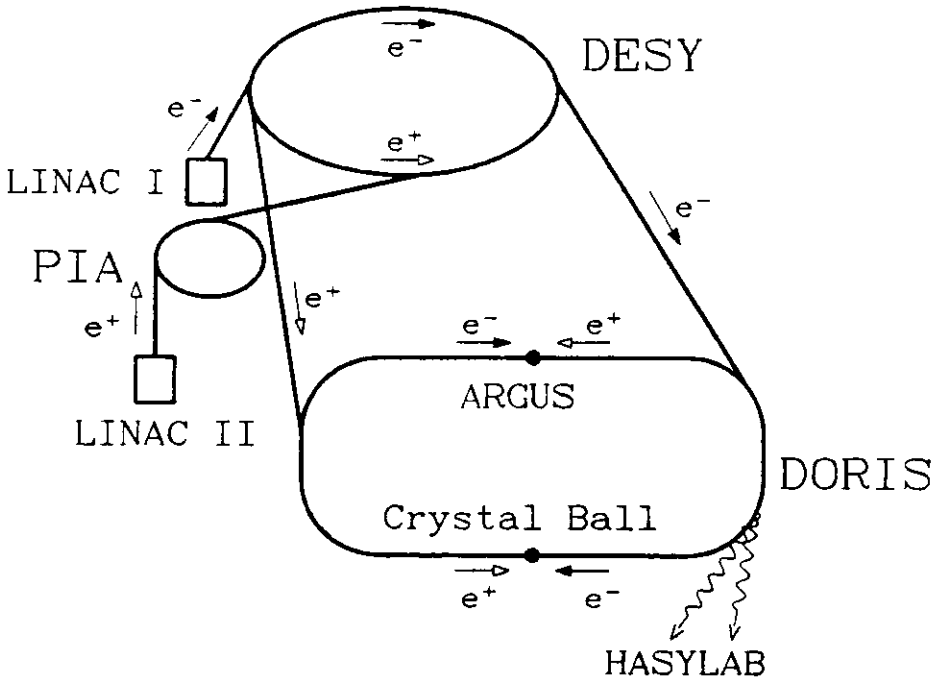

Figure 3.2: *DESY, DORIS, and injection system*

circumference	288 m
cycle time	0.96067 10^{-6} sec
number of bunches	1 per beam
maximum current	50 mA
maximum beam energy	5.6 GeV
energy resolution	≈ 5 MeV
typical luminosity	$\approx 10^{31}$ cm^{-2} sec^{-1}
size of interaction region $\sigma_x\sigma_y\sigma_z$	$(1 \times 0.1 \times 17)$ mm^3
total power consumption	≈ 7 10^6 W
duration of filling procedure	$2 - 10$ min
lifetime of a fill	$30 - 120$ min
duration of a run	$30 - 60$ min

Table 3.2: *Parameters of DORIS and conditions of high-energy physics running*

3.2 The Crystal Ball Detector

The detector was designed to detect monoenergetic γ rays or electrons with a good energy and spatial resolution. It consists mostly of NaI(Tl) crystals. The non-

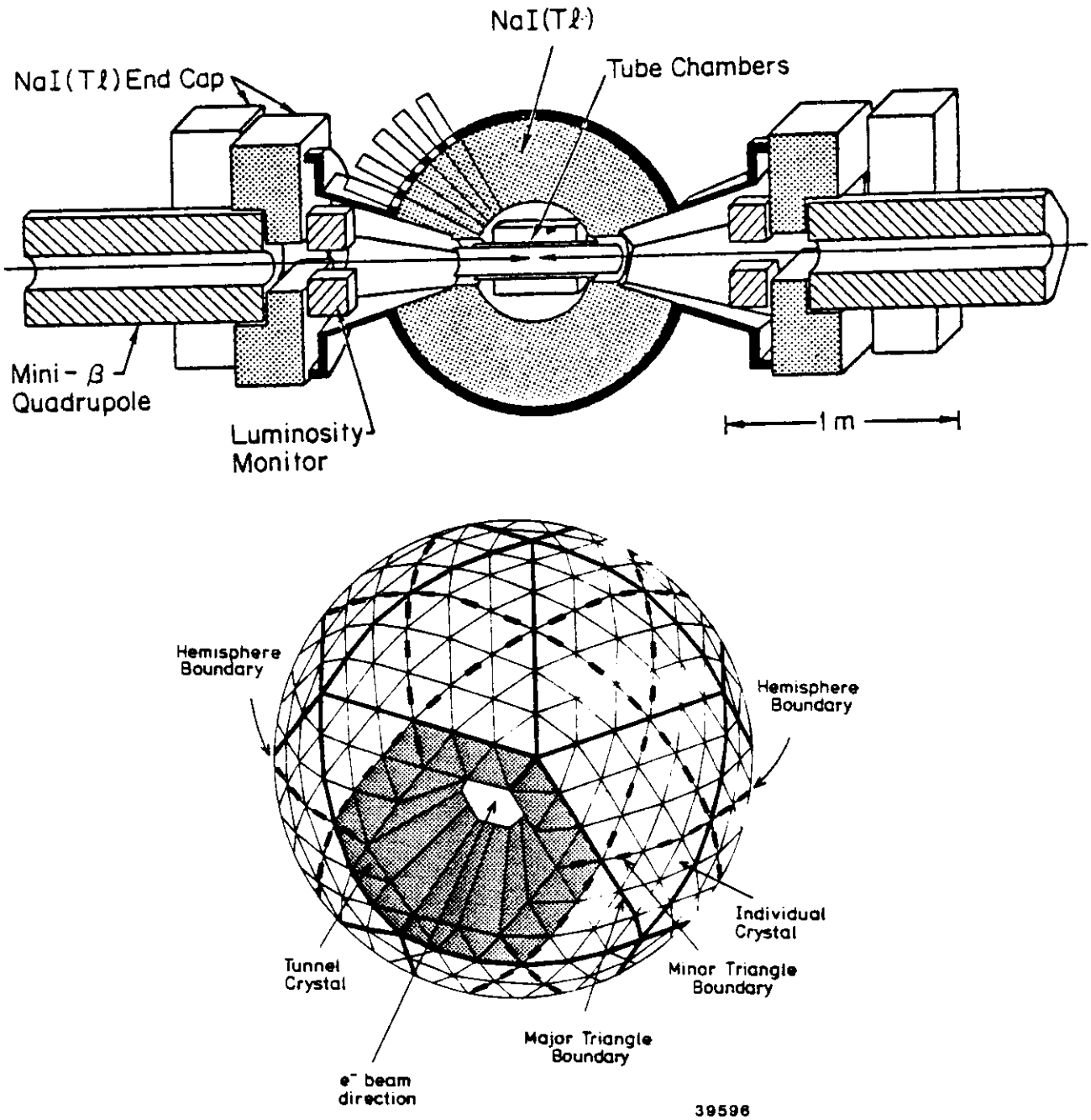

Figure 3.3: *The Crystal Ball detector. The upper part shows the full detector without the ToF counters outside the dry house.The lower part explains the geometry of the Ball.*

magnetic detector shown in figure 3.3 consists of the following components :

- the main Ball, NaI(Tl) crystal calorimeter;
- the end caps, also NaI(Tl) crystals;
- the time-of-flight system (ToF);

- the tube chambers;
- the luminosity counters.

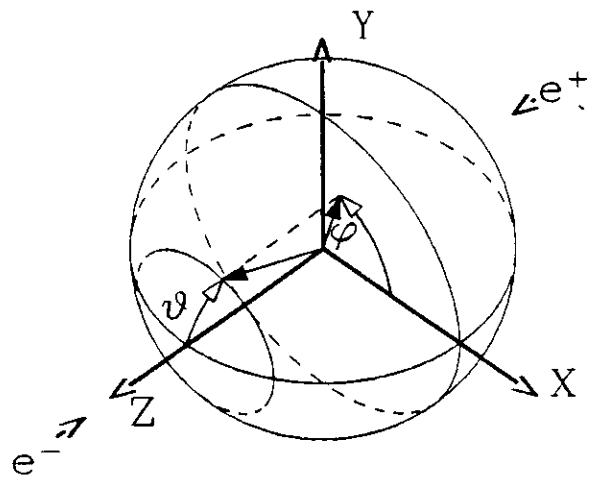

Figure 3.4: *The Crystal Ball coordinate system*

As the NaI crystals are extremely hygroscopic, the whole experiment besides the ToF counters was located in a dry house. The air in the dry house was kept at a constant temperature of $(20 \pm 0.5)^0 C$ and the humidity at less than $-40^0 C$ dew point. The coordinate system of the detector illustrated in figure 3.4 is defined as follows. The origin is at the interaction point. The X-axis points towards the center of the DORIS II storage ring. The Y-axis points upwards. The Z-axis is parallel to the flight direction of the positrons. In polar coordinates the φ angle is measured starting from the x-axis, the polar angle θ refers to the $+Z$-axis.

3.2.1 The Main Ball

Here we shall describe what is important to understand the basic setup and behaviour of the Ball. A detailed description of the construction and the assembly of the Ball can be found in [26].

From the global point of view the Ball can be looked at as an icosahedron. Each of the 20 faces of the icosahedron defines a triangle called 'major triangle'. Each major triangle is subdivided into four 'minor triangles'. Each minor triangle consists of 9 of the actual crystals, with 11 slightly different (15%) sizes. The total number of crystals is 672 which is 20 majors $\times$ 4 minors $\times$ 9 crystals - 2 $\times$ 24 crystals removed to have space for the beam pipe. The layers of 2 $\times$ 30 crystals surrounding the two openings are called tunnel modules. All crystals together cover 94% of 4π solid angle.

From the point of view of the construction the Ball consists of approximately four tons of NaI crystals. Each crystal has the form of a tapered triangular pyramid with its axis pointing to the center of the sphere. One example is shown in figure 3.5. The crystals are 16.0 inches ($\equiv$ 40.6 *cm*) long. This physical length corresponds to 15.7 radiations lengths and 1 nuclear interaction length.

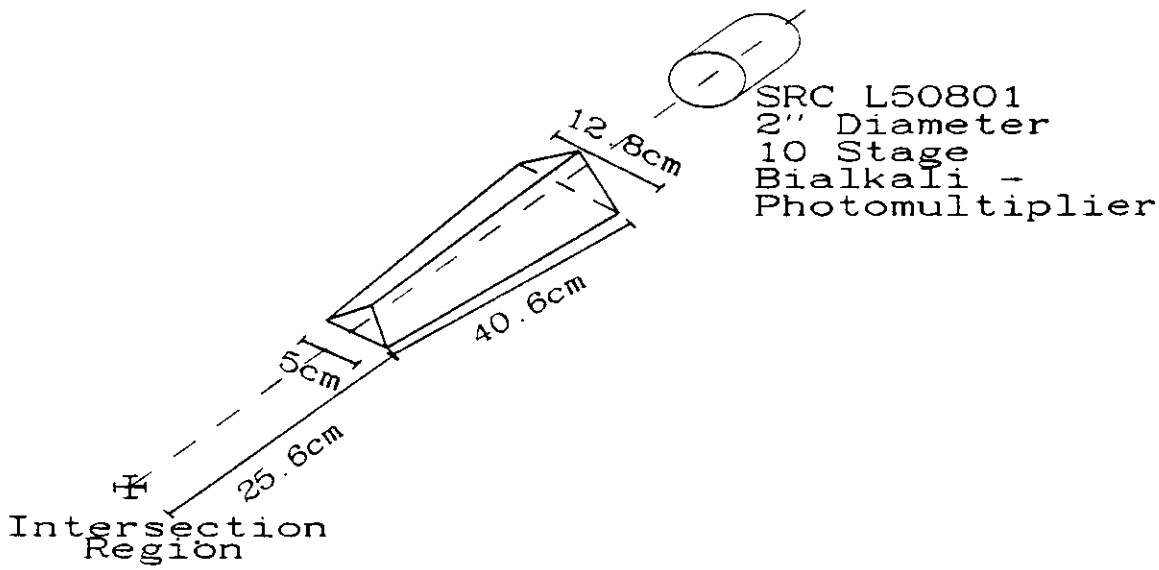

Figure 3.5: *The size and shape of a single crystal*

Each crystal was sanded and / or polished to achieve a uniform light output at the outer surface of the crystal as a response to a $Cs^{137}\gamma$ ray moved parallel to the crystal axis. The crystals are wrapped into 0.05 inch thick white paper and 0.005 inch thick aluminum foil in order to achieve optical insolation. The crystals are stacked to form two mechanically separated hollow hemispheres, an upper and a lower one. Each hemisphere is sealed in a metallic can. Each crystal points with its face towards the center.

The inner hollow sphere has a radius of approximately 10 inches. This space is used for the beam pipe and the chamber. At the outer face of each crystal a 0.5 inch diameter window is placed in the metallic can with a photomultiplier mounted outside the can. The outer face of a single crystal is viewed through the window and 2 inch air gap by the photomultiplier. In addition to permit the entry of the e^+ and e^- beam pipes 2×24 crystals nearest the Z^+ and Z^- axis are not stacked.

The two hemispheres are mounted on an elevator mechanism. They can be moved apart by 2 meters for maintenance and calibrations. This capability is also used to reduce the amount of synchrotron radiation absorbed by the crystals during injection into DORIS II or during beam studies. In addition to the separation of the two hemispheres from the beam pipe during injection a movable lead shield was put around the beam pipe with a remote control hydraulic system which further reduced the radiation damage caused by the machine.

3.2.2 Endcaps

In addition to the main Ball, 40 NaI crystals extend the coverage of the solid angle towards the beam pipe to about 98% of 4π. As the depth of NaI traversed by particles coming from the interaction point which pass through the endcap crystals varies between 3 and 9 radiation lengths the signals from the endcaps cannot be used for a true energy measurement but are only used as veto signals to indicate whether a big

fraction of energy missed the Ball.

3.2.3 Time-of-Flight System

Parts of the detector give a timing information: the main Ball, subparts of the Ball, and a set of 94 scintillation counters located on the roof of the dry house about 3 meters away from the beam axis. They are not shown in figure 3.3. The scintillation counters cover 25% of the 4π solid angle, but 80% of the cosmic muons are detected. They are read out with a TDC and an ADC on both ends. Thus apart from a timing information with a resolution of 1.4 nsec a spatial resolution of 20×25 cm is obtained, too. The timing information from the main Ball is available for the analog pulse height sum of all crystals, for the top and bottom hemisphere, and for the sum of crystals in each of the 20 major triangles. A timing resolution of ≈ 300 ps for 5 GeV electrons and ≈ 800 ps for minimum ionizing particles is achieved. In our analysis this part of the detector is used for cross checks only. A more detailed description can be found in [27].

3.2.4 The Small-Angle Luminosity Monitor

A set of scintillation and lead scintillation shower counters was positioned close to the beam pipe, see figure 3.6. As they were located near the beam axis ($\theta \simeq 8^0$) they had

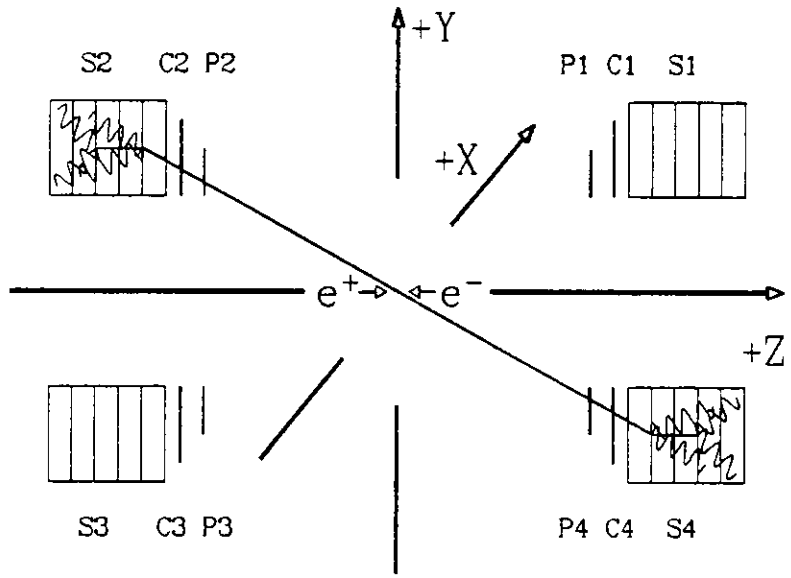

Figure 3.6: *The small angle luminosity counter*

a high counting rate for Bhabha events. To suppress accidental counts or counts due to beam losses, a coincidence of several counters was required. A detailed description of the method and results can be found in [28]. This component is used only for beam tuning and a fast online luminosity measurement. The measurement of the luminosity used for the final analysis is obtained by a measurement of large angle $e^+e^- \rightarrow e^+e^-, \gamma\gamma$ events, see appendix B for the discussion.

3.2.5 The Tube Chamber System

To detect charged particles a set of wire chambers was assembled arround the beam pipe. During its operation at DORIS II two different setups were used. The first constisted of 320 aluminum tubes assembled in three double layers around the beam pipe. Inside the tubes a $50\mu m$ thick stainless steel wire was stretched. Both ends of the wire were connected to a charge sensitive amplifier to allow a measurement of the Z-coordinate by charge division. The cathodes – the aluminum tubes – were on a negative high voltage of about 2700 Volts. The gas used in this setup consisted of $75\%Ar$, $20\%isobuthane$, $4\%methylal$, $0.25\%freon$. The system was not operated in the proportional mode, but in the limited streamer mode, which gives pulses nearly independent of the initial deposited charge. Due to high background from DORIS II – synchrotron radiation and particle losses – and the relative high gain, a degradation of the operation was observed. Organic filaments grew on the wires.

The data analysed in this analysis were taken with another setup: The chambers were replaced by a new set of 800 aluminum tubes assembled in four double layers, shown in figure 3.7. This chamber system was operated with a gas mixture of

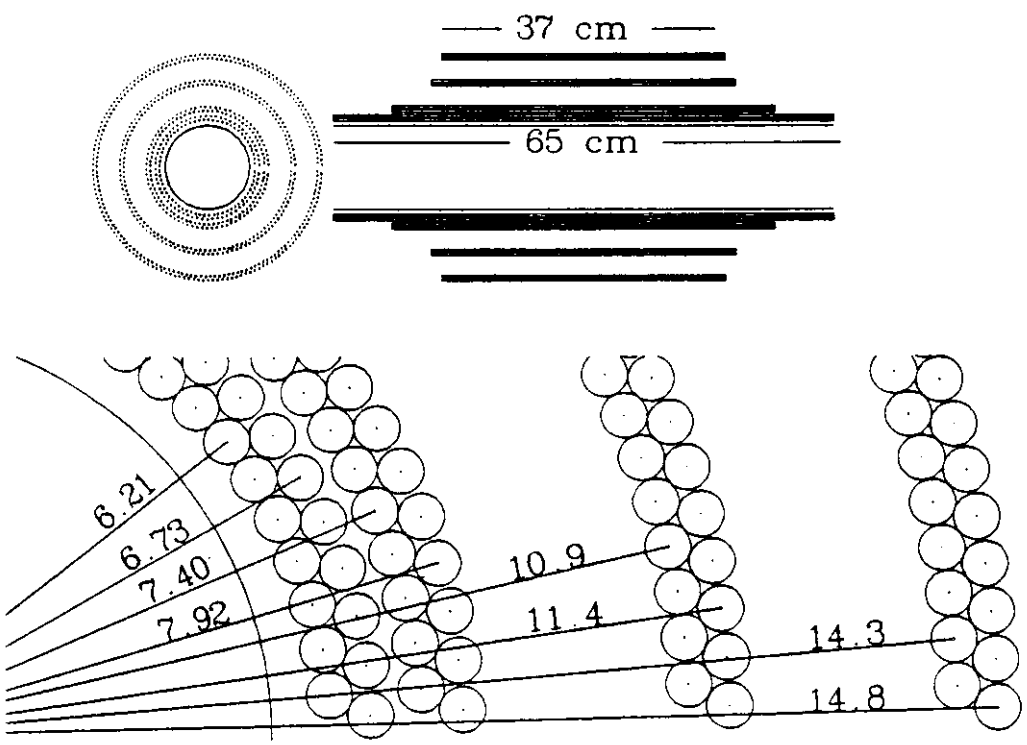

Figure 3.7: *The tube chamber configuration and dimensions. Upper two plots: projection in (R,φ) and in Z. Lower plot: part of the (R,φ) projection with the distance from the origin in cm.*

$80\%Ar$, $19\%CO_2$, $1\%CH_4$ at high voltage of $\approx$ 1800 Volts in the proportional mode to prevent degradation. The physical sizes and dimensions are given in table 3.3 and illustrated in figure 3.7. The tubes have a wall thickness of about 0.2 mm. Including the material used for the wrapping the material is equivalent to a 2% radiation length per chamber. The first two chambers were read out by a charge sensitive preamplifier built in thick film hybrid technology. The circuit of the hybrid preamplifier is shown in figure 3.8.

Chamber	Layer	number	R_{WIRE}	length	distance from beam	$\lvert cos\theta \rvert$	$\Delta\varphi$
number	number	of tubes	$[\Omega]$	$[cm]$	$[cm]$		$[degrees]$
1	1	64	321	64.77	6.23	0.98	5.63
	2	64	321	64.77	6.73	0.98	5.63
2	3	76	245	49.53	7.40	0.96	4.74
	4	76	245	49.53	7.92	0.95	4.74
3	5	112	177	39.37	10.86	0.88	3.21
	6	112	177	39.37	11.38	0.87	3.21
4	7	148	166	36.83	14.32	0.79	2.43
	8	148	166	36.83	14.84	0.78	2.43

Table 3.3: *Physical sizes of the second tube chamber setup*

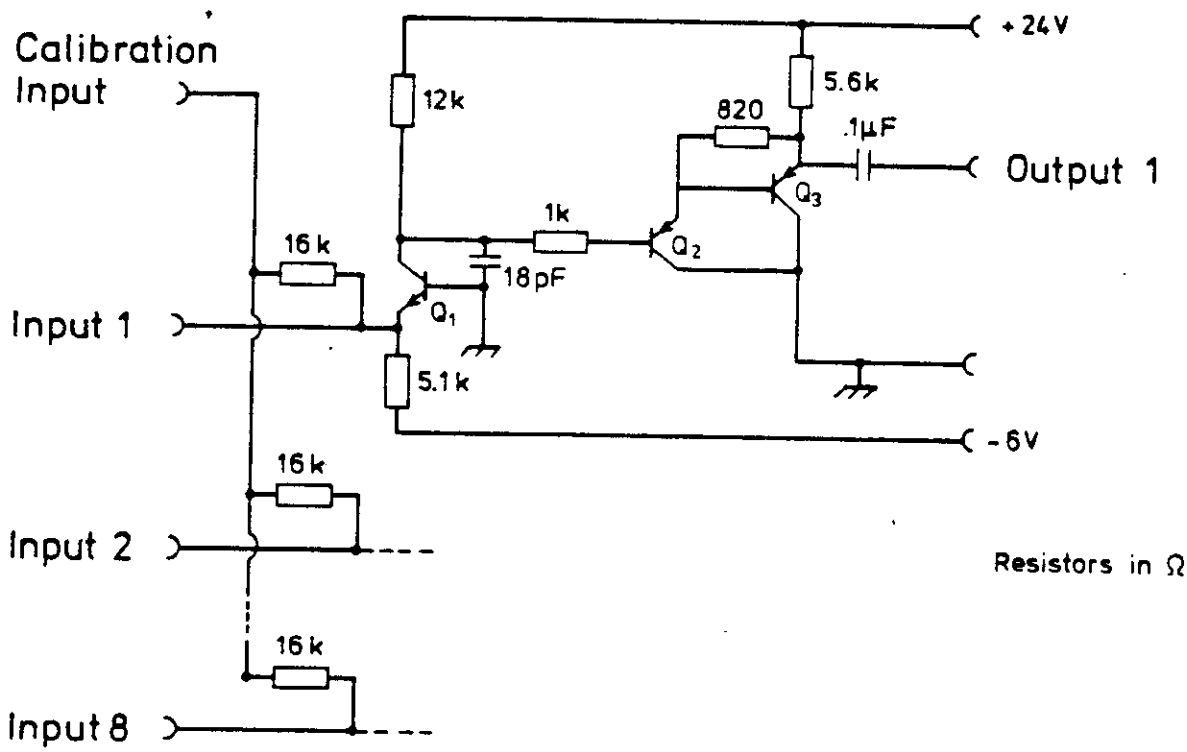

Figure 3.8: *Circuit of the Hybrid Preamplifier*

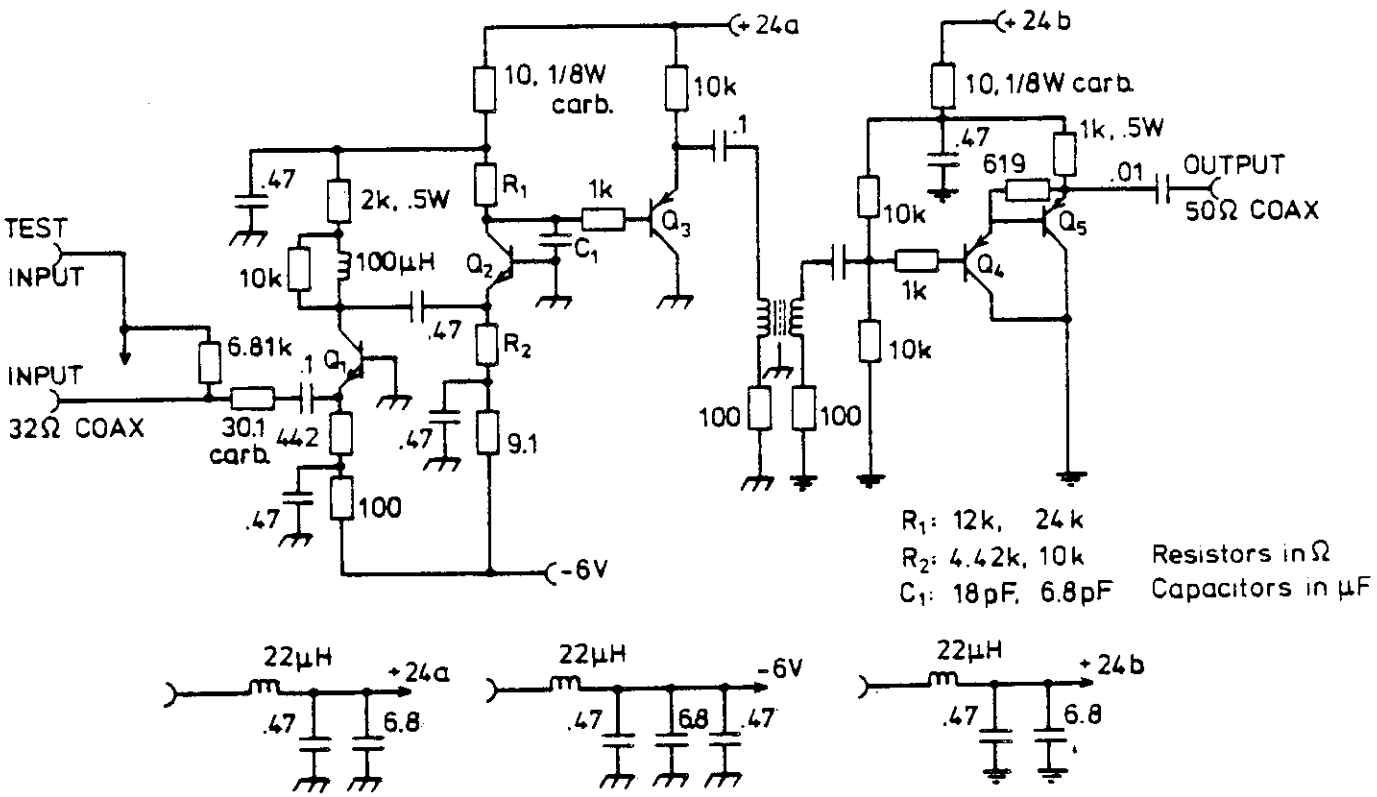

Figure 3.9: *Circuit of the Preamplifiers*

On one hybrid chip there are 8 identical amplifiers. The hybrids are directly mounted on the chamber to get a short connection to the wire of about 5 cm. The input impedance of a hybrid preamplifier is about 30Ω, the gain is approximately 400. The capacitor C_1 and resistor R_1 shape the signal, thus it has a time constant of 280 $nsec$ which is about the same as the decay time of the signals from the NaI crystals.

The wires of the outer two chambers are connected to 32Ω coax cables of about 4 meter length. They are connected to another type of preamplifiers located in the dry house. The circuit of the preamplifiers is shown in figure 3.9. Eight of these channels are on one printed circuit board of about 30 $\times$ 30 cm. The input impedance is 32Ω, too, but it is realized with a serial resistor at the input. The current into the emitter of the first stage is $\approx$ 10 mA which results in a very low equivalent input resistance. The input resistor is a carbon type resistor. It was chosen since metal film resistors tend to burn out by sparks initiated in the chamber. The time constant and the gain are the same as for the hybrids, but about a factor of 2 in phulse height is lost due to the long coax cable between the wire and the preamplifier. In a second version, operational from May 1986 on, the gain of the preamps was raised by a factor of 2 without changing the shaping time. This was done by modifying R_1, R_2, and C_1 as indicated in figure 3.9. The performance, the resolution in Z and φ, and the efficiency for detecting charged particles are discussed in appendix C.

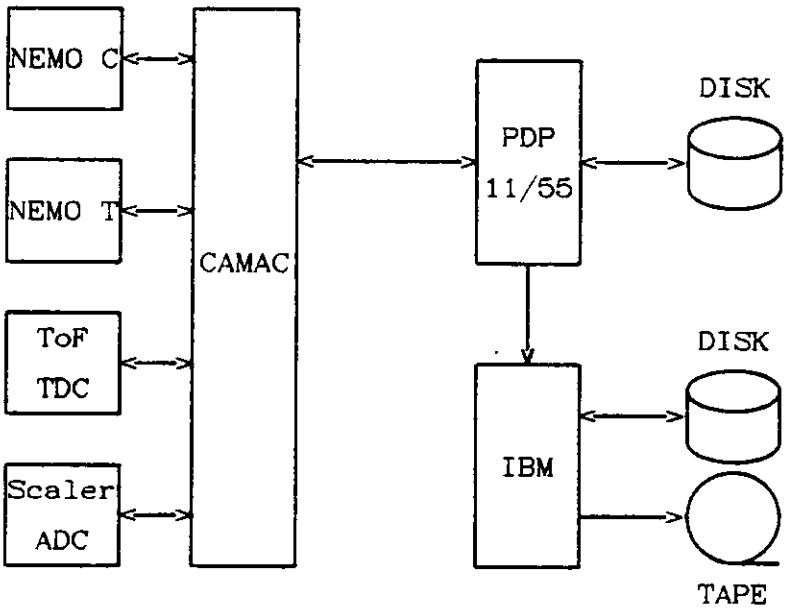

Figure 3.10: *The data acquisition system*

3.2.6 Flasher, LED, PULSER

In order to monitor and check the response and linearity of the calorimeter system two independent devices were installed. The first device was a FLASHER system. The light of a Xenon flash tube was led by optical fibers to the photomultipliers. The light intensity could be varied by different absorption filters. With this system a crude linearity check was possible.

The second device is an LED system that consisted of photodiodes directly mounted on each photomultiplier. The system served as a backup for the flasher system. A detailed description can be found in [29].

To monitor the performance of the tube chamber electronics a pulser was used to inject a fixed amount of charge into the first stage of the preamplifiers.

3.2.7 Electronics, Trigger, and Data Flow

Figure 3.10 shows the principle of the signal processing and the data flow. The 'Crystal NEMO System' is discussed first, it is sketched in figure 3.11. The anode signals from the photomultiplier tubes of the crystals were transformed such that they could run on a 124Ω shielded twisted pair cable. This cable transported the signals towards the electronics room. In the integrate & hold module (I&H) the signal was received by a transformer. The pulse from the NaI crystals which has a rise time of $\approx 30nsec$ and a decay time of $\approx 400nsec$ was stored in two capacitors of two different amplifier channels. The gain of these two channels differs by about a factor of 20. The channel with the lower gain is called 'high energy' channel and the other one 'low energy' channel.

The 9 crystals of one minor triangle were combined in one I&H module. The analog signals of the 9 channels in one minor crystal were added up and used for trigger purposes. Out of these 20×4 signals the trigger was formed.

The first trigger, E_{TOT}, was the sum of all minors in the main Ball without the tunnel modules. If the sum signal was bigger than a threshold equivalent to an energy deposition of 1900 MeV the trigger was set. Other trigger conditions did not require such a high energy, but required in addition special topologies of energy deposition in the Ball. They will not be described here, see [30] for a detailed discussion. These triggers were specially designed for two photon induced events or events with two muons. The data used in this analysis were all triggerd by the total energy trigger.

If a trigger was set the fet switches in the input of the I&H were opened, to make sure that no other signals could enter. Another signal was sent to NEMO, a special electronic box which drove the signal processing. After NEMO had received a trigger signal from the Trigger Box, signals were sent to each individual I&H channel – two per crystal – to connect the storage capacitor one after the other to the ADC. The ADC digitized – in 13 bits– the charge stored in the capacitors. The result was stored by NEMO in a digital memory. After all signals were converted the full information was sent to the online computer, a PDP 11/55. The PDP stored the data on a disk for later analysis. The whole digitizing process took about 30 $msec$. During that time no other action was possible in order not to disturb the signal processing.

In parallel to the crystals, the tube chamber signals were processed on another I&H - NEMO system, shown in figure 3.12.

The signals from the preamplifiers were sent on a 50Ω shielded coax cable to the I&H modules, very similar to those of the the crystals. But only one amplification channel per preamplifier was stored and 16 channels were assembled in one I&H module. As one tube had a preamplifier on each side, 8 tubes were connected to one I&H module. The analog sum of the I&H modules was used for the trigger as a veto for the two photon trigger conditions to select 'neutral' events only.

Beside the information from the crystals and the tubes, the information from the ToF and Small-Angle Luminosity counters were processed on standard CAMAC Lecroy ADC's and TDC's and stored on the PDP disk, too. Asynchronously to the signal

processing the PDP compressed the data and sent the compressed data via a fast link to an IBM mainframe computer, where the data were again stored on a large disk. The compression of the data suppressed information from crystals which have less than about 0.3 MeV energy deposition. For the tube chamber data it was required, that the sum of the signals from both ends of a tube had to be 8 counts above pedestal. Every 128 events all information was stored on the IBM disk, in order to be able to analyse pedestals offline.

Beside the trigger from the energy measurement with the Ball, a special trigger was included. This trigger fired every 10^7 beam crossings with no other requirement. These events are called DBM (DORIS Bunch Marker) events. They are used for background studies. In addition the Flasher, the LED, and the tube chamber pulser system caused triggers. The corresponding events were written out, too, for special detector studies.

On the IBM mainframe the data were stored temporarily on a large disk. About three times a day during normal data-taking the disk is dumped onto magnetic tape and the disk was overwritten by the new data. A copy of the magnetic tape was shipped to SLAC for the standard data processing (production). In parallel to the copy job, other jobs used the data for checks. Pedestal variations and dead channels and other exceptions were searched for. These checks were used as a fast-feed back system to keep the detector and its components in good operation conditions. Bhabha and uncompressed events which are used for calibration purposes, were stripped from the raw data tapes immediately after having been copied.

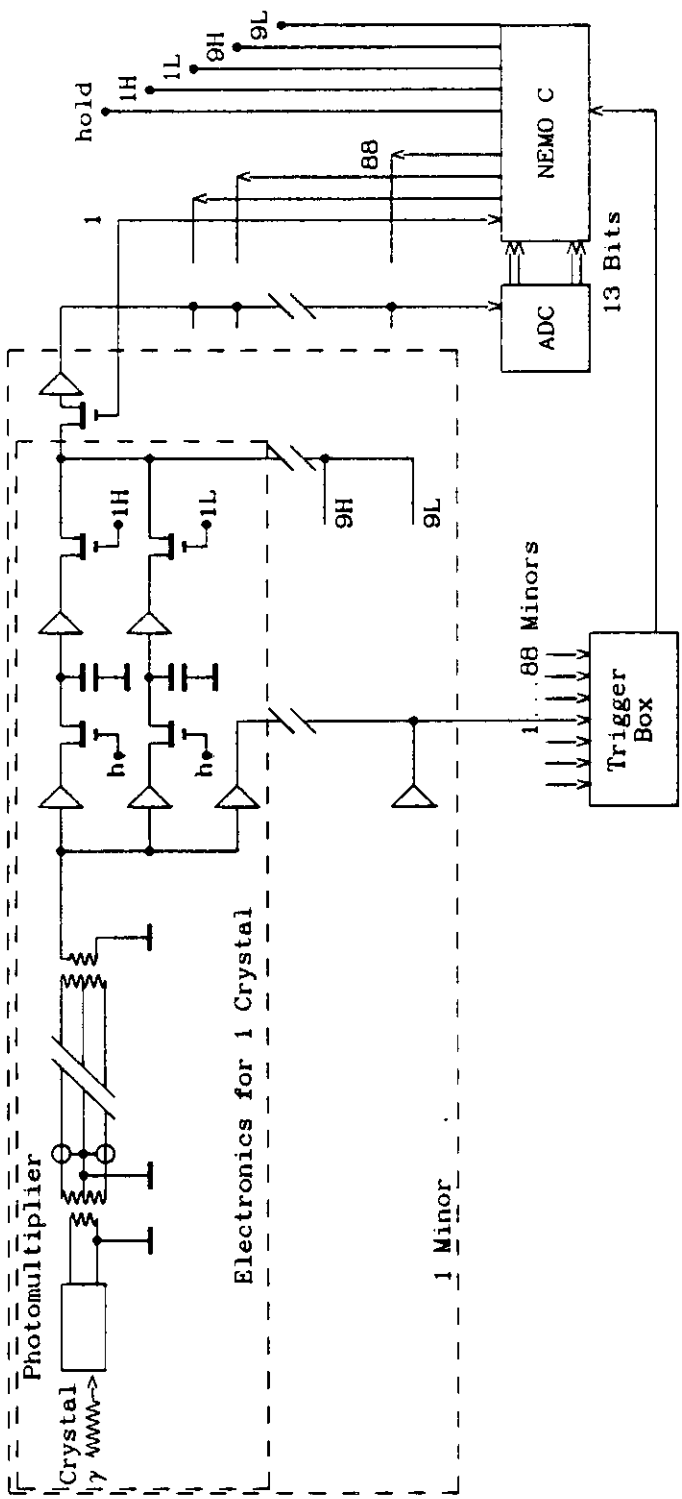

Figure 3.11: *The crystal NEMO system*

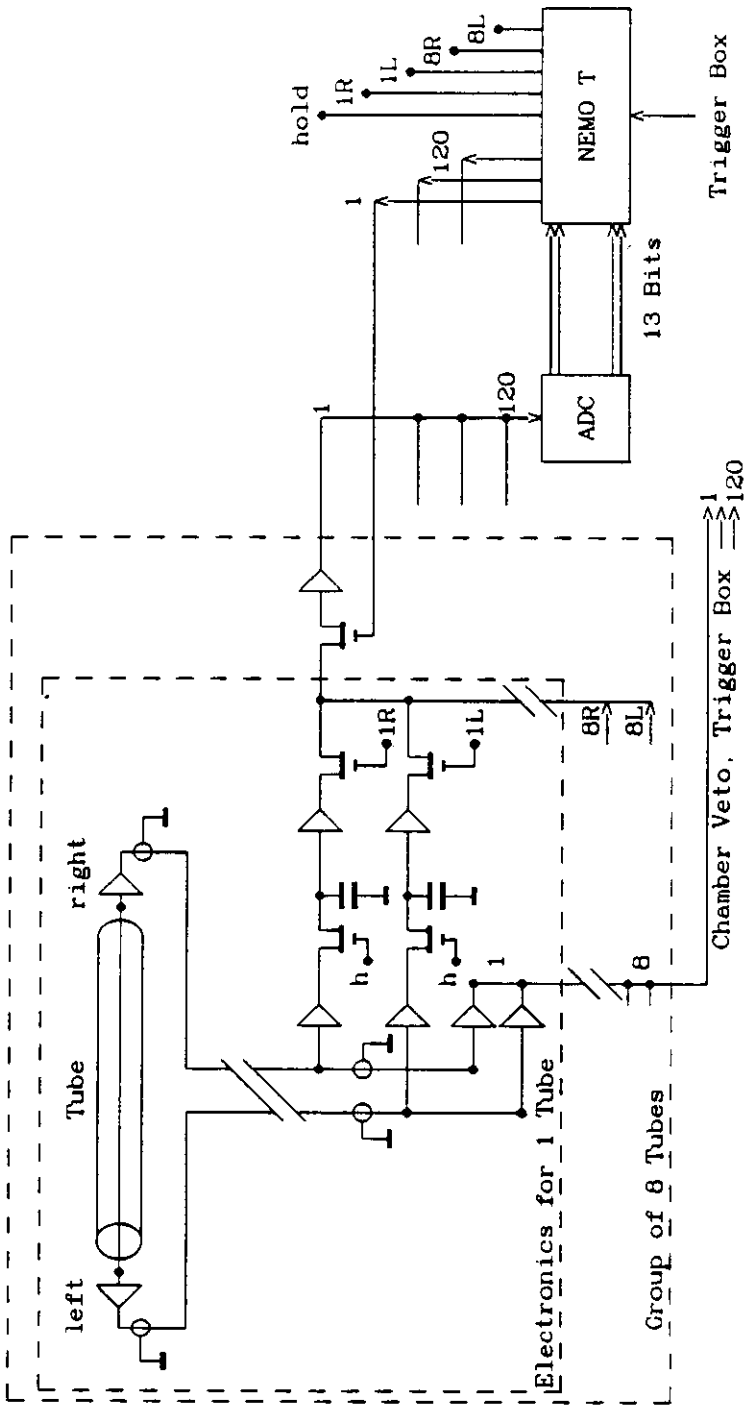

Figure 3.12: *The tube NEMO system*

Chapter 4

Data Analysis

4.1 Event Reconstruction

The conversion of the raw information on the magnetic tapes (ADC and TDC counts) to meaningful quantities like energy, tube chamber hits, and tracks is done in a procedure called 'production'. Each event is subjected to the production procedure, which consists of six separate steps:

1. ENERGY, converts the raw crystal data to energy;
2. CONREG, combines the crystals to clusters of energy;
3. BUMPS, finds local energy maxima, a preliminary track definition;
4. CHGTKS, searches for charged tracks in the tube chamber;
5. ESORT, calculates energies for each track;
6. ToF, analyses the timing information from the roof counters and the main Ball.

In the following we shall discuss each step in some detail in order to explain how direction and energy of particles are defined.

4.1.1 ENERGY

The first step converts the raw ADC numbers of the crystals into energies. The energy assigned to a crystal is

$$\begin{aligned} E_{CRYSTAL} &= (C_H - PED_H) \times SLOPE_H \text{ if } C_H > 350 \\ E_{CRYSTAL} &= (C_L - PED_L) \times SLOPE_L \text{ if } C_H \leq 350 \end{aligned} \quad (4.1)$$

where $C_{H,L}$ are the ADC counts in the high, low channels;
$PED_{H,L}$ are the pedestals for both channels and the quantities $SLOPE_{H,L}$ are the conversion factors between the ADC counts and the crystal energies in MeV. The 4 variables $PED, SLOPE$ are determined by the calibration procedure which is described in appendix A. After having calculated the energy for each crystal the total deposited energy E_{TOT} is determined. The energy of a crystal is kept for further use if $E_{CRYSTAL} > 0.3\ MeV$.

4.1.2 CONREG

This step combines the crystals to clusters. A set of crystals is called a connected region - CONREG- if each crystal has more than 10 MeV deposition and if the crystals are contiguous. Two crystals are contiguous, i.e. direct neighbours, if they share a common edge or face. The energy sum of all crystals belonging to the connected region is called the connected region energy E_{CONREG}.

4.1.3 BUMPS

A preliminary attempt to define tracks is done by the bumps algorithm. It looks for local energy maxima in the connected regions. The crystal with the highest energy deposition in a connected region is called a *bump* crystal. The three closest neighbours are associated with this *bump* crystal to form the energy sum E_4. Additional crystals are associated with this *bump* crystal

$$\begin{aligned} &if && \theta < 15^0 \\ &or \quad 15^0 < \theta < 45^0 \text{ and } E_{CRYSTAL} < E_4 \times 0.72 \times e^{-9.4(1-cos\theta)}, \end{aligned} \tag{4.2}$$

where θ is the angle between the center of the *bump* module and the crystal under investigation. The functional form was found empirically by scanning a sample of events [26].

The unassociated crystal with the highest energy is called the next *bump* crystal. The above procedure is repeated until all crystals in a connected region are associated to *bump* crystals.

4.1.4 CHGTKS

In this step the information of the tube chambers is used. First the raw tube ADC data are converted to a hit with a φ and Z-coordinate. Out of that information the directions of charged tracks are determined. The sum of the pulse height from the left and right end of the tube, $Q = Q_L + Q_R$ with pedestals subtracted, must be bigger than a minimum pulse height. The φ position of the hit is simply determined by the φ-position of the tube itself. The Z position is calculated from the charge division measured at both ends of the wires. For details see appendix C. Two attempts are made to detect charged particles which are discussed in the two following subsections.

Charged Track Finding (TBTRAK)

The first track definition method tries to construct lines in φ and Z with at least 3 close by hits. Search starts from the outermost layer with a hit moving inwards along a road in φ and Z. The definition of the road depends on the layer and the hits already found. In detail the algorithm is the following:

1. The straight line is defined as:
   $\varphi = \sum \varphi_i / N$, which assumes no off axis vertices i.e. $X_{VERTEX}, Y_{VERTEX} = 0, 0$.
   φ_i are the φ positions of the hits previously found.
   $Z = \alpha \times r + \beta$ where r is the radial distance from the origin.
   α and β are determined by a straight line fit from the hits previously found.

If less than 4 hits have been found, hits at the origin, $(X, Y, Z) = (0, 0, 0)$, are added.

2. If more than 1 hit is already correlated, the next hit is searched for by moving inwards to the next layer in a window which is defined by $\varphi_{LINE} \pm \Delta\varphi$ and $Z_{LINE} \pm \Delta Z$,
where $\Delta\varphi = 120, 120, 100, 100, 50, 50$ *mrad* for layers 6,5,4,3,2,1, respectively and $\Delta Z = 8, 8, 8, 8, 5, 5$ *cm* for 2,3,4,5,6,7 hits already found, respectively. If more than 1 hit lies in that window, that hit is kept which gives the smallest value of the residual R;
$R = \sqrt{\sum(\varphi_i - \sum(\varphi_j/N))^2}$, where i, j run over all hits found including the new one.
A hit is finally accepted if the residuals in Z are less than $9, 10, 11, 12, 13, 14$ *cm* and those in φ are less than $0.087, 0.10, 0.11, 0.112, 0.13, 0.14$.
The limits are varied as a function of the number of hits (3-8) correlated to the track.

A track must have at least 3 hits. If more than one track is found a Z vertex is calculated using the average of the points of the tracks which are closest to the Z-axis. All the track directions are then recalculated from the new common Z vertex.

In case the tracks have been found, the procedure CHGBMP tries to correlate the charged tracks with the *bump* crystals found in the Ball. A *bump* crystal is flagged 'tracked charged' if the track found traverses the *bump* crystal or the angle between a line from the origin to the centroid of the *bump* crystal and the track is less than 15^0. If two tracks might be correlated to one *bump* crystal the track which is closer to the *bump* crystal is taken. Tracks which cannot be correlated to a *bump* crystal are called 'uncorrelated charged tracks'.

Tagging Bumps Charged (TBTAG)

The second method of detecting charged tracks uses a different philosophy of correlating hits in the chamber to the *bump* crystals in the Ball. For this search the hits which have not been correlated to a charged track and those from uncorrelated charged tracks are used. Starting from the the origin $(X, Y, Z) = (0, 0, 0)$ towards the centroid of the *bump* crystals, the number of hits inside a road in φ and Z are counted. The size of the road in φ is 0.15 *rad*, while in Z the road is within $\Delta Z = 8, 8, 8, 8, 5, 5, 5$ *cm* in layers 1-8. A *bump* is 'called tagged charged' if:

A 3 hits are correlated in φ, of which 2 hits must be correlated in Z, and 1 hit is in any of layers 5-8.

B 2 hits are correlated in φ and Z
if the track does not intersect any of layers 5-8.

The efficiency of those two methods to identify particles as charged is discussed in appendix C.

4.1.5 ESORT

This step assigns energy to all the tracks and assigns directions to the neutral and the tagged charged tracks. However, the direction of tracked charged tracks is taken

from the chamber information, see above. For each *bump* two estimates are made to determine the energy correlated with the *bump*.

The first is called E_{13} ; it is the sum of the energy of the *bump* crystal and its 12 closest neighbours. One radiation length in NaI amounts to 2.59 cm. Hence electromagnetically showering particles (e^+, e^-, γ) coming from the interaction region traverse 15.7 radiation lengths and deposite nearly all their energy in the crystals. The lateral size of an electronmagnetic shower is defined by the Molièr radius, $R_M \simeq 4.35\ cm$ for NaI. In a cylinder of 2 or 3 R_M, 95% or 99% of the whole deposited energy is contained, respectively.

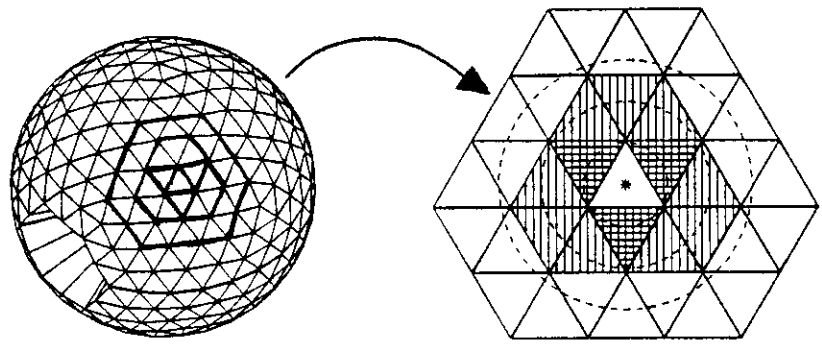

Figure 4.1: *A part of the full Ball to illustrate the group of 13 crystals. The left-hand part shows the full Ball and the right-hand part a crystal and its neighbours. For nearly all crystals – beside the tunnel crystals – a FLAT(ty) pattern as indicated in the figure exists. The 12 closest neighbours are shown as hashed and cross hashed triangles. The dashed circles correspond to 1,2, and 3 Molièr radii.*

Figure 4.1 shows the full Ball and a part of the flat pattern of the surface of the Ball. Circles of 2 and 3 R_M are plotted assuming a particle having entered the center of the central crystal. A group of 13 crystals fully contains the circle $2R_M$ and therefore most of the energy. The sum of the energy of the central crystal and of the 12 closest neighbours is therefore used to measure the energy of an electromagnetically showering particle. The nuclear interaction length in the crystals is about 41 *cm*. Therefore fast hadronic particles make a nuclear interaction only in 2/3 of the cases. In the other cases only ionization energy of the primary particle is deposited which on average amounts to about 210 MeV. Hence the energy of non-electromagnetically showering particles cannot be measured. The pattern induced by minimum ionizing and electromagnetically showering particles is described in more detail in chapter 4.3.

Two corrections are applied to E_{13} . The first correction compensates for the energy which leaks out the 13 crystals. It has been found to be 2.25% from studies with Bhabha events – see appendix A. The second correction depends on the ratio of energies deposited in the *bump* crystal and in the group of 13 crystals, called E_1/E_{13}. This ratio gives a crude measure of how close to the center of the *bump* module the incident particle entered. If a particle enters close to the corner or border, more energy is deposited outside the group of 13 crystals and in the wrapping material of the crystals. Applying all corrections the final value of E^c_{13} is:

$$E^c_{13} \equiv \sum_{i=1}^{13} E_i \times 1.0225 \times PCORR(E_1/E_{13}), \qquad (4.3)$$

with

$$PCORR(x) = \left[\begin{array}{lll} 1.055 & & x < 0.40 \\ \frac{1}{0.898+0.125 \cdot x} & if & 0.4 \leq x \leq 0.82 \\ 1 & & x > 0.82 \end{array} \right] \qquad (4.4)$$

If one connected region has two *bump* crystals and the 13 crystals of the two *bumps* overlap, the calculated energy E_{13} is clearly too high. The crystals belonging to both *bumps* are counted twice in the calculations of E_{13} .

An attempt to disentangle these effects is made in the routine ESORT. It uses the expected shape of a shower from a single electromagnetically showering particle as derived from Monte Carlo studies. The *bump* module is divided into 16 virtual submodules. The observed energy distribution in the 13 crystals is compared with those obtained from the Monte Carlo simulation for the assumption that the particle enters at one of the center of each of the 16 submodules. The direction and energy assigned to the track is taken from that submodule, which gives the most similar distribution in the 13 crystals. If more than one *bump* crystal is in a connected region, the E_4 energy is preliminarily assigned to the track. The energy in the remaining crystals is divided between the *bumps* in accordance with the energy predicted to be in each crystal by Monte Carlo shower functions. Corrections similar to those applied to E_{13} are also used for ESORT. If a *bump* is not correlated to a charged track in the chamber, i.e. neutral or only tagged, the direction of the track in the track bank is taken from the ESORT procedure.

4.1.6 ToF

In addition to the timing information from the group of 9 or 36 crystals (minor or major triangles), the roof counter TDC and ADC values are used to calculate the timing of the tracks and the position of the intersection of the tracks with the the roof counters. In this analysis the timing information is only used for cross checks of the tube chamber performance, namely to select muon pair events.

4.2 Event Selection

4.2.1 Event Classes

We first discuss typical event classes, some of which are displayed in figures 4.2 to 4.6 - before we describe the event selection for the multi-hadron events. The projection of the Ball onto a plane as shown in figures 4.2 to 4.6 can be understood as a generalization of the flat pattern shown in figure 4.1. This figure is called FLAT(ty). Each crystal is represented by a triangle and the energy measured in the crystals is written as an integer number in units of MeV (or as dot of an area proportional to the energy). The surface of the Ball in 3 dimensions can be reconstructed from such a FLATTY to a sphere by folding at the borders of the major triangles. The $\pm Y$-directions of the coordinate system are at the top and bottom of the FLATTY, respectively. The $\pm Z$-directions are at the left and right hole of the FLATTY, respectively. The $+X$-direction is in the equator in the middle between the left and right hole on the FLATTY.

In figure 4.2 the FLATTY of a typical Bhabha event, $e^+e^- \rightarrow e^+e^-$, is shown. There are two connected regions of energy in the Ball. The E^c_{13} of the the two clusters are 5.444 and 5.431 GeV, respectively. The beam energy is 5.302 GeV. The connected regions are extended over 13 crystals each. The two clusters are opposite in direction as can be seen from the chamber display.

Another event arising from the QED process $e^+e^- \rightarrow \mu^+\mu^-$ is shown in figure 4.3. There are also connected regions in the Ball, but the deposited energy per particle is much smaller - about 210 MeV each - than in the Bhabha event.

The third kind of QED process, $e^+e^- \rightarrow \tau^+\tau^-$, has a quite similar event structure as the two types shown above. An event which is suspected to come from a $\tau\overline{\tau}$ decay is shown in figure 4.4. Since the boost of the τ is very high the event shape is also very much two jet-like. The multiplicity of particles in the events is small, too: the one prong branching ratio of τ decays is $\approx 83\%$. A mixture of minimum ionizing and electromagnetically showering particles ($e, \pi^0 \rightarrow \gamma\gamma$) are present in the events.

Another class of QED events (not shown) arises from the two-photon interaction $e^+e^- \rightarrow e^+e^-\gamma\gamma \rightarrow e^+e^-X$. Here in most of the cases the electrons (and positrons) are not detected in the main Ball since they are scattered at very small angles and therefore escape detection. The energy of the two-photon systems is small in most of the cases ($< 1\ GeV$) and the events have a small multiplicity.

The fourth FLATTY in figure 4.5 shows an event which is suspected to be an event of the type $e^+e^- \rightarrow q\overline{q} \rightarrow$ hadrons. A clear two-jet structure is visible especially in the chamber display.

The fifth FLATTY in figure 4.6 shows an interaction of the beam with the rest gas in the beam pipe or with the beam pipe itself. This 'event' was recorded when DORIS II operated with one beam only, therefore no e^+e^- interaction is expected. The energy is mostly deposited in the crystals close to the beam pipe. The center-of-mass system of the interaction is boosted along the beam pipe, hence not much 'transverse' energy is expected.

The last FLATTY in figure 4.7 shows a Monte Carlo generated event of the type $\Upsilon(4S) \rightarrow B\overline{B} \rightarrow e\nu X$ (see chapter 4.4 for the description of the Monte Carlo simulation of events). This event has a much higher multiplicity of *bumps* and is much more spherical in the energy deposition than those arising from QED reactions.

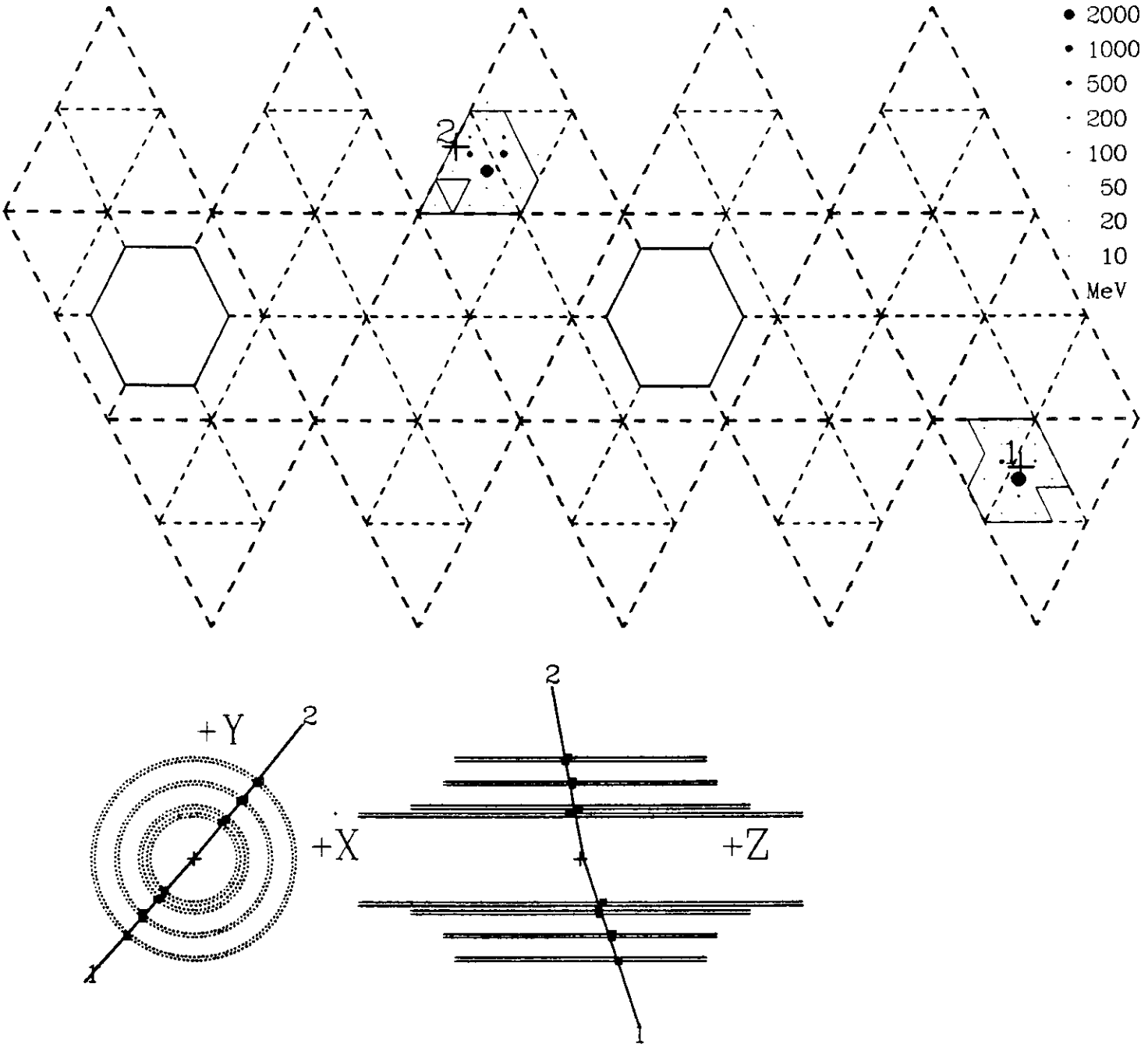

Figure 4.2: *The event display called FLATTY of a typical Bhabha event. The energies in the crystals are shown as dots. The faint dashed lines mark the borders of the minors and the bold dashed lines mark the major triangles. The thin solid lines indicate the borders of connected regions. The crosses with the number in the FLATTY display mark the directions of the tracks extrapolated from the chamber. At the bottom the chamber in a (R, φ) and Z-projection is shown. The hits and reconstructed tracks are displayed.*

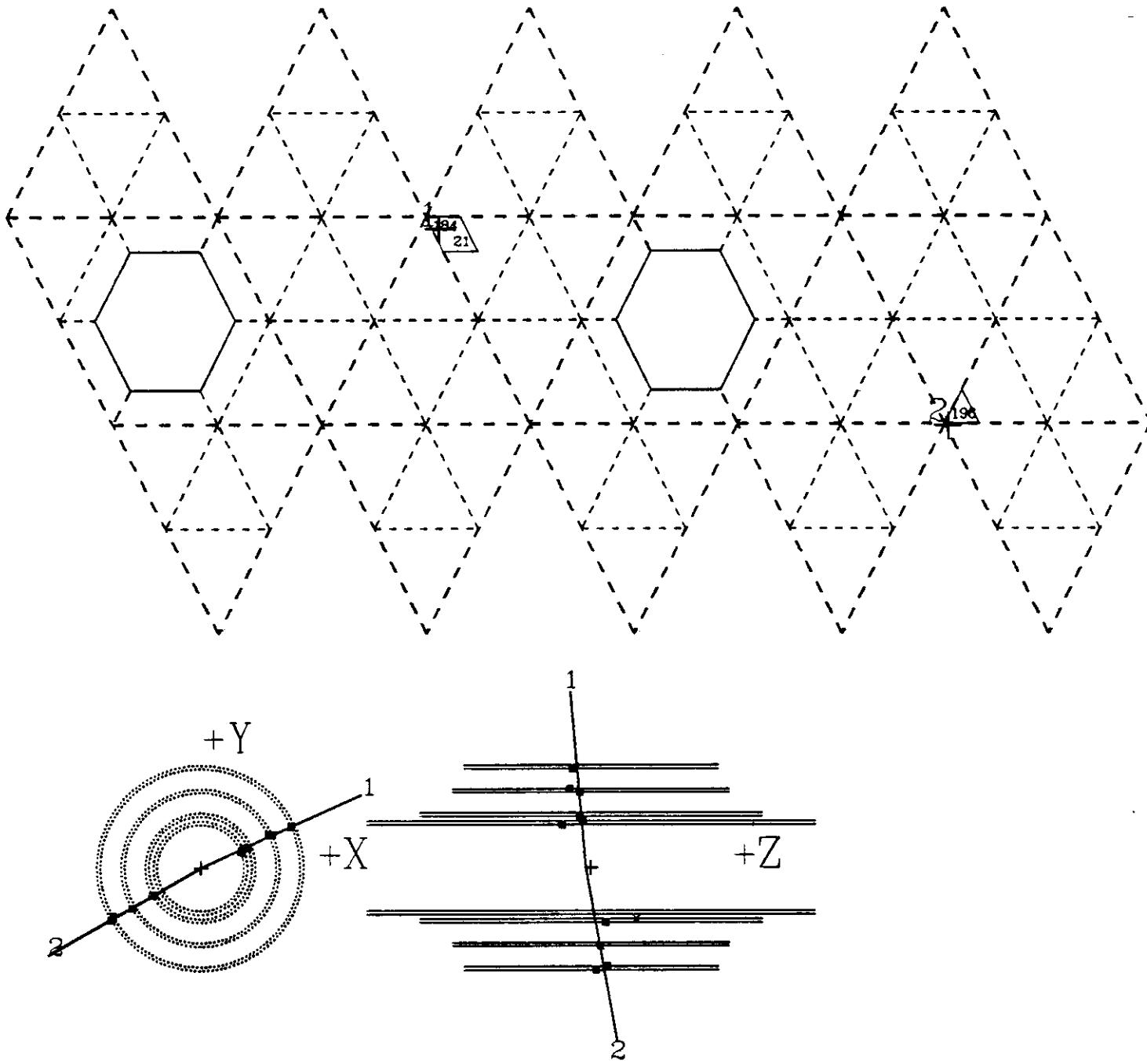

Figure 4.3: *A FLATTY of a typical $\mu\overline{\mu}$ event. The energies in the crystals are shown as numbers in MeV . The faint dashed lines mark the borders of the minors and the bold dashed lines mark the major triangles. The thin solid lines indicate the borders of connected regions. The crosses with the number in the FLATTY display mark the directions of the tracks extrapolated from the chamber. At the bottom the chamber in a (R, φ) and Z-projection is shown. The hits and reconstructed tracks are displayed.*

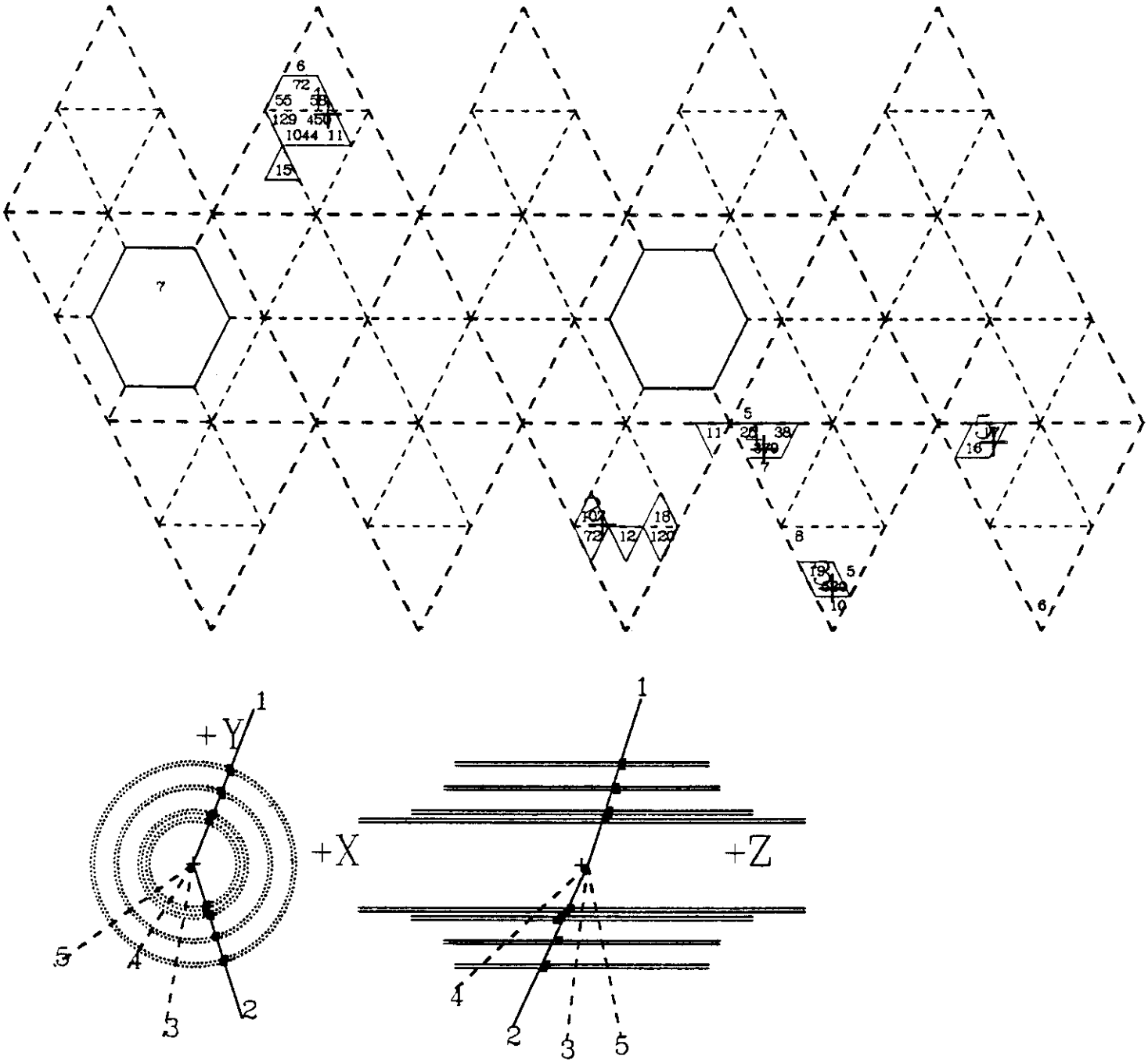

Figure 4.4: *A FLATTY of a typical $\tau\bar{\tau}$ event. The energies in the crystals are shown as numbers in MeV . The faint dashed lines mark the borders of the minors and the bold dashed lines mark the major triangles. The thin solid lines indicate the borders of connected regions. The crosses with the number in the FLATTY display mark the directions of the tracks extrapolated from the chamber. At the bottom the chamber in a (R, φ) and Z-projection is shown. The hits and reconstructed tracks are displayed.*

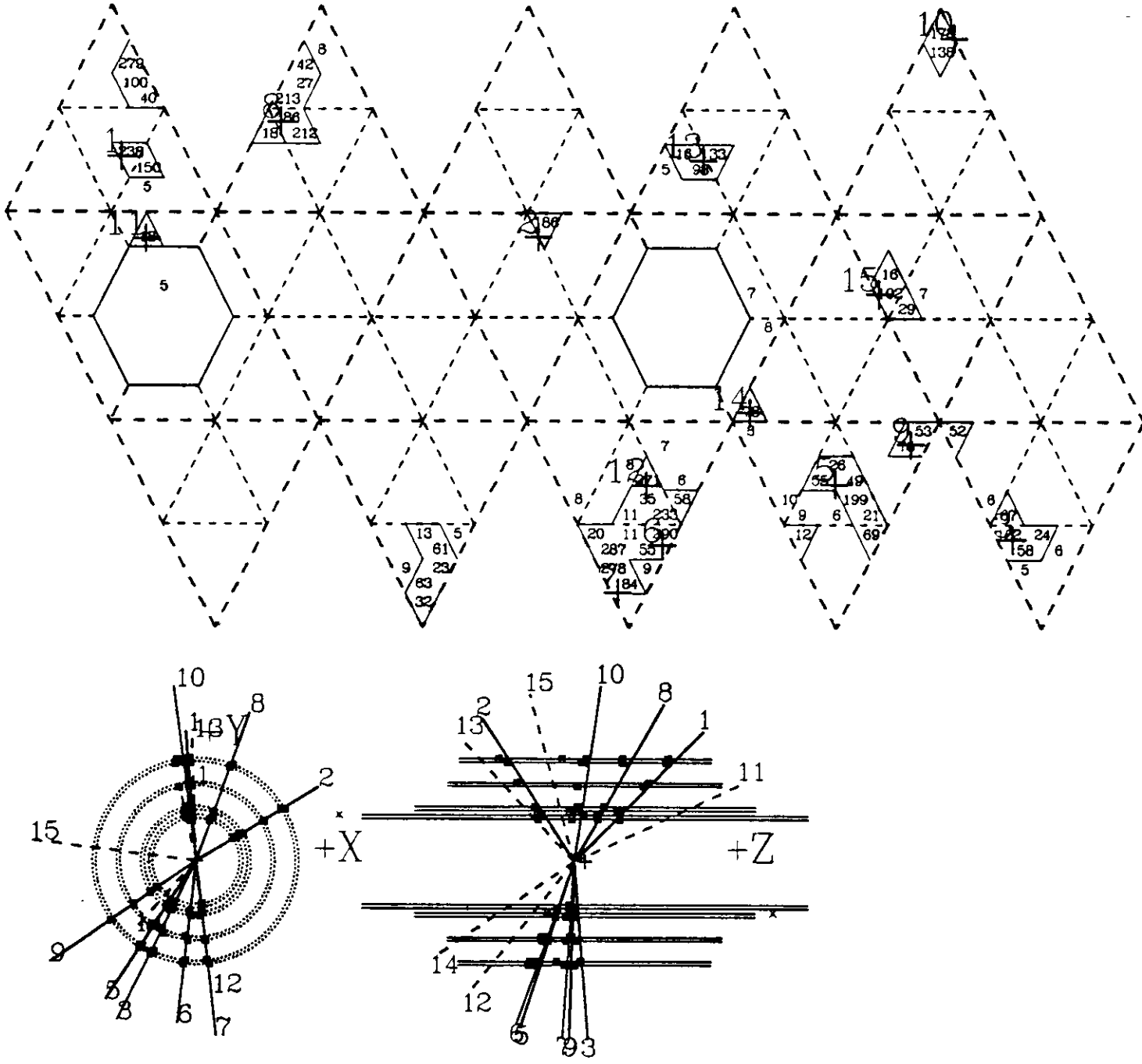

Figure 4.5: *A FLATTY of a typical $q\bar{q}$ event. The energies in the crystals are shown as numbers in MeV . The faint dashed lines mark the borders of the minors and the bold dashed lines mark the major triangles. The thin solid lines indicate the borders of connected regions. The crosses with the number in the FLATTY display mark the directions of the tracks extrapolated from the chamber. At the bottom the chamber in a (R, φ) and Z-projection is shown. The hits and reconstructed tracks are displayed.*

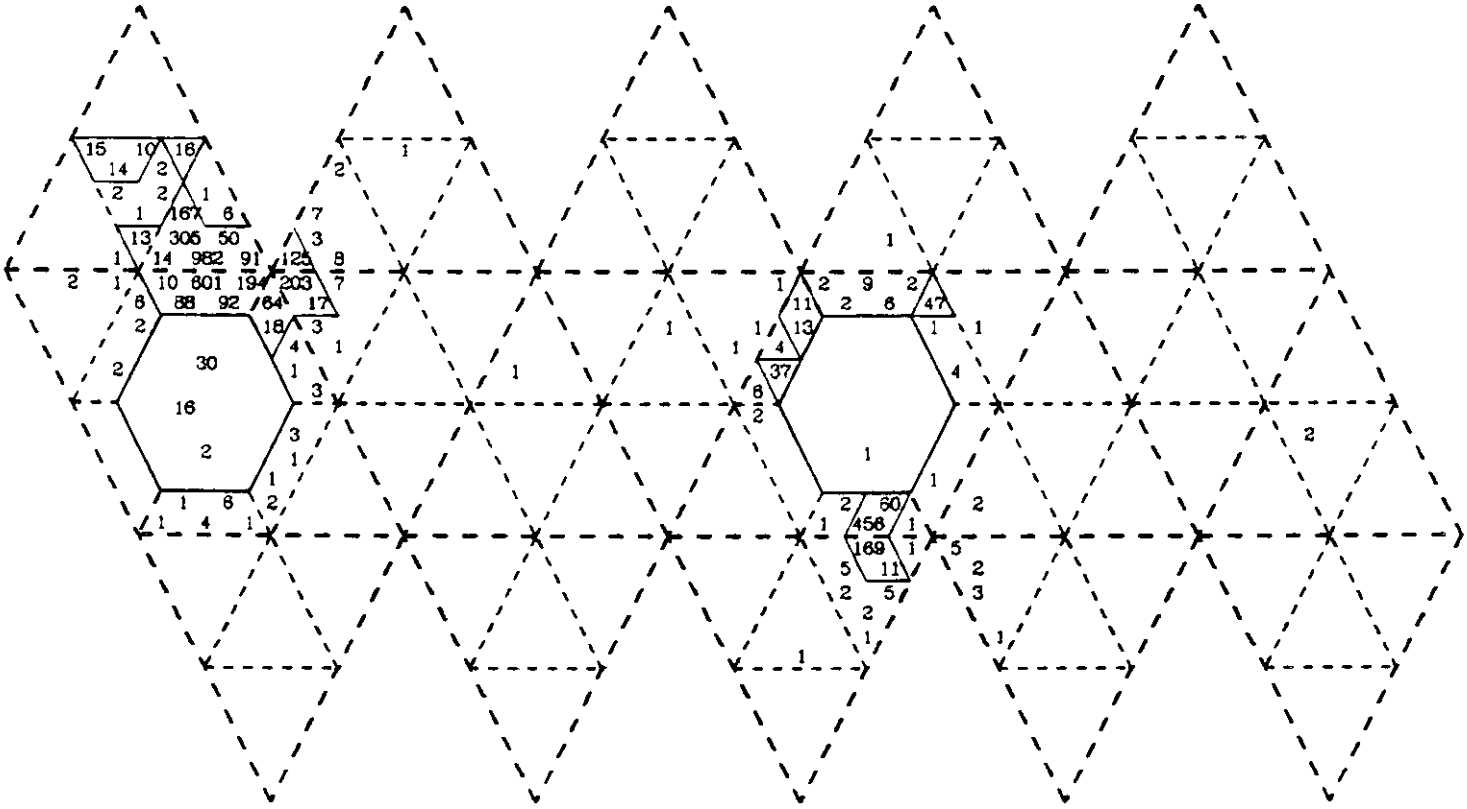

Figure 4.6: *A FLATTY of a beam-gas or beam-wall event. The energies in the crystals are shown as numbers in MeV . The faint dashed lines mark the borders of the minors and the bold dashed lines mark the major triangles. The thin solid lines indicate the borders of connected regions.*

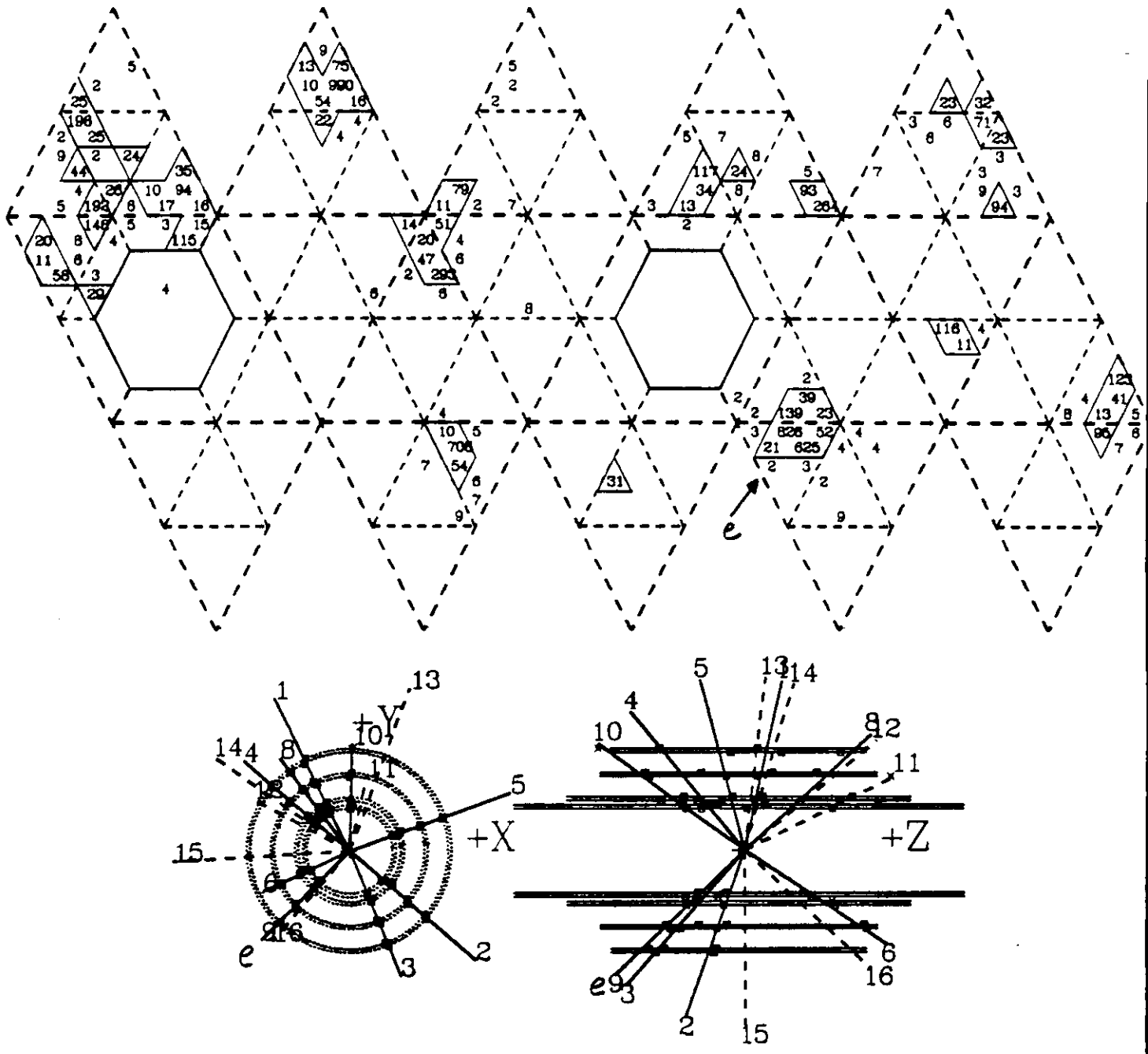

Figure 4.7: *A FLATTY of a Monte Carlo event* $\Upsilon(4S) \to \overline{B^0}B^0 \to e^+\nu_e D^{*-}, \omega\pi^- D^{*+}$. *and subsequent decays of the* D^{*+-} *and* ω. *The final state consists of 23 non-neutrino particles, including 12 photons. The energy of the electron is 1.88 GeV . It is indicated in the FLATTY and in the chamber display. Other track directions are not shown in order not to overcrowd the picture. The energies in the crystals are shown as numbers in MeV . The faint dashed lines mark the borders of the minors and the bold dashed lines mark the major triangles. The thin solid lines indicate the borders of connected regions. At the bottom the chamber in a* (R, φ) *and Z-projection is shown. The hits and reconstructed tracks are displayed.*

4.2.2 Hadron Selection

The general characteristics of the event classes discussed above are used to distinguish between the classes of the individual events. We wish to select multi-hadron events and suppress the above mentioned backgrounds. As discussed before, a cut requiring a high multiplicity discards QED events. Requiring a large fraction of energy deposited along directions perpendicular to the beam removes the background from beam-gas and beam-wall interactions. Demanding a large energy deposition removes events from two - photon induced interactions. In detail we do the following. We define the energy seen in the 672 crystals in the main Ball to be $E_{BALL} = \sum_{i=1}^{672} E_i$. Multi-hadron events have to pass the following selection cuts:

1. The first group of cuts suppresses QED events.
   We require a minimum multiplicity: There should be at least three energy clusters with an energy $E_{CONREG} > 100$ MeV each.
   If radiative Bhabhas have photons with more than 100 MeV, the two following cuts will suppress them further. Events should have at most one energy cluster with $E_{CONREG} > 0.80\, E_{BEAM}$ and should not have any energy cluster with $E_{CONREG} > 0.80\, E_{BEAM}$ if $E_{BALL} > 0.75\, E_{CM}$.

2. Beam-gas and beam-wall interactions deposit a lot of energy at small angles; we therefore demand: $E_{TUNNEL}/E_{BALL} < 0.5$, where E_{TUNNEL} is the sum of the energies deposited in the 60 tunnel crystals of the main Ball. This cut is almost 100% contained in the next cut. It is only noted for completeness.

3. Against beam-wall and beam-gas interactions we cut in the following quantities: We define the absolute value of the vector sum $|\vec{\beta}| = \frac{1}{E_{BALL}} \left| \sum_{i=1}^{672} E_i \hat{n}_i \right|$, where $\hat{n}_i$ is a unit vector pointing to the center of the i^{th} crystal , and the normalized transverse energy of an event $E_{trans} = \frac{1}{E_{CM}} \sum_{i=1}^{672} E_i \sin\theta_i$. We apply the following cut in the (E_{trans}, β) plane – see figure 4.8: events accepted if they satisfy $E_{trans} > 0.2$, $\beta < 0.7$, and $E_{trans} > 0.5\beta + 0.1$. This cut in E_{trans} implicitly requires a minimal energy $E_{BALL} > 0.2 E_{CM} = 2.1\ GeV$ at the $\Upsilon(4S)$ resonance.

An event which is accepted by all those cuts is called a multi-hadron event. Figure 4.9 shows the energy deposited in the Ball by all events and by multi-hadron events for a representative subsample of ON $\Upsilon(4S)$ data. The structures at lower energies are due to different trigger thresholds, but they are outside the interesting region of this analysis. The most effective cut against beam-gas and beam-wall events is the cut in the (E_{trans}, β) plane.

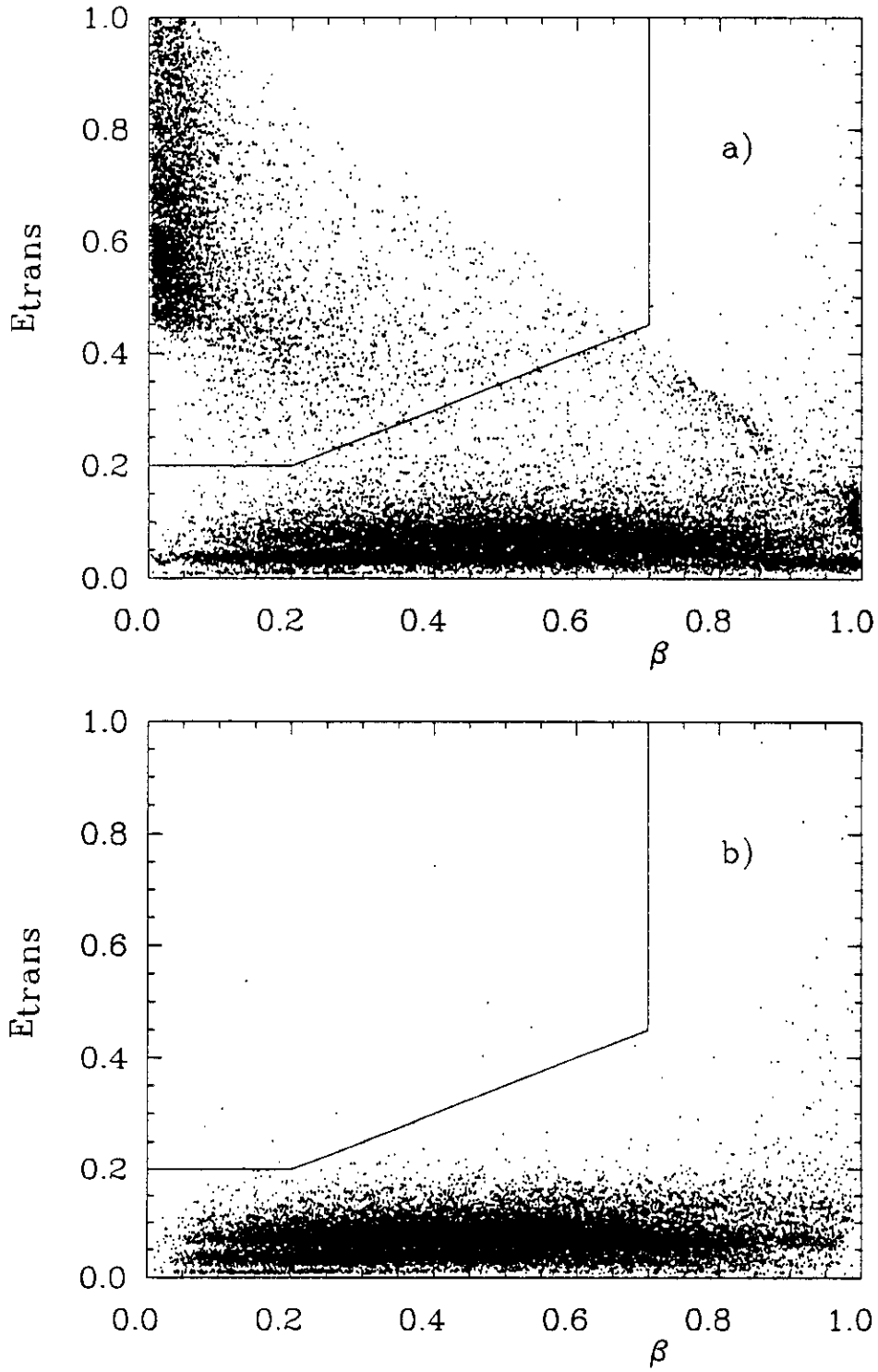

Figure 4.8: *Hadron Selection. The* (E_{trans}, β) *plane, for a representative subsample of ON* $\Upsilon(4S)$ *(a) data and for single beam data (b).*

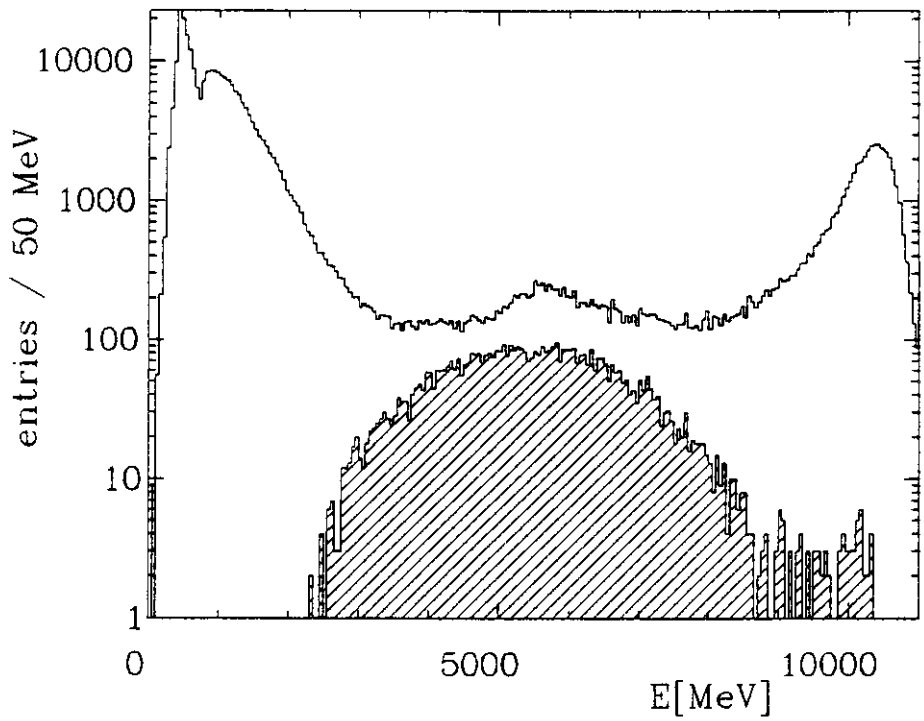

Figure 4.9: *Hadron selection, the energy deposited in the Ball. The shaded area represents entries from accepted multi-hadron events.*

Figure 4.8 shows the (E_{trans}, β) plane for colliding beam data and data taken with electron or positron beams alone. Single beam data are clearly rejected by the cut in the transverse energy. The first group of cuts rejects a lot of Bhabha events which would pass the cut in the (E_{trans}, β) plane. Table 4.1 shows the rejection of the cuts 1 to 3. Only 2 % of the recorded events are accepted as multi-hadron events. There

cut number	fraction of rejected events: if no other cut applied, normalized to initial sample [%]	after other two cuts applied, normalized to initial sample [%]	after other two cuts applied, normalized to sample left after two cuts [%]
1 ,QED	76.2	14.5	87
2 ,Tunnel	56.2	0.06	3
3 ,E_{trans}, β	79.5	15.0	88
1 + 2 + 3	97.9		

Table 4.1: *Rejection of events by the hadron selector.*

is still a contribution from QED events like Bhabha events. In figure 4.9, where the energy seen in the Ball is plotted, a small peak at the center-of-mass energy is visible. This peak originates from Bhabha events. They deposit a lot of energy and if one electron interacts with the beam pipe or chamber the multiplicity of *bumps* in the Ball is increased. As we are searching for electrons, those events are one kind of

background. The further rejection of Bhabha (and $\tau\overline{\tau}$) events is discussed after the electron selection when the properties of this background will become clearer.

4.2.3 Visible Hadronic Cross-Section

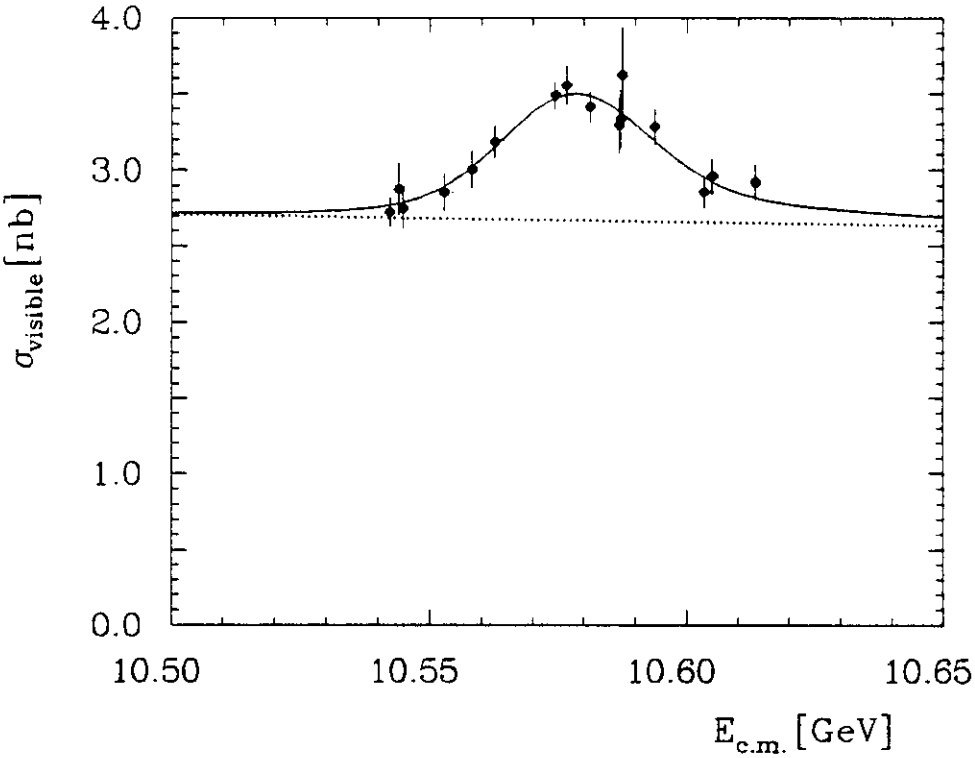

Figure 4.10: *Visible cross-section $\sigma_{visible}$ as function of the center-of-mass energy at the $\Upsilon(4S)$ resonance. The curves shown are plotted to guide the eye.*

The visible cross-section - number of events / luminosity - using the hadron selector described above is shown in figure 4.10. A scan over the $\Upsilon(4S)$ resonance is performed. The resonance has a visible cross-section of about 0.8 nb while the continuum contribution has a visible cross-section of 2.6 nb. Therefore it is neccessary to further reduce the contribution from the continuum. This will be done after the description of the electron selection, as we are looking for a special type of multi-hadron events.

4.2.4 Data Sample and Number of $\Upsilon(4S)$ Events

In order to deduce the number of multi-hadron events from the $\Upsilon(4S)$ resonance, a data sample is taken at beam energies of 20 to 40 MeV below the $\Upsilon(4S)$ resonance energy. The number of observed $\Upsilon(4S)$ decays, N_{4S}, is given by:

$$\begin{aligned} N_{4S} &= H(ONResonance) - H(Continuum) \times \frac{L_{ON}}{L_{OFF}} \left(\frac{E_{BeamOFF}}{E_{BeamON}} \right)^2 \\ &= H(ONResonance) - H(Continuum) \times \frac{M_{BhabhaON}}{M_{BhabhaOFF}}, \end{aligned} \tag{4.5}$$

where H denotes the number of multi-hadron events found in the ON and OFF resonance data samples, $L_{ON/OFF}$ is the integrated luminosity of the ON and OFF resonance data, and M the number of Bhabha events found by the luminosity event

selection in the ON and OFF resonance data samples.

The cross-section of the continuum contributions to $q\bar{q}$ and $\tau\bar{\tau}$ has the same de-

	ON $\Upsilon(4S)$	continuum	$B\bar{B}$
luminosity $[pb^{-1}]$	75.6	18.5	
number of luminosity events	872894	216682	
luminosity scale factor		4.028 $\pm$0.009	
number of multi-hadron events observed	288563	56720	60069 $\pm$1200

Table 4.2: *Data samples ON and OFF resonance used in this analysis. The data selected are taken in the years 1985 and 1986. The serial number of the first run used is 15448 and the last one is 30782. The error on the number of the observed* $\Upsilon(4S)$ *events is 2.0%. It results from the statistical error of the continuum sample of* 0.4% *- to be multiplied by the luminosity scale factor, 0.2% from the beam-gas background subtraction and 0.2% uncertainty from the luminosity measurement.*

pendence on the beam energy as the Bhabha events used to calculate the luminosity. Hence it is legitimate to drop the beam energy dependence in equation 4.5 and to use instead the number of Bhabha events ON and OFF resonance to scale the continuum contribution. This procedure has the advantage that the knowledge of the beam energy of the two samples is not required, and, therefore, a source of uncertainty is removed. The systematic uncertainty on the number of observed $\Upsilon(4S)$ decays then depends on the stability of the luminosity measurement and on the different background conditions for the two samples. In appendix B the luminosity measurement is discussed with special emphasis on the stability of the luminosity measurement. For this analysis only data are used where no problem in the luminosity measurement is found. Another requirement on the data are the stability of the tube chamber performance. As we are searching for electrons inside multi-hadron events, a difference in the tube chamber performance between the ON resonance and the continuum data sample would be harmful. The performance of the tube chamber is discussed in appendix C. Different background conditions were found to have negligible influence on the number of $\Upsilon(4S)$ events. This check is performed by varying the cut in the multiplicity of the multi-hadron event selection from a value of 3 to 7. This change is expected to suppress beside $\tau\bar{\tau}$ and $q\bar{q}$ events also beam-gas and beam-wall events. The variation on the number of $\Upsilon(4S)$ events is found to be smaller than 0.15%. Putting together all restrictions, the maximum available integrated luminosity listed in table 3.1 is reduced to that listed in table 4.2. About 14 pb^{-1} and 11 pb^{-1} of luminosity of ON and OFF resonance data,respectively, are not used.

4.3 Electron Selection

After having selected the multi-hadronic events, we search for electrons inside the events. We apply the following cuts which are explained later:

1. $|\cos\theta| < 0.76$,

2. track has to be tagged or tracked charged;

3. $E_{24_s} < 15 - \frac{30}{5000} \times E_{13}$; E_{13} in MeV:

4. $(< x^2 > - < y^2 >) < (0.005 + \frac{0.003}{5000} \times E_{13})$; E_{13} in MeV;

5. $E_3/E_9 < 0.02$; $E_9 > 1\ MeV$;

6. $0.88 < E_4/E_{13} < 0.96$;

7. $0.45 < E_1/E_4 < 0.92$.

The inclusive spectra before and after each cut together with the rejected spectrum is shown in figures 4.12 to 4.19. The binning of the histograms is logarithmic with a bin width of 3%. That kind of binning results in an approximately constant resolution per bin over the total energy range. Not all cuts are described in detail, only those which have the largest impact on the spectrum.

Cuts 1 and 2: Solid Angle and Charge

The first cut in the solid angle was chosen in order to let the particles pass all four chambers, in a way that no border effects of the chambers have to be taken into account. To become independent of the direction measurement [1] by the chamber, the routine SHOWER [31] is used to define the track direction. This routine only uses the information of the crystals.

The effect of the second cut requiring the cluster to be charged is illustrated in figure 4.12. The rejected spectrum is smooth besides a small peak at about 200 MeV. Those entries come from untagged charged minimum ionizing particles, as a consequence of the chamber not being fully efficient for those particles – see appendix C.

Cut 3: E_{24_s} Pattern Cut

The effect of the third cut in E_{24_s} is shown in figure 4.13. To understand this cut on has to look at figure 4.1. There the central *bump* crystal together with its $3 + 9 + 24 = 36$ neighbours is shown. E_{24_s} is defined as the highest energy of a single crystal on the ring of 24 around the 13 crystals used for the energy measurement of the particle. This cut serves as an isolation cut. If two particles approach each other in direction they start to illuminate the same crystals. The cut is tuned with Monte Carlo electrons in the empty Ball. It has an energy dependence correcting for the energy leakage outside the 13 crystals which increases with increasing particle energy. Figure 4.21 shows the correlation of the E_{24_s} variable to the E_{13} energy after all other cuts have been applied. At high energies a band of entries is visible. Comparing those entries with a Monte Carlo prediction of electrons in the empty Ball, the electrons are seen in the expected part of the plot. The initial spectrum is reduced in the total range, since the overlap probability with other particles does not depend too much on the energy of the incident particle.

[1] The direction of charged tracks is taken from the tube chamber, the direction of tagged tracks is taken from the ESORT algorithm, see chapter 4.5.

Cut 4: Second Moments

The 4^{th} cut is in the second moments of the lateral energy distribution. Its effect is displayed in figure 4.14. The moments are calculated in the following way. A moment is defined as: $< a^n >= \Sigma E_i a^n / \Sigma E_i$ where i runs over the crystals in the connected region.
The coordinate system of the crystal direction cosines x_i, y_i, z_i is rotated, such that $< x, y, z >=< 0, 0, 1 >$

Then a next rotation is performed, such that: $< xy > = 0$ and $< x^2 > > < y^2 >$

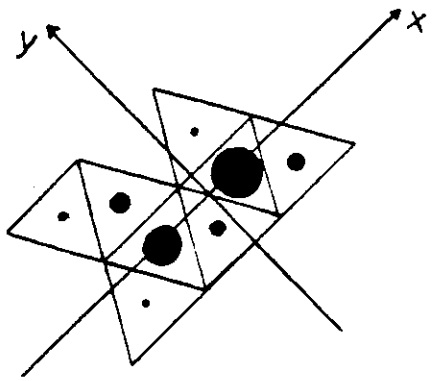

Figure 4.11: *The principal axis directions in the FLATTY display*

Figure 4.11 illustrates the choice of the principal axes with the energy deposition shown in a part of a FLATTY. Perfectly round showers give $< x^2 - y^2 >= 0$, while elongated showers give $(< x^2 - y^2 >) >> 0$. Together with the overlap cut (cut number 3) only circular connected regions are left.

Minimum ionizing particles produce clusters of circular shape, too. They deposite energy in only one or two crystals.

Cut 5: E_3/E_9 Pattern Ratio Cut

Most of connected regions from minumum ionizing particles are removed by the cut in E_3/E_9, as can be seen in figure 4.15. As in the case of the cut in E_{24}, one should look at figure 4.1 to understand the definition of this quantity. Around the central group of 4 crystals 3 groups of 3 crystals surround the center. E_9 is the sum of energies of these 3×3 crystals. E_3 is defined as the energy sum of the group of 3 crystals which has the smallest energy sum.

Strongly interacting hadrons very often deposit irregular patterns such that some crystals are not illuminated. Most of the rejections take place at lower energies ($< 1\ GeV$). When hadrons deposit more than 1 GeV, often energy from electromagnetically showering particles is involed when e.g. charged pions interact ($\pi^- + p^+ \rightarrow n + \pi^0, \pi^0 \rightarrow \gamma\gamma$). Therefore those showers extend over several crystals and this cut is not effective. After having applied this cut, a small signal at about 1.5 GeV in the ON $\Upsilon(4S)$ spectrum can be seen.

Cut 6: E_4/E_{13} Pattern Ratio Cut

The next cut in E_4/E_{13} together with the cut in E_{24}, has the largest rejection rate of all cuts. E_4 is the sum of energies of the 4 central crystals around the *bump* crystal. E_{13} is the energy sum of the 13 crystals with no energy correction. Figure 4.16 shows the

effect of this cut. It can be used very efficiently for distinguishing between electrons and non-electromagnetically showering particles. Figure 4.20 shows the E_4/E_{13} distribution of ON $\Upsilon(4S)$ and continuum data and the continuum-subtracted distribution together with a Monte Carlo prediction – right-hand part. Although all other cuts have been applied this cut still rejects about 30 % of the tracks while only a little fraction of good electrons is discarded. The data are well reproduced by the Monte Carlo prediction.

Cut 7: E_1/E_4 Pattern Ratio Cut

The last cut on the properties of the electron candidate is the cut on the ratio E_1/E_4, see figure 4.17. E_1 is the energy of the *bump* crystal, E_4 is the sum of energies of the four central crystals. This cut is only effective for energies below 1 GeV, but it still rejects minimum ionizing particles at about 200 MeV.

Spectrum after Electron Selection

After having applied all these cuts a clear signal in the ON $\Upsilon(4S)$ data is visible around 1.5 GeV. The comparison of the ON and OFF resonance data in figure 4.17 *b*) and *d*) shows that most of the flat part of the spectrum around 1.5 GeV comes from the continuum contribution. The luminosity scale factor between the ON and OFF resonance data is 4.028. Therfore the two plots can be compared directly since the Y-axis of the OFF resonance data is reduced by a factor of 4.0 compared to the ON resonance data.

Cut in the Event-shape Parameters

In order to further suppress non-$B\overline{B}$ events we demand the number of *bump* crystals to be > 7. Figure 4.24 shows on top the number of *bumps* for events which have an electron in the energy range 1.5 $GeV < E_e < 2.7\ GeV$. ON $\Upsilon(4S)$ data are compared with the continuum data. Figure 4.18 shows the effect of this cut. A large fraction of continuum events at energies above 1 GeV is rejected.

Additional suppression of the non-$B\overline{B}$ events is achieved by a cut in the pseudo Fox-Wolfram event shape parameter $H2$ [32]

$$H2 = \frac{\sum_{i,j} E_i E_j (3\cos^2\alpha_{i,j} - 1)}{2(\sum_i E_i)^2} < 0.55, \qquad (4.6)$$

where E_i is the energy deposited in the *bump* crystal i, and α the angle between *bumps*. Only *bumps* in the main Ball excluding endcaps are used. The proper definition of the Fox-Wolfram moments uses the momentum of the particles. The Crystal Ball measures total energy only of electromagnetically showering particles and sees only a small fraction of the energy of charged hadrons which are mostly minimum ionizing. If one would use e.g. the connected region energy, the energy of electromagnetically showering particles would enter with an inappropriately large weight into the Fox-Wolfram parameter $H2$.

We therefore only take the energy of the *bump* crystal in order to suppress the electromagnetically showering particles in about the same way as the energy of minimum ionizing particles is reduced. Figure 4.24 shows the distributions of the *bump* crystal multiplicity and of the quantity $H2$ for the ON $\Upsilon(4S)$ and the continuum data sample. In both quantities, *bump* crystal multiplicity and $H2$, the cuts are placed in a way such

that almost no $\Upsilon(4S)$ data are lost ($\approx 0.5\%$). This is done because we do not want to cut too hard on event shapes as the different event types ($b \rightarrow c$ and $b \rightarrow u$) we are looking for might differ in these quantities. Furthermore, cutting harder in these quantities would require a very good Monte Carlo simulation of the $\Upsilon(4S)$ events for the efficiency determination.

Another quantity where one immediately can find one source of background is the quantity E_{BALL} shown in figure 4.22. A clear peak at the center-of-mass energy is present. This bump is induced by radiative Bhabha events where one electron showers in the beam pipe (or chamber) resulting in an increased multiplicity. Therefore these events pass the multi-hadron event selection. Applying the cut on the number of *bump* crystals and on $H2$, the second peak is removed. But also at lower E_{BALL} energies a lot of events are rejected. In the next chapter, where we discuss the Monte Carlo simulation in detail, we show that those events are mostly $\tau\bar{\tau}$ events. Figure 4.19 shows the resulting electron spectrum after the cut in $H2$. Though it looks as if the cut in $H2$ had a small impact after the cut in the number of *bump* crystals, the cut still rejects about 15% of the continuum contribution. The continuum contribution to the ON $\Upsilon(4S)$ electron spectrum around 1.5 GeV is reduced by a factor of about 2 due to the two event shape cuts.

In the next chapter we shall discuss the efficiency to detect the electrons with this selection and discuss the background contributions to the electron spectrum.

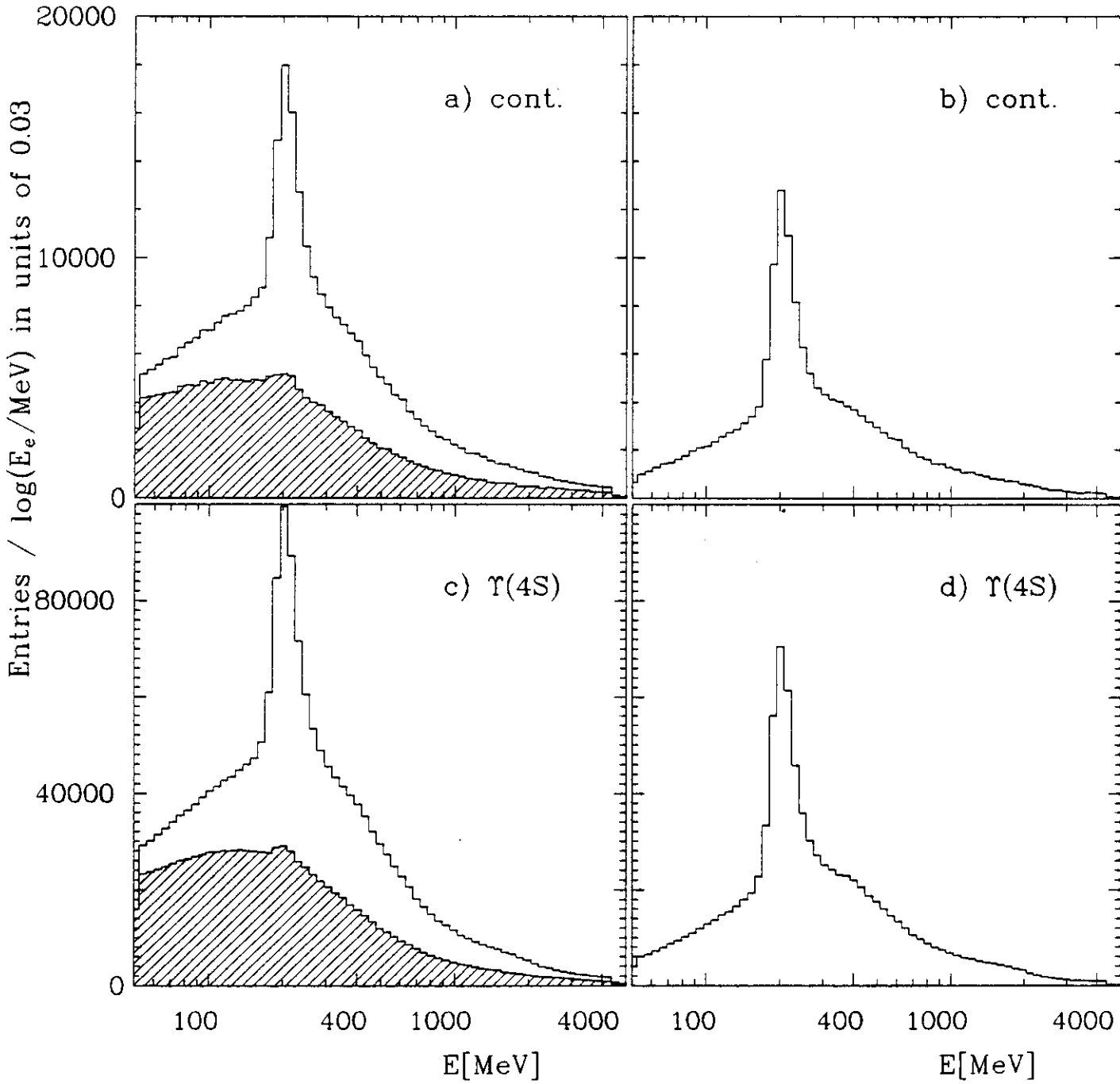

Figure 4.12: *Inclusive electron spectrum after cut 2, requiring charged particles only. We show four plots: a) Continuum spectrum before the cut together with the rejected spectrum. b) Continuum spectrum after the cut. c) ON $\Upsilon(4S)$ spectrum before the cut together with the rejected spectrum. d) ON $\Upsilon(4S)$ spectrum after the cut.*

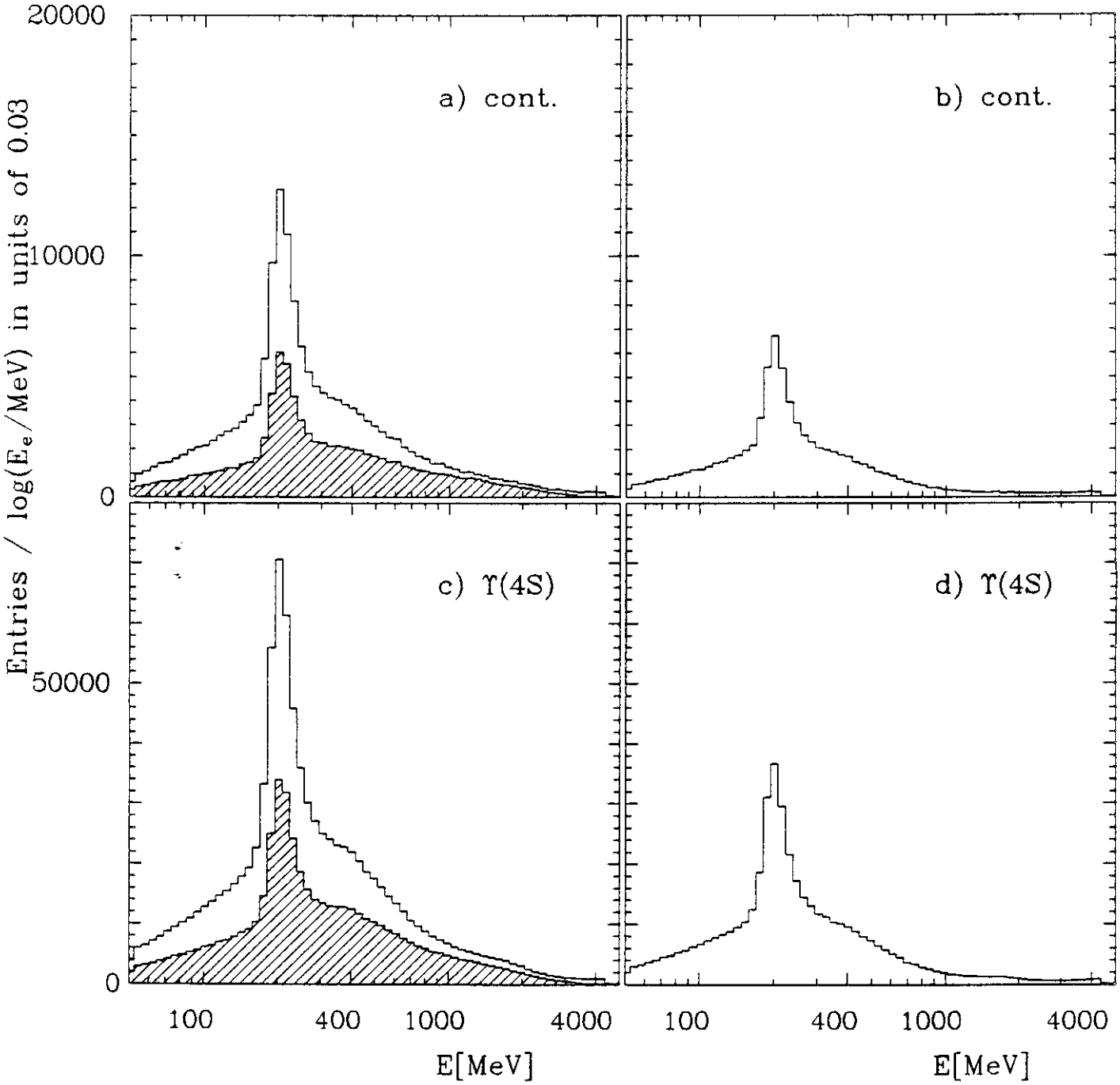

Figure 4.13: *Inclusive electron spectrum after cut 3 in E24s. We show four plots: a) Continuum spectrum before the cut together with the rejected spectrum. b) Continuum spectrum after the cut. c) ON $\Upsilon(4S)$ spectrum before the cut together with the rejected spectrum. d) ON $\Upsilon(4S)$ spectrum after the cut.*

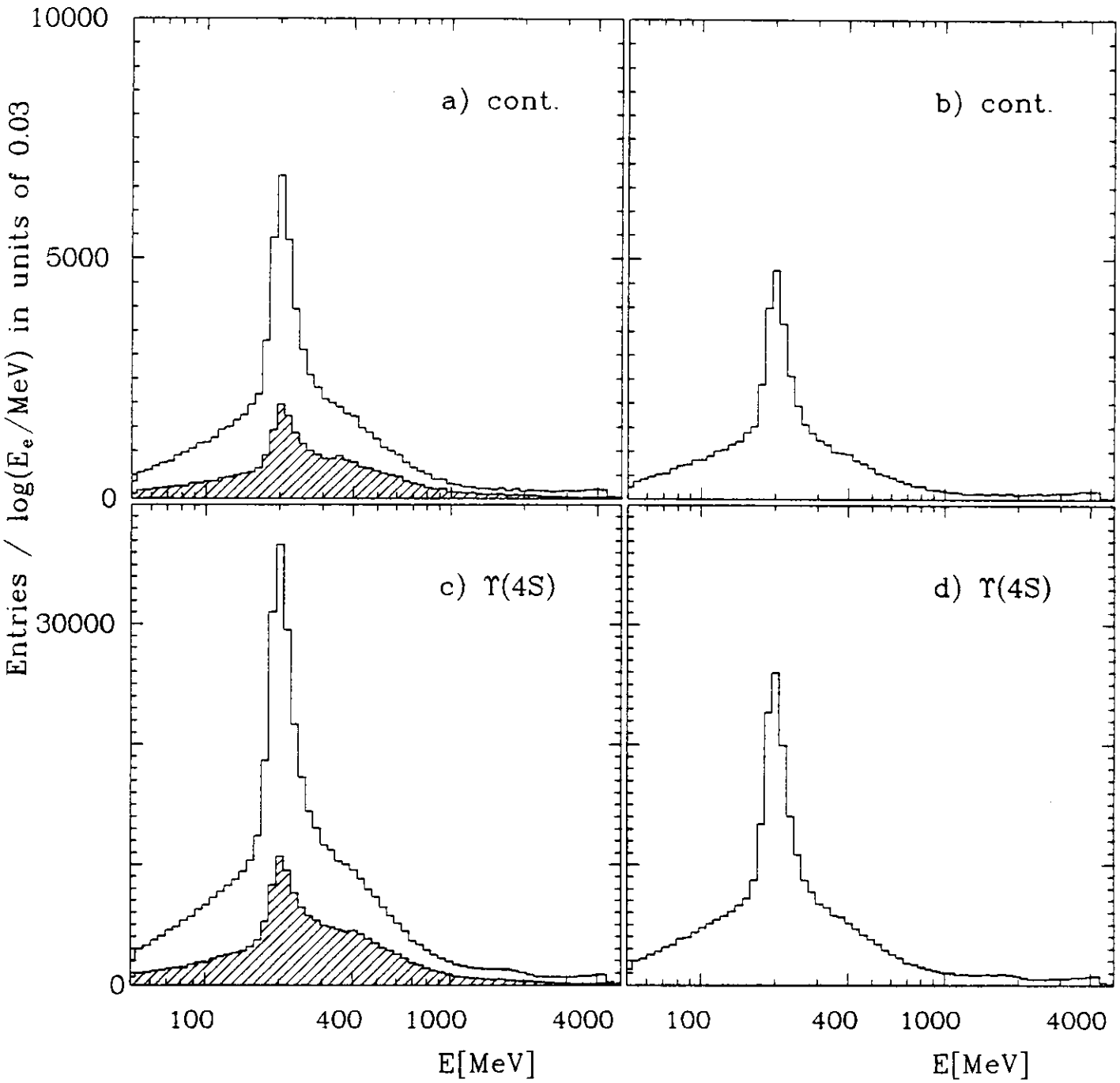

Figure 4.14: *Inclusive electron spectrum after the cut 4 in* $< x^2 - y^2 >$. *We show four plots: a) Continuum spectrum before the cut together with the rejected spectrum. b) Continuum spectrum after the cut. c) ON* $\Upsilon(4S)$ *spectrum before the cut together with the rejected spectrum. d) ON* $\Upsilon(4S)$ *spectrum after the cut.*

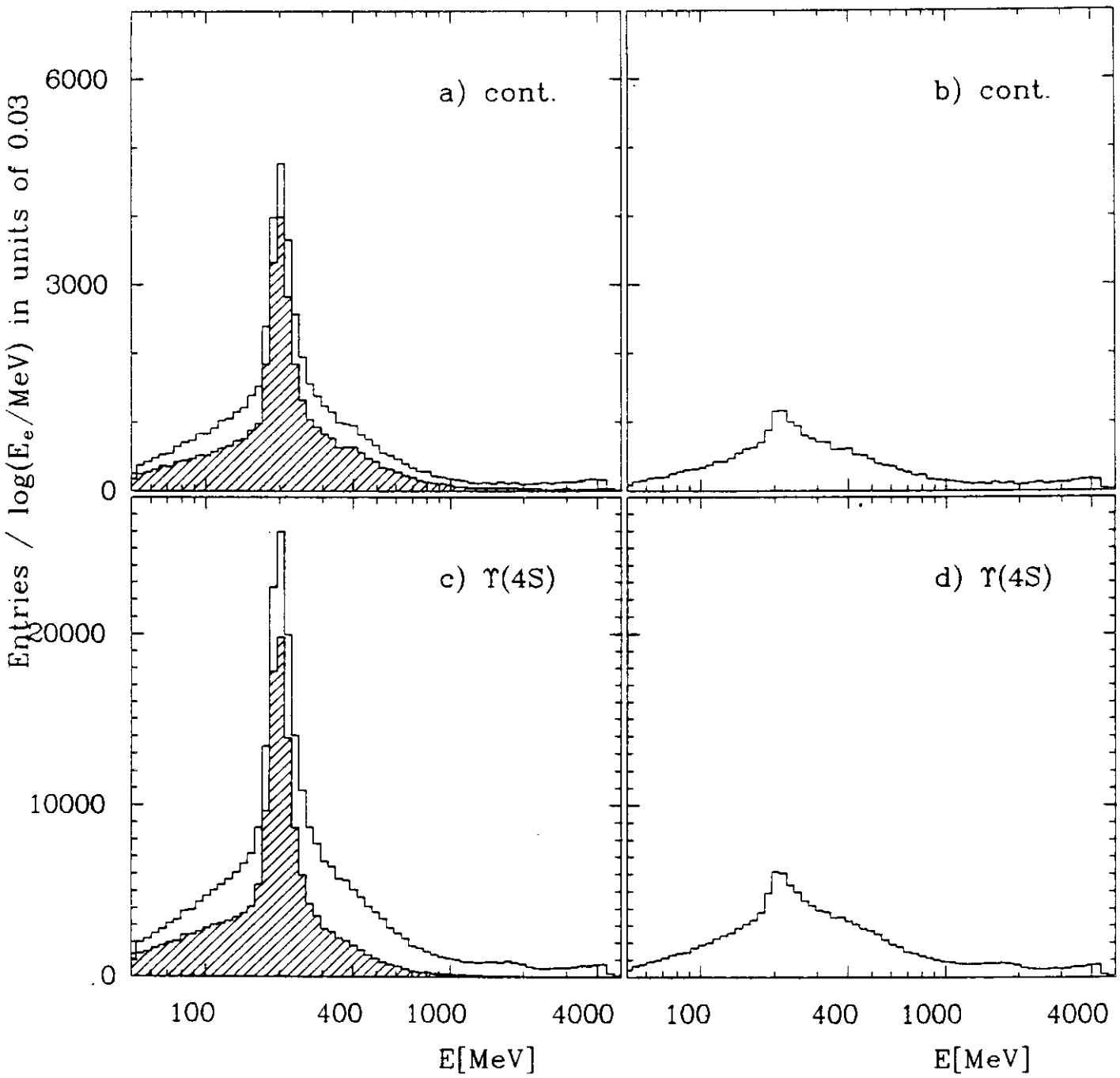

Figure 4.15: *Inclusive electron spectrum after cut 5 in E_3/E_9. We show four plots: a) Continuum spectrum before the cut together with the rejected spectrum. b) Continuum spectrum after the cut. c) ON $\Upsilon(4S)$ spectrum before the cut together with the rejected spectrum. d) ON $\Upsilon(4S)$ spectrum after the cut.*

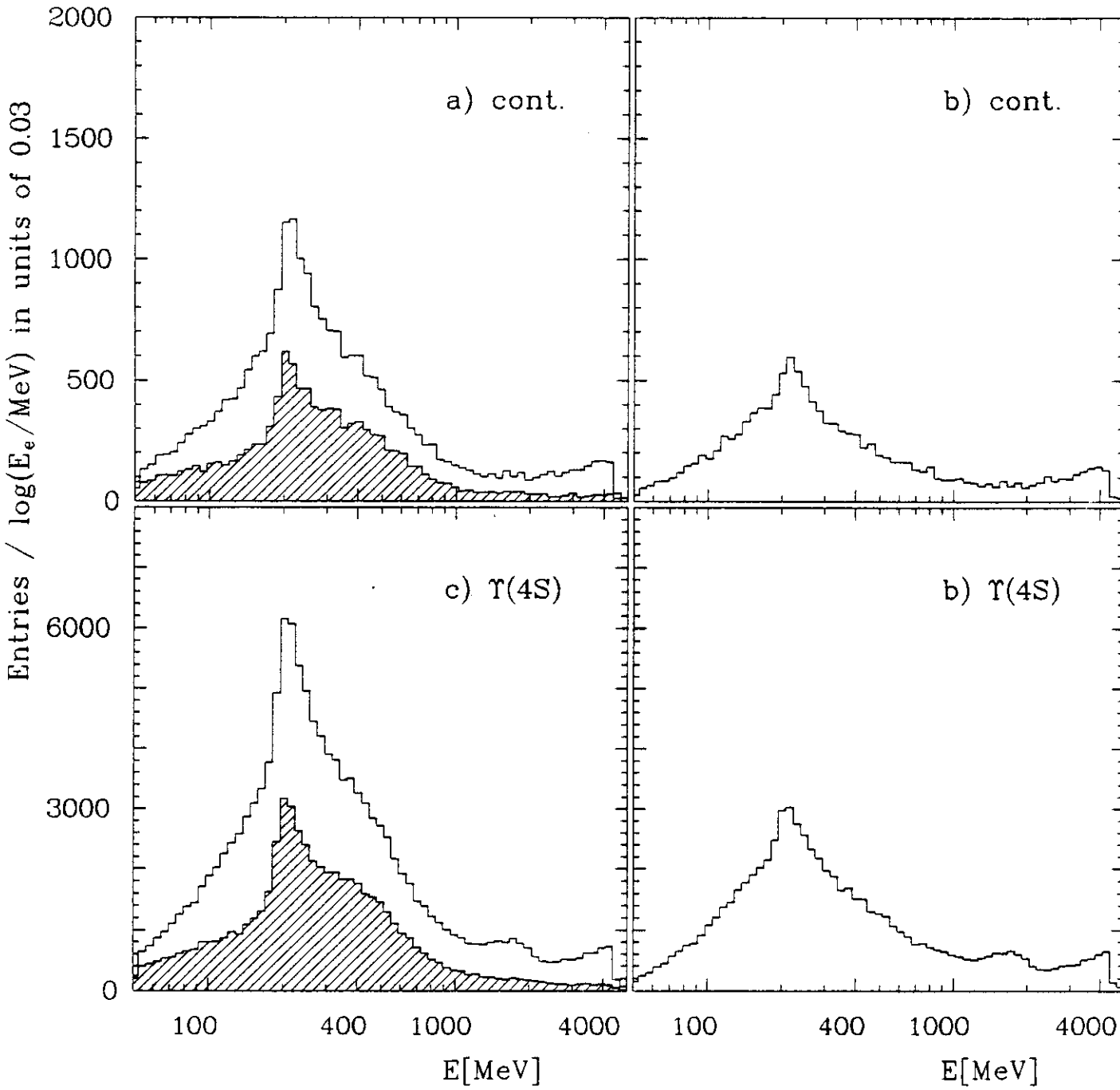

Figure 4.16: *Inclusive electron spectrum after cut 6 in E_4/E_{13}. We show four plots: a) Continuum spectrum before the cut together with the rejected spectrum. b) Continuum spectrum after the cut. c) ON $\Upsilon(4S)$ spectrum before the cut together with the rejected spectrum. d) ON $\Upsilon(4S)$ spectrum after the cut.*

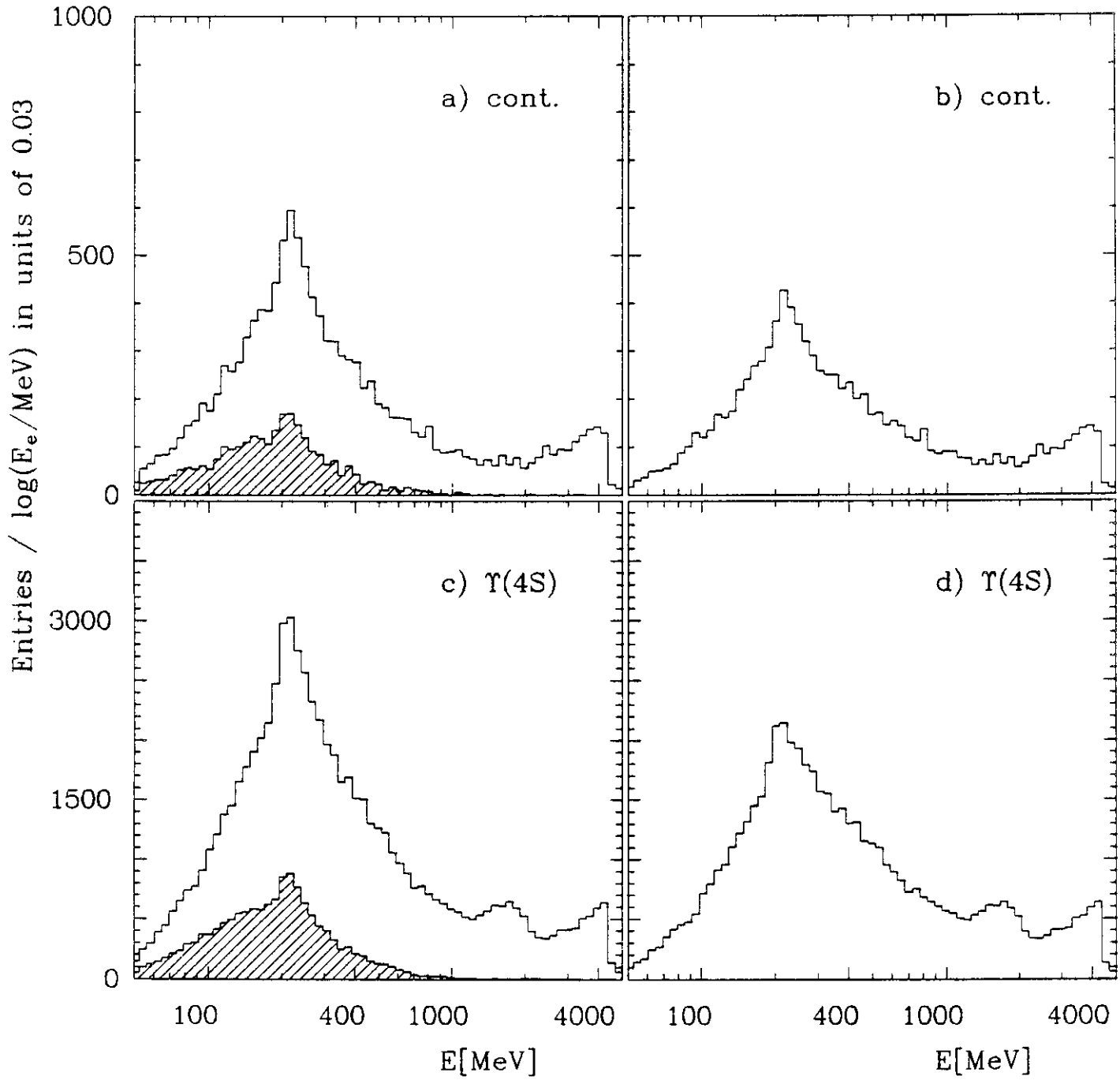

Figure 4.17: *Inclusive electron spectrum after cut 7 in E_1/E_4. We show four plots: a) Continuum spectrum before the cut together with the rejected spectrum. b) Continuum spectrum after the cut. c) ON $\Upsilon(4S)$ spectrum before the cut together with the rejected spectrum. d) ON $\Upsilon(4S)$ spectrum after the cut.*

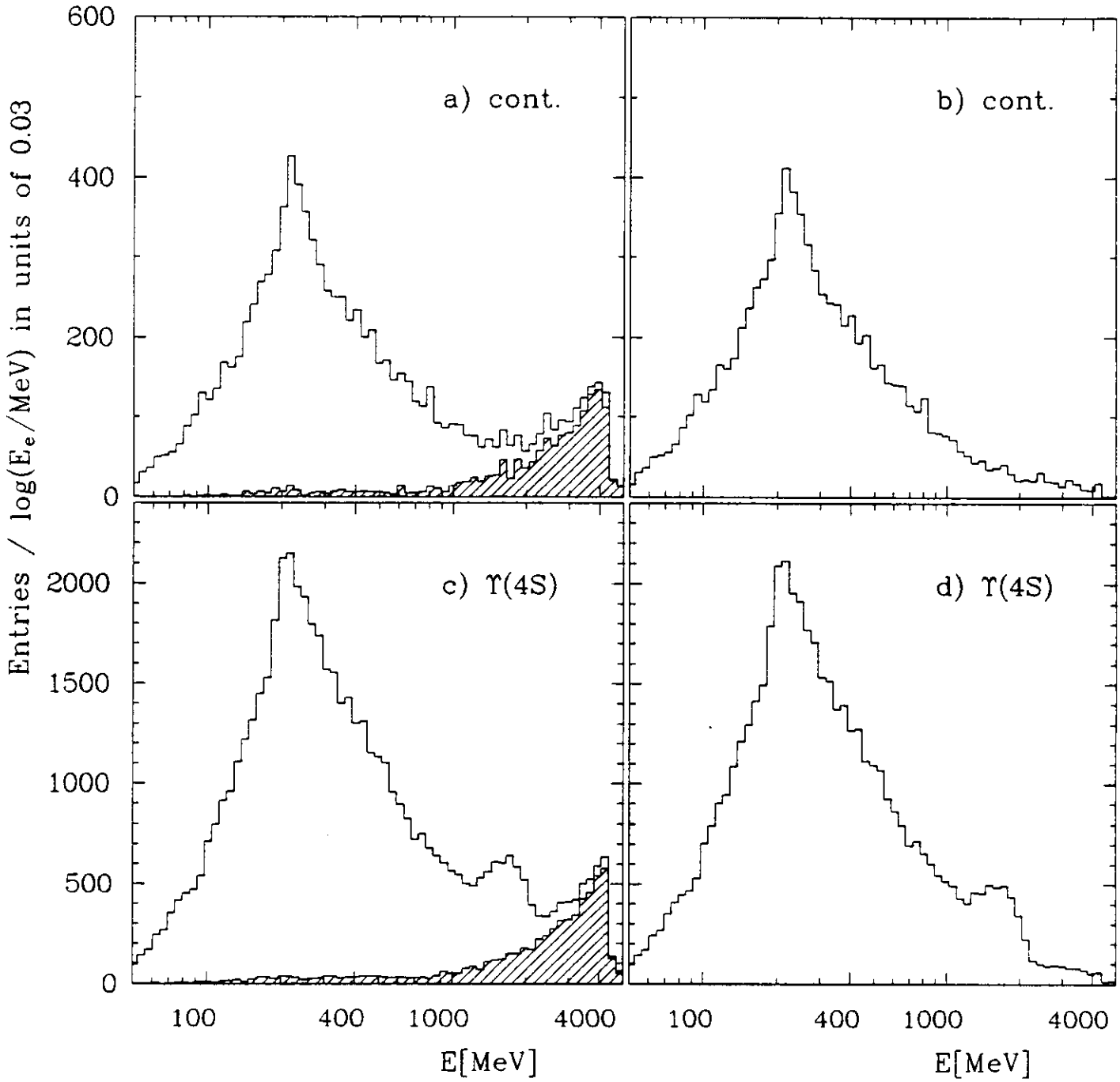

Figure 4.18: *Inclusive electron spectrum after the cut in number of bumps crystals. We show four plots: a) Continuum spectrum before the cut together with the rejected spectrum. b) Continuum spectrum after the cut. c) ON $\Upsilon(4S)$ spectrum before the cut together with the rejected spectrum. d) ON $\Upsilon(4S)$ spectrum after the cut.*

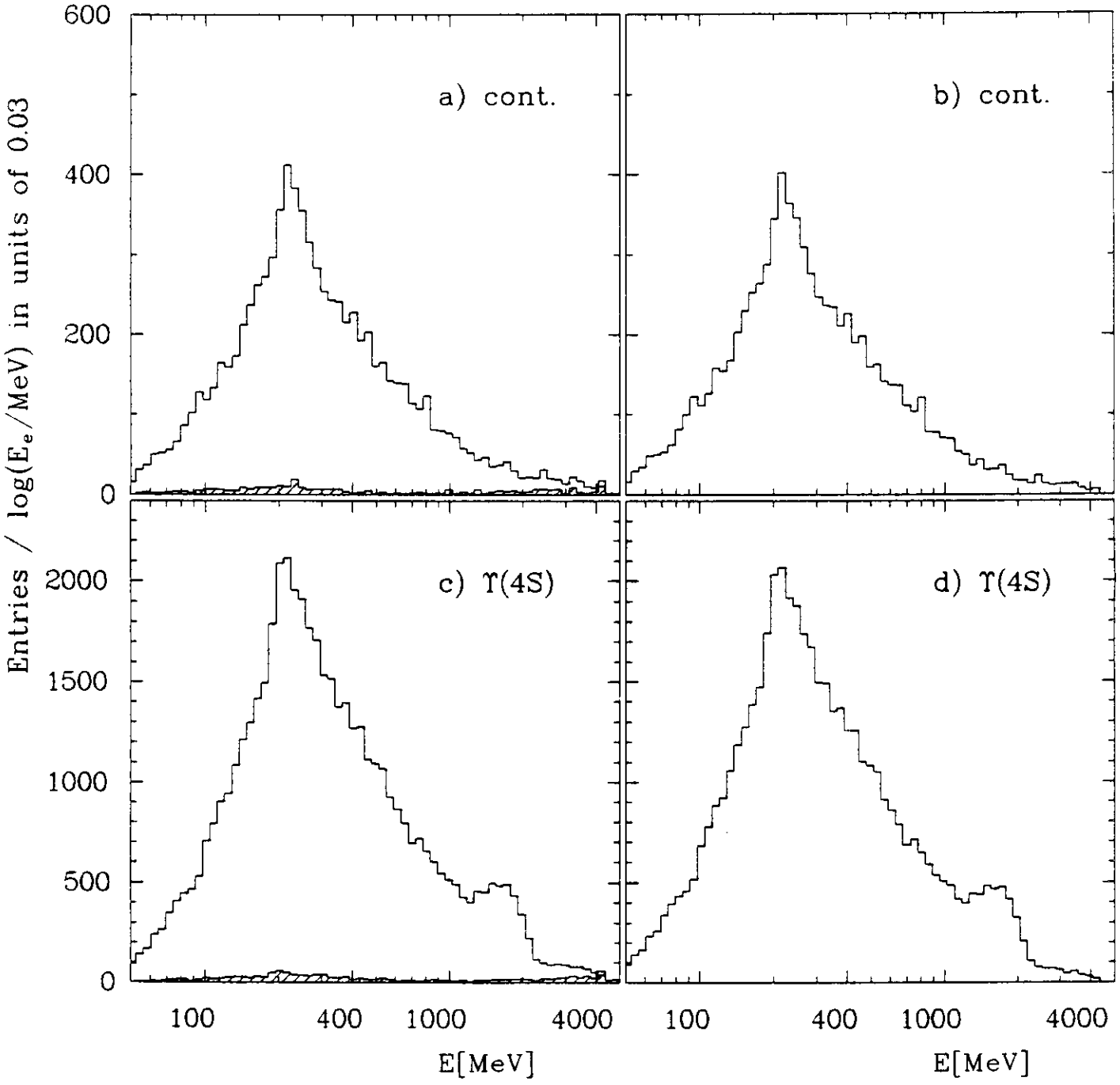

Figure 4.19: *Inclusive electron spectrum after the cut in H2. We show four plots: a) Continuum spectrum before the cut together with the rejected spectrum. b) Continuum spectrum after the cut. c) ON $\Upsilon(4S)$ spectrum before the cut together with the rejected spectrum. d) ON $\Upsilon(4S)$ spectrum after the cut.*

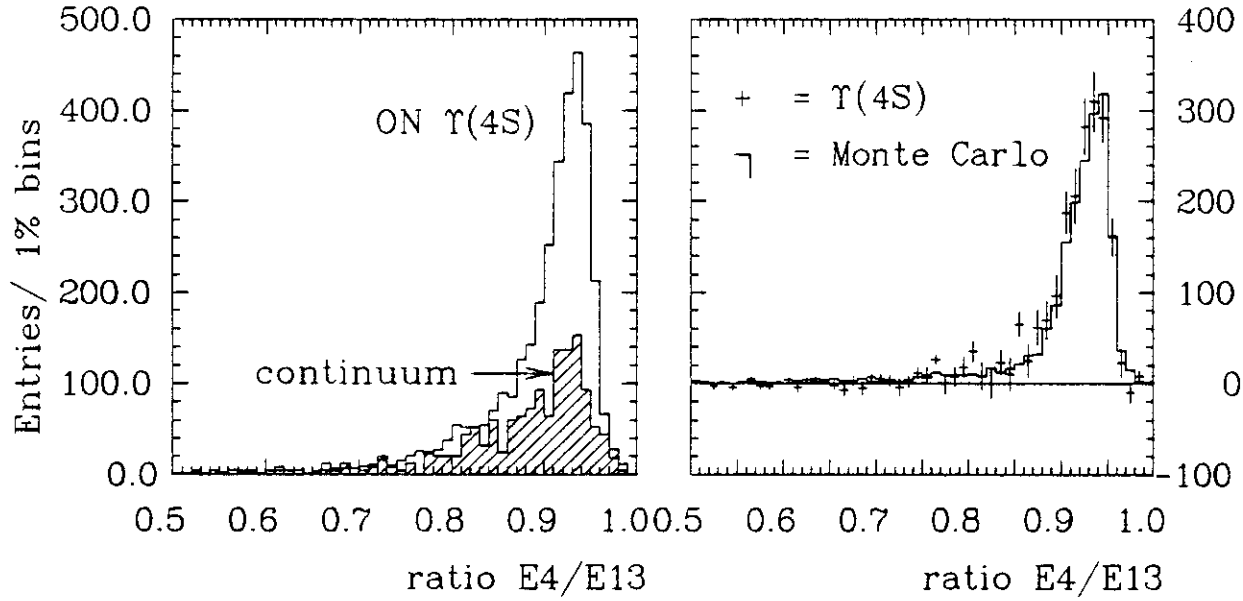

Figure 4.20: *Comparison of the ratio E_4/E_{13} between data and Monte Carlo. Electron candidates in the energy interval 1.5 – 2.7 GeV are selected. On the left-hand side the ON $\Upsilon(4S)$ and continuum distributions - scaled by the ratio of luminosities - are shown. On the right-hand side the continuum subtracted $\Upsilon(4S)$ is compared with a Monte Carlo prediction of electrons with discrete energies of 1.5 and 2.0 GeV energy.*

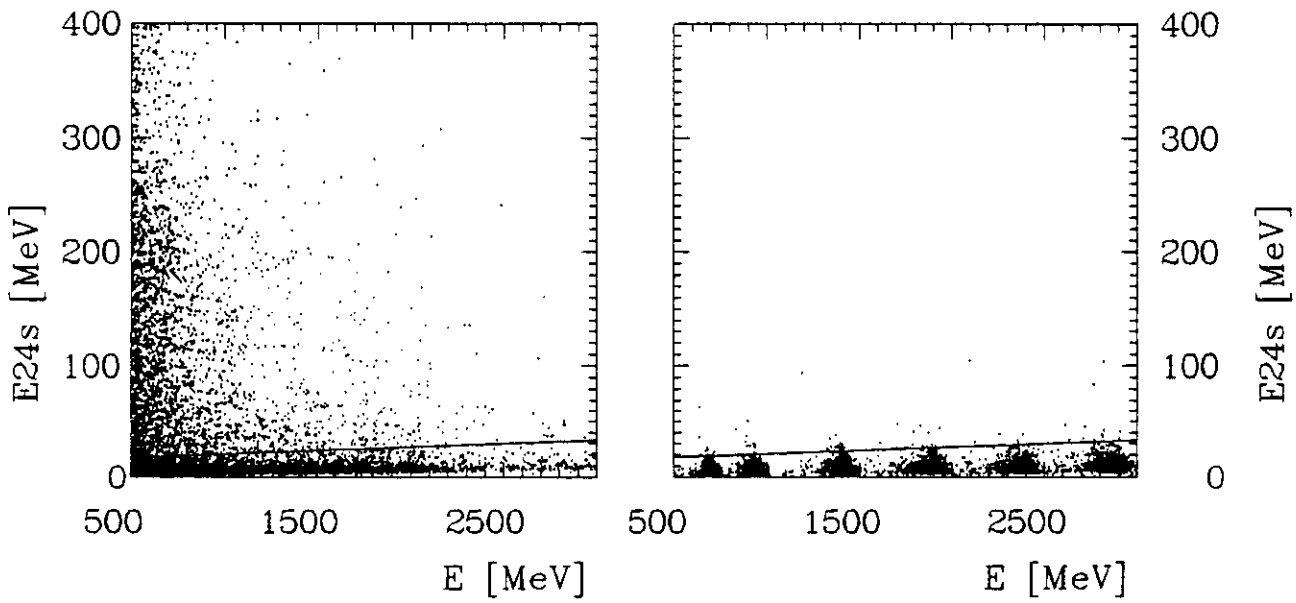

Figure 4.21: *Scatter plot of E24s versus electron energy. Comparison between data and Monte Carlo. On the left-hand side ON $\Upsilon(4S)$ data is shown. On the right-hand side the Monte Carlo prediction of electrons in the empty Ball with discrete energies energy is shown.*

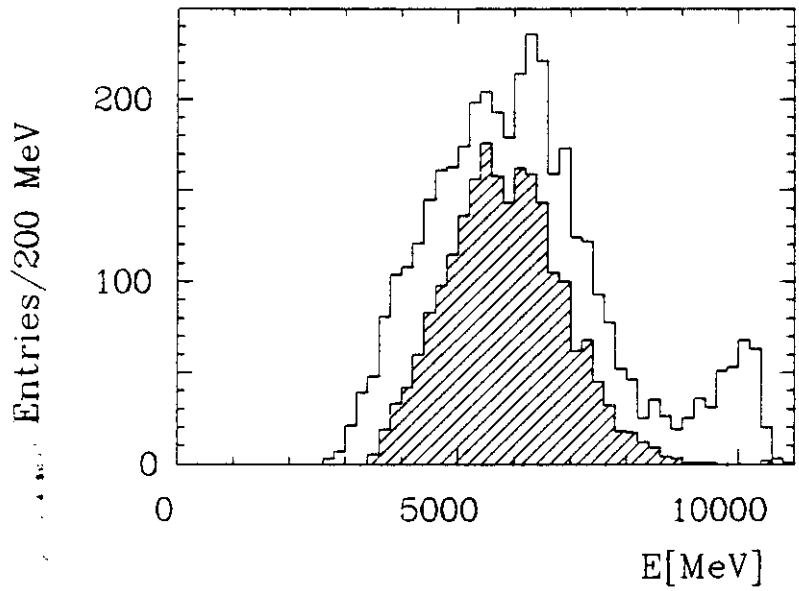

Figure 4.22: *E_{BALL} before and after the cuts requiring the number of bump crystals > 7 and $H2 < 0.55$ of ON $\Upsilon(4S)$ data for events with one electron candidate in the energy interval* $1.5 - 2.7$ *GeV*.

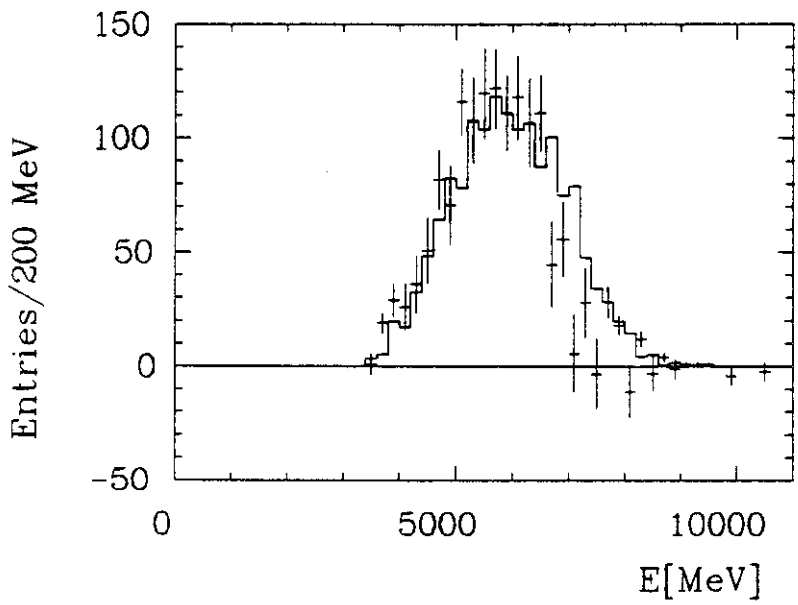

Figure 4.23: *E_{BALL} compared between continuum subtracted ON $\Upsilon(4S)$ data (Crosses) and a Monte Carlo precdiction (histogram) for events with one electron candidate in the energy interval* $1.5 - 2.7$ *GeV*.

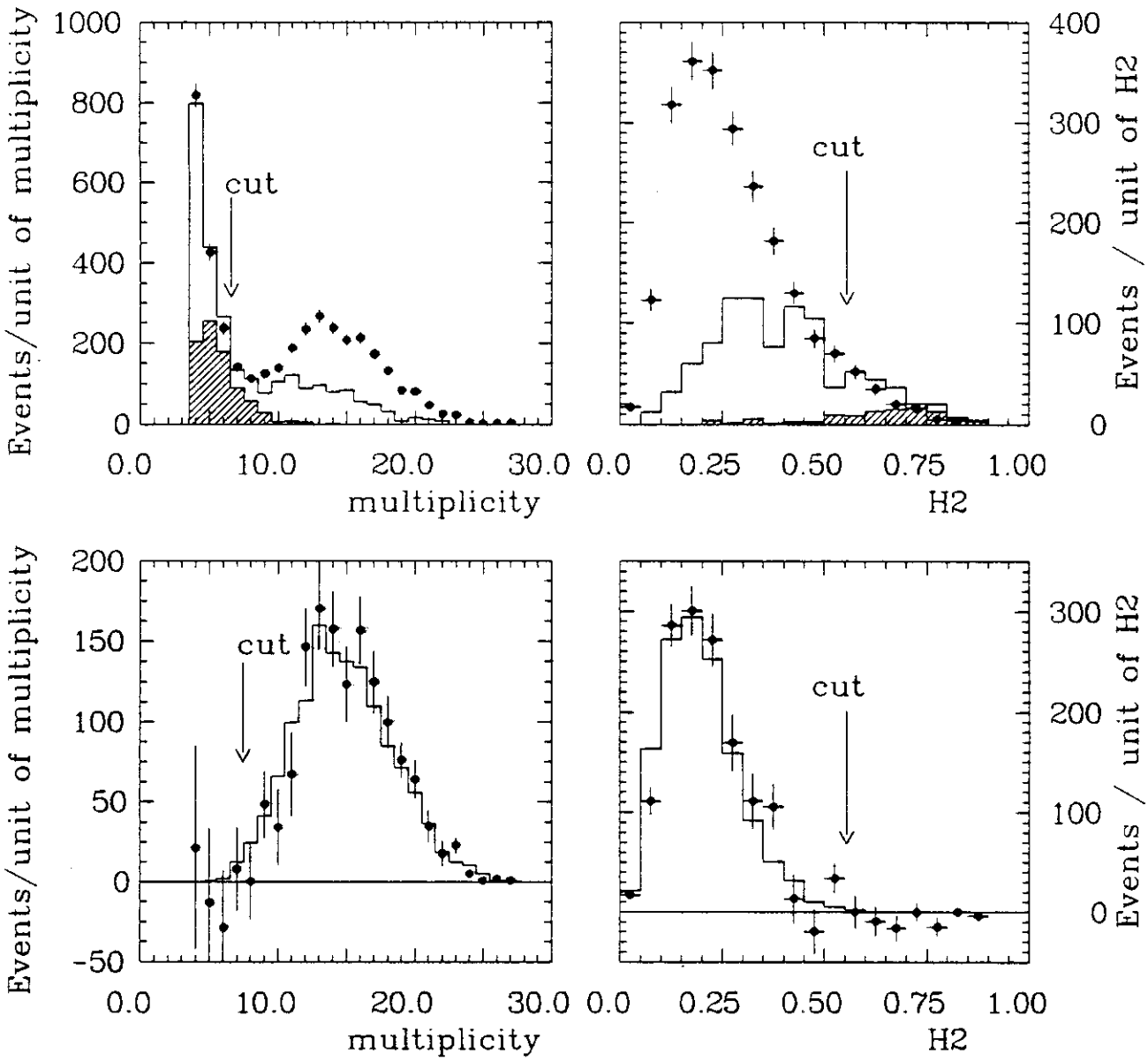

Figure 4.24: *Left hand part: multiplicity of number of bump crystals.*
Right hand part: distribution in H2.
Upper part: ON $\Upsilon(4S)$ data (dots with crosses), the continuum contribution (histogram) - scaled by the ratio of ON and OFF resonance luminosities - and the Monte Carlo prediction of the $\tau\overline{\tau}$ contribution to the continuum sample are shown (shaded area).
Lower part: continuum subtracted $\Upsilon(4S)$ data (dots with crosses) and a Monte Carlo prediction (histogram) for $\Upsilon(4S) \rightarrow B\overline{B}$ are shown.
The distributions shown are from events with electrons inside the energy interval $1.5 < E^c_{13} < 2.7$ GeV. The H2 distribution is obtained after having applied the cut in the number of bumps crystals.

4.4 Monte Carlo Studies, Efficiency, and Background

4.4.1 Efficiency

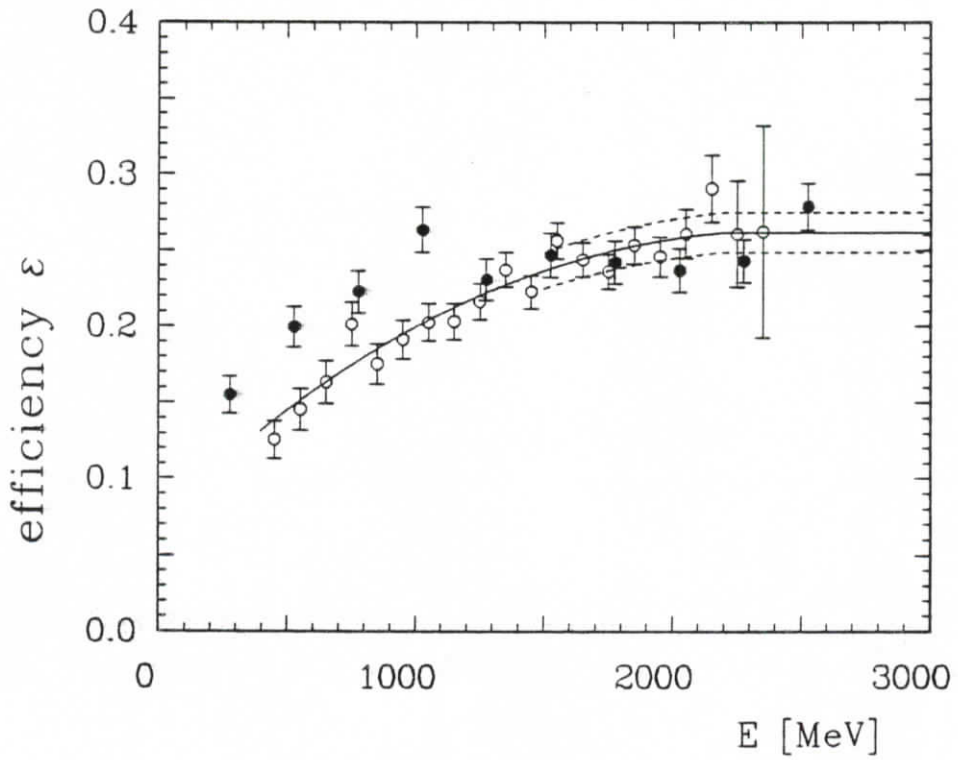

Figure 4.25: *Total electron detection efficiency* $\epsilon = \epsilon_{He}\ \epsilon_e$. *Open circles: from* $\Upsilon(4S)$ *Monte Carlo. Solid line: fit to open circles. Dashed line: fit* $\pm 5\%$. *Solid points: Efficiency from merging electrons into* $\Upsilon(1S)$ *data.*

To estimate the detection efficiencies the standard Lund string fragmentation program version 6.2 [33] was used to simulate the decay of $\Upsilon(4S) \rightarrow B\overline{B}$. The generated events are passed through a complete detector simulation. This simulation includes the following steps:

1. Electromagnetically interacting particles are handled by the electromagnetic shower developement program EGS [34].

2. The interaction of hadrons is simulated with the GHEISHA 6 program [35].

3. Extra energy deposited in the crystals by beam-related background is taken into account by adding special background events to the Monte Carlo events. These background events are obtained by triggering on every 10^{7th} beam crossing, with no other condition.

4. The events are then reconstructed using our standard software and subjected to the same cuts as the data.

Before determining the efficiency with help of the Monte Carlo program, we first compare some Monte Carlo predictions with the distributions measured with our data

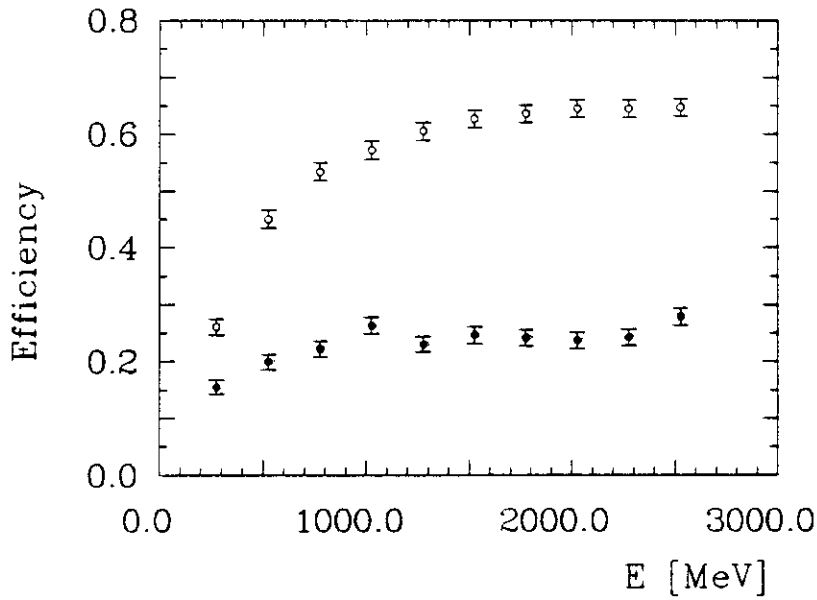

Figure 4.26: *The efficiency to find electrons in the empty Ball - including solid angle cut. In addition, efficiency from merging the same electrons into $\Upsilon(1S)$ data, including event selection efficiency, is shown as solid points.*

sample. As discussed in the last chapter, we have used cuts in multiplicity and $H2$. Figure 4.24 compares the continuum-subtracted $\Upsilon(4S)$ data and the Monte Carlo prediction of the two quantities. The distributions nicely agree, the cuts are placed as indicated. The errors of the data in the continuum-subtracted plot are dominated by the continuum statistics. In the upper part of the plots a Monte Carlo prediction of the $\tau\overline{\tau}$ contribution to the continuum contribution is overlayed. Most of the rejected events are $\tau\overline{\tau}$ events. At very small multiplicities the continuum data cannot be described by the $\tau\overline{\tau}$ contribution alone. Here the radiative Bhabha events contribute. As these processes are very rare we cannot simulate them by a Monte Carlo program, since the required CPU time to obtain a significant sample of statistics would need about 10 thousand hours of CPU time on an IBM 3081K.

The distribution of the deposited energy in the Ball – figure 4.23 – shows some disagreement on the high energy side when comparing Monte Carlo and real data. The Monte Carlo data tend to have more energy. At the low energy part the two distributions essentially agree. The hardware (and software) trigger thresholds of 1.9 GeV (and 2.1 GeV) are far below any entry in the distributions and do not contribute to systematic uncertainties.

Using the procedure described above to simulate events, we find a hadronic detection efficiency for $\Upsilon(4S) \rightarrow B\overline{B} \rightarrow hadrons$ of

$$\epsilon_H = (93 \pm 1)\%.$$

The error of 1% is due to variations using different hadron fragmentation models (0.5%) and to statistics (0.5%).

For $\Upsilon(4S)$ decays where one B meson decays semileptonically into $e\nu X$ and the energy of the electron is greater than 500 MeV, the hadronic detection efficiency is

$$\epsilon_{He} = (93.0 \pm 0.5)\%.$$

The product of the multi-hadron event selection efficiency ϵ_{He} and the electron selection efficiency ϵ_e is the total electron efficiency $\epsilon = \epsilon_{He} \times \epsilon_e$.

We use two different methods to determine the electron selection efficiency.

1. First we generate $\Upsilon(4S) \rightarrow B\overline{B}$ Monte Carlo events where one B meson decays semileptonically and the other one according to the standard LUND string fragmentation program. The events are then analysed as described above. The total efficiency ϵ to find electrons in these events is shown in figure 4.25 by open circles. We then fit a third order polynomial to the points - the solid line. The dashed lines mark a $\pm 5\%$ deviation from the fit function.

2. Monte Carlo generated electrons are merged isotropically into selected high multiplicity "ON $\Upsilon(1S)$" multi-hadron events. We require, in addition to the hadron selection, that the multi-hadron event has more than 6 *bumps*. This is done in order to reduce the $\simeq 20\%$ contribution from $q\bar{q}$ and $\tau\bar{\tau}$ events to the ON $\Upsilon(1S)$ data sample. This method gives a measurement of ϵ_e and we assume $\epsilon = \epsilon_e \times 0.93$ for those events, too. Merging electrons isotropically into a low multiplicity sample (two-jet like events), would result in too high an efficiency, since the overlap of the merged electron with other particles becomes less likely. The method of merging particles isotropically into data influences the efficiency due to accidental overlaps with other particles in the event. The size of this effect is obtained by comparing the efficiency to detect the merged electrons in the data when 1, 2; or 3 electrons are merged into one event. The undisturbed efficiency to detect electrons is the assumed to be obtained by extrapolating from merging $3 \rightarrow 2 \rightarrow 1 \rightarrow 0$ electrons. This correction is found to be $\Delta\epsilon/\epsilon = (13.0 \pm 0.5)\%$. In addition for this correction we assume a 2% uncertainty due to the merging method. In figure 4.26 the efficiency to detect the electrons in the empty Ball (including the cut in solid angle) is compared with the efficiency to detect the same electrons, but merged into $\Upsilon(1S)$ data. The reduction of the efficiency of more than 50% comes from the rejection of electrons as a consequense of an overlap with other particles in the Ball (mainly the cut in E_{24_s}). The solid points in figure 4.25 show the result obtained by this method.

We then compare the two resulting efficiencies in figure 4.25. At lower electron energies the merging method results in a significantly higher efficiency. This is due to the fact that in the merging method the electrons are distributed isotropically in the events. But for slow electrons from $B \rightarrow e\nu D, D^*$ decays, the probability for the electron is high to overlap with the decay products of the D, D^* mesons, while at higher electron energies the electron is more likely backward to the D or D^* meson. This was confirmed by the comparison of the efficiencies to detect electrons in $\Upsilon(4S)$ Monte Carlo events and to detect merged electrons in the same Monte Carlo events. We use the fitted line of figure 4.25 for the electron efficiency. From the comparison of the efficiencies obtained by the two methods we get a systematic error on the efficiency of $\Delta\epsilon/\epsilon < 5\%$ for electron energies above 1.5 GeV, where the two efficiencies obtained by the different methods agree.

The efficiency to detect electrons from the decay $B \rightarrow e\nu X$, $X = \pi, \rho$ is slightly higher than that of the decay to $X = D, D^*$ for energies above 1.5 GeV . This is due to the lower mass of the final state meson. At high electron energies the electron and X are likely to move backward to each other. But in the $b \rightarrow u$ channel the boost of the meson is higher compared to that of the $b \rightarrow c$ channel. Therefore the overlap probability of the decay products of the final state mesons X with the electron is smaller in the $b \rightarrow u$ channel compared to that in the $b \rightarrow c$ channel.

It should be noted that from this chapter on we have turned to a linear scale and binning when plotting energies. We are mostly interested in electrons from the energy range 1.5 to 2.6 GeV . The effect of the varying resolution does not influence our analysis, and furthermore the results are easier to compare with results from other experiments.

4.4.2 Background Studies

Background to the electron spectrum from direct B meson decays may come from:

1. electrons and fakes from the continuum contribution to the ON $\Upsilon(4S)$ data sample;
2. electrons from subsequent $c \rightarrow s$ decays;
3. photons converting in the beam pipe and simulating electrons;
4. charged hadrons faking electrons.

The first contribution is taken from the electron spectrum of the continuum data sample. It will be discussed when we describe the fit procedure – chapter 4.4.3.

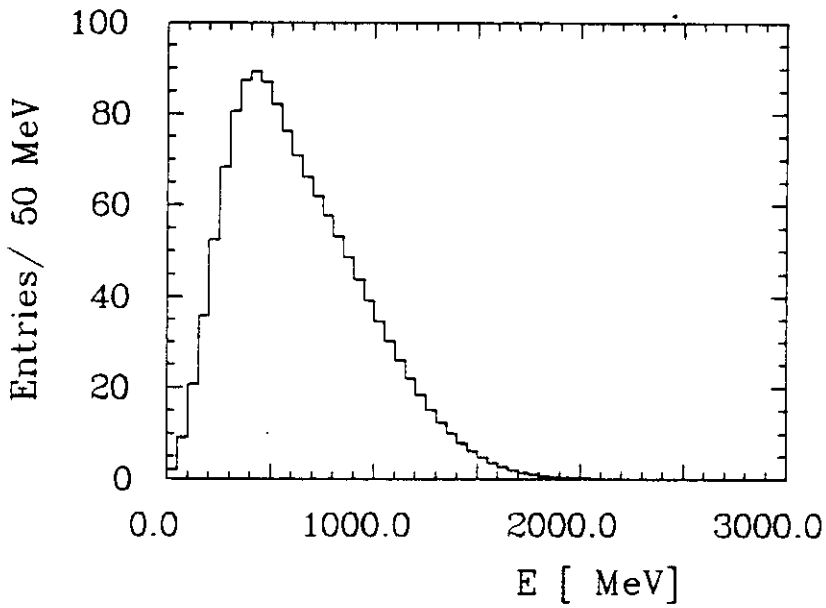

Figure 4.27: *The $c \rightarrow s$ contribution to the inclusive electron spectrum as predicted by the Lund program, corrected for detection efficiency and scaled to the number of $\Upsilon(4S)$ decays.*

The second background from $c \rightarrow s$ decays is estimated by a Lund Monte Carlo simulation and is shown in Figure 4.27. As the average branching ratio of D mesons to electrons is about 10%, this background contribution is in the same order of magnitude as the signal from direct semileptonic B mesons decays. Restricting the analysis to electron energies above 1.5 GeV reduces this contribution substantially.

The third source of background originates from photons which converted in the beam pipe or tube chamber to an e^+e^- pair and therefore simulate a charged track in the tube chamber and the pattern of a single electromagnetically showering particle

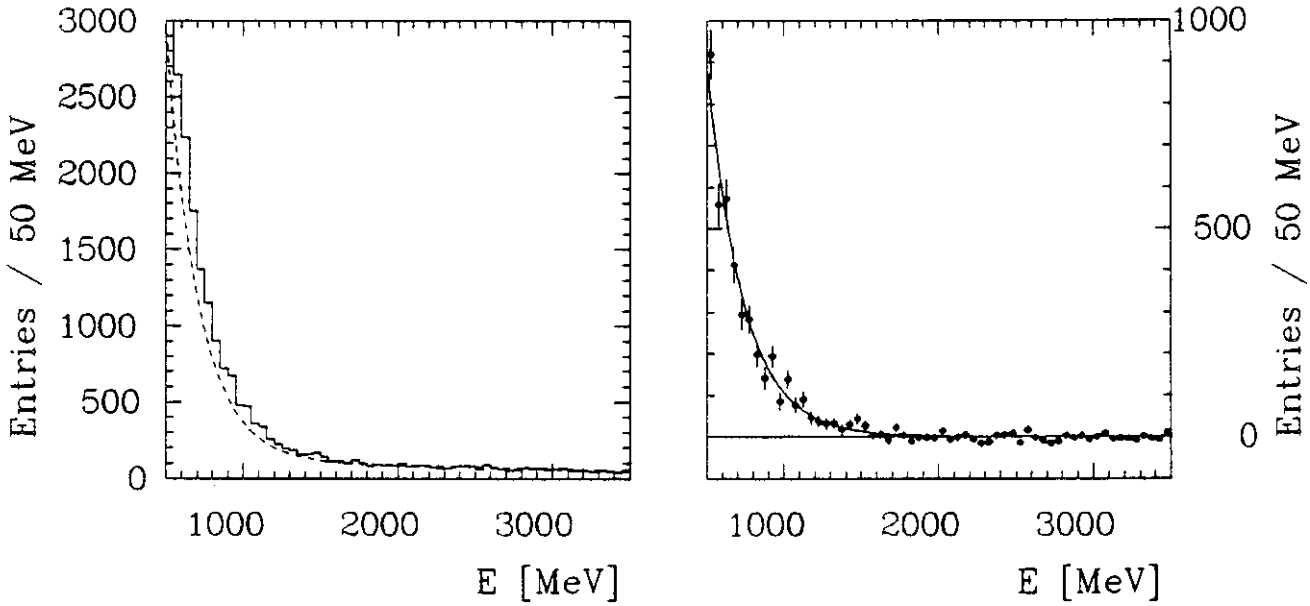

Figure 4.28: *The neutral spectrum obtained with the same cuts as used for the electron spectrum. The left-hand side shows the neutral ON $\Upsilon(4S)$ spectrum and a fit to the continuum data scaled by the ratio of ON and OFF resonance luminosities. The right-hand side shows the continuum-subtracted spectrum together with a fit to the data.*

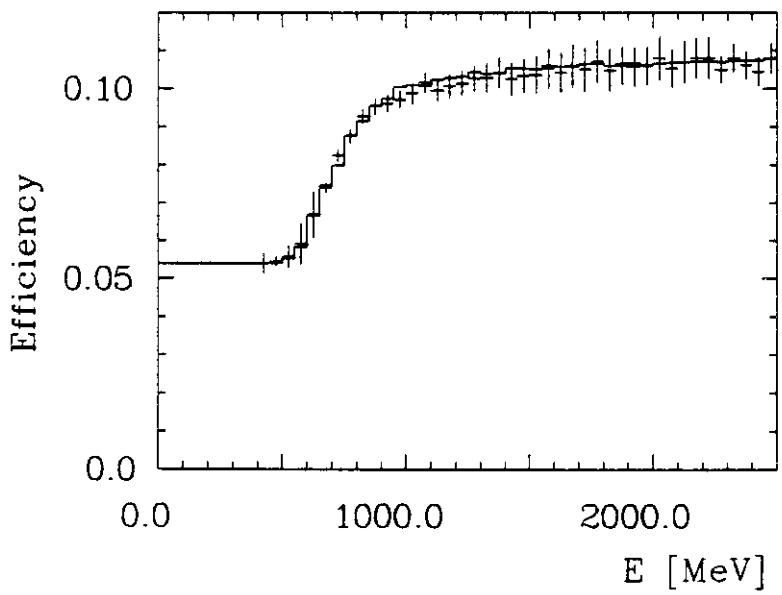

Figure 4.29: *Probability of finding neutral clusters charged, if all clusters originate from π^0 decays. The histogram results from an exponentially distributed energy spectrum of the pions, the crosses show the result for a flat energy distribution of the pions.*

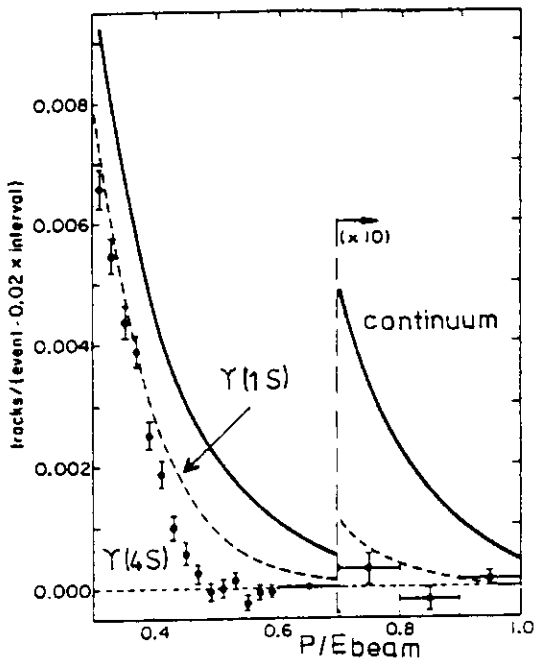

Figure 4.30: *The charged momentum spectrum from the $\Upsilon(1S)$ and $\Upsilon(4S)$ resonances and from the continuum as measured by CLEO [37]*

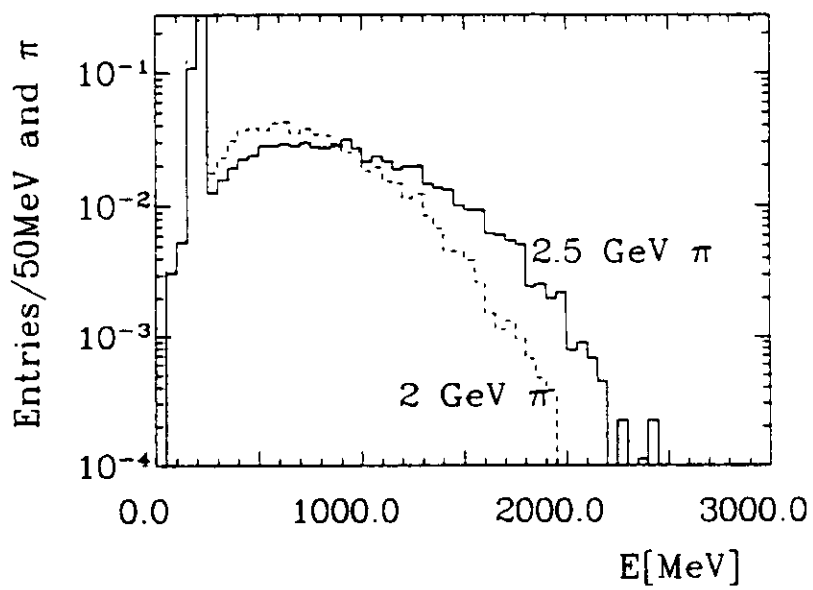

Figure 4.31: *The energy deposition of charged pions in the Ball, as predicted by the Monte-Carlo studies.*

in the Ball. The electron-positron pairs move very close in direction as the Ball has no magnetic field, and therefore the trajectories are not bent apart. This contribution is measured by multiplying the neutral spectrum by the conversion probability of the photons. The neutral spectrum as shown in figure 4.28 is obtained with the same cuts as used for the electron spectrum. Here we assume that all photons originate from the decays of neutral pions. We therefore have to take into account the probability that the two photons from the π^0 decay overlap and form one shower accepted as a single photon. When two photons point to one cluster the probability to find this cluster charged, $P_{charged}$, is:

$$P_{charged} = 1 - (1 - c_{charged})^2 = 1 - (1 - 0.054)^2 \approx 0.105, \qquad (4.7)$$

where $c_{charged}$ is the the probability to detect a single photon charged - see appendix C.

Since there is no high energetic direct photon spectrum expected from B meson decays [36] and contributions other than those from π^0 decays are small, we have to know only the ratio of probabilities to have *two / (two + one)* photons per accepted cluster in order to determine the probability to find neutral clusters charged.

For this estimate we take the prediction from a Monte Carlo generated sample of flat or exponentially ($\approx exp(-E/400MeV)$) distributed π^0 energies in the empty Ball. The conversion probability obtained with these assumptions is shown in figure 4.29. No large difference is visible between these two distributions. The background from photons to the electron spectrum is obtained by multiplying the spectra shown in figure 4.28 by the efficiency curve of figure 4.29. The number of fake electrons above 1.5 GeV from this source is found to be (10 ± 3).

The fourth and last contribution is that from charged hadrons. We use two methods to estimate this background. Figure 4.30 shows the measured charged spectrum from the $\Upsilon(1S)$,$\Upsilon(4S)$, and continuum events. The $\Upsilon(4S)$ decays have the softest spectrum. This is due to the kinematical constraints - see chapter 2. The maximum momentum is about 2.6 GeV . Limiting then the analysed spectrum to $E_e > 1.5\ GeV$ only hadrons in the interval $1.5 < E < 2.6\ GeV$ have to be taken into account. Approximately 0.1 charged hadrons per event from $\Upsilon(4S)$ decays are in this energy range, according to the Lund Monte Carlo prediction. Figure 4.31 shows the energy deposited by charged pions of 2 and 2.5 GeV in the Ball. Requiring more than 1.5 GeV energy in the Ball, a reduction factor of 200 is achieved. Applying the pattern cuts, the rejection rate increases to more than 5000. With 60000 $\Upsilon(4S)$ decays the background above 1.5 GeV is

$$0.1 * 60000/5000 < 2 \text{ fake electrons.}$$

The other method to estimate the background from charged hadrons uses the dE/dx information of the tube chamber. As described in appendix C the pulse height distribution in the tube chamber differs between tracks from electrons, and fast or slow minimum ionizing particles. Therefore a cut in the pulse height sum (PHS) requiring $PHS > 3.5$ leads to the following reduction factors

electrons	r_e	$= 0.2745$	± 0.0002,
100 MeV muons	$r_{m0.1}$	$= 0.60$	± 0.01,
5 GeV muons	$r_{m5.0}$	$= 0.43$	± 0.01,
mips inside multi-hadron events	r_h	$= 0.49$	± 0.01.

Applying the above cut the change in the electron spectrum can be used to determine the charged hadronic background, *cbg*. This is done by assuming that the measured spectrum S constists of an electron contribution e and a hadronic contribution *cbg*. Applying the PHS cut results in the spectrum F, where the electron contribution is reduced by the factor r_e and the hadronic one by r_h:

$$\begin{aligned} S &= e + cbg \\ F &= r_e\, e + r_h\, cbg \end{aligned} \tag{4.8}$$

Solving the two equations yields the *cbg* in the i^{th} bin,

$$cbg_i = \frac{r_e S_i - F_i}{r_e - r_h} \equiv S_i \frac{r_e - R_i}{r_e - r_h}, \tag{4.9}$$

where R_i is the measured reduction factor in the i^{th} bin. The errors of the two spectra S and F are correlated since F results from S.

The two spectra $S \times r_e$ and F are shown in figure 4.32 together with the charged background spectrum obtained by this method. The fit to the data using a simple exponential function in the energy range from 0.5 to 1 GeV results in 1 fake electron in the energy range above 1.5 GeV . The error on this estimate can be obtained by assuming 5 GeV or 100 MeV muons contributing to the *cbg* spectrum only. Hence replacing r_h by $r_{m5.0}$ or $r_{m0.1}$ results in a variation of the background by less than 1 track.

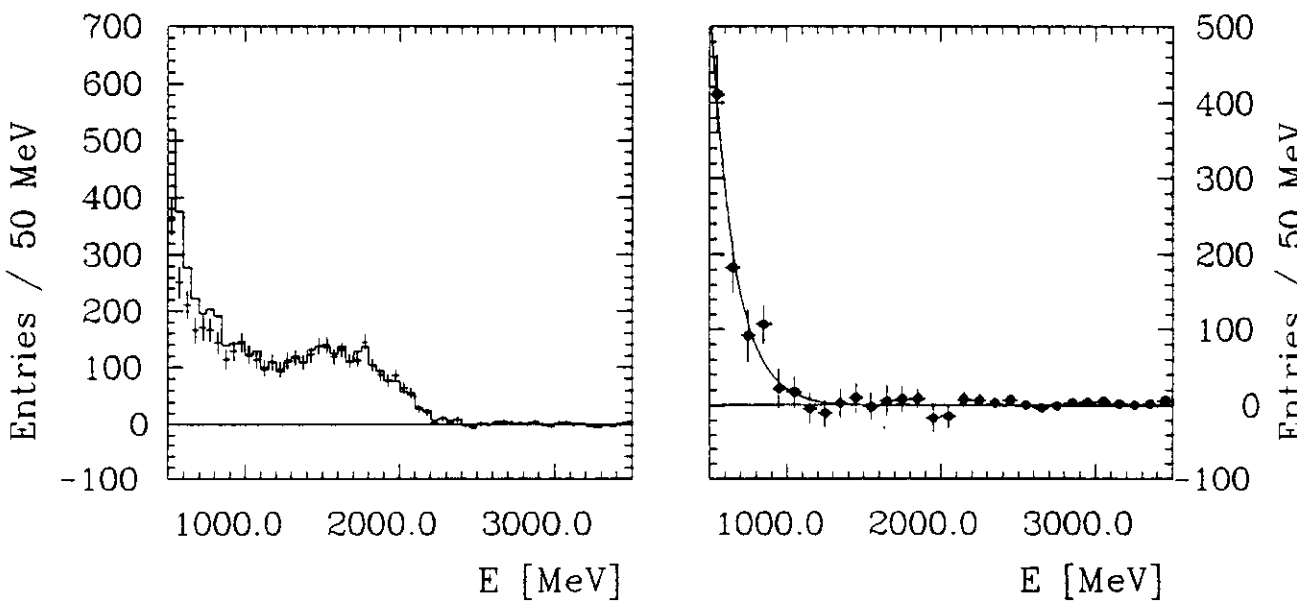

Figure 4.32: *The charged background. The left hand-side shows the charged continuum subtracted spectrum (histogram) scaled by a factor of* $(1 - r_e)$. *The crosses show the continuum-subtracted charged spectrum after the cut requiring a pulse height sum* > 3.5. *The right-hand side shows the charged background spectrum (i.e. the difference of the two spectra from the left-hand side).*

4.4.3 Method Used to Extract Branching Ratios and Kobayashi - Maskawa Matrix Elements from the Spectra

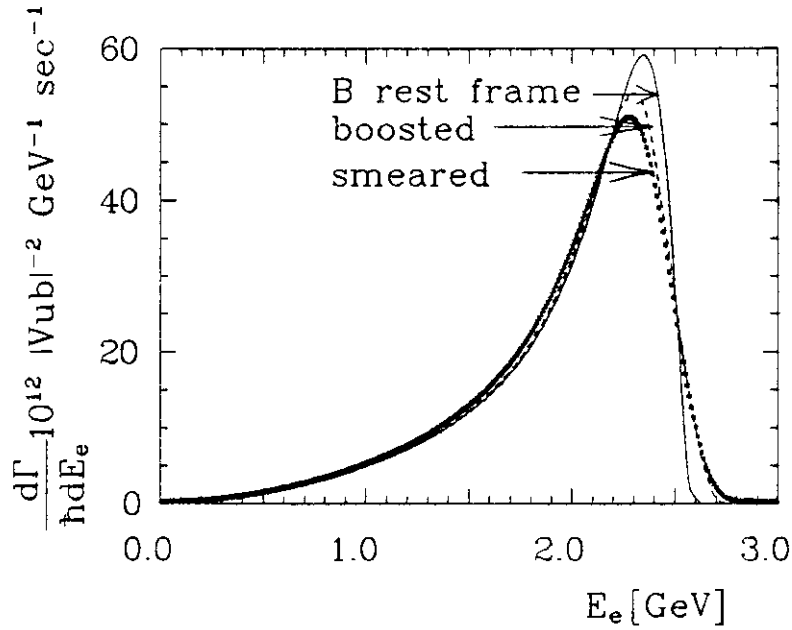

Figure 4.33: *The electron spectrum as predicted by KS from $B \rightarrow e\nu\pi, \rho$ in the B meson rest frame, after a boost ($\beta = 0.06$) to the $\Upsilon(4S)$ restframe, and after smearing with the detector resolution.*

In order to extract branching ratios from the measured spectra we have to use the predictions of theoretical models. To compare the predicted electron energy spectra with the data we have to take into account modifications introduced by the detector and the analysis procedure. In detail we boost the predicted spectra with the B momentum to the $\Upsilon(4S)$ rest frame, fold them with the energy resolution of the detector and correct by our detection efficiency. The size of those first two corrections is shown in figure 4.33.

The efficiency correction is done in the following way: let $d\Gamma'/dE_e$ be the predicted electron spectrum from B meson decays boosted to the $\Upsilon(4S)$ center-of-mass system and folded with the energy resolution. Then T is the expected spectrum for a 100% braching ratio (e.g. for the channel $b \rightarrow c$),

$$T_{b\rightarrow c}(E_e) = \frac{d\Gamma'_{cb}}{dE_e}\frac{1}{\Gamma_{cb}}\{\ \epsilon_e(E_e)\ \epsilon_{He}(E_e)\}\frac{2\ N^{obs}_{B\overline{B}}}{\epsilon_H} \qquad (4.10)$$

with $N^{obs}_{B\overline{B}} = N^{obs}_H(ON\ \Upsilon(4S)) - r \times N^{obs}_H(continuum)$

and Γ_{cb} the partial width of the model used.

For instance, when using WSB's model one has to replace Γ_{cb} *by* $\Gamma(B \rightarrow e\nu D, D^*)$. $N^{obs}_H(ON\ \Upsilon(4S))$ and $N^{obs}_H(continuum)$ are the numbers of hadrons found on the $\Upsilon(4S)$ resonance and in the continuum, respectively. $r = 4.028 \pm 0.009$ is the ratio of ON $\Upsilon(4S)$ and continuum luminosities corrected for the difference in beam energy. In

equation (4.10) the two hadron efficiencies ϵ_{He} and ϵ_H approximately cancel each other. Therefore also systematic errors of the event simulation program cancel, and only the efficiency ϵ_e to detect electrons in accepted multi-hadron events contributes to systematic uncertainties.

Spectrum from the ON $\Upsilon(4S)$ Data

$Y(E_e)$ is the functional form accounting for the observed electron spectrum from the $\Upsilon(4S)$ data

$$\begin{aligned} Y(E_e) &= \mathcal{C} \times T_{b\to c}(E_e) + \frac{\mathcal{U}}{\mathcal{C}} \times \mathcal{C} \times T_{b\to u}(E_e) \\ &\quad + \mathcal{S} \times T_{c\to s}(E_e) + \mathcal{B} \times F(E_e) + \mathcal{K} \times Q(E_e) \end{aligned} \quad (4.11)$$

The spectra $T_{x\to y}$ are the above described predictions from the various models for the $b\to c$, $b\to u$, and $c\to s$ transitions. Q and F are the continuum and fake electron contributions.

The quantities $\mathcal{C}, \frac{\mathcal{U}}{\mathcal{C}}, \mathcal{S}, \mathcal{B}$, and $\mathcal{K}$ are determined by a fit of equation (4.11) to the data. The intensities $\mathcal{C}, \mathcal{S}$ are the measured branching ratios. Using e.g. the model of WSB yields

$$\mathcal{C} \equiv BR(B \to e\nu D, D^*).$$

$\frac{\mathcal{U}}{\mathcal{C}}$ is the ratio of branching ratios $(b\to u)/(b\to c)$. For WSB's model we get

$$\frac{\mathcal{U}}{\mathcal{C}} \equiv \frac{BR(B \to e\nu\pi, \rho)}{BR(B \to e\nu D, D^*)}.$$

The Kobayashi - Maskawa matrix elements are obtained – see equation table 2.3 – by

$$|V_{cb}|^2 \equiv \mathcal{C}/(\tau_B \times \hat{\Gamma}_{cb}),$$

with τ_B being the B meson lifetime. In the model of WSB the part of the electron spectrum used in the fit corresponds to transitions $B \to e\nu D, D^*$ only, hence $\hat{\Gamma}_{cb} \equiv \hat{\Gamma}(B \to e\nu D, D^*)$

The ratio of matrix elements is obtained by

$$|V_{ub}/V_{cb}|^2 \equiv \frac{\mathcal{U}}{\mathcal{C}} \times \hat{\Gamma}_{cb}/\hat{\Gamma}_{ub},$$

e.g. using the model of WSB one has to replace $\hat{\Gamma}_{cb}$ by $\hat{\Gamma}(B \to e\nu D, D^*)$ and $\hat{\Gamma}_{ub}$ by $\hat{\Gamma}(B \to e\nu\pi, \rho)$. Analoguous considerations hold for the other models.

F represents the fake electrons, i.e. the sum of the background from charged hadrons and photons from B meson decays, as described in chapter 4.4.2.

Q is the continuum contribution described by a smooth function,

$$\begin{aligned} Q(E_e) &= \exp(\alpha X^1 + \beta X^2 + \gamma X^3 + \delta X^4) \\ \text{with} \quad & X = (E_e - 2000)/2000, \ E_e \text{ in } MeV, \end{aligned} \quad (4.12)$$

with $\alpha, \beta, \gamma, \delta$ being free parameters determined by the fit.

Spectrum from the Continuum Data

In order to better constrain the shape of the continuum background a simultaneous fit to the electron spectrum from the continuum data is performed, using the parametrization

$$V(E_e) = \mathcal{K}_C \; Q(\alpha, \beta, \gamma, \delta) \tag{4.13}$$

where $\mathcal{K}_C$ $\alpha, \beta, \gamma, \delta$ are to be determined in the fit.

The Likelihood Function

We perform a maximum likelihood fit with Poissonian error distribution. The fit is done simultaneously to the binned $\Upsilon(4S)$ data and to the binned continuum data. We define N_i and M_i as the number of electrons in the i^{th} bin of the $\Upsilon(4S)$ and the continuum data, respectively. The likelihood function - which is maximized in the fitting procedure [2] - (using the shorthand notation Y_i and V_i for $Y(E_e)$ and $V(E_e)$, respectively) reads:

$$\begin{aligned}
\mathcal{L} &= \mathcal{L}_{4S}(Y, N) \times \mathcal{L}_{continuum}(V, M) \times \\
&\quad \mathcal{L}_{BACKGROUND} \times \mathcal{L}_{LUMINOSITY-RATIO} \\
&= \prod_i \left(\frac{e^{-Y_i} \cdot Y_i^{N_i}}{N_i!}\right) \times \prod_j \left(\frac{e^{-V_j} \cdot V_j^{M_j}}{M_j!}\right) \times \\
&\quad \times \exp\left(-\frac{(\mathcal{B} - \mathcal{B}_M)^2}{2\sigma_{\mathcal{B}}^2}\right) \times \exp\left(-\frac{(\mathcal{K} - r \cdot \mathcal{K}_C)^2}{2\sigma_{\mathcal{K}}^2}\right)
\end{aligned} \tag{4.14}$$

Here the first and second term represent the likelihoods for the $\Upsilon(4S)$ and continuum data. The 3^{rd} and 4^{th} term form constraints: the third term constrains the background intensity $\mathcal{B}$ by the measured background intensity $\mathcal{B}_m$, the forth term restricts the intensity of the continuum contribution $\mathcal{K}$ to the product of the fitted continuum intensity $\mathcal{K}_C$ times the measured luminosity ratio r.

To compare results from different fits we calculate a χ^2 from the result of the fit according to [39]

$$\begin{aligned}
\chi^2 &= -2 \ln\left(\frac{\mathcal{L}_{4S}(Y,N)}{\mathcal{L}_{4S}(N,N)}\right) \\
&= 2 \sum_i (Y_i - N_i + N_i \ln\frac{N_i}{Y_i})
\end{aligned} \tag{4.15}$$

Here the denomiator $\mathcal{L}_{4S}(N,N)$ is a constant guaranteeing that χ^2 is zero if $Y_i = N_i$ in all bins.

[2] with help of the MINUIT [38] program. For numerical reasons not $\mathcal{L}$ is maximized but $-\log \mathcal{L}$ is minimized

The intensities $\mathcal{C}, \mathcal{B}, \frac{u}{c}, \mathcal{S}, \mathcal{K}, \mathcal{K}_C$ and continuum parameters $\alpha, \beta, \gamma, \delta$ are determined by the fit.

As the background ($\mathcal{B}$) and the $c \rightarrow s$ ($\mathcal{S}$) contributions above $E_e = 1.5\ GeV$ are small and rather similar in shape, the intensity $\mathcal{B}$ is very much correlated to the $c \rightarrow s$ intensity $\mathcal{S}$.

Due to the constraint of $\mathcal{B}$ to $\mathcal{B}_m$ in practice the fitted $\mathcal{B}$ is not a free parameter, but comes out to be exactly at the measured value of $\mathcal{B}_M$. The constraint was set to $\sigma_{\mathcal{B}}/\mathcal{B} = 1$, which reflects the knowledge of the background size, see chapter 4.42.

The parameters $\alpha, \beta, \gamma, \delta$ are determined by both, the $\Upsilon(4S)$ data and the continuum data. This method is useful, as we have only a small continuum data sample. The continuum contribution in the $\Upsilon(4S)$ fit is constrained in shape and intensity by the data between $E_e = 2.6\ GeV$ and $4\ GeV$ where we assume no other contributions. This method gives confidence in the parametrization representing the continuum contribution. The result agrees well with the predicted shape from the fit to the continuum data alone.

The parameter $\mathcal{K}$ (and $\mathcal{K}_C$ for the continuum data) gives the size of the continuum contribution at $2.0\ GeV$. $\mathcal{K}$ was chosen as a not normalized amplitude factor, since we use different fit ranges in the ON and OFF resonance data. Secondary – which is more important – we wish to constrain the spectrum around $2GeV$. At this energy the $(b \rightarrow u)/(b \rightarrow c)$ ratio is mostly determined. We find that the fitted value $\mathcal{K}$ is within 0.08% of the value $r \times \mathcal{K}_C$ expected from the luminosity ratio, with $\sigma_{\mathcal{K}}/\mathcal{K} = 1\%$ used in the constraint (4.14). The size of $\sigma_{\mathcal{K}}$ was chosen higher than the expected error of the luminosity ratio of $\Delta r/r = 0.2\%$, in order to allow and test for a larger fluctuation in this quantity.

A fit with the continuum function Q to the continuum data alone in the range 0.6 GeV to 4.0 GeV – see figure 5.2 – gives a $\chi^2/d.o.f. = 60.6/63$ corresponding to a χ^2 probability of 56%. Other functions like a polynomial and / or single exponentials give a much larger χ^2.

All contributions to the ON $\Upsilon(4S)$ spectrum are shown in figure 5.2. The background from charged hadrons and photons faking electrons is added up and displayed as a single line. The background- and continuum-subtracted spectrum is shown in figure 5.1. Figure 5.3 shows the spectrum efficiency corrected and normalized to the number of produced B mesons. The spectrum is also listed numerically in appendix D.

Looking at the number of observed electrons – see figure 5.1 – would suggest to use the entire spectrum, but as we want to measure $b \rightarrow c$ and $b \rightarrow u$ contributions only, we use the data above $E_e = 1.5\ GeV$, where the $c \rightarrow s$ *and* fake electron contributions are small. Using the data below $E_e \simeq 1.5\ GeV$ would require a very accurate knowledge of the background and the $c \rightarrow s$ intensities and shapes.

Because **no** obvious $b \rightarrow u$ signal at $2.4\ GeV$ is visible we calculate $(b \rightarrow u)/(b \rightarrow c)$ upper limits and measure the $b \rightarrow c$ branching ratio. The $(b \rightarrow u)/(b \rightarrow c)$ upper limits are obtained by recording the likelihood $\mathcal{L}$ for fixed $(b \rightarrow u)/(b \rightarrow c)$ ratios between 0 and 1, but fitting for each $(b \rightarrow u)/(b \rightarrow c)$ ratio all other parameters to the spectrum. A 90% C.L. upper limit is that ratio which includes 90% of the area of the recorded likelihood ratios starting from the likelihood for $(b \rightarrow u)/(b \rightarrow c) = 0$.

Chapter 5

Results

Here and in the following chapter we present and discuss the results of the fit of the data, as shown in figure 5.2, to formula (4.11) which contains the shape of the electron spectrum and the branching ratios of its various contributions. For the shapes of spectra from $b \rightarrow c$ and $b \rightarrow u$ the theoretical models described in chapter 2 are used.

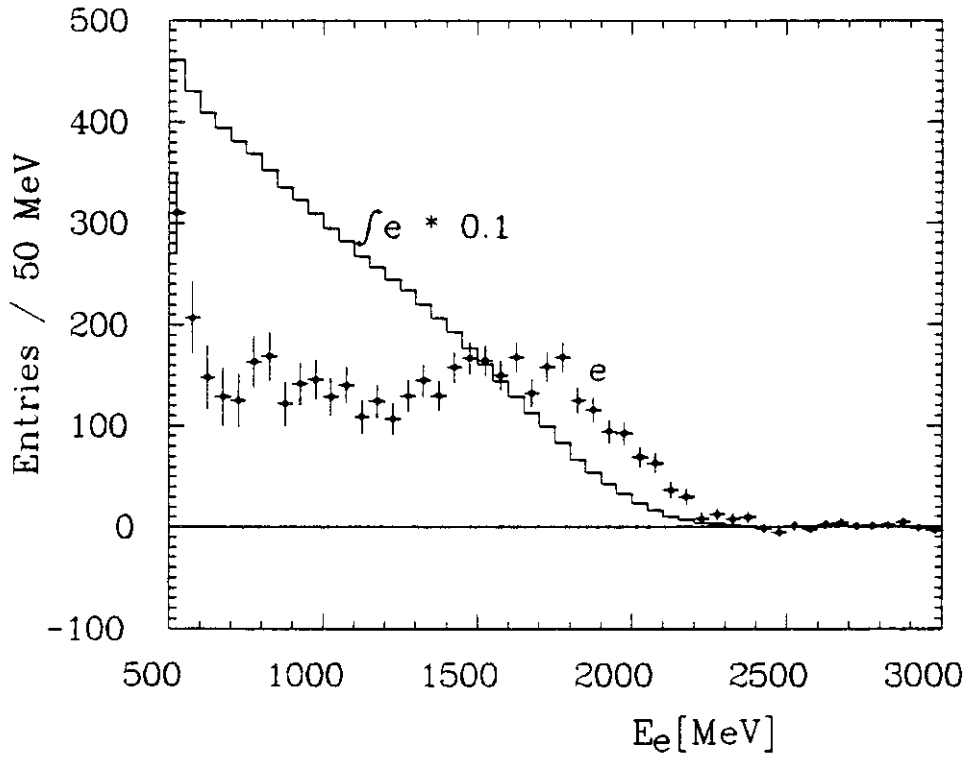

Figure 5.1: *The continuum- and background-subtracted electron spectrum (crosses) and the integral of the spectrum (histogram) scaled by a factor of 0.1.*

5.1 The Ratio of Branching Ratios $(b \rightarrow u)/(b \rightarrow c)$ and $|V_{ub}/V_{cb}|$

Starting with ACM's model, we cannot determine from our measured spectrum the free parameter m_u with meaningful errors, because no significant $b \rightarrow u$ signal is found. We therefore calculate the upper limit for various values of the u quark mass m_u,

as shown in figure 5.4. For higher masses the upper limit gets weaker, because the predicted spectrum becomes softer and comparable to the spectrum from $b\to c$ decays. A u quark mass $m_u = m_c$ would result in no upper limit since then the $b\to c$ and $b\to u$ predictions are identical. For u quark masses below 400 MeV/c^2 the upper limit is independent of m_u. Henceforth we use $m_u = 150 MeV/c^2$ as in the paper by ACM. The upper limit obtained with the different models are shown in figure 5.5 as a function of the lower limit of the electron energy interval used in the fit. Using ACM's model with p_F and m_c free, we obtain an upper limit

$$BR(B\to e\nu X_u)/BR(B\to e\nu X_c) < 4.5\% \text{ and } |V_{ub}/V_{cb}| < 0.15 \text{ at } 90\% \text{ C.L.}$$

The best fit values for those parameters are: $p_F = (388 \pm 52)\ MeV/c$ and $m_c = (1607 \pm 46)\ MeV/c^2$. With equation (2.22) we obtain for the b quark mass an average value $< m_b >= (4.85 \pm 0.68) GeV/c^2$ where $|\vec{P}| = p_F$ was used. In order to get the $(b\to u)/(b\to c)$ values independent of the measured $b\to c$ contribution we increase the lower fit limit to higher energies, where the $b\to c$ contribution becomes smaller and goes to zero above $E_e = 2.4\ GeV$. Fixing all the parameters to the best values previously found - also the $b\to c$ contribution C, but not the $(b\to u)/(b\to c)$ intensity $\frac{U}{C}$ - we obtain an upper limit

$$BR(b\to e\nu u)/BR(b\to e\nu c) < 5.4\% \text{ or } |V_{ub}/V_{cb}| < 0.16 \text{ at } 90\% \text{ C.L.}$$

independent of the $b\to c$ contribution in this energy range (see figure 5.5).

As the GIW model has no precise prediction for $b\to u$ with $E_e < 2.2\ GeV$, we proceed in the following way: we determine the intensity C of the $b\to c$ transition for electron energies $E_e > 1.5\ GeV$ together with a free $b\to u$ intensity $\frac{U}{C}$, then fix the $b\to c$ intensity C, background B, and continuum contribution K and finally find the upper limit on

$$\frac{BR(B\to e\nu X(1S,1P,2S)_u)}{BR(B\to e\nu X(1S,1P,2S)_c)} < 4.6\% \text{ or } |\frac{V_{ub}}{V_{cb}}| < 0.22 \text{ at } 90\ \% \text{ C.L.}$$

for the spectrum above $E_e = 2.2\ GeV$ (see figure 5.5). For electron energies $E_e > 2.4\ GeV$, where the $b\to c$ contribution is zero - but using the previously measured $b\to c$ contribution - we find

$$\frac{BR(B\to e\nu X(1S,1P,2S)_u)}{BR(B\to e\nu X(1S,1P,2S)_c)} < 6.5\% \text{ or } |\frac{V_{ub}}{V_{cb}}| < 0.26 \text{ at } 90\ \% \text{ C.L.}$$

Employing the WSB model results in an upper limit on

$$\frac{BR(B\to e\nu\pi,\rho)}{BR(B\to e\nu D,D^*)} < 2.5\% \text{ or } |\frac{V_{ub}}{V_{cb}}| < 0.15 \text{ at } 90\ \% \text{ C.L.}$$

using the data above $E_e = 2.4\ GeV$.

For the KS model we obtain an upper limit on

$$\frac{BR(B\to e\nu\pi,\rho)}{BR(B\to e\nu D,D^*)} < 3.0\% \text{ or } |\frac{V_{ub}}{V_{cb}}| < 0.14 \text{ at } 90\ \% \text{ C.L.}$$

when using the data above $E_e = 2.4\ GeV$.

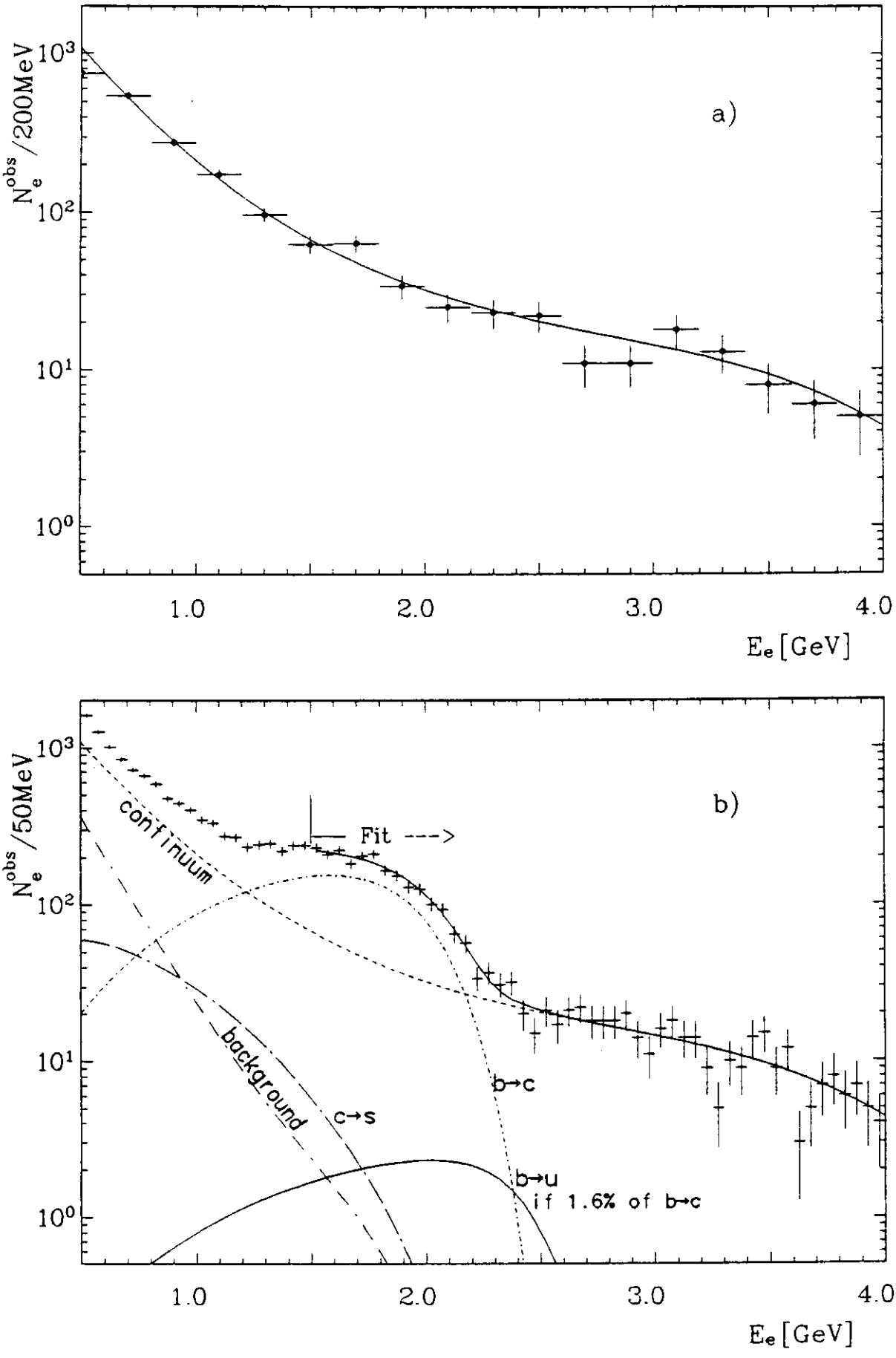

Figure 5.2: *The measured electron energy spectra. a) for continuum events. The fit shown is described in the text. Note the different bin size compared to that of the ON* $\Upsilon(4S)$ *data -figure 5.2b. The luminosity scale factor* $r = 4.028$ *practically compensates the factor 4 from the different bin size, therefore the two plots can be compared directly. b) ON the* $\Upsilon(4S)$ *resonance. The predictions shown are from ACM, they are corrected for detector response.*

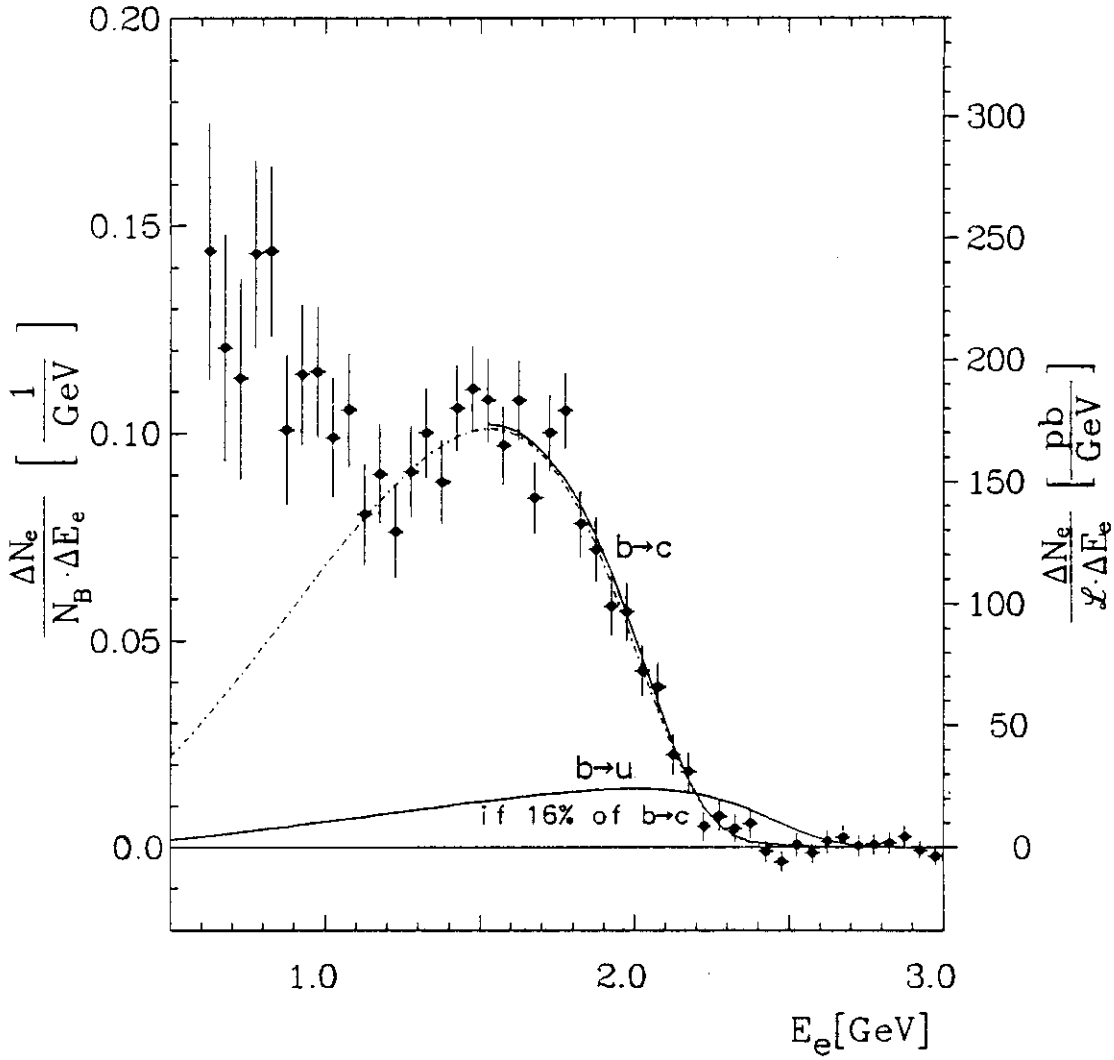

Figure 5.3: *The inclusive electron energy spectrum from B mesons from $\Upsilon(4S)$ decays, corrected for efficiency and background-subtracted. The data are normalized either to the number of produced B mesons (left-hand scale) or to the integrated luminosity (right-hand scale). Predictions are from the ACM model.*

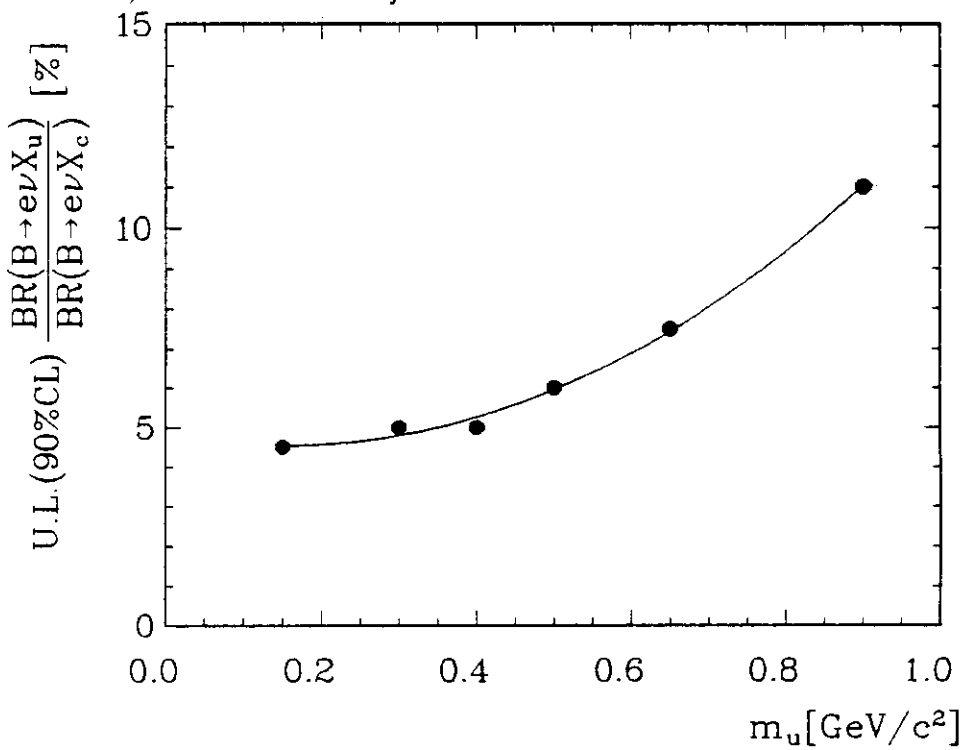

Figure 5.4: *Upper limit on $BR(B \to e\nu X_u)/BR(B \to e\nu X_c)$ using ACM's model for different u quark masses. The curve is a smooth function fitted to the points to guide the eye.*

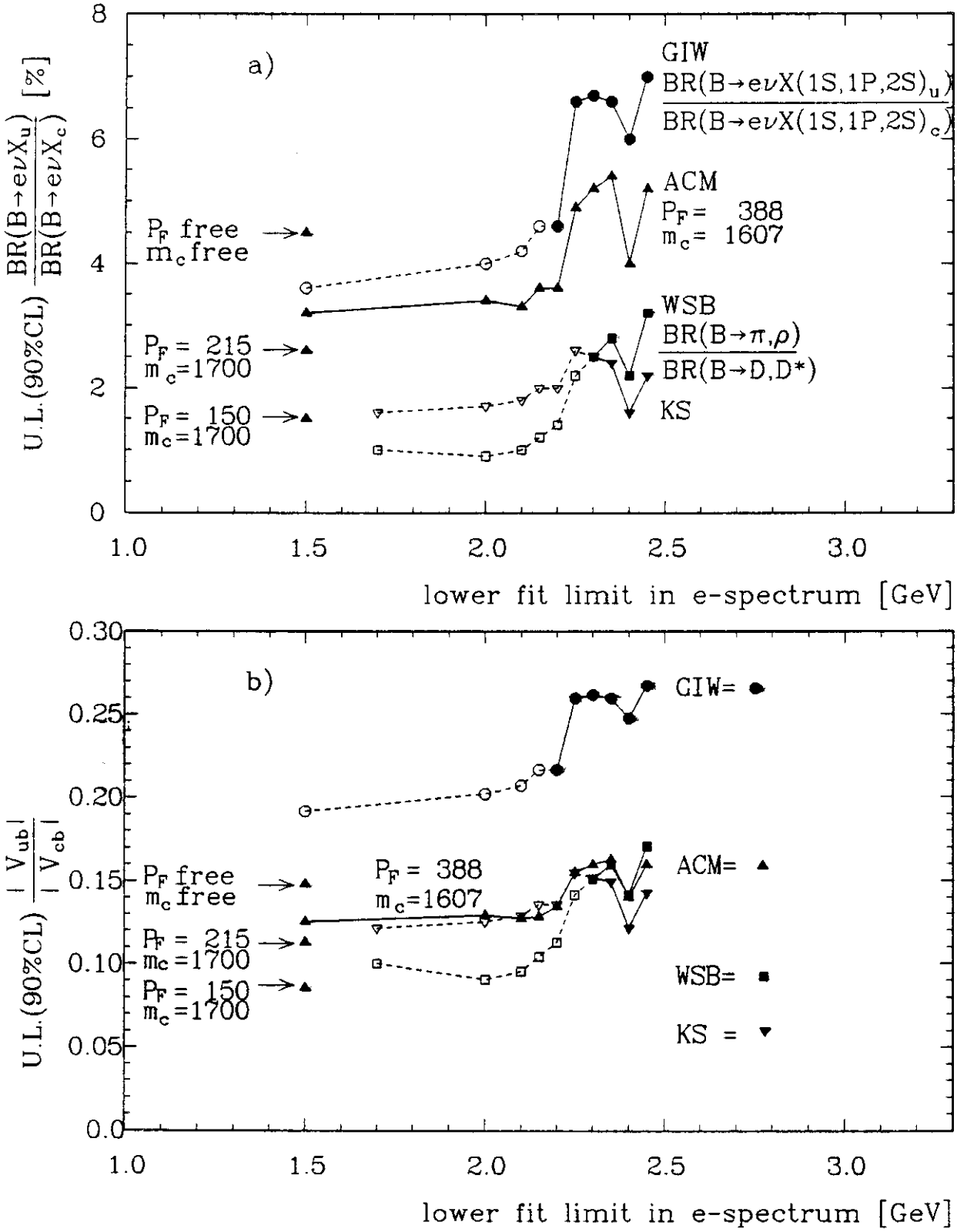

Figure 5.5: *a): Upper limit on $BR(B \to e\nu X_u)/BR(B \to e\nu X_c)$ for different models as a function of the lower limit in the electron energy E_e used for the fit. Open symbols are for comparison only, as they are outside the valid fit ranges. For GIW and WSB only some final states have been calculated: $X = (1S, 1P, 2S)$ for GIW and $X = 1S$ for KS and WSB. b): Upper limit on $|V_{ub}/V_{cb}|$ for different models and fit ranges. Open symbols are for comparison only, as they are outside the valid fit ranges. The masses and momenta given in the pictures are in units of MeV/c^2 and MeV/c, respectively.*

5.2 The Branching Ratio $B \to e\nu X_c$ and $|V_{cb}|$

Model	$BR(B \to e\nu X_c)$ [%]	$\lvert V_{cb}\rvert$ 10^{-2}	$\frac{b\to u}{b\to c}$ 10^{-2}	$\frac{\chi^2}{d.o.f.}$
ACM p_F and m_c free, best $p_F = (388 \pm 52)\ MeV/c$ $m_c = (1607 \pm 46)\ MeV/c^2$	$12.0 \pm 0.5 \pm 0.7$	5.3 ± 0.5	1.6 ± 1.6	39.2/40
GIW ; X = all	$11.9 \pm 0.4 \pm 0.7$	4.2 ± 0.5	2.0 ± 1.3	39.9/42
GIW + AW	$11.9 \pm 0.4 \pm 0.7$	5.1 ± 0.5		
WSB ; X = (1S)	$10.8 \pm 0.4 \pm 0.7$	5.5 ± 0.5	$0.0\ ^{+0.8}_{-0.0}$	39.8/38
KS ; X = (1S)	$10.1 \pm 0.5 \pm 0.7$	5.0 ± 0.5	$0.6\ ^{+1.7}_{-0.6}$	40.2/38
PS ; X = (1S)	$14.1 \pm 0.8 \pm 0.7$	4.0 ± 0.6		35.5/38
Average; X = all **ACM+AW+WSB+KS**	$11.7 \pm 0.4 \pm 0.7$	5.2 ± 0.5		

Table 5.1: *Results on $BR(B \to e\nu X_c)$ and $|V_{cb}|$. The errors quoted are statistical and systematic for the branching ratio measurement. In the case of $|V_{cb}|$ the experimental error of $|V_{cb}|$ is calculated by adding the statistical and the systematic errors and that one of the B meson lifetime in quadrature. It is dominated by the error on the B meson lifetime measurement. The error on $|V_{cb}|$ due to theoretical uncertainties quoted by all models is about 10%.*

If the $b\to u$ contribution would not be small, it would be incorrect to measure the inclusive $b\to c$ intensity with the models by GIW, WSB, KS, and PS which do not fully predict the $b\to u$ spectrum at lower electron energies where the $b\to c$ intensity is determined. However, since the $b\to u$ contribution is small we can calculate the branching ratio $BR(B \to e\nu X_c)$ and $|V_{cb}|$ using all meson decay models.

With free $b\to u$ contributions, which are not significant and therefore only quoted for completeness, and a B meson lifetime of $\tau_B = (1.18 \pm 0.14) \times 10^{-12} sec$ [40], we get the results listed in table 5.1. The models of ACM, GIW with the AW correction, WSB, and KS give consistent results.

The model by PS gives a very high branching ratio of 14.1% for the 1S states alone. This is due to the fact, that the predicted spectrum is very soft and only the high energy part is fitted. The model cannot describe the lower energy part, where the predicted spectrum lies above the measured one when fixing the amplitude by the fit to energies greater than 1.7 GeV where only D and D^* contribute. Therefore this model can be ruled out by our measurement and is not used any further.

If we assume that the higher spin states - which have not been calculated - add 10% to WSB's and KS's branching ratio we obtain the average total branching ratio

$$BR(B \to e\nu X_c) = (11.7 \pm 0.4 \pm 0.7)\%$$

as an average of the remaining four models.

Applying the correction by AW to GIW's we average the results from the four models and obtain

$$|V_{cb}| = 0.052 \pm 0.005 \pm 0.005.$$

5.3 Systematic Errors

In the following we discuss the contributions to the systematic error of the $b \to c$ branching ratio measurement as quoted in table 5.1.

- When shifting the energy scale within the uncertainty of the energy measurement of 10 MeV the effect on the $b \to c$ branching ratio is less than 0.1%.

- The largest contribution to the systematic error on the $b \to c$ branching ratio ($\Delta BR/BR = 6\%$) comes from the efficiency determination, to which we assigned an error of $\Delta\epsilon/\epsilon = 5\%$.

Other sources of systematic errors are:

- relative efficiency to accept an event as multi-hadron for events where one B meson decays semileptonically compared to all other decays: $\Delta\epsilon/\epsilon = 1\%$,

- number of observed $\Upsilon(4S)$ events: $\Delta N/N = 2\%$,

- varying the fit range gives a change of less than 1% in $\Delta BR/BR$,

- changing the energy scale by 10 MeV changes $\Delta BR/BR$ by less than 1%.

The total systematic error is obtained by adding the individual sources in quadrature.

For the $(b \to u)/(b \to c)$ limit the knowledge of the absolute energy scale is essential. The scale of the measured energy has been found to be $E_{true} = E_{measured} - (5 \pm 6) MeV$ at 2 GeV. The energy measurement is described in appendix A. We have verified that

- the upper limit becomes smaller, if one scales the measured electron energy to lower energies.

- the efficiency for the $b \to u$ channel is greater or equal compared to that for the $b \to c$ channel.

5.4 Comparison with Other Experiments

It turns out to be difficult to compare the results stated above with results obtained by other experiments, as various models and methods have been used to deduce upper limits on $(b \to u)/(b \to c)$. We therefore try to repeat the analysis with their models and parameters used and then compare our results with the results obtained by those experiments.

Comparison with results from ARGUS [41] [42] [43]

ARGUS quotes an upper limit on $\frac{BR(B \to e\nu X(1S,1P,2S)_u)}{BR(B \to e\nu X(1S,1P,2S)_c)} < 6\%$ obtained with GIW's model in the electron energy range $E_e > 1.6\ GeV$. With a modified free quark spectator model and a limited data sample of 12 pb^{-1} ARGUS gets a branching ratio $BR(B \to e\nu X_c) = (12.0 \pm 0.9 \pm 0.8)\%$. They have measured the decays $B^+ \to p\bar{p}\pi^+$ and $B^0 \to p\bar{p}\pi^+\pi^-$ with branching ratios of $(3.7 \pm 1.3 \pm 1.4)\ 10^{-4}$ and $(6.0 \pm 2.0 \pm 2.2)\ 10^{-4}$, respectively. From these measurements they deduce a lower limt of $|V_{ub}/V_{cb}| > 0.07$.

Comparison with results from CLEO [44] [45]

Beside other models CLEO used ACM's model with a parameter choice fixed to $p_F = 215\ MeV/c$ and $m_c = 1700\ MeV/c^2$. They get an upper limit of

$$\frac{BR(B \to e\nu X_u)}{BR(B \to e\nu X_c)} < 2.7\% \text{ at } 90\ \%\ \text{C.L.}$$

A branching ratio $BR(B \to e\nu X_c) = (11.0 \pm 0.3 \pm 0.7)\%$ is measured.

Using the same fit parameters, the Crystal Ball experiment obtains

$$\frac{BR(B \to e\nu X_u)}{BR(B \to e\nu X_c)} < 2.6\% \text{ at } 90\ \%\ \text{C.L.}$$

and $BR(B \to e\nu X_c) = (11.0 \pm 0.4 \pm 0.7)\%$ with a $\chi^2/d.o.f. = 43/42$ - a very similar result.

Comparison with results from CUSB [46]

Using ACM's model with a fixed parameter choice of $p_F = 150\ MeV/c$ and $m_c = 1700\ MeV/c^2$ an upper limit of

$$\frac{BR(B \to e\nu X_u)}{BR(B \to e\nu X_c)} < 5.5\% \text{ at } 90\ \%\ \text{C.L.}$$

is obtained. A branching ratio $BR(B \to e\nu X_c) = (13.2 \pm 0.8 \pm 1.0)\%$ is measured. Doing the same we obtain

$$\frac{BR(B \to e\nu X_u)}{BR(B \to e\nu X_c)} < 1.5\% \text{ at } 90\ \%\ \text{C.L.}$$

and $BR(B \to e\nu X_c) = (10.7 \pm 0.4 \pm 0.7)\%$ with a $\chi^2/d.o.f. = 52/42$.

Chapter 6

Conclusions

With the Crystal Ball detector we have measured the inclusive electron spectrum from B mesons originating from $\Upsilon(4S)$ decays. The models by ACM, GIW, KS, and WSB fit the data while the model by PS does not fit.

Using the four different theoretical models for the matrix elements and the shape of the electron spectrum, an average branching ratio

$$BR(B \rightarrow e\nu X_c) = (11.7 \pm 0.4 \pm 0.7)\%$$

has been obtained.

The average result on the Kobayashi - Maskawa matrix element is

$$|V_{cb}| = 0.052 \pm 0.005 \pm 0.005$$

using the same models - with the correction by AW to GIW's model.

For the ratio of $|V_{ub}/V_{cb}|$ we obtain an upper limit dependent on the model used. WSB, KS, and ACM give a conservative upper limit of

$$|V_{ub}/V_{cb}| < 0.15 \text{ at } 90\%\text{C.L.},$$

if one uses the data above $E_e = 2.4\ GeV$ where no $b \rightarrow c$ contribution is present. GIW gives a significantly weaker upper limit of

$$|V_{ub}/V_{cb}| < 0.26 \text{ at } 90\%\text{C.L.},$$

due to the softer spectrum in the $b \rightarrow u$ channel and due to the larger semileptonic width predicted for the $b \rightarrow c$ channel. Applying the AW correction to the $B \rightarrow e\nu D^*$ channel the upper limit goes down to $|V_{ub}/V_{cb}| < 0.21$.

Appendix A

Energy Calibration of the Calorimeter

We need to know the absolute energy scale as well as the resolution for the analysis of the inclusive electron spectrum. First we describe the procedure used to calibrate the constants of the crystals, then we discuss the energy response function used to describe the energy depositon of mono-energetic electromagnetically showering particles which includes the resolution and the absolute energy scale.

A.1 Calibration

The energy measurement for each crystal is done in two separate electronic channels – the high and low energy channel. Therefore four constants per crystal are needed, two pedestals and two slopes, as defined in equation(4.1).

During normal data-taking – once every two weeks – the running is suspended and an online calibration is performed. The pedestals are taken with no beam and no radioactive sources present.

The slopes are determined by two different procedures. The first procedure uses gamma rays of 0.6 MeV from a Cs^{137} source to determine the slope of the low energy channel, $SLOPE_L$, of each single crystal, separately.

The second one utilises $6.131 MeV$ $\gamma's$ produced by stopping protons of 340 KeV kinetic energy in a LiF target. The protons are accelerated by a Van de Graaff generator. The showers induced by these 6.131 MeV photons extend over several crystals and therefore a different procedure is used. It is described in detail in [47]. These constants are first used to perform equipment checks and then as starting points for the offline final calibration.

The offline calibration, which finally determines the calibration constants, is done in the following way. First the pedestals are determined with events having no energy cut in writing on tape – see chapter 3. For each crystal the mean energy is calculated using only entries close to the previous pedestal. After some iterations with closer and closer windows the last mean value is taken as the pedestal for that crystal. The obtained pedestal width is less than one channel.

The procedure to determine the slopes of the low and high channel uses $e^+e^- \rightarrow e^+e^-$ and $e^+e^- \rightarrow \gamma\gamma$ events. First events with two clusters of $E^c_{13} > 0.8 \times E_{BEAM}$ are selected. For this selection the slopes from the previous calibration are taken.

As the energy of a single electromagnetically showering particle is distributed over several crystals, a single crystal cannot be calibrated without knowing the constants

of the other crystals. Therefore an iterative procedure is performed. If both clusters fulfil the constraint, $0.6 < E_1/E_{13} < 0.8$, both values of $(E^c_{13} - E_{BEAM})$ are stored for each *bump* crystal separately in a histogram. The bins within 2% of the peak position of each distribution are used to determine the slope of the high energy channel, $SLOPE_H$, for that specific crystal. $SLOPE_H$ is tuned, resulting in the mean value of those bins becoming zero. The slope of the low channel is determined using data where a crystal has sufficient information from both channels L and H. In this energy range - 100 to 400 MeV - the following quantity is minimized:

$$\chi^2 = \sum \left(\frac{E_H - E_L}{E_H + E_L} \right)^2 \tag{A.1}$$

This procedure is repeated until only small changes in the resolution of the peak in the distribution are left after a new iteration step.

A.2 Energy Response Function

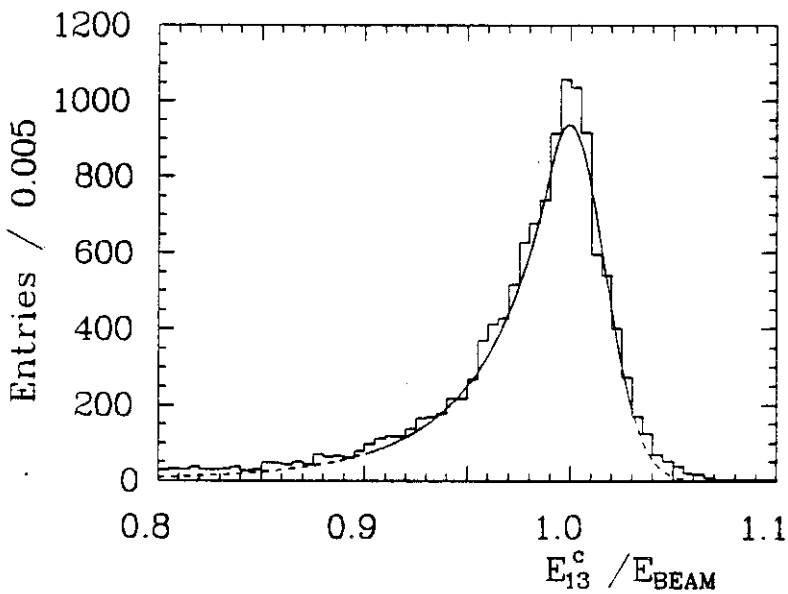

Figure A.1: *Energy response function fitted to E^c_{13} of Bhabha events. The best fit values are: $E^c_{13}/E_{BEAM} = 0.9998 \pm 0.0004$; $\sigma_0 = (2.59 \pm 0.07)\%$; $r = 8.6 \pm 3.0$; $\alpha = 0.54 \pm 0.04$. For an explanation of the parameters see text.*

Figure A.1 shows the energy distribution of the two clusters of Bhabha events. The probability density distribution f for measuring the energy E_M of an electromagnetically showering particle of energy E_0 is [48]:

$$f(E_M, E_0) = \frac{1}{N} \begin{cases} exp[-\frac{1}{2}\left(\frac{E_0 - E_M}{\sigma_E}\right)^2] & if \quad E \geq E_0 - \alpha \times \sigma_E \\ \left(\frac{A}{(B - E_M)^r}\right. & if \quad E < E_0 - \alpha \times \sigma_E \end{cases} \tag{A.2}$$

$$\text{where} \quad N = \sigma_E \left[\frac{r}{\alpha} \cdot \frac{1}{r-1} e^{-\frac{1}{2}\alpha^2} + \sqrt{\frac{\pi}{2}} \left(1 + erf(\frac{\alpha}{\sqrt{2}}) \right) \right],$$

$$A = \left(\frac{r\sigma_E}{\alpha}\right)^r e^{-\frac{1}{2}\alpha},$$
$$B = E_0 + \frac{r\sigma_E}{\alpha} - \alpha.$$

In the latter expression, σ_E stands for $\frac{E_0\sigma_0}{\sqrt[4]{E_0}}$, where σ_0 denotes the the relative energy resolution at 1 GeV , $\sigma_0 = (2.7 \pm 0.2)\%$; α sets the limit of Gaussian versus power tail part; r describes the power of tail of the measured energy towards lower energies; N is the normalization factor of the distribution. The function is separated into a Gaussian part at the high energy side and a power tail towards lower energies. This power tail reflects the effect of energy leakage outside the rear part of the crystals. The energy dependence of the resolution has been obtained with data-taken at $E_{BEAM} \approx 5$ GeV at the storage ring DORIS II, at $E_{BEAM} \approx 2$ GeV at the storage ring SPEAR, and with monoenergetic gamma rays from exclusive events of the type $\Upsilon(2S) \rightarrow \gamma\gamma\Upsilon(1S)$; $\Psi' \rightarrow \gamma\gamma J/\Psi$ in the energy range from 100 to 600 MeV.

A.3 Energy Scale

The absolute energy scale is fixed by the assumption that E_0 of the E_{13}^c distribution is tuned to peak at E_{BEAM}. A small empirical correction to gamma rays in a range from 100 to 600 MeV has been found to be [49]:

$$E_{13}^{c'} = E_{13}^c \frac{1}{1 + 0.0137 \ln \frac{E_{13}^c}{E_{BEAM}}} \tag{A.3}$$

The curve and the points where this correction is found and / or tested is shown in figure A.2. This correction was introduced to get the measured π^0 mass from

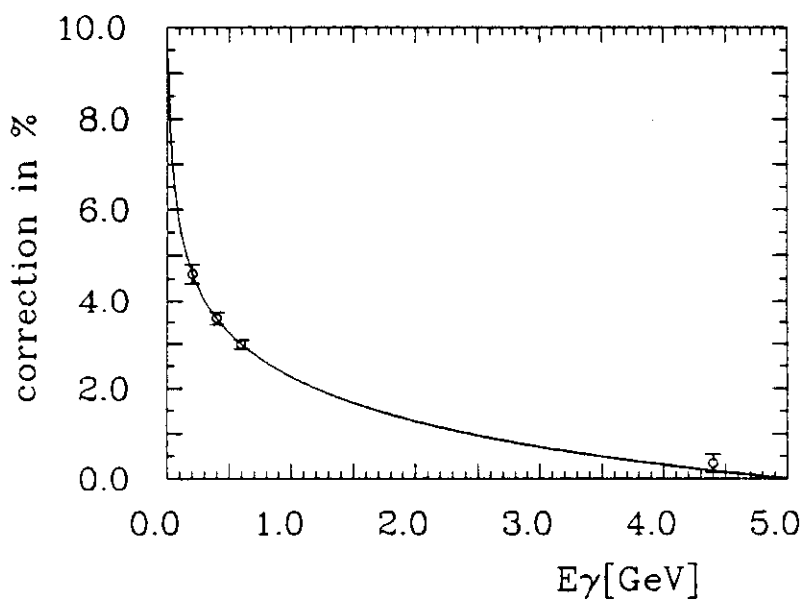

Figure A.2: *Energy corretion to* E_{13}^c *at* $E_{BEAM} = 5.0$ GeV.

$\gamma\gamma$ pairs to the correct value. Photons from the process $\Upsilon(2S) \rightarrow \pi^0\pi^0\Upsilon(1S)$ were

subjected to this correction. Furthermore, this correction was applied in the process $\Upsilon(2S) \to \gamma\gamma\Upsilon(1S)$ for measuring the energy of the monoenergetic γ rays. In addition it was used in two photon induced events, namely $e^+e^- \to e^+e^-\pi^0, \eta, \eta'(\to \gamma\gamma)$.

A test point at 600 MeV below E_{BEAM} was obtained by using a set of calibration constants, obtained from a run at $\Upsilon(4S)$ with $E_{BEAM} = 5290\ GeV$, for Bhabha events from the continuum below the $\Upsilon(1S)$ with $E_{BEAM} = 4.690\ GeV$, and vice versa. Both data sets were taken within two days, therefore the drifts in the calibration constants are small.

Table A.1 shows the measured energy E_0 and the resolution of the track with the highest value of E_{13}^c from Bhabha events. Only that track was taken, instead of both tracks as in the above described calibration procedure, since the width of this E_{13}^c distribution is smaller in width and therefore also more sensitive to shifts of the peak position. The numbers are obtained by a fit of the lineshape function to the distributions obtained using the different calibration constants for the crystals. The

data sample	$\Upsilon(1S)$ calibration $(E_0 - E_{BEAM})/E_{BEAM}$ [%]	σ_0 [%]	$\Upsilon(4S)$ calibration $(E_0 - E_{BEAM})/E_{BEAM}$ [%]	σ_0 [%]
$\Upsilon(1S)$	0.68 $\pm$0.02	2.4 $\pm$0.05	0.004 $\pm$0.02	2.6 $\pm$0.05
$\Upsilon(4S)$	1.02 $\pm$0.03	2.6 $\pm$0.05	0.38 $\pm$0.03	2.3 $\pm$0.05

Table A.1: *Peak position E_0 and resolution σ_0 of the E_{13}^c distributions from Bhabha events. Only one track is used, the track with the highest energy.*

change of the peak position for both cases with mixed calibration compared to the right constants is $(0.34 \pm 0.04)\%$. The beam energy of the $\Upsilon(1S)$ continuum data sample is known to an accuracy of 10 MeV, the $\Upsilon(4S)$ beam energy to 4 MeV. This error on the beam energy dominates the error on this test point shown in figure A.2 at 600 MeV below E_{BEAM}.

A.4 Energy Measurement in This Analysis

The corrections discussed so far are valid only for electromagnetically showering particles in events with low multiplicity, e.g. two-photon events.

In multi-hadron events hadronic debris adds extra energy to the real energy of the electrons. Hadronic debris means other particles arising from hadronic interactions in the crystals. Those particles add energy to the energy of the 13 crystals used in the evaluation of E_{13} . This may happen when the clusters from an electron and another particle – e.g. a minimum ionizing one – overlap and this cluster passes the electron selection cuts.

This effect is analysed in the following way. The measured energy of Monte Carlo electrons in the empty Ball and the measured energy of the same electrons inside multi-hadron events are compared. The difference gives the energy added from other particles to the real electron energy. The mean energy shift is $(23 \pm 5)\ MeV$. The size of the error comes from the fact that this extra energy is not a smooth shift of

the measured energy of a single electron, but has a discrete behaviour. Sometimes a particle overlaps, howerver, most of the times it does not. If e.g. a minimum ionizing particle overlaps, 200 MeV are added.

Two other small effects must be taken care of. The first comes from the beam energy used for the calibration. It is taken from the 'DORIS telegram', which is automatically written on tape. The beam energy recorded in the telegram is 13 MeV too high compared to the nominal $\Upsilon(4S)$ mass [15]. This change leads to a 5 MeV correction at 2 GeV electron energy. The second small correction is due to different selection procedures used for the electron selection used in this analysis and the calibration procedure. This analysis cuts much stronger in the energy around the 13 crystals than the calibration procedure. Therefore using the pattern cuts employed in this analysis instead of the calibration pattern cuts, the measured energy comes out to be 0.1% higher.

Summing the effects – see table A.2– of energy mis-measurement, the correct energy turns out to be (5 ± 6) MeV lower at 2 GeV electron energy compared to the measured E^c_{13} value. The effect of this energy correction is small compared to other systematic uncertainties, therefore it is neglected in this analysis.

correction type	correction at 2 GeV electron energy
$E^{c'}_{13} - E^c_{13}$	+ 25.0 $\pm$5.0 MeV
hadronic debris	- 23.0 $\pm$4.0 MeV
Beam energy	- 5.0 $\pm$0.5 MeV
pattern cuts	- 2.0 $\pm$0.1 MeV
sum	- 5.0 $\pm$6.0 MeV

Table A.2: *Corrections to the E^c_{13} energy measurement.*

Appendix B

Luminosity Measurement

In order to determine the continuum contribution to the ON $\Upsilon(4S)$ data sample another data sample about 50 MeV lower in beam energy than the $\Upsilon(4S)$ resonance is used. This data sample is needed to calculate the number of $B\overline{B}$ events and to estimate the background from continuum events in the electron spectrum. For this procedure the integrated luminosity of the two data samples is needed. The integrated luminosity is defined as :

$$L = N/\sigma_{visible} \tag{B.1}$$

where N is the number of events detected and $\sigma_{visible}$ is the visible cross-section of the selected reaction. The standard reactions to measure the luminosity are:

$$\begin{array}{rcccl} e^+e^- & \rightarrow & e^+e^- & + & (\gamma) \\ & \rightarrow & \gamma\gamma & + & (\gamma) \end{array} \tag{B.2}$$

The theoretical cross-sections of these processes are well known and can be used to determine the luminosity. To deduce the luminosity we perform a Monte Carlo simulation of the above processes and run a selection on these generated events. This selection has to have a good efficiency for the luminosity events and has to reject the background from other processes like $e^+e^- \rightarrow \tau\overline{\tau}$.

B.1 Selection of Luminosity Events

The following cuts are used to select events:

- For the energy deposited in the Ball we require:
  $0.5 < E_{BALL}/(2 \times E_{BEAM}) < 1.2$.

- Two and only two clusters must have $E^c_{13} > 0.7 E_{BEAM}$.
  They must be within $|cos\theta| < 0.75$.

For the direction determination the routine SHOWER [31] is used. The visible cross-section for the two processes at $E_{BEAM} = 4.73\ GeV$ is predited by the Monte Carlo studies to be:

$$\begin{array}{lllcll} \sigma_{VISIBLE} & (e^+e^- \rightarrow e^+e^- & (\gamma)) & = & 12.85 & nb \\ \sigma_{VISIBLE} & (e^+e^- \rightarrow \gamma\gamma & (\gamma)) & = & 1.61 & nb \\ & & \Sigma & = & 14.46 & nb \end{array} \tag{B.3}$$

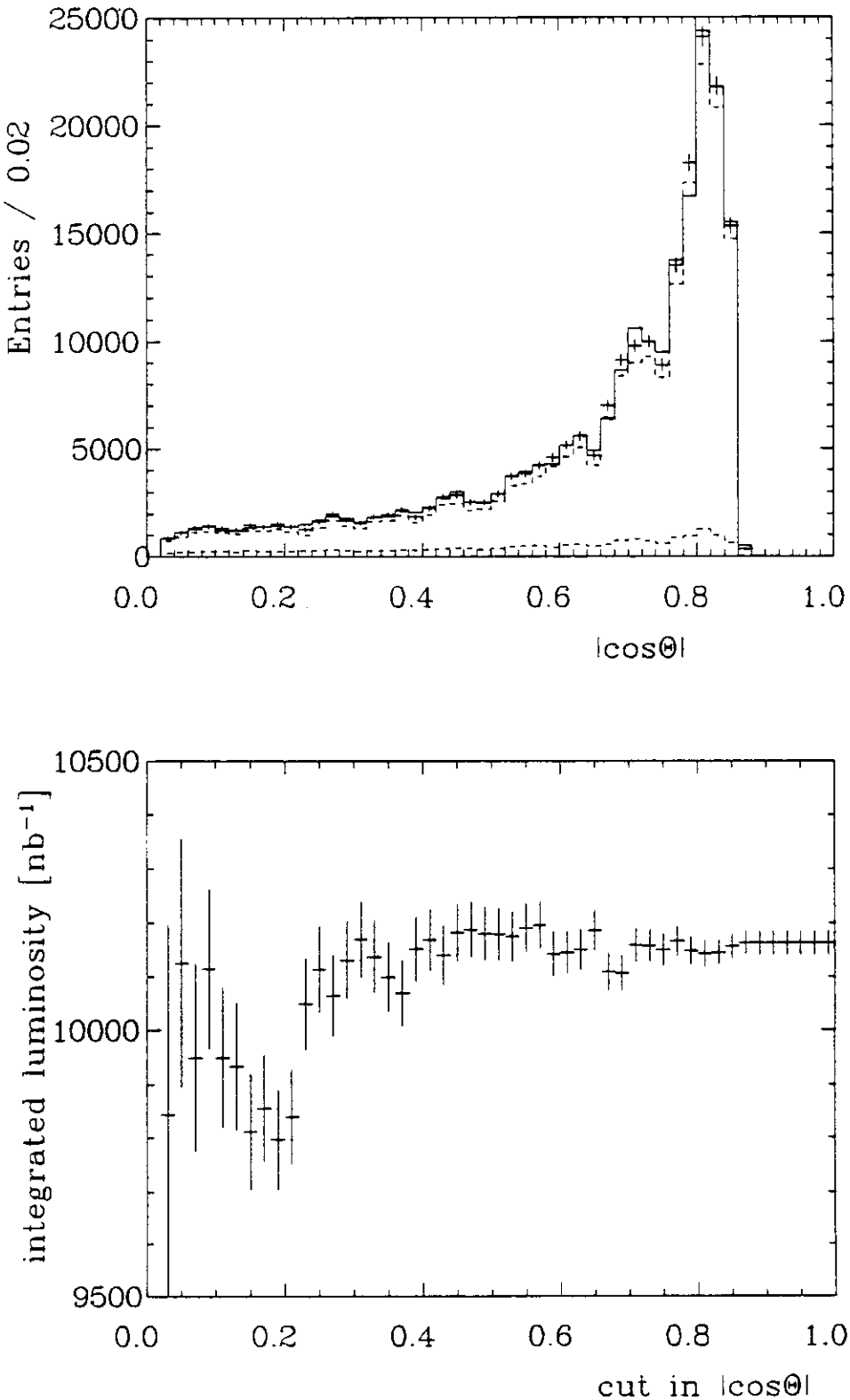

Figure B.1: *Top: $|cos\theta|$ distribution, comparison between data and Monte Carlo prediction. Histogram : data; dashed histograms: e^+e^- and $\gamma\gamma$ Monte Carlo prediction; crosses : fit. A $\chi^2/d.o.f.$ of 0.71 is achieved for a fit from 0 to 0.75. Bottom: integrated luminosity as function of cut in $|\cos\theta|$.*

where we have used an event generator by Berends and Kleiss [51] and the EGS program to simulate the detector response. For different beam energies the processes $e^+e^- \rightarrow e^+e^-(\gamma)$ and $e^+e^- \rightarrow e^+e^-(\gamma)$ used to measure the luminosity L scales like $1/s$, hence

$$L = N \times s/C, \tag{B.4}$$

where N is the number of luminosity events found, $\sqrt{s}$ is the center-of-mass energy in GeV, and $C = \sigma_{VISIBLE} \times s_{MC} = 1294\ nb\ GeV^2$, $\sqrt{s}_{MC} = 9.46\ GeV$ is the center-of-mass energy of the Monte Carlo data sample.

B.2 Systematic Error on the Luminosity Measurement

In order to obtain an estimate of the systematic error of the luminosity measurement we vary the cuts in a wide range and observe the change in the luminosity for some selected run periods.

We use run periods at the $\Upsilon(4S)$ resonance, since at the $\Upsilon(1S)$ resonance the resonance itself decays with a significant branching ratio of about 3% into e^+e^- pairs which simulates luminosity events. These extra events increase the luminosity by about 1.1%. The cross-section for producing the $\Upsilon(1S)$ resonance at the storage ring DORIS II is $\approx 10\ nb$ compared to the visible cross-section for the luminosity events of $14.5nb$. Assuming an efficiency of 50% for accepting those $\Upsilon(1S)$ events as luminosity events, gives the above quoted 1.1% too high luminosity.

The first cut investigated to estimate the systematic error on the luminosity mesurement is the cut in the solid angle $|cos\theta|$. Figure B.1 shows the luminosity as function of the cut in $|cos\theta|$. No obvious dependence is visible. One has to take into account that the bins are not statistically independent. Figure B.1 top shows the $|cos\theta|$ distribution of the cluster with the highest $|cos\theta|$ value – closest to the beam axis. Together with the data the Monte Carlo predictions from the $e^+e^- \rightarrow e^+e^-(\gamma)$ and the $e^+e^- \rightarrow \gamma\gamma(\gamma)$ is overlayed. The Monte Carlo prediction clearly agrees with the data. A fit where the amplitude of the Monte Carlo prediction is fitted to the data gives a $\chi^2/d.o.f.$ of 0.71. We state a systematic error of $\Delta L/L$ of 0.5% for the cut in $|cos\theta|$. We cut at $|cos\theta| < 0.75$ since there the number of luminosity events has a flat dependence on this cut, see figure B.1 top. Choosing a cut at higher $cos\theta$ values would make the luminosity measurement sensitive to changes in the mechanical adjustment – see appendix B.4 for the vertex measurement.

The other cut in the energy of the showers has a much bigger systematic error. Figure B.2 shows the dependence of the luminosity on the cut in the energy of the second highest E^c_{13} . There are several reasons for this dependence. The first one originates from the Monte Carlo generator. The event generator has a cut-off in the energy of the radiated photon at 1% of the electron energy. Photons below that energy are not radiated, the energy stays with the initial particle (e, γ).

The other reason is due to the change of width of the E^c_{13} distribution as function of the electron or photon energy – due to different beam energies. Therefore the simulation of the E^c_{13} close to the peak value is not very reliable. Placing the cut at 0.7 in E^c_{13}/E_{BEAM} makes sure that the simulation of the soft photon radiation and the non-proper simulation of the E^c_{13} distribution close to the peak has a minor impact.

Figure B.3 shows the E^c_{13} distribution of the shower with the highest energy for the data and the Monte Carlo data sample. The energy of this shower has a weaker

dependence on the radiated photon than the track with the second highest E^c_{13} . The distributions are in agreement close to the peak although the widths differ since the Monte Carlo sample is generated at $E_{BEAM} = 4.78\ GeV$ while the data are taken at $5.3\ GeV$.

At lower E^c_{13} energies the data show some enhancement compared to the Monte Carlo prediction. The relative rise of the luminosity cutting at lower E^c_{13} values comes from background passing the cuts. This is confirmed by the plot shown in figure B.4. There we require that the track with the second highest energy has $E^c_{13}/E_{BEAM} < 0.7$ in order to enhance the background contribution. Then the energy of the track with the highest E^c_{13} normalized to the Monte Carlo prediction is plotted. The enhancement of the measured luminosity at lower cut values is due to events, where both tracks have low energy. This is a clear sign for background. Figure B.5 shows the energy distribution of E^c_{13}/E_{BEAM} of the track with the second highest E^c_{13} from $\tau\tau$ Monte Carlo events. This figure suggests a cut at 0.7, where the contribution from $\tau\bar{\tau}$ events becomes negligible.

The background contribution to the luminosity measurement from all Monte Carlo simulated events - like $q\bar{q}, ggg, \tau\bar{\tau}$ - is less than $(0.05 \pm 0.2)\%$ for a cut at 0.7. A systematic error of 2% is assumed for this cut. This value nearly covers the full variation of the luminosity as function of that cut.

In addition a 1 % systematic error due to the Monte Carlo statistics and a 1% error from the contribution of the 4^{th} order processes like $e^+e^- \rightarrow e^+e^-\gamma\gamma$ [52] has to be added. This process is not included in the simulation. The last contribution may be the source of the systematic error in the energy cut. The overall systematic error of

$$2.5\%$$

is obtained adding the individual sources in quadrature.

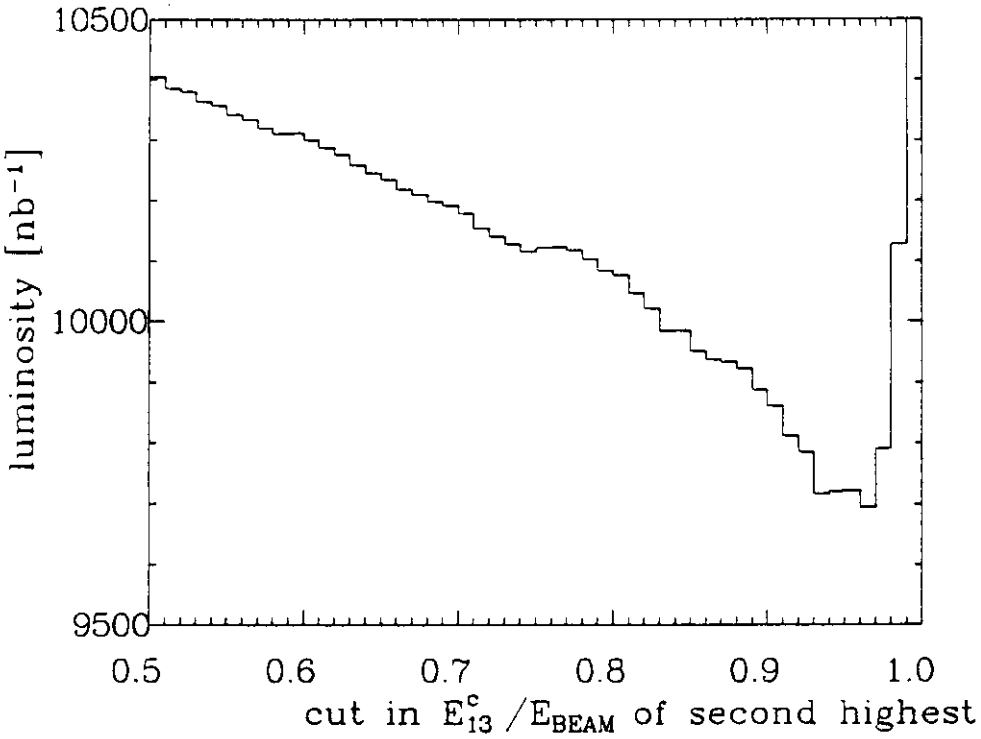

Figure B.2: *Luminosity as function of cut in E^c_{13} for a specific run period.*

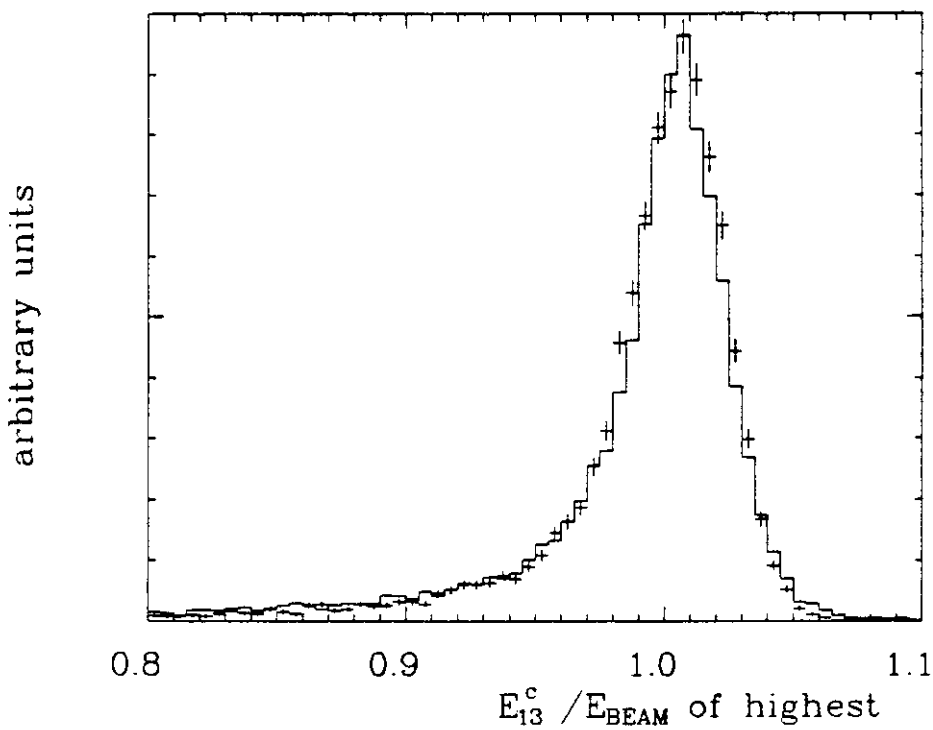

Figure B.3: *Comparison of Monte Carlo (crosses) and data (histogram) of the track with the highest energy for a specific run period.*

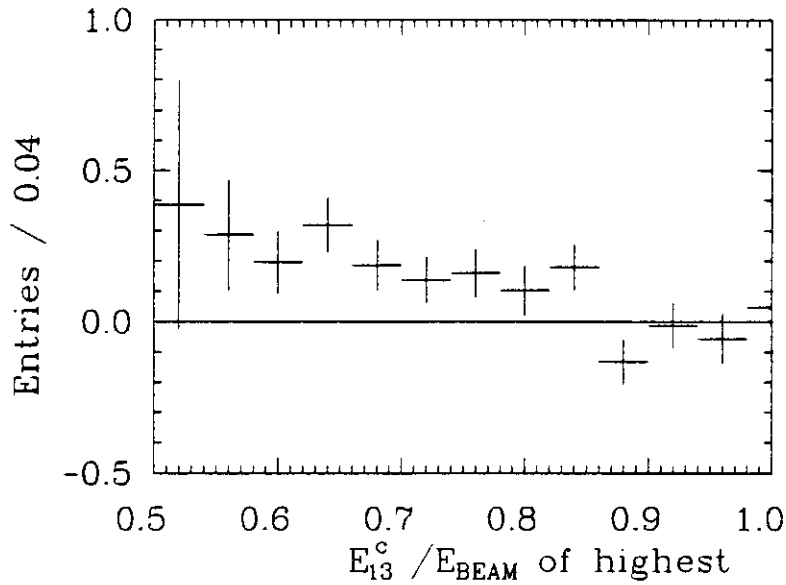

Figure B.4: *(Data - Monte Carlo)/(Data + Monte Carlo) of track with the highest energy, if the second highest has* $E^c_{13} < 0.7E_{BEAM}$

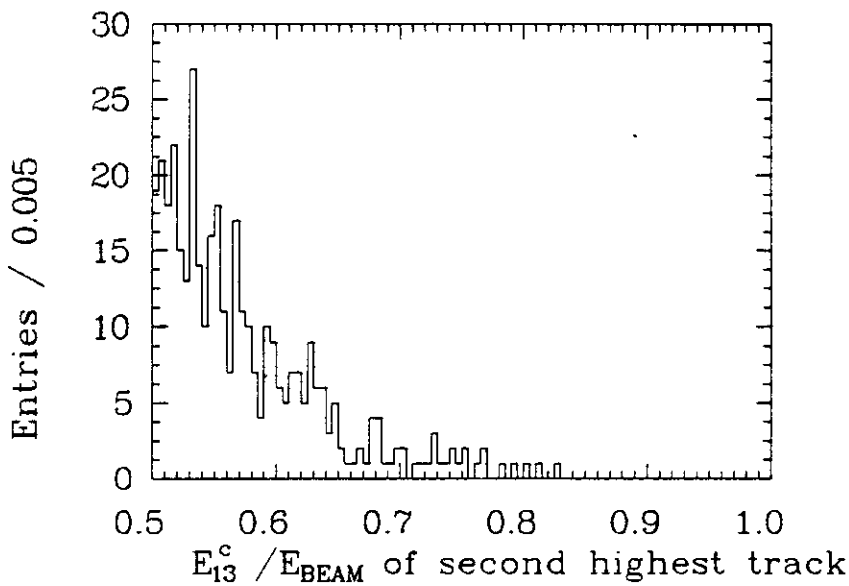

Figure B.5: E^c_{13} *of the track with the second highest* E^c_{13} *for a* $\tau\bar{\tau}$ *Monte Carlo data sample*

B.3 Stability of the Luminosity Measurement

In order to determine the number of $B\overline{B}$ events we need to subtract the continuum contribution from the ON $\Upsilon(4S)$ data. For this purpose the continuum data below the $\Upsilon(4S)$ are taken and scaled by the number of luminosity events of the ON and OFF resonance data samples. This procedure is justified because the cross-sections of the luminosity events and that of the $q\bar{q}$ have the same $1/s$ dependence. Using that relation has the advantage that the beam energy is not required, which is a possible source of systematic errors. Hence we only need to know the relative stability of the luminosity mesurement of the ON and the OFF resonance data samples.

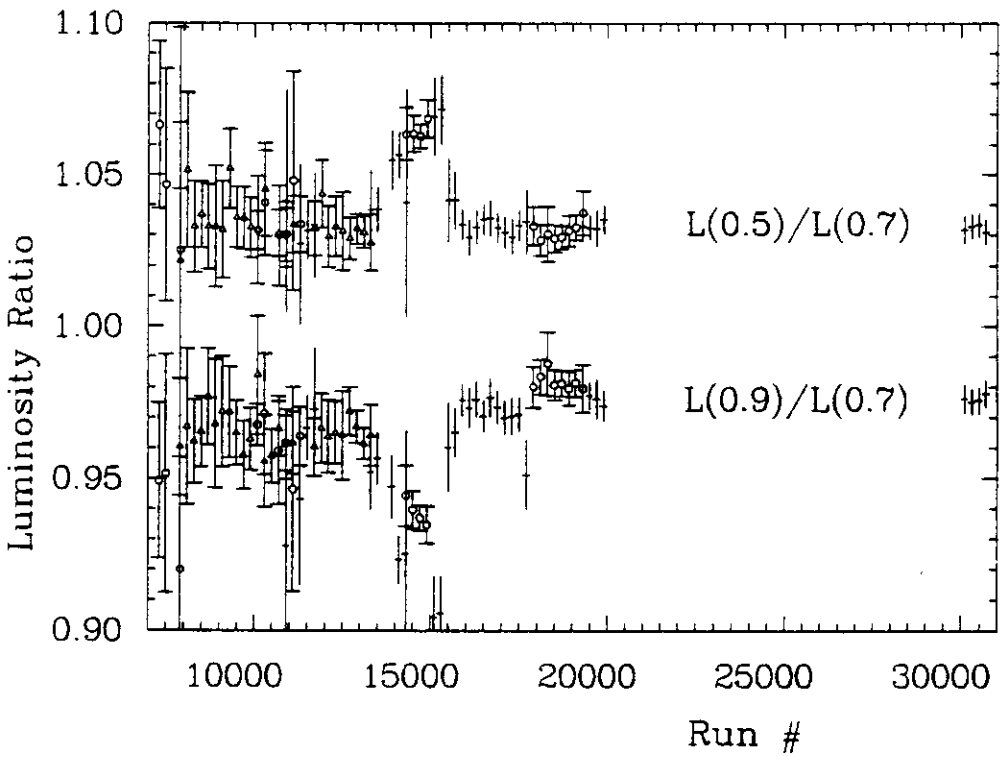

Figure B.6: *Stability of the luminosity measurement versus run period. The ratio of luminosities for different cuts in E^c_{13} is plotted. Crosses mark the data at the $\Upsilon(4S)$ resonance, open circles denote the data taken at the $\Upsilon(1S)$ resonance, and the triangles are the data from the $\Upsilon(2S)$ resonance. The data used in this analysis starts at run 15448.*

Therefore the luminosity for different cuts in E^c_{13} is plotted as a function of the run number in figure B.6. Around run number 15000 a deviation from the flat distributions is visible. During that run period the crystal read-out system had a non-linear behaviour. Crystals which should have had an energy of 1 GeV had sometimes 0 energy. A cut in $E^c_{13}/E_{BEAM} > 0.9$ rejects a lot of luminosity events where 1 GeV is missing. A Monte Carlo simulation indicates that the cut at 0.5 accepts nearly all the events rejected by cuts at 0.7 or 0.9. Therefore the luminosity measurement can be corrected by the enhancement of the luminosity measurement with the cut placed at 0.5 compared to that at 0.7. A linear dependence as function of the run number was chosen to correct for the non-linear behaviour of the luminosity L in the range $13236 < run < 15447$:

$$L(run) = L(run) \times \left(1 + 0.04 \frac{run - 13236}{15447 - 13236}\right)$$

All other run periods show a stable behaviour of the luminosity measurement. In this analysis the data with the non-linear behaviour are not used. In principle the luminosity measurement can be corrected, but the data themselves are also effected. The electrons under investigation have an energy of about 2.5 GeV. They are effected in the same way, and therefore the efficiency would be uncertain. Therefore the data used in this analysis are restricted to a range where $run > 15447$.

B.4 Vertex Distributions

Another check on the stability of the luminosity is performed by looking at the vertex distributions for the different run periods. The vertex distribution is only needed on a statistical basis and not on an event by event basis. The average vertices found are input data to the Bhabha Monte Carlo. The following cuts are used to select Bhabha events and to determine the vertex distributions:

- The events must have exactly two connected regions.
- The events must have exactly two *bumps*.
- The endcap energy must be less than 100 MeV.
- Both connected region energies must be greater than 95% of the beam energy.
- Beside the two clusters the remaining energy in the Ball must be less than 0.04 of the total energy.

The directions of the tracks are then defined with a modified version of 'SHOWER' [31]. This routine is especially tuned for 5 GeV Monte Carlo photons (electrons). It gives an angular resolution of $\approx 0.7^0$. The centers of the two showers in the Ball are connected with a straight line. This line is assumed to be the flight path of the e^+ e^- or $\gamma\gamma$ particles. The shower maximum in radial diretion C_R in cm is defined as [50]:

$$C_R = DOME + RDL \times \log\left(\frac{E_{BEAM}[GeV]}{0.0174} - 6.2\right), \qquad \text{(B.5)}$$

where $DOME$ is the radius of the inner dome= 25.4 cm, RDL is the radiation length in NaI = 3.0 cm, and the logarithmic form accounts for the radial dependence of the center as function of the energy of the incident particle.

The vertex is determined in the X, Y plane. Figure B.7 illustrates the method. The vertex is assumed to be the point which has the smallest distance between the straight line and the Z-axis. This requirement also fixes the point in the Z-coordinate. This method is correct as the X, Y-coordinates of the vertices are much smaller than the Z-coordinate – see chapter 3. The vector in figure B.7 marks the point of the reconstructed vertex in the X, Y plane, while the black dots indicate the position of the possible real vertex. Plotting the resulting average X, Y-coordinates in bins of

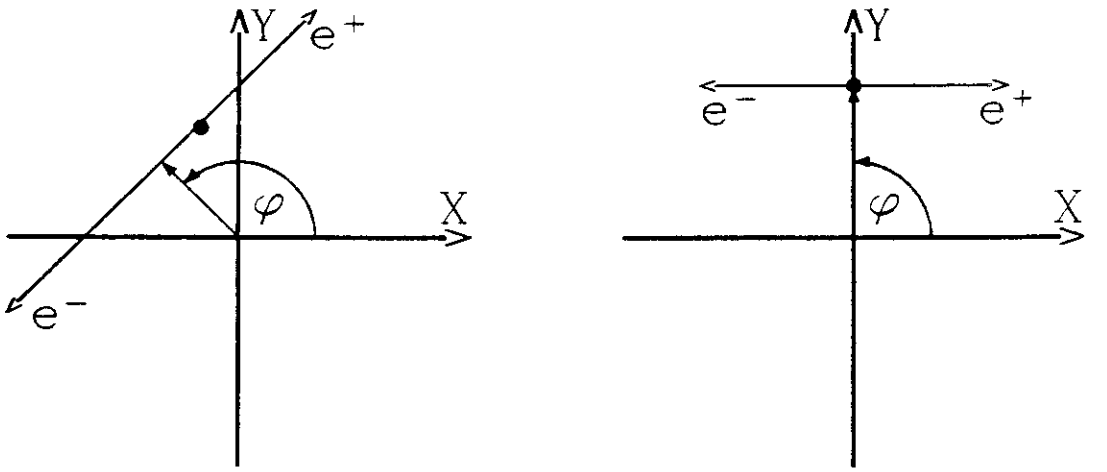

Figure B.7: *The reconstruction of the vertex. The big dots indicate the true vertex, while the arrow points to the reconstructed vertex*

the azimuthal angle φ results in sinusoidal curves. At $\varphi = 90, 270^0$ the X-vertex is measured correctly, while for $\varphi = 0, 180^0$ the Y-vertex is measured correctly. Figure B.8 shows the dependence of the obtained vertices in X and Y as function of the φ angle for a specific run period. The deviations from a sinusoidal curve at $\varphi = 0^0$ are due to the gap between the two hemispheres.

Figure B.9 shows the measured Z-coordinate of the vertex distribution together with a fit of a Gaussian function to the data using the above described method. The distribution of X and Y versus φ suggests that the resolution of the vertex reconstruction is smaller than 1 mm. This resolution is much better than needed for the Z vertex measurement as it has a width in the order of 1 cm.

The vertices as function of run number are shown in figures B.10 and B.11. Always 100 runs are collected in one bin. In Y the vertex seems to be pretty stable. Only once the mechanical adjustment of the Ball was changed. In X the vertex shows a rather strong run dependence. This is due to the different orbits of the beam for different energies and due to beam tuning. The vertex in Z and the width σ_Z shows some dependence on the beam energy. This may result from different beam optics used at differnt run periods. An average value $\sigma_Z = 1.20$ cm is used for the Monte Carlo simulation studies.

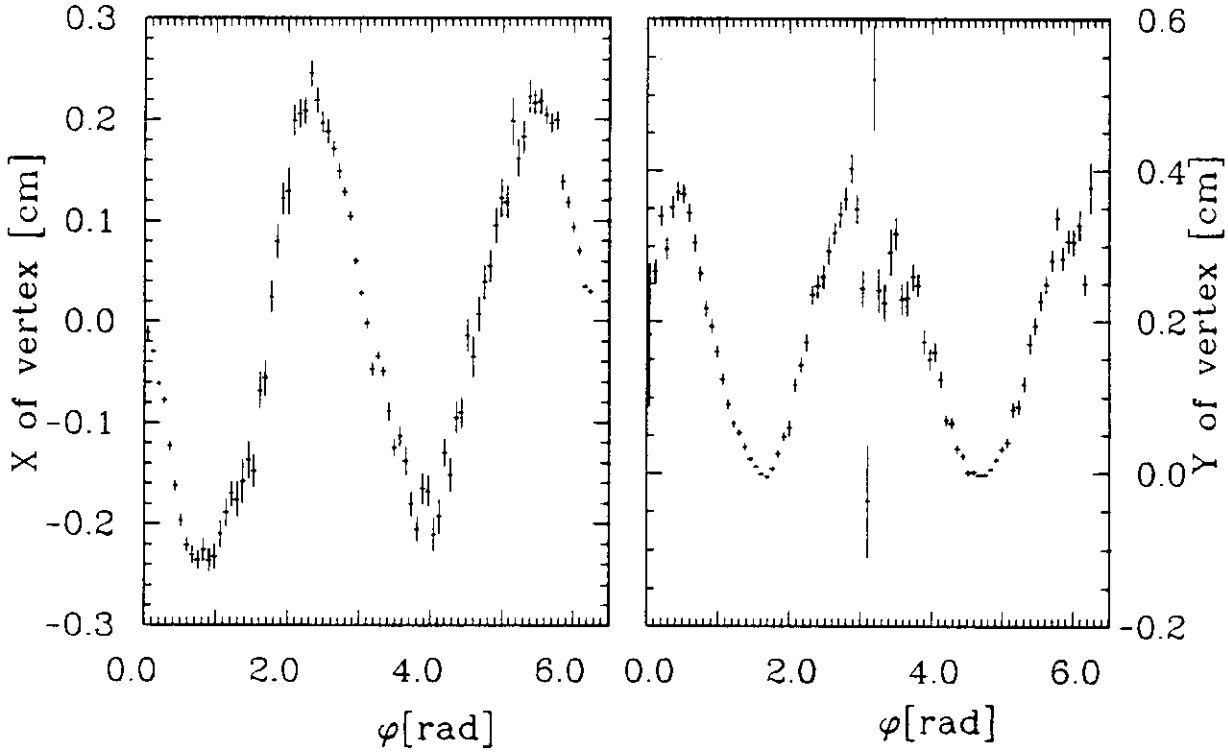

Figure B.8: *X and Y-Coordinate of vertex versus φ for a specific run period*

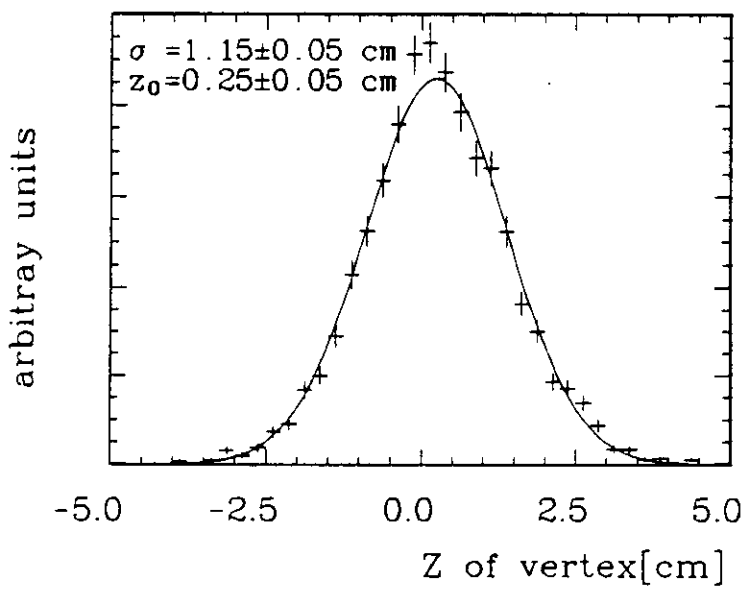

Figure B.9: *Z-coordinate of vertex distribution for a specific run period*

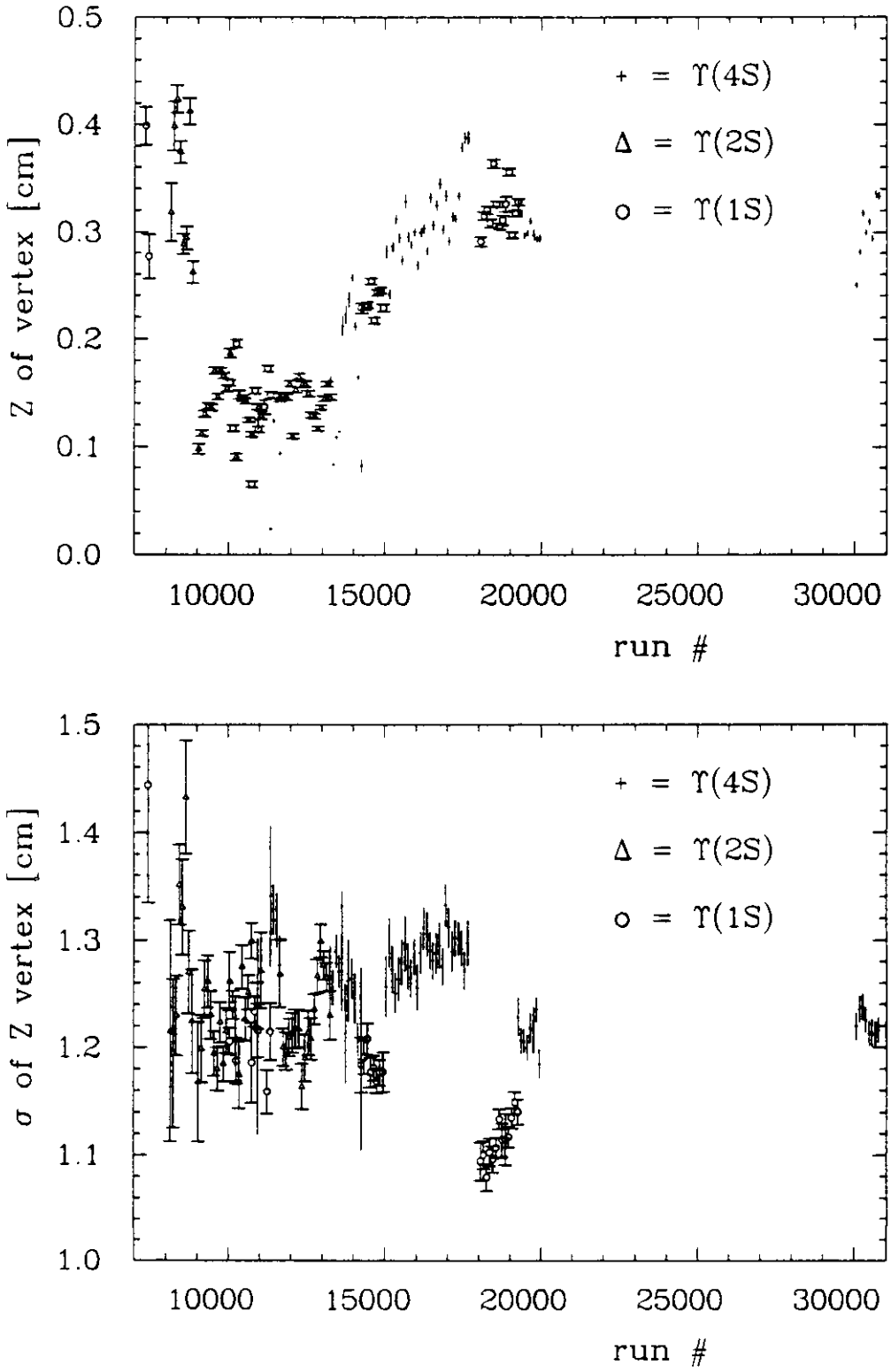

Figure B.10: *Z of vertex and σ_Z vertex versus run period. Always 100 runs are collected in one bin.*

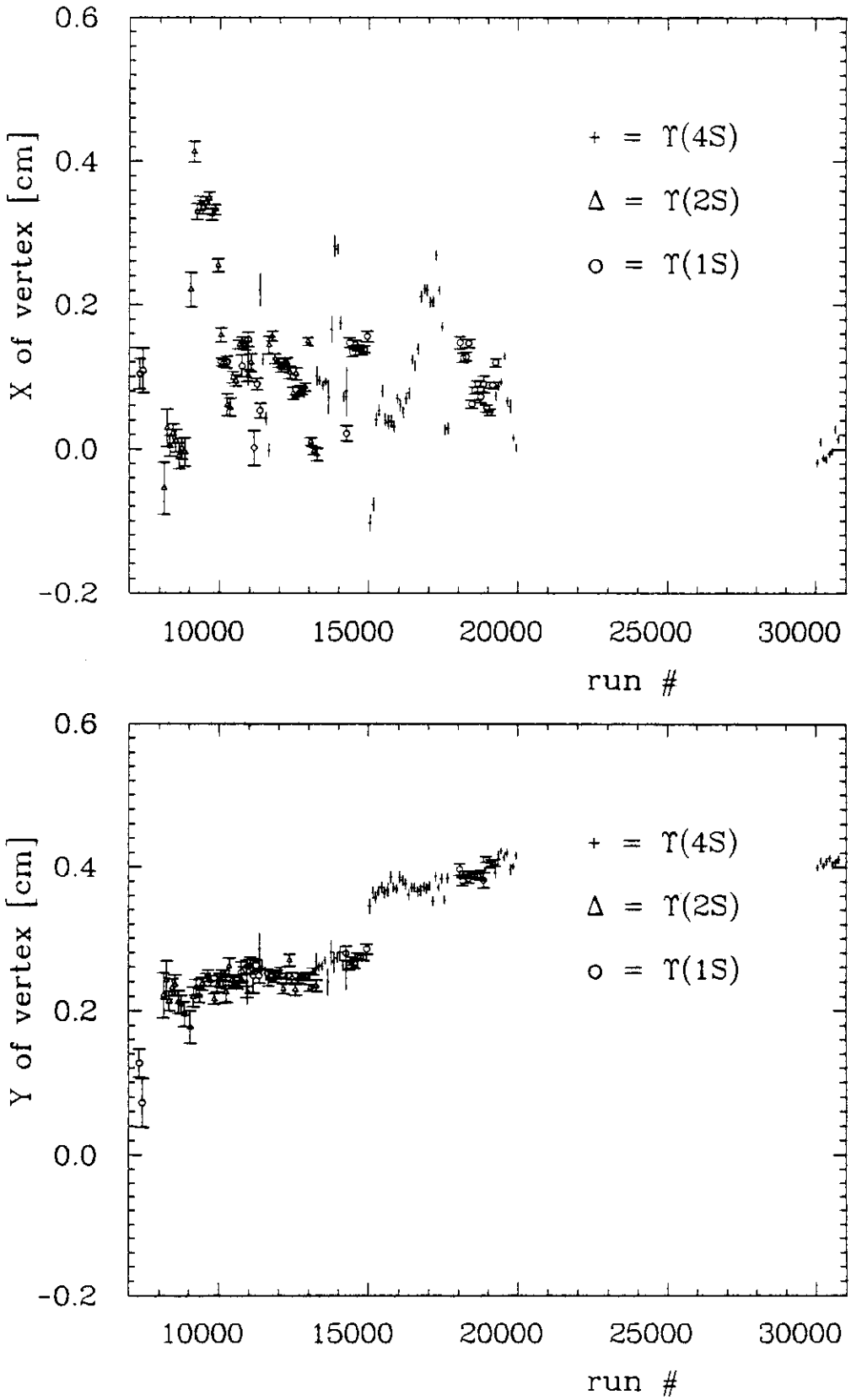

Figure B.11: *X, Y of vertex versus run period. Always 100 runs are collected in one bin.*

Appendix C

Tube Chamber Calibration

The purpose of the calibration is to find the constants needed to convert the raw pulse heights to the φ and Z-position of hits in the tube chambers and to keep the efficiency to detect charged particles constant. The φ position of a hit is simply given by the coordinate of the tube. The Z position is calculated using the pulse height from both ends of the tube:

$$Z/L \equiv \frac{Q_L - \alpha\, Q_R}{Q_L + \alpha\, Q_R} \times (1 + \beta_L + \beta_R) - (\beta_L - \beta_R), \qquad \text{(C.1)}$$

where $Q_{L,R}$ is the pulse height left, right, pedestal-subtracted;
α is the ratio of gains of the left- and right-hand side amplifiers;
$\beta_{L,R}$ are the input impedances of the of amplifiers left, right, divided by the wire impedance;
L is half the length of the tube.

One set of parameters is determined once and then kept. These parameters are the length L, the φ position of the tubes, and the amplifier impedances. The pedestals and the gain ratios may vary because of drifts in the electronics and different background conditions in different running periods.

C.1 Phi Calibration

For the calibration of the φ position of the tubes Bhabha events are used. The same selection as used for the vertex determination is taken – back to back e^+ e^- . The difference in φ between the e^+ e^- direction and the closest tube hit is recorded for each tube. After calculating the average φ positions for each tube from the recorded e^+e^- directions, the φ position of the individual tube φ_i is fitted to a straight line in φ: $\varphi_i = \varphi_0 + \alpha \times \varphi \times i$, using no tubes close to the equator plane.

Figure C.1 shows the φ resolution obtained in layer 8. All positions are determined to an accuracy of about 2 *mrad* beside the tubes at the edges ($\varphi = 0^0, 180^0$) where the direction determination in the ball is poorer due to the gap in the Ball at the equator. This position accuracy in φ is much better than the spacing of the tubes: for the individual layer simply the number of tubes determines the resolution, see table 3.3. The φ resolution per chamber (double layer) is about a factor of 1.5 better because the two layers of one chamber are displaced in φ by half a tube diameter.

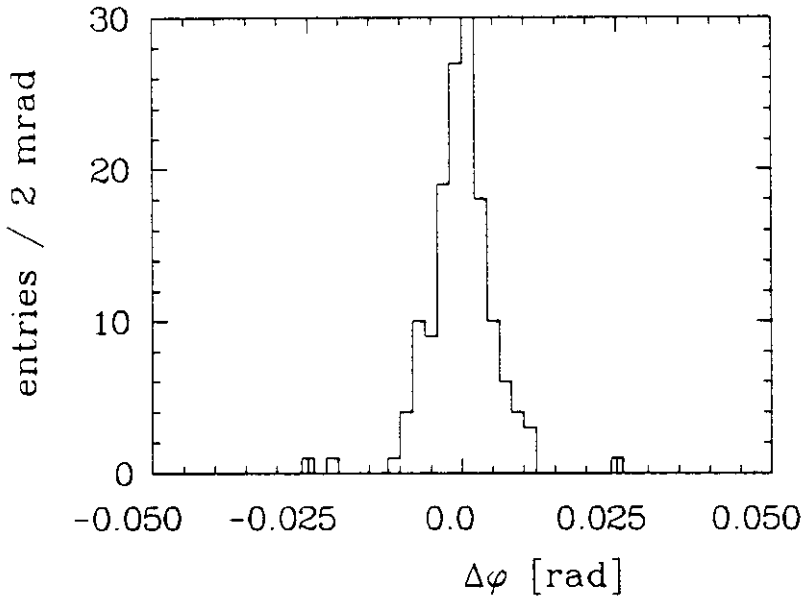

Figure C.1: *The measured φ resolution in layer 8*

C.2 Pedestal Calibration

The pedestals are calibrated with normal events having no pulse height cut. In a first step the average pulse height for each tube is calculated. In an iterative process – two to three iterations– the same events are used again. Only hits which are closer in pulse height than 20 mV to the last average are taken. The variation of the average in the second or third iteration is smaller than 0.5 mV. The averages are then defined as pedestals.

Figure C.2 shows the pedestals for two wires during a certain run period. The variations are bigger in the innermost layer compared to the outermost one. Figure C.3 shows the pedestal width – which mainly determines the Z resolution– for the different layers. In the outermost layers the width is comparable to digitalization (1 bit = 1 mV), while in the innermost layers the width is mainly determined by random hits due to synchrotron radiation and not by electronics.

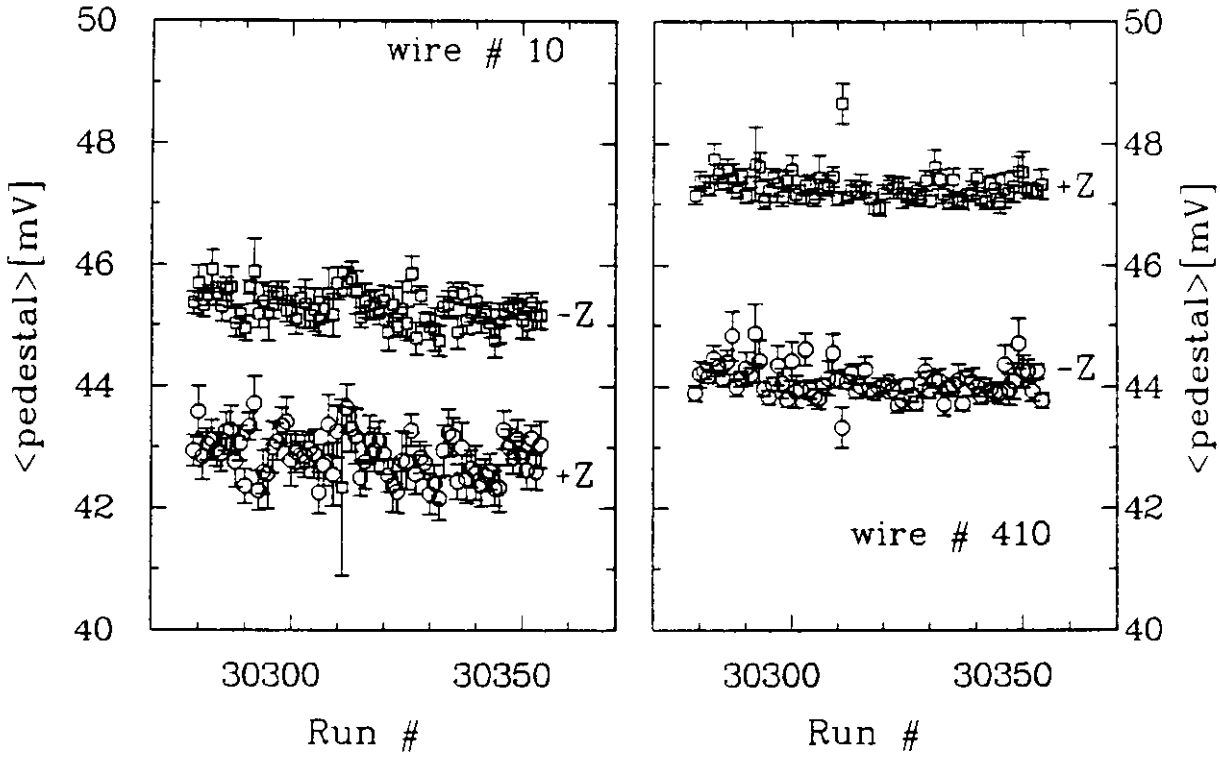

Figure C.2: *The measured pedestals of two different wires versus run number with the error bar indicating the pedestal widths.*

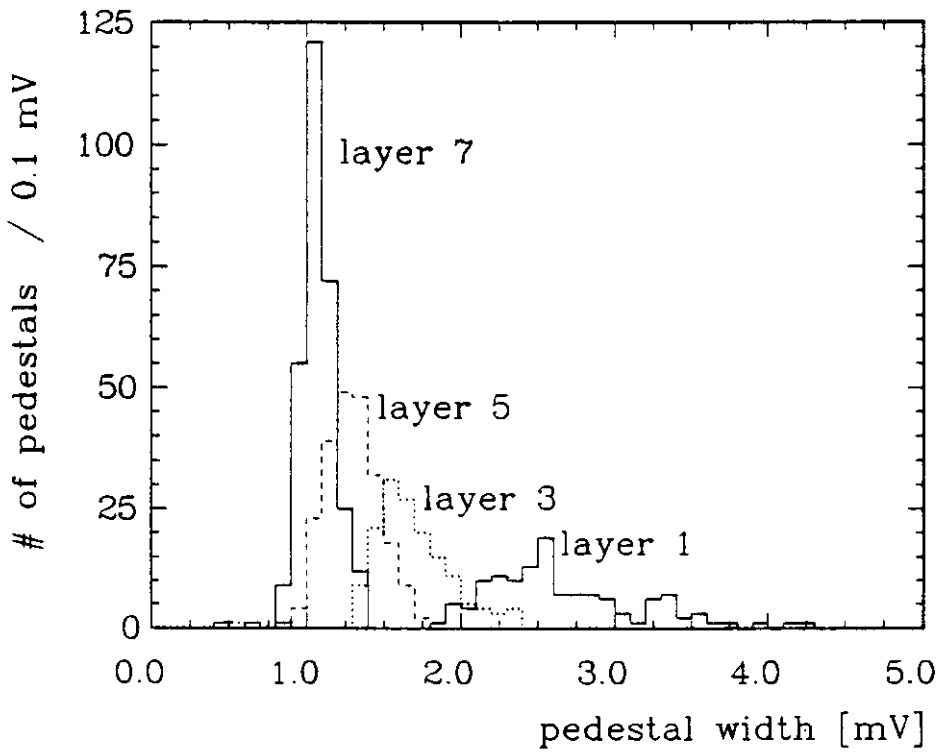

Figure C.3: *The measured distribution of pedestal width in different layers, one entry per amplifier.*

C.3 Z Calibration

To calibrate the constants needed for the Z measurement the same tracks used for the φ calibration are taken. The position predicted by the Bhabha track Z_B and the left and right pulse height is stored for each tube for further use. A fit of the Z position measured by the tubes (Z_T) to the predicted Z position Z_B with formula (C.1) for each individual tube is performed with the gain ratio left as a free parameter. The result of the fit to all tubes of a layer is inspected and the impedances are changed for all tubes in a layer at the same time. As expressed in formula (C.1) a change in $(\beta_L + \beta_R)$ is equivalent to a change in L. The effect of a wrong $(\beta_L + \beta_R)$ could be seen in a plot $\Delta Z = Z_T - Z_B$ against Z_B. If the impedances would be wrong the points would lie online with a non-zero slope. A difference in the impedances between the left and right amplifier would show up in a shift of the line in this plot. After corrections to the impedances to tune ΔZ to zero, the gain ratios are fitted again. The fitting procedure is stopped when no improvement is visible. The impedances are then fixed and only the gain ratios are calibrated about once a week.

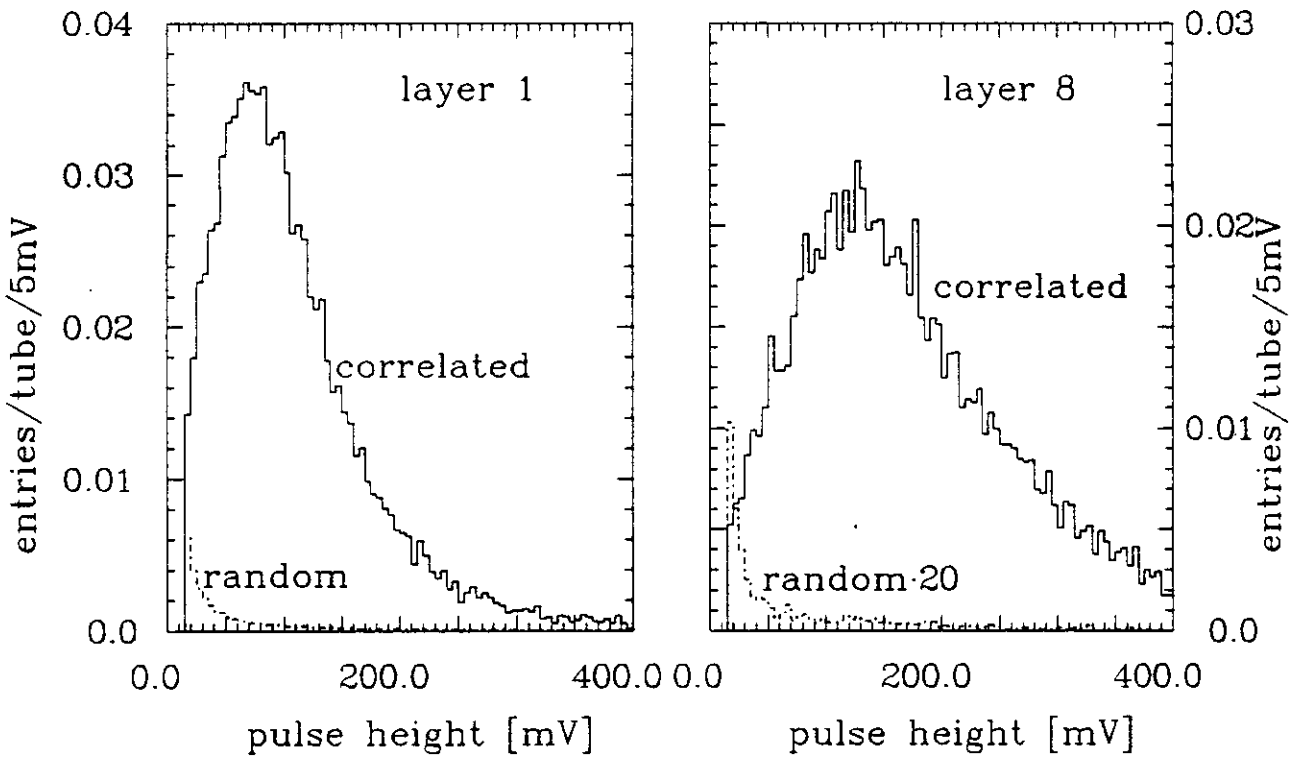

Figure C.4: *Pulse height distribution of random and correlated hits in layer 1 and 8*

C.4 Pulse Height Cut

To get a stable efficiency for detecting charged particles, a pulse height cut is introduced. Pulse heights which are below this threshold are not considered to be a hit. Figure C.4 shows the pulse height distributions of correlated and random hits for different layers. They are taken from the same Bhabha sample used for the other tube chamber calibration procedures. A hit is correlated if it is closer than 1.5 tubes in φ to the predicted track direction as determined in the Ball. Random hits are taken

from the direction perpendicular in φ to the predicted tracks, where no hit from the tracks is expected. The pulse height distribution of correlated hits is not separated from the random hit distribution. This is due to the geometrical acceptance of a single tube. The path length of a track which passes through the center of the tube is longer than the path length of tracks passing close to the wall of the tube. Therefore also the deposited energy varies.

To become independent of this effect we use the '2 layer or' pulse height, which is defined as the pulse height of a hit correlated with the track with the largest signal in the 2 layers. The random hit probability is obtained by the same procedure but using a virtual track with a direction perpendicular in φ to the track predicted by the Ball. Figure C.5 top shows the '2 layer or' for random hits and for correlated hits. Now a better separation is achieved. The efficiency to get a correlated - or random hit- is obtained by integrating the pulse height distribution from the cut to infinity. This integrated spectrum is shown in figure C.5 bottom. The cut is placed in such a way that a high efficiency is obtained together with a low random hit probability. For other calibration periods the cuts are scaled with the average pulse height of the correlated hits in one chamber. See chapter C5 for the behaviour of the efficiency during different run periods.

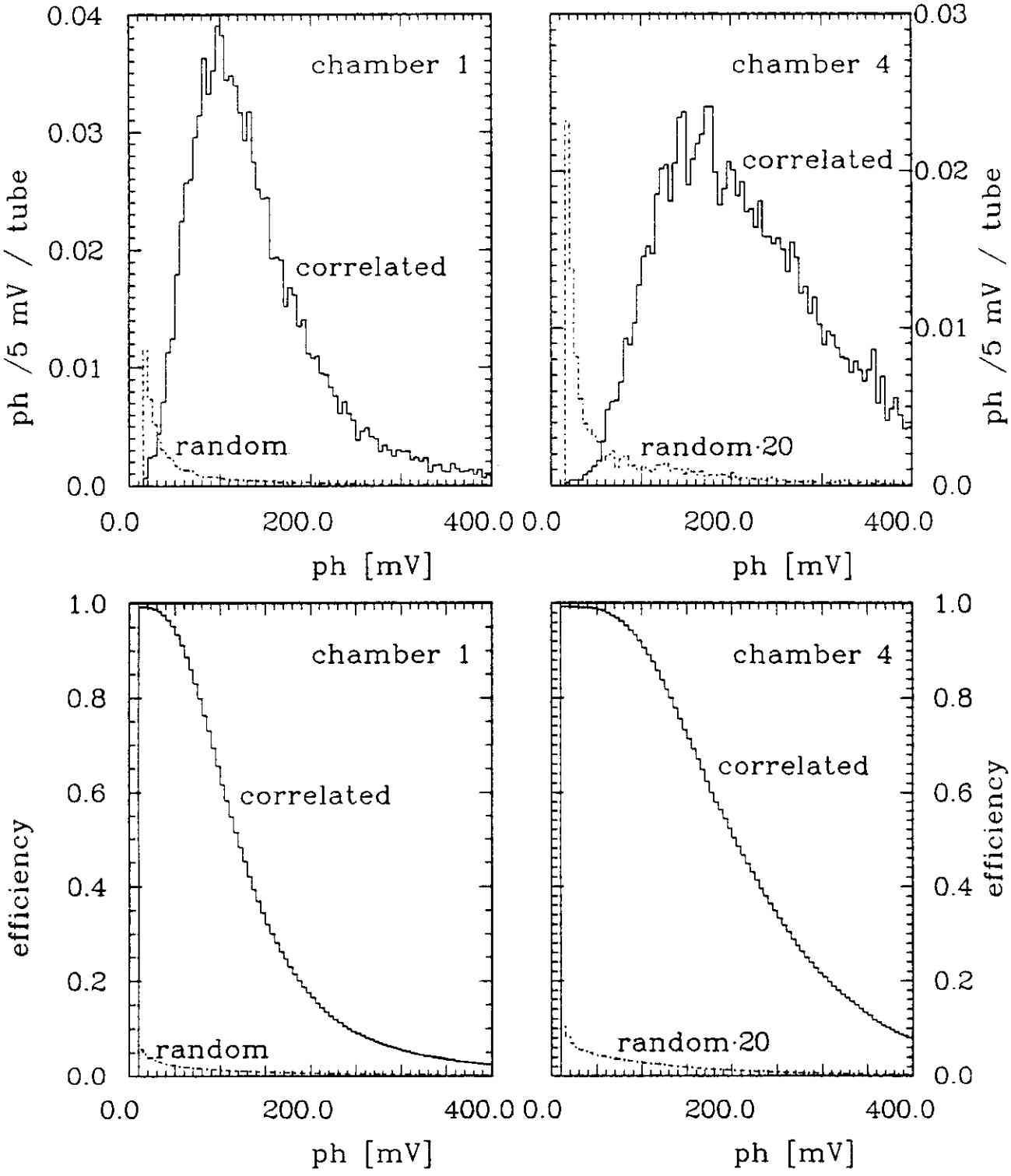

Figure C.5: *Pulse height distribution of random and correlated hits and efficiencies in chambers 1 and 4. For instance cutting at 50 mV results in : a 95% efficiency to have at least one hit in chamber 1 and a 2% probability for at least one random hit. For the same cut values in chamber 4 the numbers are 99 % and 0.2 % , respectively.*

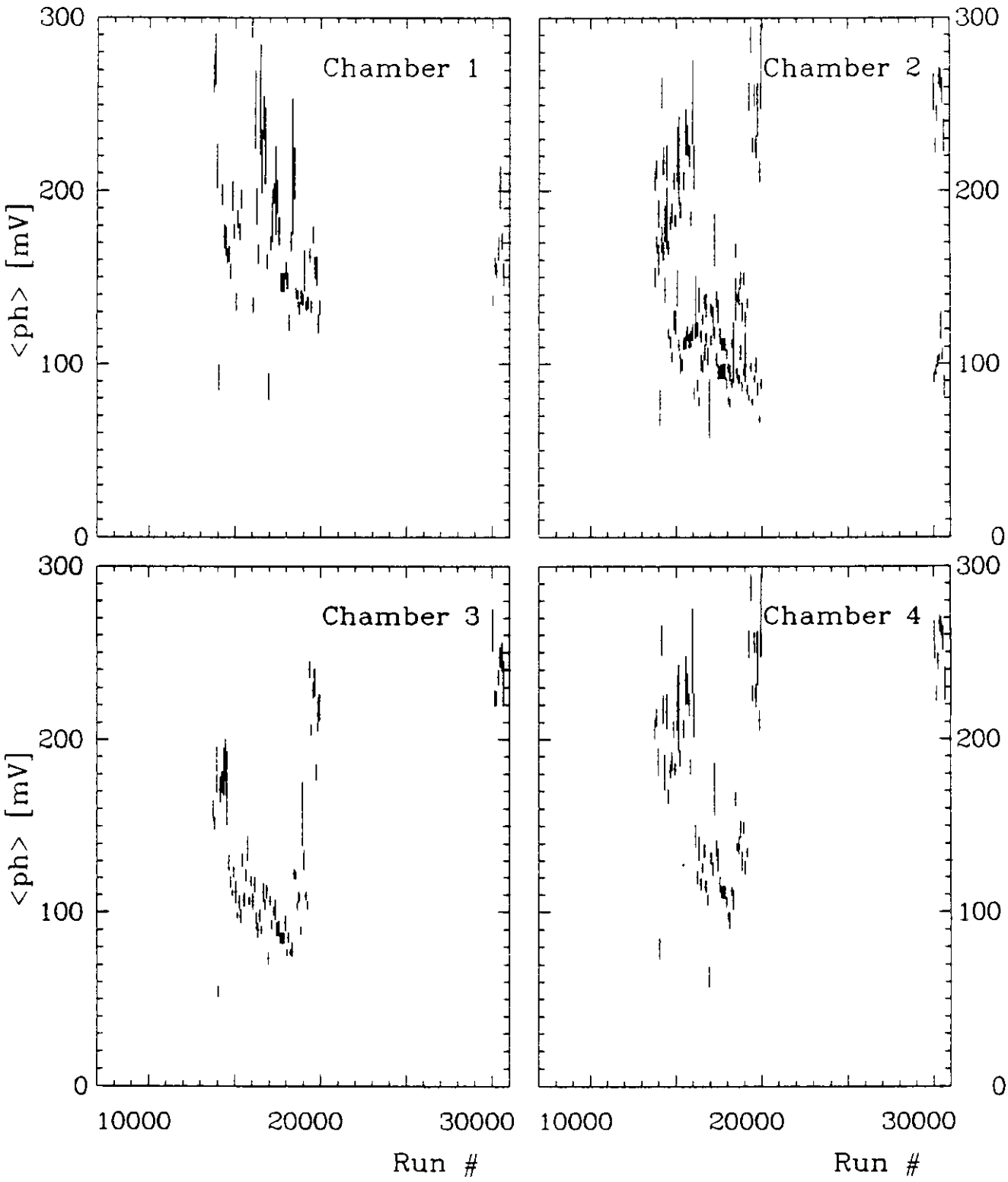

Figure C.6: *Mean pulse heights for the 4 chambers and different runs. Always 100 runs are collected in one bin. No entries for runs 20000 to 30000 which are MC runs.*

C.5 Tube Chamber Performance for Different Run Periods

In this chapter we discuss the long term stability of the tube chamber performance. Only those runs are used in the analysis where the tube chamber had a reasonably smooth behaviour. We therefore check the efficiency and the Z resolution as a function of the run number. First we look at the tube pulse heights.

Figures C.6 show the average pulse heights for all 4 chambers for the different running periods. The changes of the average pulse heights have several reasons. Figure C.7 shows the average pulse height as function of the high voltage. Although

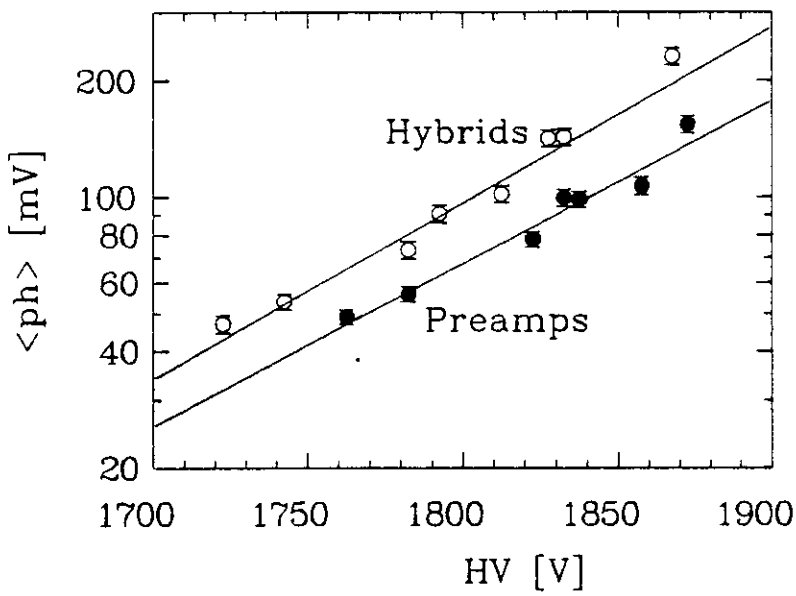

Figure C.7: *Measured pulse height versus high voltage for 'Hybrid' and 'Preamp' channels. The solid lines are fits to the data with an exponential.*

the hybrids and the preamps – old version – have the same gain, the hybrids have a factor of two higher output at the same high voltage. The cables between the tubes and the preamps damp the signal by a factor of two, the hybrids are directly connected with thin wires of ≈ 3 *cm* length. The hybrids are sensitive to sparks induced in the tubes. When the charge of a chamber is dumped into an amplifier the input transistor may be damaged. This does not happen with the preamps, as the input is protected by a carbon type resistor of 30 Ω which limits the current.

Therefore the high voltage of the chambers 1 and 2 were lowered in order to reduce the spark frequency, when the beam conditions were bad. To raise the output of the preamps the gain was increased by a factor of two. Other changes of the output are due to changes of the density of the gas in the tubes. The gas system was an open system, the outlet leading to open air. Therefore the pressure – and the density – varied with the athmospheric pressure. A higher density results in a linear increase of dE/dx, but the gas amplification is exponentially decreased. The exponent is proportional to the mean free path of the electrons in the gas. This path length is clearly inverse proportional to the density of the gas. All these modifications and changes together explain the variations of the mean pulse heights.

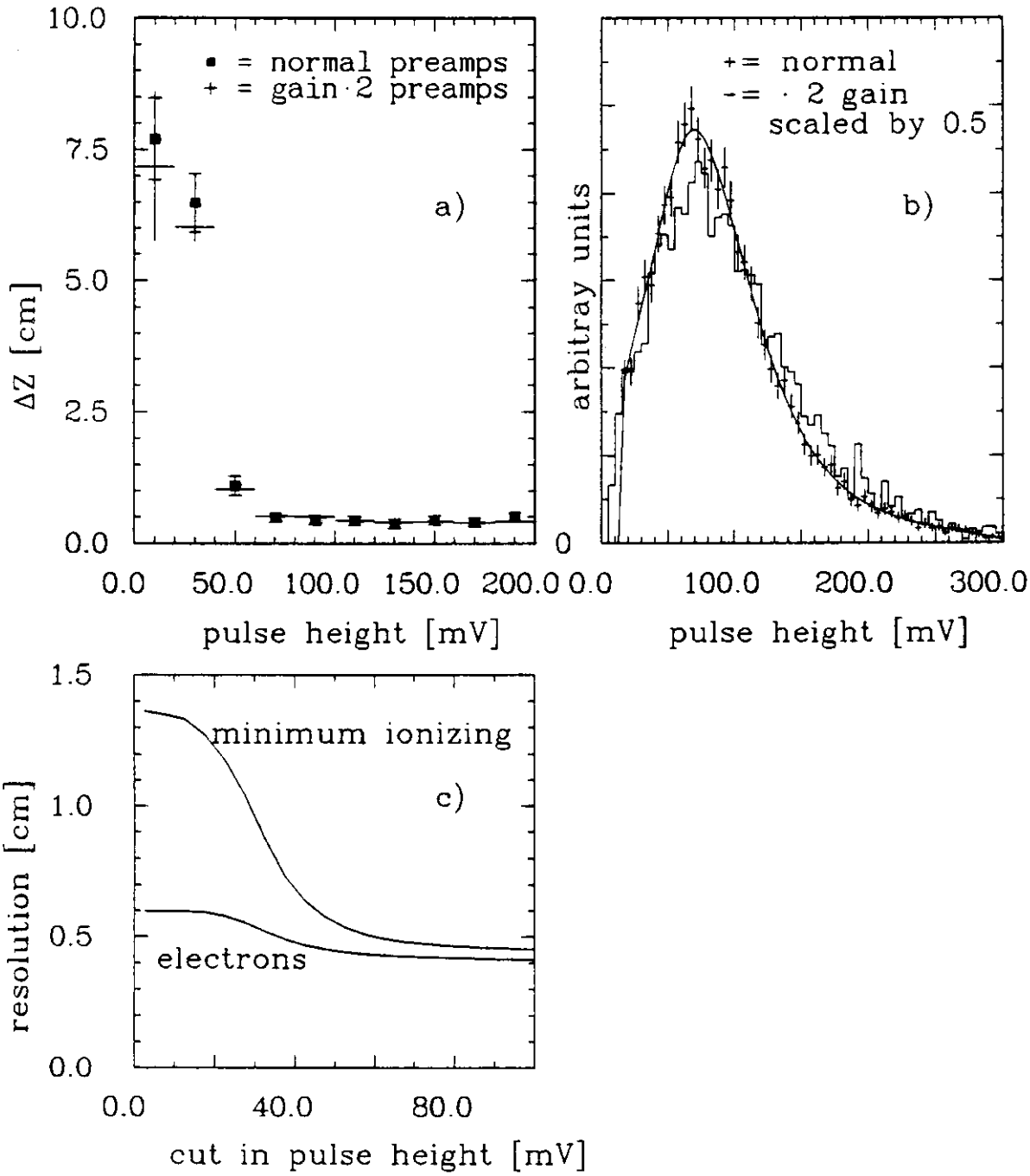

Figure C.8: *a) pulse height distributions, b) ΔZ versus pulse height.and c) Z resolution versus pulse height cut for normal and improved (factor 2 gain) preamps*

C.5.1 Z Resolution

The different pulse height distributions and pedestal widths naturally have an impact on the Z resolution of the chambers. As the average pulse heights with the 4 chamber setup are around 100 mV, the pedestal width of about 1 mV has the largest impact: assuming a pulse of 50 mV at both ends yields in a 3% resolution, only from the pedestal width. Therefore the installed preamplifiers were modified in order to increase the signal output by a factor of two.

Raising the gain of the preamps results in a better Z resolution for minimum ionizing particles. Figure C.8b proves that the pulse height distribution is indeed a factor of two higher than that from preamps with the normal gain. The Z resolution as a function of pulse height is displayed in figure C.8a for normal and modified preamps. The resolution as function of pulse height is the same for both types of the preamplifiers. The average observed resolution for all particles is given by the convolution of the pulse height distribution and the Z resolution. Minimum ionizing particles have a factor of two lower pulse heights than the electrons from Bhabha events. Figures C.8c shows the influence of the pulse height cut on the Z resolution for electrons and minmum ionizing particles. As the new preamps have a factor of two higher gain, the pulse height cut is raised by the same factor in order to keep the efficiency constant.

With the new preamplifiers the Z resolution for electrons changes only slightly, but for minimum ionizing particles it improves from $\approx$ 1 cm to $\approx$ 0.6 cm. Figure C.9 and C.10 show the measured Z resolution for electrons in all chambers as a function of the run number. Large fluctuations are visible. In the run period 13800 to 14500 the tube chamber ADC was damaged, it had a non-linear response. Therefore the Z resolution became worse. The data used in this analysis starts with run 15448.

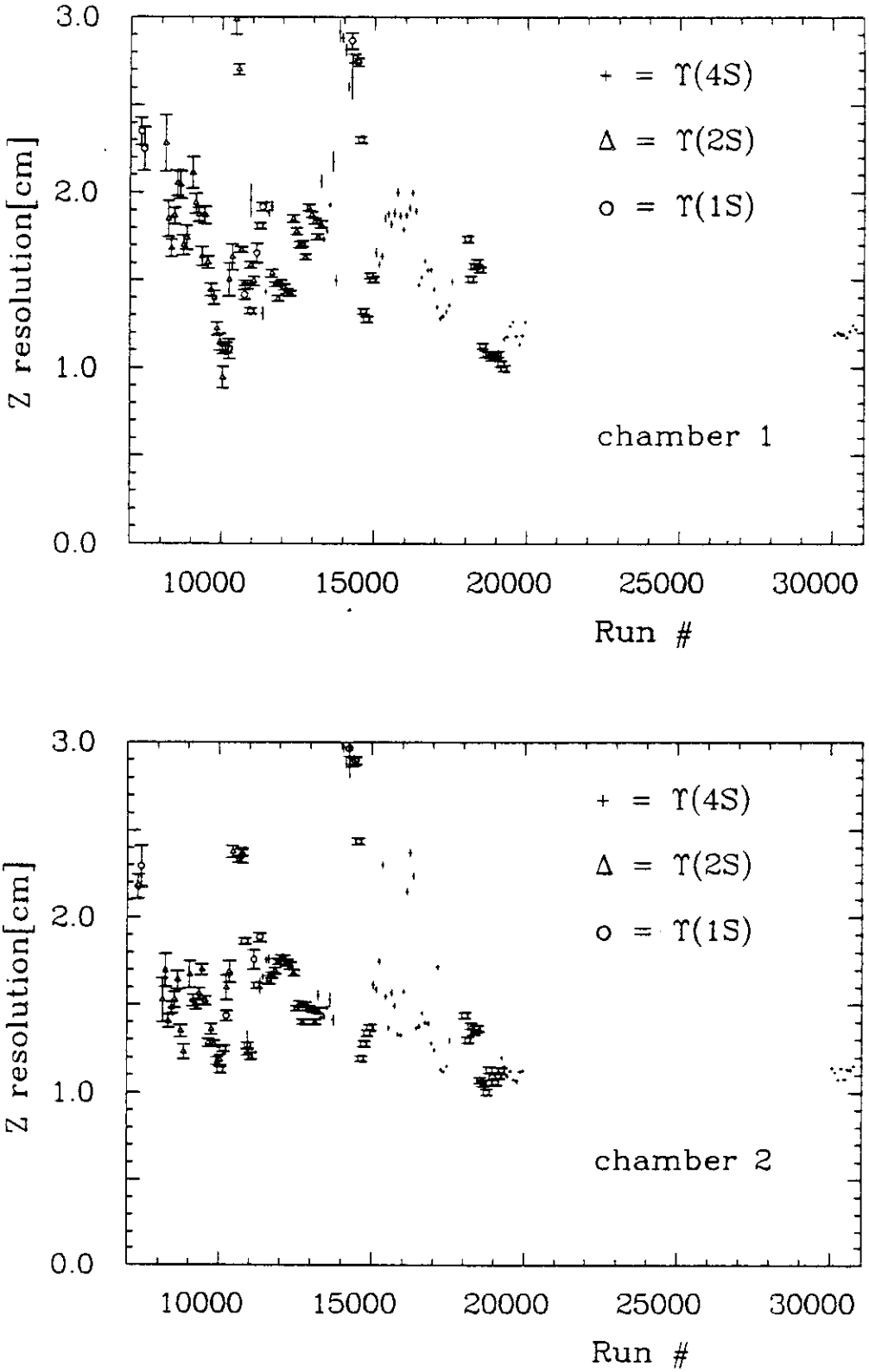

Figure C.9: *Z resolution of chamber 1 and 2 versus run period. Always 100 runs are collected in one bin.*

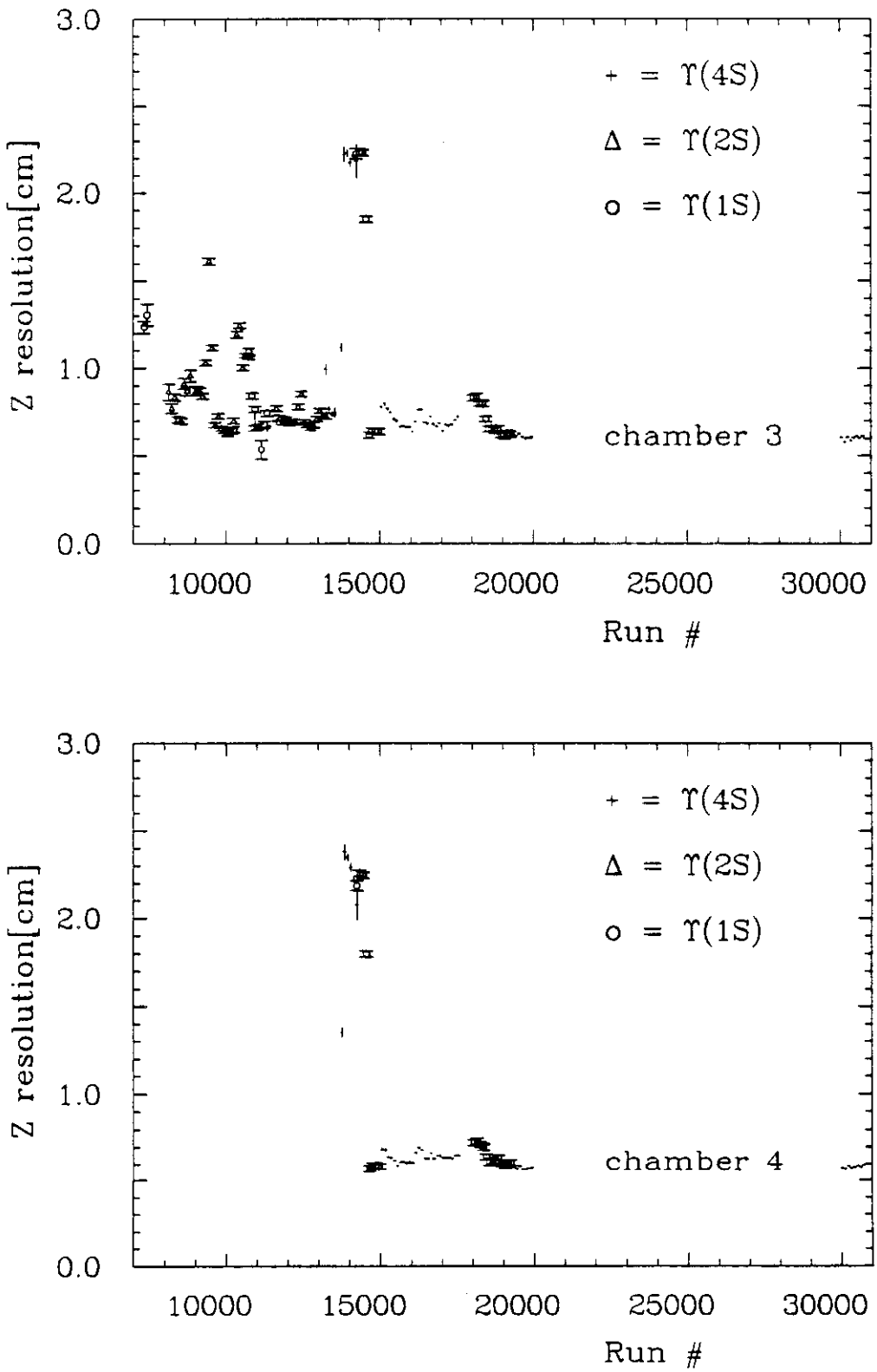

Figure C.10: *Z resolution of chamber 3 and 4 versus run period. Always 100 runs are collected in one bin. Before run 13600 no* 4^{th} *chamber was installed*

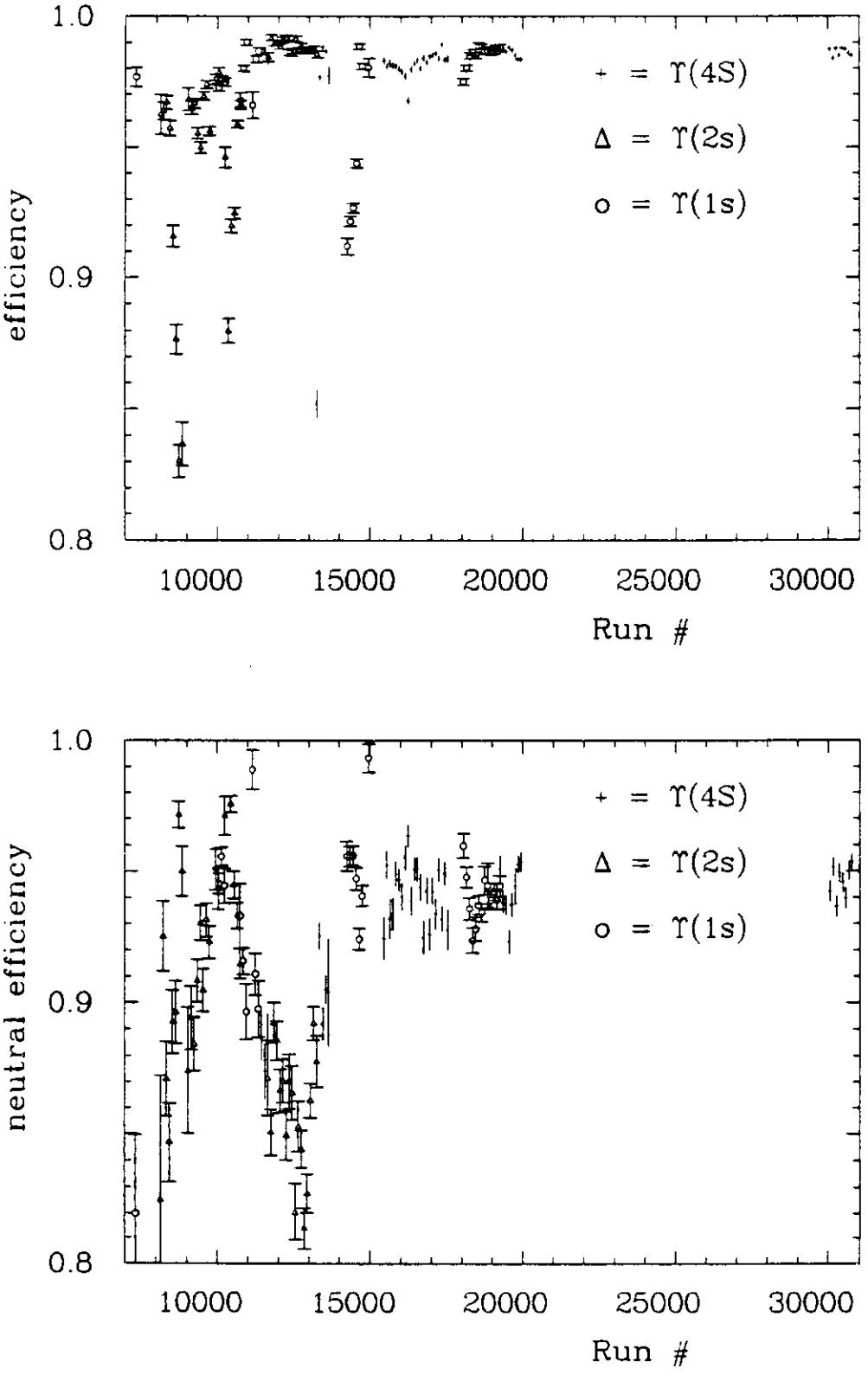

Figure C.11: *Chamber efficiciency to tag electrons charged and to find photons neutral versus run period. Always 100 runs are collected in one bin.*

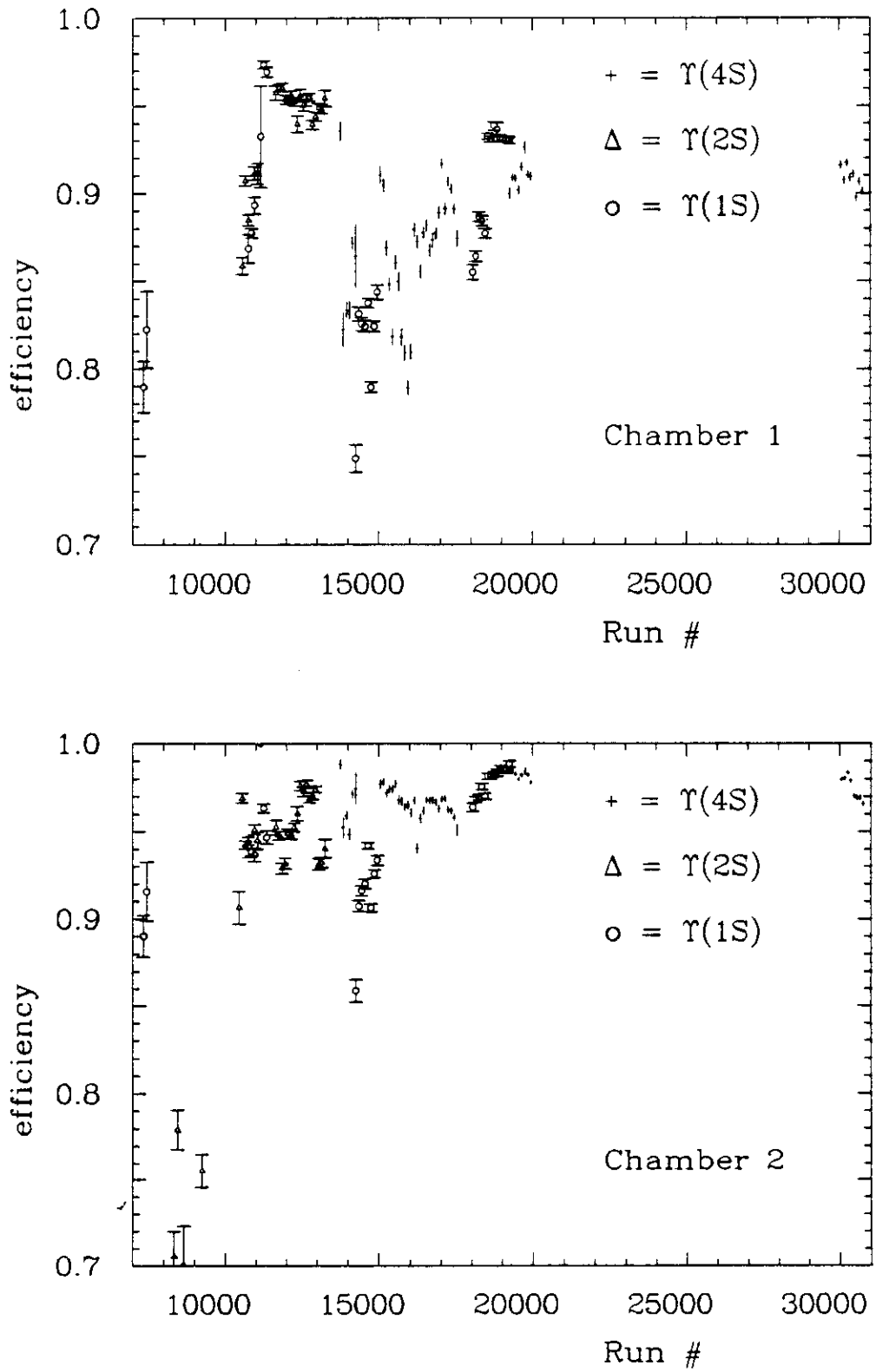

Figure C.12: *Efficiency of chamber 1 and 2 to have at least one hit per electron versus run period. Always 100 runs are collected in one bin.*

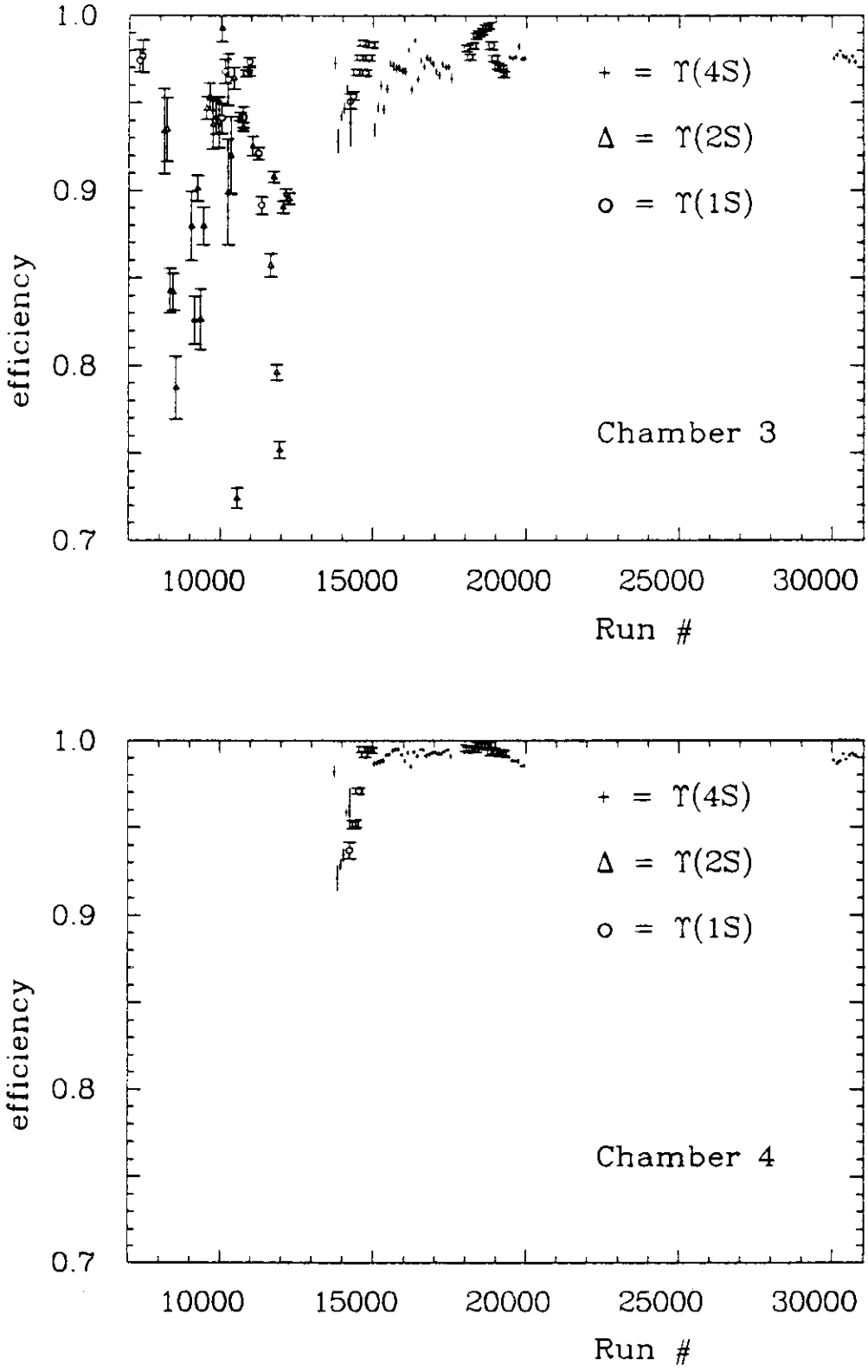

Figure C.13: *Efficiency of chamber 3 and 4 to have at least one hit per electron versus run period. Always 100 runs are collected in one bin. Before run 13600 no 4^{th} Chamber was installed*

C.5.2 Tagging Efficiency

At first the method to determine the efficiency to tag or track electrons as charged and tag photons neutral is explained. In addition the efficiency of all chambers is discussed. Then the average efficiency for the data sample used here is calculated for different particle types.

The efficiency for finding a track from electrons in the tube chamber is obtained in the following way. One uses events with two high energetic clusters– $E^c_{13} > 0.7 \times E_{BEAM}$. The background from non-e^+e^- or - $\gamma\gamma$ events contained in this sample is less than 0.2%, see appendix B.

All events in the above sample are assumed to come from e^+e^- or $\gamma\gamma$ events. The number of events with two charged, N_{CC}, one charged and one neutral, N_{CN}, and two neutral tracks, N_{NN}, are:

$$\begin{array}{rcccc} N_{CC} & = & \epsilon_c^2 & \times N_{ee} + & (1-\epsilon_n)^2 \times N_{\gamma\gamma} \\ N_{CN}/2 & = & \epsilon_c(1-\epsilon_c) & \times N_{ee} + & \epsilon_n(1-\epsilon_n) \times N_{\gamma\gamma} \\ N_{NN} & = & (1-\epsilon_c)^2 & \times N_{ee} + & \epsilon_n^2 \times N_{\gamma\gamma} \\ r & = & N_{ee}/N_{\gamma\gamma} & & \end{array} \qquad \text{(C.2)}$$

The unknowns are the charged efficiency ϵ_c, the neutral efficiency, ϵ_n, (i.e. the probability that a photon does not produce a charged track in the chamber and is therefore found to be neutral), and the number of ee, N_{ee}, and $\gamma\gamma$ events, $N_{\gamma\gamma}$. The measured quantities are N_{CC}, N_{CN}, N_{NN}. The quantity r in the fourth equation is taken from Monte Carlo calculations. Only a small dependence on the Monte Carlo simulation is expected as the systematic errors of the detector simulation and of the event generation cancel. Equation C.2 is solved by matrix inversion.

Figure C.11 shows the efficiency of finding an electron charged by this method as a function of the run number – for an isotropic distribution in $|cos\theta| < 0.75$. The neutral efficiency is shown in figure C.11. Large fluctuations are visible. They are due to bad chamber performances and problems of the electronics.

The data used in this analysis are restricted to periods when the behaviour is stable, i.e. for run number > 15447. The average efficiencies for the $\Upsilon(4S)$ data sample used in this analysis are $\epsilon_c = (98.5 \pm 0.5)\%$ and $\epsilon_n = (94.6 \pm 0.5)\%$ for the electrons and photons, respectively.

This 'matrix inversion' method is cross-checked by another method using the same events. If one track is charged, it is taken as a tag of the charge of the other track. The efficiency then is simply given by number of charged tracks on the non-tagged side divided by all trials.

A small contamination from two-photon events must be taken into account. A photon may convert in the chamber and simulate a tagging particle. The contribution from $\gamma's$ to the electron sample is the conversion probability times the two-photon event contamination. The two-photon contamination is about 8 to 15 % depending on the solid angle coverage. Together with the conversion probability of photons of 5.4% quoted above, the efficiency obtained by this method must be about 1% smaller than the efficiency obtained by the matrix inversion method. This is found to be true.

The performance of the individual chambers over the run periods can be seen in figures C.12 and C.13. To avoid the geometrical inefficiency of a single layer, the 'two layer or' is used to define the efficiency of a chamber. In addition, to the tag by

one particle three extra hits on the track are required to measure the efficiency. This reduces the $\gamma\gamma$ contamination to less than 0.1%.

The efficiency to detect other charged particles is shown is table C.1.

particle type	electrons	5 $GeV\mu$	100 $MeV\mu$	mips from $\tau\overline{\tau}$ events	mips from multi-hadron events
efficiency[%]	98.5 ± 0.5	96.9 ± 1	94.0 ± 1	95 ± 1	93.7 ± 1

Table C.1: *Charge efficiency for different particles and isotropic distribution in cosθ. The different selection procedures are described in the text. Mips stands for minimum ionizing particles.*

The efficiency for other particles than electrons could in principle be obtained by using the electron data and scaling the pulse height cut by the ratio of mean pulse heights of the particle types. The pulse heights vary due to the different energy losses of the particles in matter.

Instead of that we use other particles selected as follows:

- Events with two muons of 5 GeV are selected by pattern cuts and a hit in the roof ToF counters.
- Events with two muons of about 100 MeV are selected by the same pattern cuts and a ToF counter veto. They are produced in two-photon reactions.
- Minimum ionizing particles from $\tau\overline{\tau}$ decays are from events with (e, μ) or $(e, \pi^{\pm})$ in the final state. They are selected by the following cuts: one cluster with minimum ionizing pattern and of energy of 100 to 300 MeV, one charged electromagnetically showering particle of more than 1.5 GeV energy and no other connected region are required.
- The minimum ionizing particles inside multi-hadron events are selected by a very strong pattern cut: $E_1/E_{13} = 1.0$. This cut makes sure, that no overlap with other particles is possible. This sample of minimum ionizing tracks consists of a mixture of all charged hadrons (and muons) with different momenta.

The charge efficiency of the different particle types and momenta varies between 93.6% and 98.5%. This effect can also be seen by comparing the pulse height distributions of the different particles (e, 5 GeV μ, 100 MeV μ, mips from multi-hadron events). They are shown in figure C.14 and obtained by the following procedure: the pulse height from each layer is normalized to the mean pulse height from Bhabha events of that run period. This compensates the variations of the mean pulse height due to e.g. different high voltages during different run periods. In additon the pulse height is multiplied by $sin\theta$ which corrects for the different path lengths of the particles through the tubes.

Electrons of 5 GeV give the highest pulse heights. The measured energy losses, compared to that of electrons, of muons of 5 GeV and 100 MeV is in nice agreement with the theoretical prediction [53] using the peak values of the distributions.

The distribution of minimum ionizing particles from multi-hadron events lies between that obtained from low energy (100 MeV) and high energy muons (5 GeV).

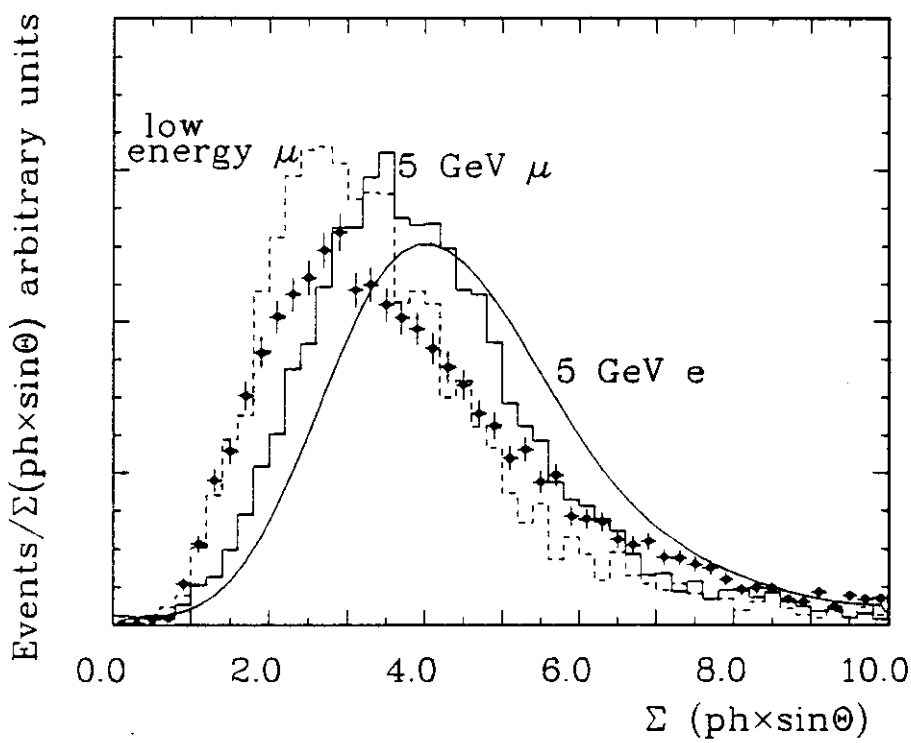

Figure C.14: *Pulse height distribution for different particle types normalized to the mean electron pulse height and corrected for the different path lengths in the tubes. The distribution are labeled with particle type and energy. The dots with crosses refere to minimum ionizing particles from multi-hadron events.*

Appendix D

The Efficiency-Corrected Electron Spectrum

Energy $[GeV]$	$\frac{10}{N_B}\frac{dN}{dE}$ $[1/GeV]$	error$\times 10$ $[1/GeV]$	Energy $[GeV]$	$\frac{10}{N_B}\frac{dN}{dE}$ $[1/GeV]$	error$\times 10$ $[1/GeV]$
0.625	1.44	0.31	1.825	0.779	0.080
0.675	1.21	0.27	1.875	0.718	0.076
0.725	1.13	0.24	1.925	0.582	0.070
0.775	1.43	0.22	1.975	0.569	0.068
0.825	1.44	0.20	2.025	0.426	0.061
0.875	1.01	0.18	2.075	0.386	0.058
0.925	1.14	0.16	2.125	0.224	0.049
0.975	1.15	0.15	2.175	0.183	0.045
1.025	0.989	0.14	2.225	0.051	0.035
1.075	1.06	0.13	2.275	0.076	0.037
1.125	0.803	0.12	2.325	0.046	0.033
1.175	0.902	0.11	2.375	0.058	0.034
1.225	0.761	0.10	2.425	- 0.010	0.027
1.275	0.907	0.10	2.475	- 0.035	0.023
1.325	1.00	0.10	2.525	0.006	0.027
1.375	0.882	0.10	2.575	- 0.014	0.025
1.425	1.06	0.10	2.625	0.014	0.027
1.475	1.11	0.10	2.675	0.024	0.028
1.525	1.08	0.099	2.725	0.003	0.025
1.575	0.970	0.094	2.775	0.007	0.025
1.625	1.08	0.096	2.825	0.010	0.025
1.675	0.843	0.086	2.875	0.026	0.027
1.725	1.00	0.090	2.925	0.00	0.022
1.775	1.05	0.091	2.975	- 0.002	0.020

Table D.1: *The electron spectrum of B meson decays including electrons from subsequent decays of B meson decay products, as for instance $c \rightarrow e\nu s$. The spectrum is normalized to the number of B mesons. Background and continuum contributions are subtracted. The data are corrected for detection efficiency. The errors quoted are statistical only. A common systematic error of $\Delta N/N = 6\%$ has to be added.*

Appendix E

Acknowledgement

This work would have not been possible without the combined effort of the whole Crystal Ball collaboration. We therefore want to thank all members for their contributions. Their names are listed on the next page.

Special thanks have to go to M. Bauer, Dr. M. Wirbel, Dr. G.Schuler, and Prof. J.Körner who helped a lot in understanding many aspects of the theory.

From the Crystal Ball group I would like to give prominence to Dr. A. Bizzeti, to Dr. T. Skwarnicki, and especially to Dr. W. Koch. They were always willing to discuss problems and had very often good suggestions for this work.

Miss U. Rehder has to receive many thanks for preparing plots and proof-reading

Prof. Dr. J. K. Bienlein did not only prepare an ideal working athmosphere in the group F31 at DESY, but was a 'Doktorvater' more than I ever expected.

I would like to thank the DESY directorate for the financial support I got. This enabled me to attend many seminars, schools, and conferences abroad.

Appendix F

The Crystal Ball Collaboration

The current members of the Crystal Ball collaboration are:

D. Antreasyan[8], H.W. Bartels[4], Ch. Bieler[7], J.K. Bienlein[4], A. Bizzeti[6], E.D. Bloom[10], K. Brockmüller[4], A. Cartacci[6], M. Cavalli-Sforza[2], R. Clare[10], A. Compagnucci[6], G. Conforto[6], S. Cooper[10], D. Coyne[2], G. Drews[4], K. Fairfield[10], G. Folger[5], A. Fridman[11], D. Gelphman[10], G. Glaser[5], G. Godfrey[10], K. Graaf[7], F.H. Heimlich[7], F.H. Heinsius[7], R. Hofstadter[10], J. Irion[8], Z. Jakubowski[3], K. Karch[11], S. Keh[11], T. Kiel[7], H. Kilian[11], I. Kirkbride[10], M. Kobel[5], W. Koch[4], A.C. König[9], K. Königsmann[11], S. Krüger[7], G. Landi[6], S. Leffler[10], R. Lekebusch[7], A.M. Litke[10], S. Lowe[10], B. Lurz[5], H. Marsiske[4], W. Maschmann[7], P. McBride[8], H. Meyer[4], B. Muryn[3], W.J. Metzger[9], B. Monteleoni[6], B. Niczyporuk[10], G. Nowak[3], C. Peck[1], C. Pegel[7], P.G. Pelfer[6], M. Reidenbach[9], M. Scheer[11], P. Schmitt[11], J. Schotanus[9], J. Schütte[5], A. Schwarz[10], F. Selonke[4], D. Sievers[7], T. Skwarnicki[4], V. Stock[7], K. Strauch[8], U. Strohbusch[7], J. Tompkins[10], B. van Uitert[10], R.T. Van de Walle[9], A. Voigt[4], U. Volland[5], K. Wachs[4], K. Wacker[10], W. Walk[9], H. Wegener[5], D. Williams[8]

They are from the following institutions:

[1] *California Institute of Technology, Pasadena, CA 91125, USA*
[2] *University of California at Santa Cruz, Santa Cruz, CA 95064, USA*
[3] *Cracow Institute of Nuclear Physics, PL-30055 Cracow, Poland*
[4] *Deutsches Elektronen Synchrotron DESY, D-2000 Hamburg, Germany*
[5] *Universität Erlangen-Nürnberg, D-8520 Erlangen, Germany*
[6] *INFN and University of Firenze, I-50100 Firenze, Italy*
[7] *Universität Hamburg, I. Institut für Experimentalphysik, D-2000 Hamburg, Germany*
[8] *Harvard University, Cambridge, MA 02138, USA*
[9] *University of Nijmegen and NIKHEF NL-6525 ED Nijmegen, The Netherlands*
[10] *Department of Physics, HEPL, and Stanford Linear Accelerator Center, Stanford University, Stanford, CA 94305, USA*
[11] *Universität Würzburg, D-8700 Würzburg, Germany*

Bibliography

[1] For an introduction to the Standard Model see for example
I.J.R. Aitchison, A.J.G. Hey, Gauge Theories in Particle Physics, 1983.

[2] M. Kobayashi and T. Maskawa, Prog. Theor. Phys. **49** (1973) 652.

[3] Particle Data Group, Phys. Lett. **170B** (1986) 11

[4] The Glashow - Salam - Weinberg Theory is described by e.g.
E. Albers, B,.W Lee, Phys. Reports **9** (1973) 1

[5] For text books and reports about QCD see e.g.:
P. Becher, M. Böhm, H. Joos, Eichtheorien, 1981;
W. Marciano, H. Pagels, Phys. Reports **36** (1978) 137.

[6] Limits on the top quark mass from the $B^0 - \overline{B^0}$ mixing are given by: W. Schmitt-Parzefall, Talk given at the International Symposium on LEPTON PHOTON Interactions at High Energies, Hamburg, July 27-31,1987.

[7] For an introduction to particle physics and Feynman graphs see for example
I.J.R. Aitchison, A.J.G. Hey, Gauge Theories in Particle Physics, 1983.
D.H. Perkins, Introduction to High Energy Physics, 1982.
E. Lohrmann, Hochenergiephysik, 1981.

[8] Particle Data Group, Phys. Lett. **170B** (1986) 83

[9] D. Andrews *et al.*, Phys. Rev. Lett. **45** (1980) 219.

[10] Z. Jakubowski,*et al.*(Crystal Ball), to be published

[11] S.L. Glashow, J. Iliopoulos, L. Maiani, Phys. Rev. **D2** (1970) 11285

[12] N. Cabbibo Phys. Rev. **10** (1963) 531

[13] L. Maiani, in: Proc. of the 1977 International Symposium on Lepton and Photon Interactions at High Energies, DESY, Hamburg (1977), p 867, and in: Particle Data Group, Phys. Lett. **170B** (1986) 75

[14] A compilation of measurements on the Kobayashi - Maskawamatrix elements is given by K. Kleinknecht, Proceedings of the Leptonic Session of the 22^{nd} Rencontre de Moriond, Les Arc, March 8-15, 1987, p 361.

[15] New measurements of the $\Upsilon(4S)$ and the B masses are reported in: D. Kreinick, Recent B Meson Results from CLEO, in: Proc. of The International Symposium on Production and Decay of Heavy Hadrons, Heidelberg, May,1986, K.R. Schubert, R. Waldi (Ed.);

S. Weseler, Experimental Review on B Meson Decays, in: Proc. of The International Symposium on Production and Decay of Heavy Hadrons, Heidelberg, May,1986, K.R. Schubert, R. Waldi (Ed.);
C. Bebec, Exclusive Decays and Masses of the B Mesons, The CLEO Collaboration, Cornell preprint CLNS, 86/742.

[16] G. Altarelli, N.Cabibbo, G.Corbo, L.Maiani, G. Martinelli, Nucl. Phys. **B208** (1982) 365. In this paper refered to as ACM.

[17] N. Cabibbo and L. Maiani, Phys. Lett. **79B** (1978) 109.

[18] B. Grinstein, M. B. Wise, N. Isgur, Phys. Rev. Lett. **56** (1986) 298 and California Institute of Technology preprint CALT-68-1311. In this paper refered to as GIW.

[19] T. Altomari and L. Wolfenstein, Carnegie Mellon University preprint, CMU - HEP 86 - 1987. Refered to as AW in this paper.

[20] M. Wirbel , B. Stech and M. Bauer, Z. Phys. **C29** (1985) 637. In this paper refered to as WSB.

[21] J.G. Körner and G.A. Schuler, DESY 87-135 or MZ-TH/87-16. In this paper refered to as KS.

[22] J.G. H. Pietschmann and F. Schoeberl, Europhys. Lett. **B** (1986) 583. In this paper refered to as PS.

[23] S. Herb *et al.*, Phys. Rev. Lett.**39** (1977) 252

[24] The ARGUS detector is described in H. Albrecht *et al.*, Phys. Lett.**134B** (1985) 137 and M. Danilov *et al.*, Nucl. Instr Meth. **217** (1983) 153

[25] K. Wille, DESY-81-047 (1981).

[26] M. Oreglia *et al.*, Phys. Rev. **D25** (1985) 2259;
E. D. Bloom and C. W. Peck, Ann. Rev. Nucl. Part. Sci. **33** (1983) 143.
M. Oreglia Ph.D Thesis, Stanford University, SLAC-236 (1980)

[27] M. Kobel, Diploma Thesis, University of Erlangen, DESY-F31-86-03 (1986),unpublished.

[28] K. Brockmüller; Diploma Thesis, University of Hamburg, DESY-F31-87-05 (1987),unpublished

[29] G. Folger, Ph.D. Thesis, University of Erlangen, DESY-F31-86-04 (1986),unpublished.

[30] H. Marsiske, Ph.D. Thesis, University of Hamburg, DESY-F31-88-02 (1987), unpublished.

[31] J.E. Gaiser, Ph.D Thesis, Stanford University, SLAC-255 (1982), unpublished.

[32] G. C. Fox and S. Wolfram, Nucl. Phys. **B149** (1979) 413.

[33] T. Sjøstrand, Lund preprint, LU TP 85-10, October 1985.
also CERN Pool programs W5035/W5045/W5046/W5047 long writeup.

[34] R. Ford and W. Nelson, SLAC-210 (1978).

[35] H. Fesefeldt, Aachen preprint, PITHA 85/02

[36] J. Schütte, Diploma Thesis, Universität Erlangen, DESY-F31-87-01 (1987), and R.D. Schamberger *et al.*, Phys. Rev. **D30** (1984) 1985

[37] R. Poling, in: Proc. of the 23^{rd} Int. Conf. on High Energy Physics, Berkeley, 1986;

[38] Minimizer program from the CERN Pool programs long writeup D506.

[39] S. Baker and R.D. Cousins, N.I.M. **221** (1984) 437.

[40] For a compilation of the B meson lifetime measurements see e.g. Sau Lan Wu, Lifetimes of Heavy Flavour Particles, talk given the International Symposium on Lepton Photon Interactions at High Energies, Hamburg, July 27-31, 1987.

[41] K.R. Schubert, in: Proc. of the 23^{rd} Int. Conf. on High Energy Physics, Berkeley, 1986.

[42] S. Weseler, Ph.D. thesis, University of Heidelberg, unpublished, 1987.

[43] W. Schmitt-Parzefall, Talk given at the International Symposium on Lepton Photon Interactions at High Energies, Hamburg, July 27-31, 1987.

[44] M. Gilchriese, in: Proc. of the 23^{rd} Int. Conf. on High Energy Physics, Berkeley, 1986; R. Poling, ibid.

[45] T. Jensen, talk given at the 2^{nd} Topical Seminar on Heavy Flavours, San Miniato, May 25-29, 1987

[46] C. Klopfenstein *et al.*, Phys. Lett. **130B** (1983) 444.

[47] W. Maschmann, Diploma Thesis, University of Hamburg 1984, unpublished.

[48] Roger Lee, Ph.D Thesis, Stanford University, SLAC-282 (1986), unpublished.

[49] D. Gelphman *et al.*, Phys. Rev. **D32** (1985) 2893
D. Gelphman, Ph.D Thesis, Stanford University, SLAC-286 (1985);
D. Williams, Ph.D thesis, Harvard University (1987), unpublished.

[50] The formula is from: Particle Data Group, Phys. Lett. **170B** (1986) 45

[51] F.A. Berends, R. Kleiss, Nucl. Phys. B228, 537 (1983),
F.A. Berends, R. Kleiss, Nucl. Phys. B186, 22 (1981)

[52] B. Naroska, DESY-86-113 (1986), e^+e^- Physics with the JADE Detector at PETRA

[53] Experimental data on energy loss in thin media in: F. Harris *et al.*, Nucl. Instr. Meth. **107** (1973) 413